

Turbine Design Development for Pressure Gain Combustion Engines

vorgelegt von
M. Sc.
Majid Asli

an der Fakultät V - Verkehrs- und Maschinensysteme
der Technischen Universität Berlin
zur Erlangung des akademischen Grades

Doktor der Ingenieurwissenschaften
-Dr.-Ing.-

genehmigte Dissertation

Promotionsausschuss:

Vorsitzender:	Prof. Dr.-Ing. Abdulla Ghani
Gutachter:	Prof. Dr.-Ing. Christian Oliver Paschereit
Gutachter:	Prof. Dr.-Sc. Panagiotis Stathopoulos
Gutachter:	Prof. Antonio Andreini
Gutachter:	Prof. Alessandro Sorce

Tag der wissenschaftlichen Aussprache: 16. August 2022

Berlin 2022

Zusammenfassung

Die Energieerzeugung und der Verkehrssektor sind zwei der Emittenten, die in den letzten zehn Jahren einen erheblichen Anteil am globalen Wachstum der Treibhausgasemissionen hatten. Die Zahl der Flugpassagiere sowie stromabhängiger Technologien wächst kontinuierlich. Diese Wachstumsrate ist schneller als die Entwicklung erneuerbarer Energien mit den damit verbundenen Emissionen umgehen kann, daher sind Abhilfemaßnahmen erforderlich, um die Emissionen der aktuellen Technologien zu ändern. Dennoch sind die Gasturbinenkomponenten so ausgereift, dass der Triebwerkswirkungsgrad bei Leistungssteigerungen nicht um mehr als ein halbes Prozent ansteigt. Daher kann eine sprunghafte Änderung des Gasturbinenwirkungsgrads einen Paradigmenwechsel erfordern. Unter den Abhilfemaßnahmen hat sich herausgestellt, dass die Druckverstärkungsverbrennung (PGC) den herkömmlichen Verbrennungstyp mit konstantem Druck ersetzt, was den Gasturbinenwirkungsgrad signifikant erhöht. Für eine zuverlässige Implementierung von PGCs in Gasturbinenkreisläufen müssen jedoch noch viele Herausforderungen gelöst werden.

Abgesehen von den verbrennungsbezogenen offenen Fragen ist die effiziente Energiegewinnung aus PGCs noch ein Engpass beim Einsatz dieser Verbrennungstechnik in Gasturbinen. Eine Turbine in einer konventionellen Gasturbine ist üblicherweise so ausgelegt, dass sie das Abgas einer eher stationären Verbrennungsarbeit mit einem Wirkungsgrad von über 90% entspannt. Diese Turbine verliert jedoch ihre Leistung, wenn sie PGC-Geräten ausgesetzt wird. Der pulsierende Charakter und das stark instabile Abgas von PGCs sind für solche Turbinen so schädlich und werden den gesamten Effizienzgewinn, der von einer PGC-betriebenen Gasturbine erwartet wird, zunichte machen. Daher ist die Entwicklung einer Turbine, die in der Lage ist, Energie aus PGCs effizient zu extrahieren, notwendig, um die Gasturbinenemission deutlich zu reduzieren.

Die vorliegende Dissertation trägt durch zwei Hauptteile zur Integration von Turbinen mit PGC-Geräten bei. Zunächst wird die Wechselwirkung einer stationären Leitschaufelreihe als erste Reihe einer typischen Turbine mit einem rotierenden Detonationsbrenner (RDC) untersucht. Der RDC-Abgasstrom, der durch die stationären Leitschaufeln strömt, wird durch numerische Simulationen charakterisiert, die einen tieferen Einblick in die Details des Strömungsfelds bieten, die in experimentellen Arbeiten unerreichbar sind. Schaufelgeometrieparameter und Schaufeleinstellwinkel werden geändert, um die Rolle der Leitschaufel bei solchen instationären periodischen Strömungen weiter zu untersuchen. Gesamtdruckverlust, Schwankungsdämpfungsfunktion und Leistung der Schaufeln werden analysiert und mit den stationären Betriebsbedingungen verglichen. Die Ergebnisse zeigen, dass der Gesamtdruckverlust der Schaufeln nicht notwendigerweise den herkömmlichen Verlustkorrelationen folgt, die für eine stationäre Strömung entwickelt wurden. Außerdem hat sich herausgestellt, dass

die Leitschaufelreihe mehr als 57% der Schwankung dämpfen kann, während ein höheres Dämpfungsniveau durch Verkürzen der Strömungswegfläche erreicht werden kann, indem entweder die Festigkeit oder die Dicke der Schaufeln erhöht wird. Diese Rolle der Leitschaufeln macht die Strömung günstiger für alle stromabwärtigen Laufschaufeln, die so empfindlich auf die Variation des Einfallswinkels reagieren. Die generische Form der Leitschaufeln, die in dieser Arbeit betrachtet wird, bietet eine Vielzahl von Anreizen für Folgeuntersuchungen zur Gestaltung einer möglichst effektiven Leitschaufel für RDC-Abgasströmung.

Die Wechselwirkung einer mehrstufigen Turbine mit einem gepulsten Detonationsbrenner (PDC) wird im zweiten Teil untersucht, wobei der Schwerpunkt auf der Einführung einer Simulationsmethodik für instationäre Turbinen liegt. Es wird ein eindimensionales Verfahren zur Simulation einer mehrstufigen Axialturbine entwickelt, die mit einer Anordnung von PDC-Rohren verbunden ist. Die Methodik umfasst einen 1D-Euler-Gleichungslöser auf einer axial diskretisierten Turbinendomäne. Ein intern entwickeltes Meanline-Programm unterstützt den 1D-Euler-Löser, indem es die Turbomaschinen-Quellkraft und Arbeitsquellterme für die Euler-Gleichungen bereitstellt. Die Genauigkeit der entwickelten Methodik wird anhand der dreidimensionalen URANS-Simulationen verifiziert. Verschiedene PDC-Konfigurationen, einschließlich einer unterschiedlichen Anzahl von PDC-Röhren, werden verwendet, um die Stärke der Methodik unter verschiedenen Bedingungen zu bewerten. Der Vergleich der Ergebnisse mit denen von 3D-CFD bestätigt die Zuverlässigkeit der 1D-Euler-Methodik für die Turbinensimulation in PDC-Anwendungen, mit dem Vorteil, robust und schnell genug zu sein, um in die frühen Design- und Optimierungsphasen integriert zu werden.

Darüber hinaus wird als praktische Umsetzung der entwickelten Methodik eine Turbinenoptimierung unter Verwendung der 1D-Euler-Methode als Zielfunktionsauswerter durchgeführt. Als am stärksten von der instationären Anströmung betroffene Schaufelreihe wird die erste Stufe der Turbine einer Optimierung unterzogen. Die optimierte zweistufige Turbine zeigt eine bessere Leistung (16% geringere Entropieerzeugung und 14% höhere Ausgangsleistung) im Vergleich zu ihrem ursprünglichen Design, während sie unter PDC-Abgasströmung arbeitet.

Abstract

Power production and transport sectors are two of the emitters which have had a considerable share in the global growth of greenhouse gas emissions for the last decade. The number of air passengers as well as electricity-dependent technologies is continuously growing. This growth rate is faster than renewable energy developments can deal with their related emissions, hence remedies are required to decrease the emission from the current technologies through some modifications. Nevertheless, the gas turbine components are mature enough that any effort to achieve higher performance will not raise the engine efficiency by more than half a percent. Therefore, a step-change in the gas turbine efficiency may require a change of paradigm. Among the remedies, substituting pressure gain combustion (PGC) for the conventional constant pressure combustion type has proven that will raise the gas turbine efficiency significantly. However, plenty of challenges needs to be solved for a reliable and efficient implementation of PGCs in gas turbine cycles.

Apart from the combustion-related open questions, an efficient way of extracting energy from PGCs is still a bottleneck in using this combustion technique in gas turbines. A turbine is usually designed in such a way to expand the exhaust gas from a rather steady isobaric combustion with an efficiency of more than 90%. But, this turbine loses its performance while being exposed to PGC devices. The pulsating character and highly unsteady exhaust of PGCs are so deteriorative for such a turbine and will spoil the whole efficiency gain expected from a PGC-driven gas turbine. Therefore, developing a turbine able to extract energy from PGCs efficiently is necessary toward cutting the gas turbine emission significantly.

The present dissertation contributes to the integration of turbines with PGC devices by two main parts. First, the interaction of a stationary vane row, as the first row of a typical turbine, with a rotating detonation combustor (RDC) is studied. The RDC exhaust flow passing through the stationary vanes is characterized by numerical simulations which provide a deeper insight into the detail of the flow field where is unreachable in experimental works. Blade geometrical parameters and blade setting angle are altered to further study the role of the guide vane in such unsteady periodic flows. Total pressure loss, fluctuation damping role, and performance of the vanes are analyzed and compared to the steady operating conditions. Results show that total pressure loss of the vanes does not necessarily follow the conventional loss correlations developed for steady flows. Besides, it is found that the vane row can damp more than 57% of the fluctuation, while a higher damping level can be achieved by shortening the flow path area by raising either solidity or thickness of the blades. This role of the guide vanes makes the flow more favorable for any downstream rotor blades which are so sensitive to the incidence angle variation. The generic shape of the vanes considered in this thesis provides

a wide range of incentives for follow-up investigations on designing a most effective guide vane for RDC exhaust flow.

The interaction of a multistage turbine with a pulsed detonation combustor (PDC) is explored in the second part of the thesis, focusing on introducing a turbine unsteady simulation methodology. A one-dimensional method is developed for simulating a multistage axial flow turbine connected to an array of PDC tubes. The methodology comprises a 1D-Euler equations solver on an axially discretized turbine domain. An in-house developed meanline program supports the 1D-Euler solver by providing the turbomachinery force and work source terms to the Euler equations. The accuracy of the developed methodology is verified using the three-dimensional URANS simulations. Different PDC configurations, including different numbers of PDC tubes are employed to assess the methodology strength in various conditions. The comparison of the results with those of 3D-CFD confirms the reliability of the 1D-Euler methodology for turbine simulation in PDC applications, with the advantage of being robust and fast enough to be integrated into the early design and optimization phases.

Furthermore, as a practical implementation of the developed methodology, turbine optimization is performed using the 1D-Euler method as the objective function evaluator. As the most affected blade rows of the unsteady incoming flow, the first stage of the turbine is subjected to optimization. The optimized two-stage turbine shows better performance (16% lower entropy generation and 14% higher output power) against its original design while working under PDC exhaust flow.

*To my parents,
Maman and Baba.*

Acknowledgements

First and foremost, I would like to express my sincere gratitude to Prof. Panagiotis Stathopoulos for introducing me to the PGC topic and allowing me to work with him. Throughout almost five years of my Ph.D. study, I learned a lot from him, not only in the research but also in attitude toward life. He was always open to my questions and played his supportive role in the best way possible. I appreciate all lessons that were imparted on me. Furthermore, I would like to thank Prof. Christian Oliver Paschereit as my second supervisor that I always feel his support whenever needed. I must also admit that I am very honored to be part of your friendly team and enjoy helping you to further develop your department. Additionally, I would like to thank Prof. Abdulla Ghani, Prof. Antonio Andreini and Prof. Alessandro Sorce for taking part in the doctoral committee and the evaluation of this thesis.

For giving me the opportunity to join TU Berlin, I want to thank Dr. Christian Navid Nayeri, who accepted my application to join his group in 2017 and was very open and helpful in changing my topic. His coordinating role helped me during the years after, up to the graduation, and that made him a first contact person when I had official needs.

Next, I would like to acknowledge my colleagues with whom I worked closely at some points. Among all, Dr. Cleopatra Cuciumita and Nicolai Neumann, I spent hours of discussions on turbomachinery topics and had some successful collaborations with them. I want to thank Niclas Garan, Dr. Eric Bach, Prof. Myles Bohon, Roman Klopsch, and Josch Meister for fruitful discussions in Monday's meetings using a puzzling online platform hosted by Panos. A thank you to my colleagues at the Hermann-Föttinger-Institute for the great times we shared during office hours and extracurricular activities and nice guys as my office mates Prof. Paris Fokaides, Khaled Almawri, Dr. Tom Tanneberger, Dr. Richard Blümner, Liza Zander, Johann Vinkeloe, Sirko Bartholomay, Marvin Jentzsch, Benjamin Church, Mohammad Toudefallah and Gokkul Raj. I'm so thankful to the two nice ladies at the HFI office, Maria Lück and Sandy Meinecke, who always try to help with the university bureaucracy and official paperwork, with happy faces.

Finally, a special thanks to my parents, siblings and friends in Iran for giving me the good feelings when I went to visit them. I cannot skip mentioning my previous supervisor name, Prof. Mesgarpour Tousi, who built my solid fundamental understanding of propulsion; besides, his personality was very inspiring to me.

I want to give immeasurable thanks to my lovely wife, who stands with me all the time, ups and downs. Undoubtedly I could not have done this without you.

Table of Contents

Title Page	i
Zusammenfassung	iii
Abstract	v
List of Figures	xiii
List of Tables	xv
Nomenclature	xix
1 Introduction	1
1.1 Energy Related Concerns	1
1.2 Pressure Gain Combustion	3
1.3 Scope and Structure of the Thesis	5
2 State of the Art	7
2.1 PDC-Turbine interaction	7
2.2 RDC-Turbine interaction	12
3 Methods	17
3.1 Meanline turbomachinery analysis	17
3.1.1 Flow velocity calculation	18
3.1.2 Thermodynamic parameters calculation	20
3.1.3 Loss correlations	21
3.1.4 Program logic	26
3.2 One-dimensional Euler solver	27
3.2.1 Governing equations	28
3.2.2 Integration of meanline and 1D-Euler methods	30
3.3 Pressure gain combustion devices	32
3.3.1 Rotating detonation combustor model	32
3.3.2 Pulsed detonation combustor model	34
3.4 Three-dimensional CFD	36
3.5 Surrogate-based optimization	38
3.6 Turbine test case	40

TABLE OF CONTENTS

4 Publications	43
4.1 Publication I	45
4.2 Publication II	54
4.3 Publication III	62
4.4 Publication IV	77
5 Discussion	93
5.1 RDC-turbine	93
5.2 PDC-turbine	97
6 Conclusions and Outlook	103
References	107
Appendix A Associated Publications	121

List of Figures

1.1	Emission production by sector, taken from [4].	2
1.2	Thermodynamic comparison between ideal cycles of Brayton, Humphrey and detonation cycle (ZND), reproduced from [10]	4
1.3	An illustration of a typical PDC periodic operation in a tube, adapted from Publication III.	5
1.4	An sketch of an RDC flow field features using temperature contour, (a) three-dimensional domain, (b) unwrapped RDC domain neglecting the annulus height, adapted from [12]	6
2.1	PDC-Turbine experiments at the University of Cincinnati using 80% bypass air, (a) cross-sectional view and a picture of the PDC-Turbine configuration, (b) turbine performance results for different rotational speeds showing steady (open symbols) and PDC-fired data (closed symbols), adapted from [25]	9
2.2	Mass-averaged rotor incidence angle, normalized total temperature at the inlet and exit planes of the turbine stage, and stator exit angle, adapted from [40].	12
2.3	(a) An architecture of a turbofan engine embedded with a rotating detonation duct burner showing two possible shapes of circular and track-shaped chambers, (b) comparison of running lines for baseline, rotating detonation duct burner engine (RDDDB), and isobaric duct burner turbofan engines (ICDB), taken from [61]	15
3.1	Overview of the methods used in the thesis.	18
3.2	A meridional reference of a turbine stage and the flow velocity vectors.	19
3.3	(a) Model for off-design incidence correction factor, and (b) stall incidence angle model.	23
3.4	(a) Nozzle blade profile loss for $\alpha'_1 = 0$, and (b) impulse rotor blade profile loss for $\beta_2 = \alpha'_1$	24
3.5	Overall flow chart of the turbine meanline performance analysis.	27
3.6	Meanline program block diagram including inner loops.	28
3.7	Force balance on a control volume around a turbine blade, taken form Publication IV.	31
3.8	(a) A cross sectional view of the RDC setup, adapted from Blümner [101], and (b) the RDC annulus equipped with a row of stationary guide vanes, adapted from Bach et al. [74]	33
3.9	The model of a PDC configuration comprising three tubes.	36

LIST OF FIGURES

3.10	A representation of CSM operations in a two-dimensional design space, which is consistent with the notations in Publication IV.	40
3.11	Complex shape algorithm flow chart.	41
5.1	Total pressure trace at the blade downstream over a detonation time period. . .	94
5.2	Comparison of total pressure loss for staggered vanes downstream of the RDC. . .	95
5.3	Static pressure damping throughout the turbine connected to different PDC tube arrangements.	99

List of Tables

5.1 Total pressure loss along the stationary vane downstream the RDC for different setting angles. 95

Nomenclature

Latin characters

A	Cross section area
C	Absolute velocity
c	Chord length
C_L	Lift coefficient
c_p	Heat capacity of the flow at constant pressure
c_{ax}	Axial chord length
E	Internal energy per unit mass
e	Roughness height
F	Force
g	Gravity acceleration
h	Enthalpy
h_b	Blade height
i	Incidence angle
i_s	Stall incidence angle
L_A	Loading parameter
M	Absolute Mach number
M'	Relative Mach number
P	Pressure
Q	Heat
R	Ideal gas constant
R_c	Curvature radius of the blade suction surface
Re	Reynolds number
rpm	Round per minute
S	Entropy
s	Pitch
S_{ij}	Mean rate of deformation component
T	Temperature
t	Time
t_2	Trailing edge blade thickness
t_{max}	Maximum blade thickness
U	Blade speed

NOMENCLATURE

V	Relative velocity
v	Volume
v_{sp}	Specific volume
W	Turbine work
Y_{sp}	Vector of mass fraction of the species
\dot{m}	Mass flow rate
$\dot{Y}_{sp,chem}$	Kinetical source term, chemical composition change

Greek Symbols

α	Absolute flow angle with respect to the turbine rotational axis
α'	Blade angle with respect to the turbine rotational axis
β	Relative flow angle with respect to the turbine rotational axis
β_g	Blade gauging angle
δ	Blade tip clearance
γ	Heat capacity ratio
κ	Specific turbulent kinetic energy
Λ	Reaction ratio
μ	Dynamic viscosity
ϕ	Flow coefficient
ψ	Loading coefficient
ρ	Density
τ	Viscous effect
ξ	Total pressure loss coefficient

Subscripts

$()_a$	Axial component
$()_s$	Static thermodynamic condition
$()_t$	Total thermodynamic condition
$()_w$	Tangential component
$()_b$	Bleed flow
$()_{cl}$	Tip clearance loss
$()_{cp}$	Compressor plenum
$()_{ex}$	Supersonic expansion loss
$()_p$	Profile loss
$()_{rel}$	Relative thermodynamic quantity
$()_{se}$	Secondary loss
$()_{sh}$	Shock loss
$()_{te}$	Trailing edge loss

$()_{tp}$ Turbine plenum

Acronyms

ARS Algebraic Reynolds Stress

CFD Computational Fluid Dynamics

CSM Complex Shape Method

ICDB Isobaric Duct Burner

LHS Latin Hypercube Sampling

PDC Pulsed Detonation Combustion

PGC Pressure Gain Combustion

RDC Rotating Detonation Combustion

RDDDB Rotating Detonation Duct Burner

RST Reynolds Stress Transport

SBO Surrogate-Based Optimization

SST Shear Stress Transport

URANS Unsteady Reynolds Averaged Navier-Stokes

1

Introduction

*"I'm looking for a lot of men who have an infinite capacity to not know what can't be done."
Henry Ford*

1.1 Energy Related Concerns

The Industrial Revolution changed very basic forms of energy our ancestor relied on such as animal muscle, human muscle and burning biomass, to fossil fuels. Since then, fossil energy has become a fundamental driver of developments in technology, economy and even politics. Fossil fuel consumption has changed significantly over the past years – in terms of what and how much we burn. In the beginning, coal was the only fossil fuel type people could use. From late 19th, oil and gas were added to the consumption cycle. Despite the world is in debt to the fossil fuels for being developed, it suffers from several negative impacts resulting from burning these fuels. Carbon dioxide (CO₂) is the largest driver of global climate change. This excess harmful gas produced by burning fossil fuels is also a major contributor to local air pollution, which is estimated to be linked to millions of premature deaths each year. According to the September 2019 World Meteorological Organization (WMO) report, we are at least one degree Celsius above pre-industrial levels and close to what scientists warn would be “an unacceptable risk.” If we don’t slow global emissions, the temperature could rise to above three degrees Celsius by 2100, causing further irreversible damage to our ecosystems. Climate change would threaten the peace and security between nations resulted by a competition for resources such as water and land leading to mass displacement [1]. According to the World Bank report [2], if no measures are taken, more than 140 million people in Sub-Saharan Africa, Latin America, and South Asia will be forced to migrate within their regions by 2050. Therefore, a rapid transition from fossil fuels to efficient, renewable and sustainable energy is crucial. The Paris agreement is the first legally binding international treaty on climate change made in 2015. Its goal is to limit global warming to well below 2 degrees, preferably to 1.5 degrees Celsius, compared to pre-industrial levels. The main contributors of emission is shown graphically in Fig.1.1. Energy sector, including electricity, heat and transport, is responsible for more than 73% of the global greenhouse gas emissions. Having a rise from 7 to 9 billion in the world population

1. Introduction

by 2050, the demand for energy consumption is forecasted to increase by approximately 56% [3]. Hence the energy related emissions become even bolder.

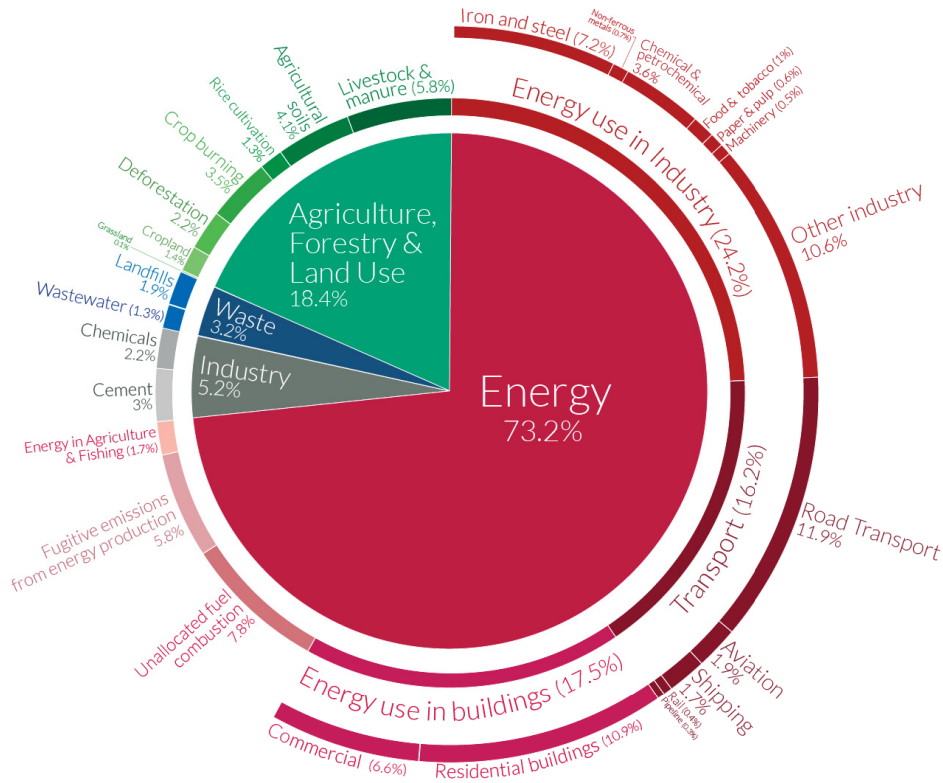


Figure 1.1: Emission production by sector, taken from [4].

The use of renewable sources such as wind, solar, hydro, biomass, tidal and geothermal energy are increasingly growing. Among all, wind, solar and biomass are the three renewable energy sources that have the greatest growth rate between 2009-2019 across the EU. Wind energy provides a domestic source of energy and can be built on existing farms or ranches without occupying a huge area. Nevertheless, wind power has to still compete with low price conventional energy sources, even though the cost of wind energy has lowered in the past decades. Besides, some regions do not have enough wind during the calendar year that building a wind farm can make sense. Often suitable wind farms are located far from consumption centers like big cities, so that creating long transmission lines is required. Solar energy as the other renewable source has a great potential if it is coupled with battery storage. The main challenge for solar power and also wind energy is their dependency on the weather. Solar power generation curve in a sunny day and power consumption trend are mismatched. Rising energy demand in the morning and the evening is not aligned with the level of energy captured from the sunlight during these hours. Consuming biofuels for energy production is still a controversial topic. Having a lower energy density compared to fossil fuels make biofuels less commercially attractive. However, biofuel production can be combined with nitrogen-rich, municipal wastewater, and carbon dioxide flue gas treatment to become more sustainable and cost-effective [5].

Since 1939 when the first gas turbine was installed in in the municipal power station in Neuchâtel, Switzerland, this technology has played a big role in power generation. Today gas

turbines are a major technology in both electricity generation and aviation. The advantages of this technology are not only limited to its quick response time but also the ability to burn different types of fuel ranging from fossil to biomass and hydrogen. Considering the already installed gas turbines in the power and aviation sectors, decarbonization of gas turbines can be one of the cost-effective solutions toward carbon-free energy production and air transportation. Gas turbines consist of three main parts namely compressor, combustor and turbine to shape a thermodynamic process of Brayton cycle. Having the compressor and turbine conceptually fixed, the combustor where the fuel is burnt can be modified with respect to environmental concerns. The conventional combustion type is the process of constant pressure heat addition. Beside the use of clean fuel, the total pressure loss occurring in the conventional combustion process can be replaced with the constant volume combustion process in which total pressure increases. The periodic operation, in which a reactive mixture is burnt in a constrained combustion volume, results in a rise in total pressure and allows work extraction by expansion to the initial pressure. This rise in total pressure through the combustion process introduces the concept of Pressure Gain Combustion (PGC) engines. Therefore, using pressure gain combustion burning hydrogen in the gas turbine technology can be one of the promising and low cost solutions for rapid transition toward sustainable energy generation.

The current research is focused on the use of PGC and the related challenges to extract energy from it in a form of gas turbine cycle. Within this chapter, the scope of the dissertation will be elaborated after a short introduction to the pressure gain combustion concept.

1.2 Pressure Gain Combustion

The concept of pressure gain combustion has been almost as long as the gas turbine. The attributes of PGC have been studied for over a century and have resulted in proposals to develop practical engines. Due to its potential advantages, the past few decades have seen a pickup interest spreading rapidly worldwide in pressure gain combustion. Research and development have been put to solve the challenges related to the use of PGC for a safe operation. These efforts have led to sufficient understanding for the first flight of a Pulsed Detonation Combustion (PDC) engine in 2008 by Air Force Research Laboratory and Rotating Detonation Combustion (RDC) engine in 2021 by Japan Aerospace Exploration Agency. The idea of pressure gain combustion cycle has been derived by switching from heat addition at constant pressure process in the form of Brayton cycle to heat addition at constant volume process in the form of Humphrey cycle. Within the Humphrey cycle, less entropy is generated and hence the ideal thermal efficiency is increased. The Humphrey cycle is best described in the form of shockless explosion combustion [6] and pulsed resonant combustion [7]. The ideal thermal efficiency of Humphrey cycle can be even enhanced through the use of detonative combustion process. The detonative combustion process can be described by the Zeldovich-von Neumann-Döring (ZND) model [8]. Based on the ZND model which is a one-dimensional model for the process of detonation of an explosive, a leading shock wave is coupled to a self-propagating reaction zone that comprises a detonation wave. The leading shock wave increases pressure and temperature to auto-ignition condition. The coupled chemical reaction zone releases a significant amount of heat in a frictionless, non-adiabatic flow and constant-area region known

1. Introduction

as Rayleigh flow and drives the leading shock wave. Figure 1.2 shows a comparison between the three cycles in temperature-entropy and thermal efficiency diagrams. According to the temperature-entropy diagram, it is clearly seen that the work extraction is much increased by rising the peak temperature as a result of heat addition while lowering the entropy. This is achieved in the ZND model compared to Humphrey and Brayton cycles. The thermal efficiency, plotted against the combustor inlet temperature for a constant amount of heat addition, highlights that ZND and Humphrey offers a remarkable efficiency superiority over Brayton cycle. The difference is higher in lower combustor inlet temperature. Stathopoulos et al. [9] showed a 20% higher efficiency at low turbine inlet temperature can be achieved. Another notable point in the diagram is that even if no compression exists in the cycle ($T_2/T_1 = 1$), both Humphrey and ZND have a positive efficiency while it is zero for Brayton cycle. However, the component efficiencies on which the mentioned thermodynamic analysis is based are ideal as in the conventional Brayton cycle. If the realistic component efficiencies are taken into account, the efficiency gain could be lower by implementing PGC into gas turbine engines [10]. This introduces one of the main challenges related to the use of PGCs. Compressor and turbine in a gas turbine ideally work with constant steady flow. When PGCs substitute for constant pressure combustion, the turbines have to work under unsteady flow conditions caused by PGCs that cause a significant amount of losses in these components. This challenge is addressed in the scope of this research. In overall, the significant higher efficiency of PGC driven cycle than the constant pressure combustion brings lower specific fuel consumption and subsequently thrust enhancement for aero engines or power output increase for land-based power generation.

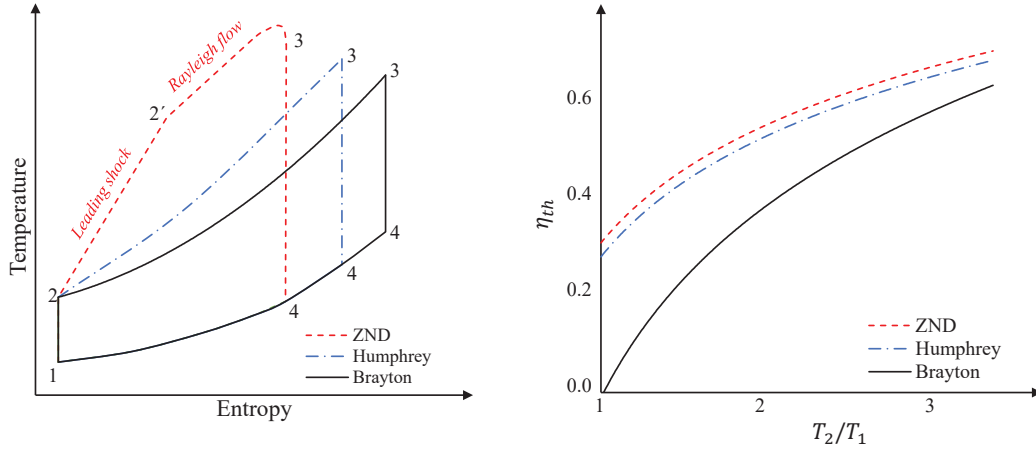


Figure 1.2: Thermodynamic comparison between ideal cycles of Brayton, Humphrey and detonation cycle (ZND), reproduced from [10]

PDC and RDC are the two well-known realizations of PGC. In PDC, the detonation wave propagates downstream a tube in a cyclic manner, shown graphically in Fig.1.3. First, a flammable mixture fills the tube. Then an ignition is occurred by an external ignition source, and subsequently, the flame front flows into a relatively long section of deflagration to detonation transition duct. The exhausting flame is accelerated to detonation wave burning the flammable mixture instantly with a high propagating speed. The propagation speed is high enough that no expansion is happened so that the combustion process is considered

as constant volume. After blowing down the combustion product, air is injected into the tube to expel the remaining products from the tube. This cycle is repeated which forms the periodic pulse detonation combustion. Because of these phases in each period and the tube's length, PDC operating frequencies are limited on the order of 10 Hz to 100 Hz [11]. In contrary to PDCs, in which for every cycle an ignition is required, in RDCs only one ignition is needed to initiate the RDC continuous operation. Figure 1.4 depicts an RDC flow field and its unwrapped representation. Within an RDC operation, firstly, fuel and oxidizer are injected into the annulus and an initial ignition by an external source starts the combustion phenomena and the respective detonation wave. The moving detonation wave burns the fuel-oxidizer mixture. As long as the reactants are supplied at the combustor inlet, the detonation wave is maintained. The higher pressure of the products behind the detonation front than the injector pressure prevents the combustible mixture to blow in. Once the pressure gets lower, and the detonation front gets far enough, the injectors open automatically. Therefore, there is no need for any mechanical system. Depending on the annulus back pressure, the exhaust flow could be subsonic or supersonic while one or several detonation waves can rotate around the annulus. Thanks to the speedy detonation wave, compact and simpler geometry with no mechanical valve, RDCs operate at frequencies of 1 kHz to 10 kHz, which is much higher than the PDC operating frequency range.

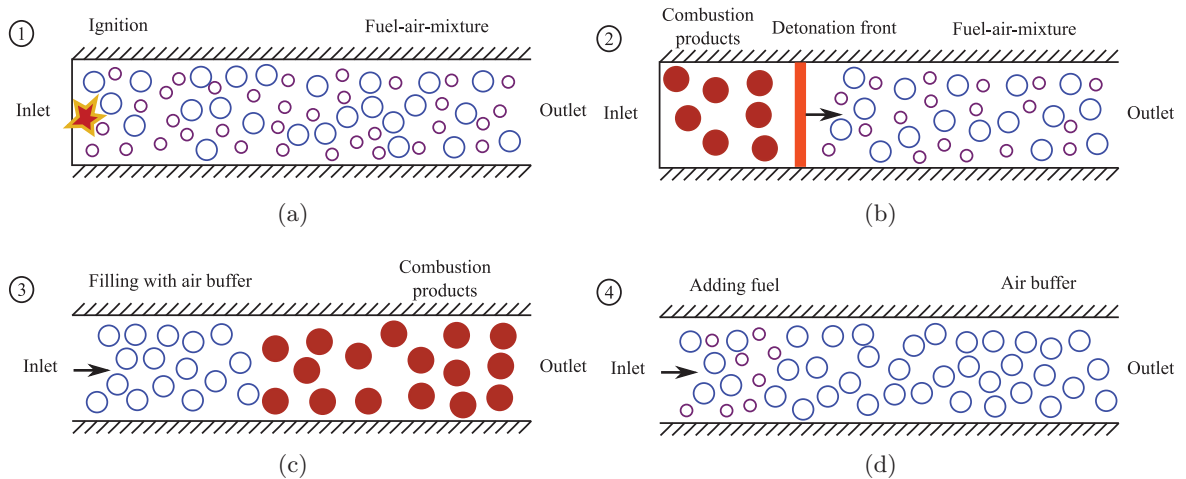


Figure 1.3: An illustration of a typical PDC periodic operation in a tube, adapted from Publication III.

1.3 Scope and Structure of the Thesis

One of the obstacles toward practical implementation of PGCs in gas turbine cycles is the challenge related to the component matching. Due to the nature of PGC operation which is defined by a periodic combustion cycle, a level of unsteadiness is imposed to the turbomachinery components, whether compressor upstream or turbine downstream the combustor. To this end, conventional turbomachinery are designed to work under steady flow with a peak efficiency at their design point and with a relatively lower at off-design conditions. In conventional gas turbines, turbines work with their top rated efficiencies of above 90%. However, when they are exposed to the unsteady flow, they have to operate under far off-design conditions, that

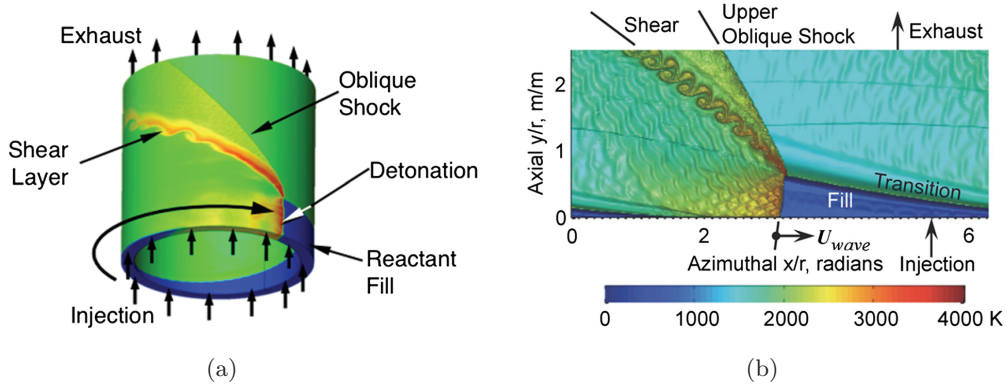


Figure 1.4: An sketch of an RDC flow field features using temperature contour, (a) three-dimensional domain, (b) unwrapped RDC domain neglecting the annulus height, adapted from [12]

spoils their favorable performance. The question that arises here is how a turbine should be designed, so that it can efficiently harvest the high level of energy by PGCs in gas turbine configurations. This question cannot be answered without characterizing the PGC flow field at the turbine inlet.

Toward addressing the challenge, the present thesis focuses on the interaction of PGC and turbine. Firstly, the exhaust flow of RDC is characterized when passing through a nozzle guide vane row numerically. Further investigation of unsteady turbine operation requires a fast simulation tools, because three- or two-dimensional CFD methods are too expensive to be used for any design optimization work. Therefore, a one-dimensional transient simulation tool is developed for a fast and reliable turbine simulation that works with PGCs. The methodology comprises a meanline turbomachinery performance analysis, a PGC model, and a 1D-Euler equation solver. These tools are developed and tested for PDC applications in the course of this thesis. Finally, an optimization methodology is developed using the transient 1D-Euler solver as the objective function evaluator. The optimization algorithm is explained and applied for a two-stage turbine driven by a PDC configuration.

This thesis is divided into six chapters. The first chapter presents a brief introduction to the topic with regard to the environmental concerns and the role of PGC concept in addressing how to cut the CO₂ emission from energy production sector. Chapter two will provide state of the art information on the PGC-turbine interaction. The literature review is separated into PDC-turbine and RDC-turbine studies, and their findings are discussed. In the third chapter, the methodologies applied for the goal of the research work are explained. This includes meanline method, 1D-Euler solver, CFD method, optimization algorithm, and PGC models and the turbine test case. This is followed by presenting four publications as a part of the results in chapter four. After a discussion on the findings, in chapter five, the thesis is concluded in chapter 6, providing a summary of the research as well as an outlook for future works is elaborated to close the dissertation.

2

State of the Art

Regardless of past and ongoing research in the field of pure PGC operation, including detonation phenomena [13, 14], combustion instabilities, and controllability of the periodic combustion cycles [15, 16], that do not lie in the scope of this research, several researchers have considered integrating PGC devices into gas turbine engines. Most of the early studies focused only on the applicability of the concept that showed PGCs could replace conventional burners. After proving the concept, the investigations were headed toward evaluating the performance of PGC-driven gas turbine and component matching. This chapter provides an overview of the studies on PGC and turbine interaction. The emphasis is placed on recent literature related to the interaction of turbines with PDC and RDC.

2.1 PDC-Turbine interaction

One of the early efforts on the integration of PDC into a gas turbine was made by Petters et al. [17] in 2002. Using a 1D performance evaluation code, they compared a conventional turbofan with a PDC-driven turbofan. They showed that the engine with an embedded PDC had an 11% lower thrust specific fuel consumption (fuel mass flow rate per thrust). According to their results, a three-hour flight of a medium-sized passenger aircraft with two PDC integrated turbofan engines would save around 440 gallons of fuel (JP-8/Jet-A class). As a rule of thumb, for a round flight from Berlin to Moscow with a two-engine aircraft, 17160 kg less CO₂ would be produced and released into the atmosphere. This is equal to the CO₂ emission produced by a passenger car in around four years. Assuming a daily flight for the same route in a year, the saving would be as much as greenhouse gas emissions avoided by a wind turbine running for one and a half years. In another work using the same numerical model, Jones and Paxson [18] studied the integration of PDC into small, medium, and large aircraft engines to analyze the potential fuel burn benefits of pressure gain combustion technology in the aerial transportation sector. They replaced the constant pressure combustion with a PDC combustion model. The results showed a thrust-specific fuel consumption decrease of 3.9%, 5.6% and 3.4% for small, medium and large aircraft, respectively.

Among the experimental studies in the field of PDC-turbine interaction, Schauer et al. [19, 20, 21, 22] integrated a centrifugal turbine taken from an automotive turbocharger (Garrett T3) to a PDC tube. A centrifugal compressor with regulated outlet pressure and measured inlet flow was connected to the system to determine the achieved operating conditions. The turbine was successfully run and reached a rotational speed of 130k rpm. Compared to the theoretical calculations, a considerable amount of losses were observed through the expansion process in the turbine. Also, a significant amount of attenuation in pressure fluctuations was seen throughout the turbine. Although the turbine was not designed for such a detonative flow and its performance was very poor, fully developed detonations flowing into the turbine inlet, and the turbine survival were confirmed. Comparing just a PDC tube with a PDC-turbine configuration, they showed that the PDC tube produced about four times greater thrust than the work output from the PDC driven turbine.

Rasheed et al. [23, 24] at General Electric Global Research Center performed some experimental tests on a PDC-turbine hybrid system. The system consists of eight PDC tubes positioned in a can-annular configuration of 800.1 mm long. The turbine was a single-stage axial type taken from a locomotive scale turbocharger designed for nominal flows of 3.62 kg s^{-1} , 25 000 rpm, and 1000 hp. Different firing patterns were examined, and the test rig was operated up to 30 Hz for each tube. The turbocharger compressor was connected to the turbine shaft and was used as a dynamometer. Having the compressor inlet and outlet thermodynamic parameters measured, the work extraction from the turbine was calculated. A separate air line providing a secondary air flow was used to cool down the primary flow to the average temperature within the turbine material temperature limits. Because of the high amount of bypass air, the analysis of their experimental results showed that the turbine efficiency is almost indistinguishable from the related steady-state performance within 8% measurement uncertainty. Around 4% higher efficiency was measured in PDC-driven turbines than steady-state turbines. This increase can be explained by PDC's fuel benefits to the turbine working fluid.

Glaser et al. [25] at the University of Cincinnati suggested a hybrid system in which the high-pressure core of a gas turbine, including a high-pressure compressor, constant pressure combustion, and high-pressure turbine, is replaced by a PDC array containing multiple PDC tubes. The low-pressure compressor is maintained to deliver the airflow required to fill and purge the PDC tubes. A low-pressure turbine is also needed to power the compressor. They built up a PDC-Turbine system to investigate the effectiveness of driving an axial flow turbine, taken from a model JFS-100-13A gas turbine engine, with a PDC, shown in Fig.2.1(a). The PDC system comprised six tubes that operated sequentially with a frequency of 20 Hz for each tube. More than 80% bypass air flow was used to supply the required mass flow through the turbine section. The turbine performance was evaluated from low load level up to 67% of its rated pressure ratio. The comparison of the results for PDC-driven turbine and steady flow turbine showed comparable performance data as depicted in Fig.2.1(b). They indicated that the efficiency of the PDC-driven turbine is decreased by increasing the combustion tube fill-fraction. Although most of the turbine working flow was supplied by the bypass air that reduced the unsteadiness into the turbine, the performance results were found encouraging for the applicability of PDC in a gas turbine cycle.

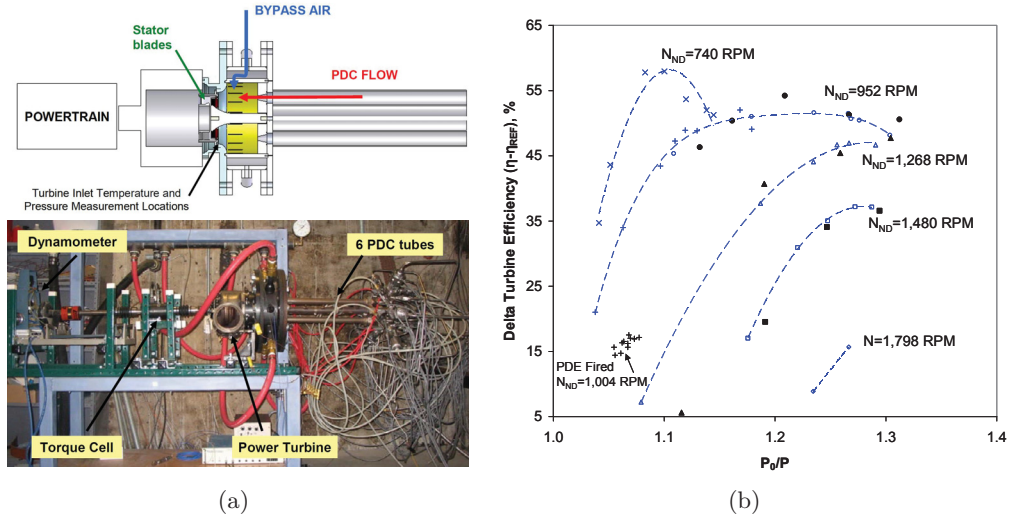


Figure 2.1: PDC-Turbine experiments at the University of Cincinnati using 80% bypass air, (a) cross-sectional view and a picture of the PDC-Turbine configuration, (b) turbine performance results for different rotational speeds showing steady (open symbols) and PDC-fired data (closed symbols), adapted from [25]

In another investigation at the University of Cincinnati, Anand et al. [26] positioned a PDC array comprising six tubes upstream of an axial turbine as applied by Glaser et al. [25]. To maintain the maximum level of fluctuation entering to the turbine from the PDCs, the tubes were fully partitioned in identical-length tubes from the engine end wall up to upstream of the turbine stator vanes. PDCs were run under two frequencies of 5 Hz and 10 Hz and fired sequentially. This firing pattern allowed no interaction between combustor tubes when there was no downstream element. Their analysis showed that the duty cycle is increased by reducing the cycle time through increasing the firing frequency but does not significantly extend the blow-down duration. Also, a substantial decrease in the turbine efficiency compared to its design efficiency was observed, which was four times lower. A "purge braking" phenomenon was detected as a result of adjacent admission sectors working under different phases of the PDC cycle. This phenomenon occurs when the tube purging gases are extracting power from the turbine while at the same time a neighboring tube is imparting power to the turbine.

Unlike the investigations discussed above that used bypass air for cooling the hot gas and attenuating the fluctuations, Panicker et al. [27] directly connected a 1 m long PDC tube to a turbocharger used in Volkswagen Passat 1.8T and Audi A4/A6 1.8T model cars. Since the aim was to assess power generation using PDC, a small AC generator is mounted on the turbine-compressor shaft. Speed reduction wheels were utilized to connect the generator to the turbine shaft because the turbine spun up to 127,000 rpm, while generators are typically run at low thousands of rpm. Therefore, speed-reducing gear assemblies will have to be employed to match the rotational speeds and torques of the two devices. The PDC frequency was 15 Hz, and it could run for a period of about 20 s, so that the generator produced electric power at 27 W. Having concluded that PDCs can be made to self aspirate if combined with a turbine and compressor, they suggested using multistage axial turbine for electrical power generation from PDCs because they captured significant losses and hot spots from turning the flow around 90° .

Qiu et al. [28, 29, 30] at Northwestern Polytechnical University presented a prototype of two PDC tubes directly connected to a turbocharger turbine. The turbine outlet is connected to a convergent nozzle to enhance the propulsive performance. The compressed air from the compressor is supplied to the PDC tubes so that the hybrid system operates in the air-breathing mode. The ignition frequency of the tubes was raised up to 20 Hz, with equivalence ratios of around unity. Running the system for about 6 minutes, the propulsive performance of the system reached a 27% higher maximum specific thrust compared to that of the traditional engine based on the ideal Brayton cycle. They also concluded that the difference in pressure peak between turbine inlet and outlet has little effect on the turbine speed. However, the turbine speed was affected indirectly by two factors of the equivalence ratio of fuel and air mixture and the transition structure between PDC and turbine. The equivalence ratio mainly affects the detonation wave's velocity, intensity, and stability, while the transition structure changes the pressure curve of the detonation wave. The momentum difference per unit area between the turbine inlet and outlet can be enlarged through designing an appropriate transition structure. Therefore mastering the engine's optimum operating point and developing an optimal transition structure are essential for the PDC-turbine hybrid engine.

Besides investigating turbines driven by PDC exhaust, some researchers have focused on pulsed cold air to imitate the PDC flow upstream of turbines. Among recent research works, George et al. [31] used a Chevrolet Vortec 4200 six-cylinder automotive engine to generate high-pressure air pulsations to a single-stage axial turbine used later by Anand et al. [26]. The operating map of the turbine was covered for four frequencies ranging from 5 Hz to 20 Hz. They found that the turbine efficiency under pulsating flow is a strong function of corrected mass flow rate and mass-averaged rotor incidence angle, but pulse frequency has no significant effect. They also tried different averaging methods and concluded that mass-averaged, work-averaged, and integrated instantaneous methods yield meaningful values and comparable trends for all frequencies. However, time-averaged methods poorly represented the physics, implying much higher efficiencies under pulsed flow than under steady conditions.

Fernelius et al. [32] used compressed air and a rotating ball valve with a motor to create pressure pulses in place of PDC exhaust flow. They utilized a JetCat P-200 gas turbine engine as the testbed, having a single-stage axial turbine. The turbine operating map under pulsating flow was found very similar in shape to the steady turbine map. But a decrease in the turbine performance was captured, which was a function of the pulsing frequency. They showed that for high pulse frequencies, the turbine pressure ratio increased with pulsed flow less than for low pulse frequencies. Lower peak efficiency and specific power were observed for pulsating flow turbine than the steady flow, stating that the difference between peak efficiencies was less severe at high pulsating frequencies. Later, they [33, 34] used the same setup and generated pulses with sinusoidal shape providing different frequencies and amplitudes to assess their effects on the turbine performance. Their experimental measurement together with CFD results illustrated that the driving factor in lowering turbine efficiency and pressure ratio in pulsating flow is pulse amplitude, not frequency. A correlation was proposed which expresses the relation between amplitude and efficiency. And they concluded that the main reason for the deficiency of the turbine was rotor incidence angle variation caused by pulsed flow. Applying the sinusoidal pulsating flow in place of PDC exhaust flow, they optimized a turbine

stage with respect to entropy generation as the objective function to be minimized [35]. A surrogate model was utilized while the objective function was evaluated by two-dimensional steady RANS simulations, one at the maximum and one at the minimum of the pressure pulse in each objective function call. The rotor profile shape in terms of blade inlet and outlet angles and tangential location of the blade trailing edge was subjected to optimization. The optimized stage achieved a 35% lower entropy generation than the baseline case while exposed to the pulsating flow. According to the results, it was recommended to weigh the turbine design for pulsating flow toward the peak of the pressure pulse. In this way, the camber angle near the leading edge and the blade turning angle were reduced. Although using pulsed cold flow to imitate the presence of PDC flow for turbine investigation can solve the problems related to the hot measurement and visualization, there are some key differences between the pulsed air and PDC exhaust flow. The pulse shape is usually assumed sinusoidal [36, 35] in the pulsed flow, and the flow temperature effects are ignored. In the case of pulsed detonative flow, there is a maximum volumetric flow rate for a specific pulse frequency, which is the product of the PDC tube volume and the firing frequency. Going beyond this maximum volumetric flow rate causes the detonation wave to propagate through the turbine. Moreover, the length of deflagration to detonation (DDT) part limits the minimum partial fill of the PDC tube. These restrictions draw a connection between pulse frequency and the fired PDC flow rate, which is not the case in pulsed combustion-free flows.

Within the scope of numerical studies, Van Zante et al. [37] used a three-dimensional numerical simulation for an axial turbine stage exposed to a PDC exhaust flow. They observed a low turbine efficiency of 26.7%, while the pressure fluctuations were decayed completely through the turbine. Additionally, they detected a reverse flow during the early phases of blowdown. Suresh et al. [38] carried out a two-dimensional numerical study for a rotor under a boundary condition provided by a PDC tube, out of a one-dimensional detonation analysis program [39]. They evaluated two averaging techniques for turbines working under pulsating flow. The difficulty of efficiency calculation is mainly related to calculating the isentropic work of an ideal turbine operating under the same conditions as the actual turbine. The time-averaged technique assumes the ideal turbine operates under the same work-averaged total pressures as the real turbine. The second technique, called the time-resolved method, takes the ideal turbine operating under the same total pressure time-traces as the actual turbine. This definition is based on the assumption that an instantaneous expansion occurred through the ideal turbine. According to their simulations, the two definitions of efficiency can result in different values with around 10 points (10%) discrepancy.

Xisto et al. [40] performed a two-dimensional numerical study for a coupled axial turbine-PDC configuration, including detailed chemistry to replicate the detonation phenomena of combusting hydrogen-air mixture. Their simulations indicated that the turbine losses were mainly affected by the incidence angle variation. The mismatch between the time-varying rotor inlet condition and the constant rotor speed caused severe periodic variations of rotor incidence angle, which was identified as the cause for the very low or negative turbine torque. Besides, the turbine operated more efficiently when the PDCs were in purge and fill conditions for the studied turbine case. Figure 2.2 explains the reason for changes in turbine efficiency in different PDC phases. The rotor incidence angle is almost constant in the purge phase while

both rotor incidence angle and stator exit angle are strongly fluctuating during the detonation phase which cause flow separation and generating losses. The rotor incidence angle decreases slightly during the fill process showing that the colder purge air is hitting the rotor, lowering the speed of sound locally. It was concluded that increasing pressure and temperature of fill and purge flow could result in higher stage efficiency since they observed an increase in stage efficiency when operating at higher input power settings.

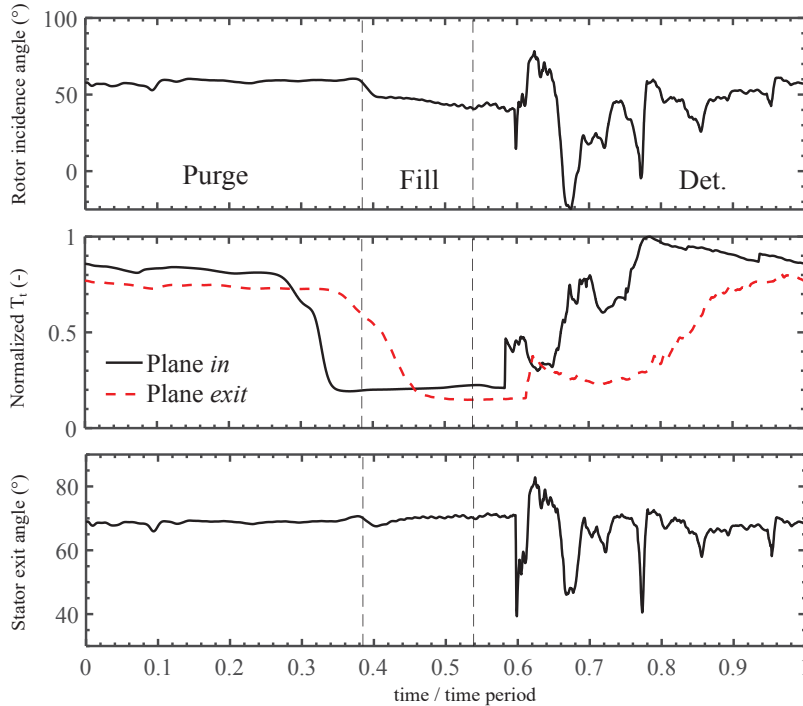


Figure 2.2: Mass-averaged rotor incidence angle, normalized total temperature at the inlet and exit planes of the turbine stage, and stator exit angle, adapted from [40].

2.2 RDC-Turbine interaction

Pressure gain combustion through rotating detonation phenomena produces different high energy exhaust flow than pulsed detonation. The main difference is related to the nature of detonation wave propagation which is axially in PDC and rotating through an annulus in RDC. The continuous detonation wave is provided without the need for repetitive ignition, purge, and fill phases and subsequent mechanical valve systems that make the RDCs run with frequencies in the order of thousands of Hz. One of the benefits of RDC compared to PDC, from a turbomachinery point of view, is the closer flow field to the steady version thanks to the high-frequency fluctuations [41]. Higher power density [42] is another advantage of RDC that justifies the shift from PDC towards RDC. Despite considerable investigations on the use of RDCs in gas turbine configurations, substantial research is still required to understand the physics and to apply the RDCs for real-world applications. To date, investigations have claimed that RDCs provide a remarkable total impulse over PDCs [41], a total pressure increase of up to 15% through the combustion process resulting from detonation phenomena [43], a 5% increase in thermal efficiency in the form of a gas turbine taking advantage of RDC [44] and 4.6% increase with just having the combustor without turbomachinery parts [45], a

9% reduction in fuel consumption over conventional gas turbine cycles [18], and up to 14% improvement in power plant efficiency compared to the traditional Jule-Brayton plants [46].

The rotating detonation combustion generates a very high varying velocity vector flow [47] hitting the turbine blades. This variation in flow velocity presents a significant challenge for integrating RDCs with turbine expanders because turbine loss is a strong function of incidence angle [48]. Additionally, the RDC exhaust flow regime can range from supersonic to subsonic flow [49], making the integration challenge even more severe. Among other studies, Wolański [50] and Kalina et al. [51] at the Institute of Aviation in Warsaw performed experimental and numerical studies on integrating an RDC into the GTD-350 helicopter engine. The setup includes an RDC connected to a single-stage turbine driving the engine compressor. The exhaust flow from the first turbine drives the second two-stage turbine that generates the necessary power. A gearbox delivers the torque to the helicopter rotor. The tests ran for around 20 s. Measuring the fuel consumption and turbine power showed that the unoptimized integration of an RDC into a gas turbine can bring up to 5% lower specific fuel consumption than the original engine. Rhee et al. [52] replaced the combustor of a commercial jet engine with an RDC. In this configuration, the air is compressed through a centrifugal compressor and subsequently separated into two streams. One enters the combustor, and the other goes for cooling the combustor and the turbine. The combusted gas and the bypass air are expanded by the axial turbine. They could measure the turbine rotational speed, and inlet and outlet temperature in both rich and stoichiometric conditions and also confirmed the feasibility of driving a turbine by rotating detonative combustors, which was also addressed by Zhou et al. [53]. Naples et al. [54] deployed an RDC in an open-loop Allison T63 gas turbine engine at the Air Force Research Laboratory (AFRL) facility in Dayton, Ohio. The original combustor was replaced by an RDC operated by Hydrogen fuel. The compressor of the original engine was decoupled from the facility through a controllable valve. Therefore, the compressor connected to the first turbine played a measurable load role for the first turbine to which it was connected. The power turbine drove a dynamometer on a separate shaft. A cooling system was designed to provide the dilution air inside and outside the RDC annulus. This system cooled down the high-temperature exhaust flow of the RDC to the turbine design temperature of 1300 K, which enabled the test stand to run for up to 20 minutes without any damage. The dilution air reduced pressure wave magnitude by 60-70% and maintained the temporal characteristics of the pressure waves. In that setting, the turbine blades experienced an unsteady pressure fluctuation of 25% of the mean pressure. Compared to the conventional deflagration combustion, they claimed an increase in turbine factor, i.e., the comparison of the total fuel energy input to the system to the energy extracted by the turbines, also confirmed by Kindracki et al. [55]. In another work using the same experimental setup, Paxson and Naples [56] illustrated that the integrated RDC operated with the subsonic flow throughout the exhaust plane. Although their setup had a considerable overall pressure loss due to the length of the device and the substantial flow restriction at the inlet, they concluded the possibility of an across-the-board pressure rise through an RDC using some minor alterations to their design. Later they [57] modified the instruments to measure flow enthalpy and pressure in high frequency flows. The amount of dilution air for cooling and lowering unsteadiness was up to 5.3 times the RDC exhaust mass flow rate. For the specific RDC operations, the high-pressure turbine experienced up to 700%

higher unsteadiness than in the case operated by a conventional combustor. However, this unsteadiness dropped down to around 70% through the high-pressure turbine, which is at the level of traditional combustors for the low-pressure turbine. In terms of turbine efficiency, they measured around 2 points discrepancy between the turbine operated with the RDC and the conventional combustor. Nevertheless, this comparison cannot be very promising since it was done on two different operating lines. Their results demonstrated that the unsteadiness of the RDC having high-frequency fluctuations is rapidly dissipated in the turbine. Athmanathan et al. [58, 59] at Purdue University designed an RDC equipped with a guide vane. The RDC exhaust flow is conditioned through a smooth divergent nozzle to increase Mach number and reduce flow angle variation entering the supersonic stationary blades. Their 3D-URANS simulations showed a total pressure penalty of around 10% in the unsteady case compared to the steady operation. The exhaust flow conditions obtained were utilized by the members of the same group [60] as the inlet conditions of a supersonic turbine stage. The turbine stage was designed to operate at Mach 2. Their numerical simulations indicated that more than 80% of the angular fluctuations were attenuated throughout the supersonic nozzle vanes. In terms of total pressure loss, the stator and rotor rows were responsible for almost an identical amount of pressure loss, 23.1% through the stator and 26.5% through the rotor, while the leading shock wave was captured as the primary loss source.

A multi-annular RDC was conceptually designed and integrated into a turbofan engine by Ji et al. [61]. They presented a new architecture of a turbofan engine comprising of multiple RDCs positioned in the annular channel of the bypass duct depicted in Fig.2.3(a). Since the bypass flow pressure is lower than the main combustor inlet and it has enough oxygen compared to the engine exhaust flow where an afterburner is usually employed, the RDC can be arranged there as an alternative to the mixed-exhaust turbofan engines having an afterburner. As a result of the performance analysis, the proposed architecture was superior in terms of specific fuel consumption and efficiency to the baseline engine; however, the improvements were diminished as the fan pressure ratio increased. Additionally, compared to the baseline engine, the operating line of the developed concept moved away from the surge line on the high corrected shaft speed, proclaiming an improvement in the fan stability margin. This trend is inverted in conventional turbofan engines as shown in Fig.2.3(b).

The disk-radial RDC concept was initially introduced by Bykovskii et al. [62, 63, 64]. In a disk shape RDC, the reactants are provided radially either inward or outward. Between the straight-walled confines of the disk-shaped combustor, one or more rotating detonation waves are created, and the exhaust flow is expanded through the central axis. Because of the radial shape, the flow inside experiences continuously changing cross-sectional area from the inlet to the outlet when the two chamber walls are parallel to each other [65]. Huff et al. [66, 67] coupled a turbocharger turbine to a radial RDC that is based on a disk-shaped type in which reactants come inward radially, detonate and then exit horizontally, similar to a radial turbine flow path. Their results suggested that the setup has a potential thermal efficiency of up to 40%. At the same time, it suffered from numerous losses, which was mainly due to the interaction of the nozzle guide vane and the combustor. They also observed that the addition of the compressor upstream and the turbine downstream of the radial RDC did not affect the operating mode of the detonative combustor. In similar ongoing attempts in Japan presented

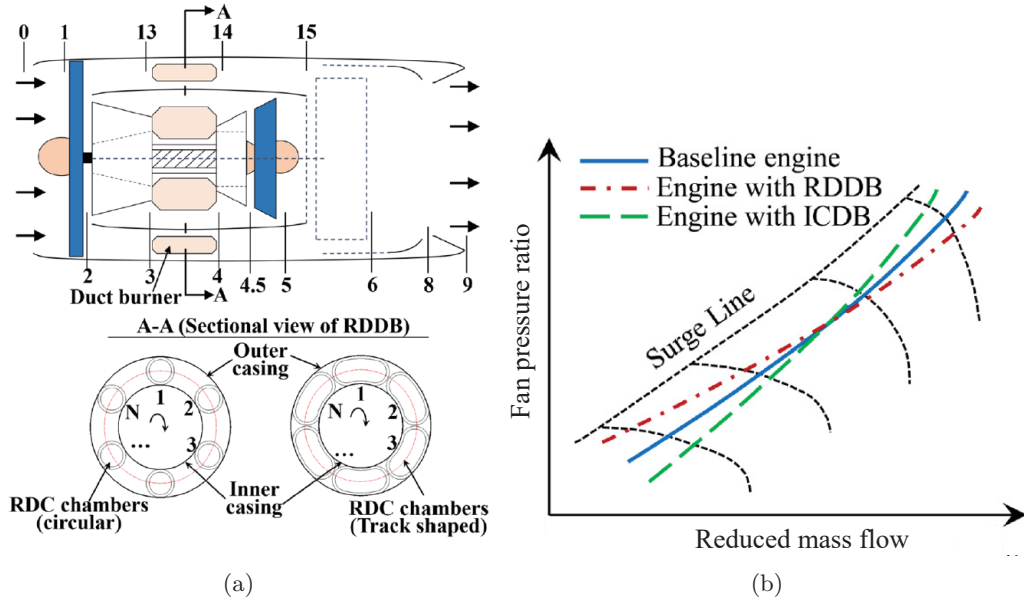


Figure 2.3: (a) An architecture of a turbofan engine embedded with a rotating detonation duct burner showing two possible shapes of circular and track-shaped chambers, (b) comparison of running lines for baseline, rotating detonation duct burner engine (RDDB), and isobaric duct burner turbofan engines (ICDB), taken from [61]

overallly by Higashi et al. [68], some experimental studies were done by Ishiyama et al. [69], and Higashi et al. [68] using a coupled compressor, a radial RDC, and a turbine. Since their component designs were not properly matched, the measured performance was considerably away from the design value, mainly because of huge losses that occurred in the turbine.

As a part of RDC-turbine integration studies, RDC exhaust flow passing through the stationary vanes has been characterized by many authors as well. DeBarmore et al. [70] and Welsh et al. [71] focused on the features of an RDC exhaust flow flowing through a turbine nozzle guide vane as part of the T63 helicopter engine. Their experimental pressure measurements showed that the stationary vanes decrease almost 60% of the incoming unsteadiness. The vane outlet flow angle was in a range of 40° to 55° . Considering an exit metal angle of 62° , the large deviation angle affirms that the vanes produced considerable losses due to the flow separation from the blade surfaces. Total pressure drop by the vanes was measured 4.2%. They deduced that this total pressure loss is not correlated to equivalence ratio, mass flow, or detonation velocity of the RDC [72].

Bach et al. [73, 74] at TU Berlin Energy Lab instrumented a simple guide vane row, having NACA0006 profile, downstream of the RDC experimental rig developed by Blümner et al. [75]. The primary goal of their investigations was to characterize the RDC operation considering different outlet restrictions, where a turbine expander can be mounted. By varying the number of blades and blade setting angle, they showed that the presence of guide vanes does not negatively affect the pressure gain of the RDC. The pressure measurement through the vanes captured a substantial attenuation in unsteadiness across the blades, independent of the detonation wave configuration. The interaction of guide vanes with the operating mode of the RDC indicated that the downstream geometry could be a useful tool to dampen the pressure fluctuations, condition the exhaust flow, and imprint a desired detonation wave direction.

Zhou et al. [76] used a guide vane row to study the propagation characteristics of the RDC wave. They showed a significant reduction in pressure oscillation of 64% by the vanes. They reported an unstable RDC operation due to the reflected shock wave to the combustor. This claims that the propagation mode of the reflected wave is related to the propagation direction of the rotating detonation wave.

Wei et al. [77] and Wu et al. [78] installed a turbine guide vane downstream an RDC to investigate its operational performance. They observed that when the detonation wave propagates in the clockwise direction, a higher static pressure of about 15% is achieved than the case with counterclockwise wave direction. The wave propagation direction also affects the RDC operating frequency, which is higher in the counterclockwise wave case. Additionally, they beheld that the direction of wave propagation influences the pressure oscillation attenuation by the stationary vane. Their work showed that if the wave propagation direction and the flow path direction of the guide vane are opposite to each other, the pressure oscillation attenuation increases, which is consistent with the findings of Bach et al. [73].

3

Methods

The present chapter outlines the methodologies developed and applied in the scope of this thesis. Figure 3.1 depicts an overview of the methods developed and utilized in this research. To begin with, the meanline analysis method is presented in sec. 3.1, which is coded as a part of in this work for steady-state turbine performance analysis. The method is based on a pressure distribution guess along the turbine mean radius and uses several correlations for calculating performance parameters. Meanline analysis is a powerful tool for quick performance evaluation of turbomachinery in steady-state operations. Section 3.2 describes a one-dimensional Euler equations solver which has been developed in the scope of SFB-1029 and adapted in this thesis for unsteady turbine simulation. The solver is modified and tuned to accept PDC exhaust flows as the inlet boundary conditions. RDC and PDC models are explained in sec. 3.3. The RDC model is based on the geometry of an existing test rig at the TU Berlin Energy lab. The PDC model comprises a one-dimensional Euler solver with a zero-dimensional plenum model. Thereupon, the three-dimensional CFD simulation method, used as a high fidelity turbine simulation tool employed for obtaining more details of the flow field and verifying other methods, is described in sec. 3.4. The CFD tool, as a Reynolds-averaged Navier–Stokes equations solver, and the associated settings are explained both for steady and unsteady simulations. This is followed by sec. 3.5 where an optimization methodology is elaborated. The optimization method is exploited for optimizing the turbine blade shapes. At last, the turbine case used as the baseline in part of the investigations is sketched out in sec. 3.6.

3.1 Meanline turbomachinery analysis

Turbomachinery design is often associated with several optimization iterations that involve performance evaluation for each design. Several turbomachinery modeling methods have been developed since the mid 19th century [79, 80, 81]. The primary differentiation of the methods lies in the levels of complexity and capability. Generally, raising the spatial dimensions employed in each technique makes them more accurate while getting more complex. In this regard, three-dimensional modeling approaches provide the most faultless representation of the fluid flow inside a turbomachinery, enabling detailed investigation of mass, momentum,

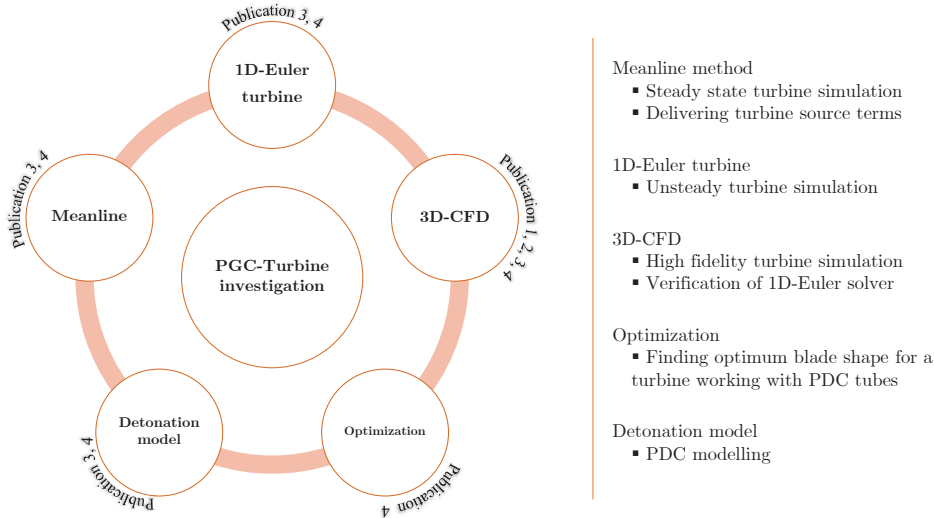


Figure 3.1: Overview of the methods used in the thesis.

and energy transfer throughout the geometry. Two and one-dimensional methods also use the same governing equations but with lower computational costs caused by reducing dimensions. Among the methods for turbomachinery simulation, the meanline method, usually referred to as zero-dimensional modeling, is extensively utilized in the early design stages of conventional turbomachinery. Although it is not a new approach [79, 82], it still remains popular as a powerful, handy and quick tool [83, 84, 85]. In general, meanline models rely mainly on empirical correlations developed and updated continuously based on several real experiments. Having time-independent flow phenomena and neglecting all dimensions are the two main assumptions in the meanline method. The flow conditions at the mean radius are taken as a reasonable average representing the flow over the full blade span. In this section, the meanline turbine analysis method used for the steady-state performance evaluation of the turbine is explained.

3.1.1 Flow velocity calculation

Figure 3.2 shows a typical turbine stage with a representation of flow velocity vectors at the inlet and outlet of the blades, called velocity triangles. In general, meanline analysis at design point requires three non-dimensional parameters of flow coefficient (ϕ), loading coefficient (ψ) and reaction ratio (Λ), expressed in Eq.3.1 to Eq.3.4. These three non-dimensional parameters form the non-dimensional velocity triangles, so that an additional dimensional parameter is required to define all the velocity magnitudes. Based on the definition of flow coefficient and the shape of velocity triangle in Fig.3.2, if the blade speed is kept constant, any increase in flow coefficient raises axial velocity, which increases both absolute and relative velocities, but swirl velocities (C_w) is not affected; hence the power output does not change. However, this increase in axial velocity or mass flow rate can cause higher losses in the turbine passage. The loading coefficient shows the amount of flow turning caused by the rotor blades. If blade speed and mass flow rate are assumed unchanged, the stage power will increase by increasing the work coefficient. The third non-dimensional parameter, reaction ratio, indicates the share of nozzle and rotor blade rows in the stage pressure drop. Based on Eq.3.4, zero reaction means all the

pressure drop is done through the nozzle blade row while increasing reaction ratio implies more pressure drop occurs in the rotor blade row. The stage exit flow angle can replace this parameter. If one is supplied, the other is uncontrolled and can be calculated by solving the velocity triangles. There are many different naming strategies for defining velocity triangles and the related calculations. Therefore, to avoid any confusion about plus-minus signs in the relations between the parameters, readers are referred to the available reference textbooks [48, 86, 87]. Having the flow coefficient and loading coefficient prescribed, the Smith chart [80] specifies the approximate turbine stage efficiency. Besides, there are some other charts developed for estimating the efficiency. Fielding [88] provides a turbine stage efficiency diagram which was developed based on Ainley-Mathieson [79] performance calculation. He considers the last stages with zero exit swirl, interior stages with 50% reaction ratio, and single-stage turbines with no swirl at their inlet and exit. Kacker and Okapuu [89] presents a predicted efficiency chart, with which experimental performance data are in good agreement, reported by Aungier [86]. In a meanline design procedure, one can use the approximate efficiency and through few iterations can obtain the correct efficiency and scale the turbine stage.

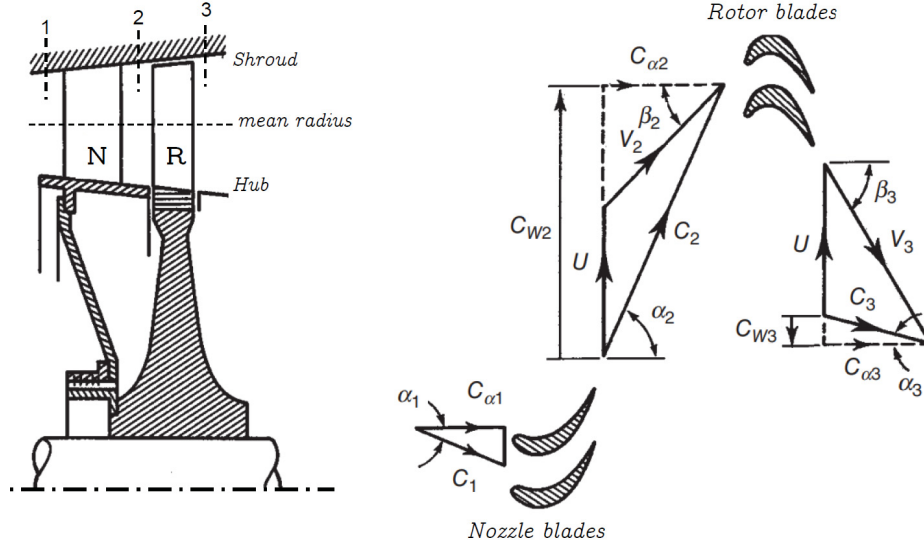


Figure 3.2: A meridional reference of a turbine stage and the flow velocity vectors.

$$\phi = \frac{C_a}{U} \quad (3.1)$$

$$\psi = \frac{\Delta h_t}{U^2} \quad (3.2)$$

If axial velocity is assumed to be constant along the turbine stage, the loading coefficient can be computed based on the change in the swirl velocity, as in Eq.3.3.

$$\psi = \frac{C_{w2} - C_{w3}}{U} \quad (3.3)$$

$$\Lambda = \frac{\Delta h_{s,rotor}}{\Delta h_t} \quad (3.4)$$

A turbomachine does not always work at its design point. Any deviation from the design operating values, e.g., a change in the design incidence angle, causes the machine to run at off-design conditions. Once a turbomachine runs at off-design conditions, velocity triangles and subsequently performance parameters such as pressure ratio, power, and efficiency will deviate from the design values.

3.1.2 Thermodynamic parameters calculation

A turbomachine can be represented thermodynamically using four primary properties of pressure (P), temperature (T), enthalpy (h), and entropy (S). The simplest version of the equation of state for a thermally perfect gas relates the pressure and temperature with density (ρ), as in Eq.3.5, where R is the ideal gas constant.

$$P = \rho RT \quad (3.5)$$

Enthalpy is defined as the sum of the system's internal energy and the product of its pressure and volume. Specific enthalpy is defined as the enthalpy per unit mass in Eq.3.6.

$$h = E + Pv_{sp} \quad (3.6)$$

Enthalpy itself is a relative parameter and a direct function of temperature. Assuming a reference state point, Eq.3.7 defines the enthalpy, where c_p is the heat capacity of the flow at constant pressure.

$$h = h_{ref} + c_p(T - T_{ref}) \quad (3.7)$$

The first law of thermodynamics prescribes that the total energy of an ideal Brayton cycle is conserved. Therefore, the work extracted by a turbine assuming an ideal expansion process is equal to the enthalpy change, defined in Eq.3.8 as work per unit mass.

$$W = \Delta h = c_p \Delta T \quad (3.8)$$

In any thermodynamic process, e.g., an expansion in a turbine stage, entropy is generated. Entropy is also a relative parameter and defined as the change in heat over the temperature of the flow that represents the amount of loss in the system.

$$\delta S = \frac{\delta q}{\Delta T} \quad (3.9)$$

By setting an arbitrary reference state point, the entropy of the system can be formulated as Eq.3.10.

$$S = S_{ref} + c_p \ln(T/T_{ref}) - R \ln(P/P_{ref}) \quad (3.10)$$

In turbomachinery, absolute and relative flow velocities are defined because of the rotor rotational speed, as shown in velocity triangles of Fig.3.2. Therefore, total quantities are expressed in both relative and absolute frames of reference.

$$h_t = h_s + \frac{1}{2}C^2 \quad \& \quad h_{t,rel} = h_s + \frac{1}{2}V^2 \quad (3.11)$$

$$P_t = P_s + \frac{1}{2}\rho C^2 \quad \& \quad P_{t,rel} = P_s + \frac{1}{2}\rho V^2 \quad (3.12)$$

$$T_t = T_s + \frac{1}{2c_p}C^2 \quad \& \quad T_{t,rel} = T_s + \frac{1}{2c_p}V^2 \quad (3.13)$$

Isentropic expansion relations are also used in the meanline calculation, as follows.

$$T_t = T_s \left(1 + \frac{\gamma - 1}{2} M^2\right) \quad (3.14)$$

$$P_t = P_s (T_t/T_s)^{(\gamma-1)/\gamma} \quad (3.15)$$

Based on the stated equations, if two state properties are known, the third can be calculated within the meanline program. If only one state variable is known at a blade outlet station, guessing a value for entropy and calculating the third parameter in an iterative process is done. Actually, the entropy guess at the blade outlet means assuming a loss magnitude through the respective blade row, and then, the loss correlations will tune the entropy to reach the correct value.

3.1.3 Loss correlations

If it is assumed that the flow is isentropic in any flow channel, the total pressure will be conserved. However, there is always a source of total pressure loss in a flow passage, which makes the process irreversible. In a turbine stage, including a stator vane row and a rotor blade row, the total pressure is decreased primarily due to the turbine work output. Part of the total pressure drop in the turbine is related to the losses in stator and also in rotor blade passages. The sources of losses and their magnitude have been identified following several experimental tests, and the related correlations for calculating their amounts have been developed. According to the notation in Fig.3.2, the loss coefficients for a nozzle vane row and a rotor blade row are defined as Eq.3.16 and Eq.3.17, respectively.

$$\xi_N = \frac{P_{t1} - P_{t2}}{P_{t2} - P_{s2}} \quad (3.16)$$

$$\xi_R = \frac{P_{t2,rel} - P_{t3,rel}}{P_{t3,rel} - P_{s3}} \quad (3.17)$$

The pressure loss occurring through the blade rows can be used to compute the entropy generation. Using Eq.3.10 and the loss coefficient definitions, entropy change through nozzle vane row and rotor blade row of a turbine are formulated as in Eq.3.18 and Eq.3.19.

$$S_2 - S_1 = -R \ln\left(1 - \xi_N \frac{P_{t2} - P_{s2}}{P_{t1}}\right) \quad (3.18)$$

$$S_3 - S_2 = -R \ln\left(1 - \xi_R \frac{P_{t3,rel} - P_{s3}}{P_{t2,rel}}\right) \quad (3.19)$$

The total pressure loss coefficient comprises different loss coefficients from various sources, including profile loss, secondary flow loss, tip clearance, trailing edge loss, supersonic expansion loss, and shock loss, represented in Eq.3.20 which is applicable for stator vane and rotor blade rows.

$$\xi = \xi_p + \xi_{se} + \xi_{cl} + \xi_{te} + \xi_{ex} + \xi_{sh} \quad (3.20)$$

Profile loss

The loss system definition in this work is based on the work of Aungier [86], Ainley-Mathieson [79] and Kacker and Okapuu [89]. The profile loss coefficient is defined as in Eq.3.21, which is developed by Ainley-Mathieson and corrected later by Kacker and Okapuu to modify the model to account for modern designs by a factor of K_{Kac} . This factor can lower the profile loss coefficient of old designs by a factor of up to 0.67 for modern designs. The Ainley-Mathieson model includes the trailing edge loss coefficient assuming a trailing edge blade thickness over blade pitch (t_2/s) of 0.02. Since the trailing edge loss coefficient is separately computed in the overall loss model, $\Delta\xi_{te}$ is subtracting the trailing edge loss for $t_2/s = 0.02$.

$$\xi_p = K_{Kac} K_{Inc} K_{Mach} K_{Comp} K_{Re} \left([\xi_{p1} + (\alpha'_1/\beta_2)^2 (\xi_{p2} - \xi_{p1})] (5t_{max}/c)^{\alpha'_1/\beta_2} - \Delta\xi_{te} \right) \quad (3.21)$$

The off-design incidence correction factor (K_{Inc}) is a function of the incidence angle (i) and the stall incidence angle (i_s) based on Ainley-Mathieson data and the empirical model that Aungier has fitted to them, shown in Fig.3.3. The stall incidence angle itself is a function of the blade inlet angle and the relative outlet flow angle. Note that the stall incidence angle correlation by Ainley-Mathieson plotted here is for a pitch on chord ratio (s/c) of 0.75. Aungier model extrapolates the values for two ranges of s/c , namely higher and lower than $s/c = 0.8$. For the sake of brevity, the readers are referred to the original reference text [86].

Mach number correction factor (K_{Mach}) can be calculated as a function of outlet relative Mach number ($M_{2,rel}$) and the ratio of pitch to the radius of the curvature of the blade suction surface (s/R_c) as in Eq.3.22. This equation supports the Mach number correction factor for $0.6 < M_{2,rel} \leq 1$. For $M_{2,rel} \leq 0.6$, the Mach number correction factor is unity. The associated loss for $M_{2,rel} > 1$ is calculated in the form of supersonic expansion loss.

$$K_{Mach} = 1 + \left(1.65(M_{2,rel} - 0.6) + 240(M_{2,rel} - 0.06)^2 \right) (s/R_c)^{3M_{2,rel}-0.6} \quad (3.22)$$

Turbomachinery loss data are usually derived from low-speed cascade tests, as the Ainley-Mathieson profile loss model. At high Mach numbers, the compressibility effect shortens the boundary layer thickness and suppresses the flow separation. To account for these positive effects of the compressibility, K_{Comp} was introduced by Kacker and Okapuu, which is a function of relative inlet and outlet Mach numbers, as formulated in Eq.3.23. For relative outlet Mach

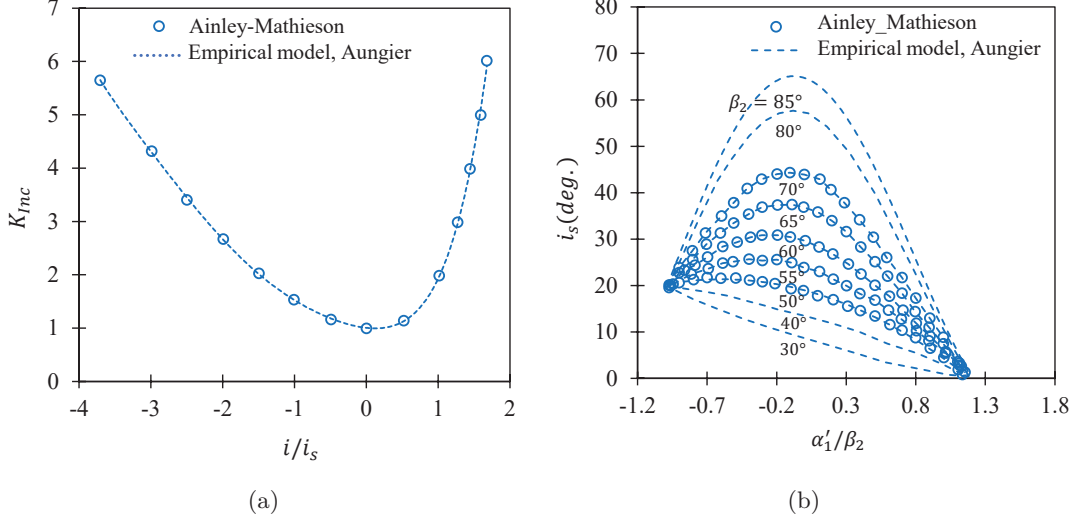


Figure 3.3: (a) Model for off-design incidence correction factor, and (b) stall incidence angle model.

numbers below 0.2, K_{Comp} will be unity since the flow speed is close to the cascade tests.

$$K_{Comp} = 1 - 0.625 (M_{2,rel} - 0.2 + |M_{2,rel} - 0.2|) (M_{1,rel}/M_{2,rel})^2 \quad (3.23)$$

To account for the effect of different working Reynolds numbers than those in the cascade tests upon which the loss model developed, K_{Re} is introduced based on boundary layer skin friction models, which have been developed according to the total drag force on a flat plate. The Reynolds correction factor for turbine blade rows is based the blade chord Reynolds number at outlet flow conditions ($Re_c = \rho_2 V_2 c / \mu_2$). In this regard, K_{Re} is defined in three bounds of Re_c , as in Eq.3.24 based on laminar skin friction model, Eq.3.25 in the transition region similar to the cascade test conditions, and Eq.3.26 based on the turbulent skin friction model.

$$Re_c < 10^5 \rightarrow K_{Re} = \sqrt{10^5 / Re_c} \quad (3.24)$$

$$1 \times 10^5 \leq Re_c \leq 5 \times 10^5 \rightarrow K_{Re} = 1 \quad (3.25)$$

$$Re_c > 5 \times 10^5 \rightarrow K_{Re} = \left(\log(5 \times 10^5) / \log Re_c \right)^{2.58} \quad (3.26)$$

In turbulent flow, the Reynolds correction factor is further tuned by Aungier to include the blade surface roughness based on the corresponding Reynolds number ($Re_e = \rho_2 V_2 e / \mu_2$), where e is the roughness height defined as peak-to-trough. Since blade roughness has no effect in laminar flows, only Eq.3.26 is modified to include the roughness effect in turbulent flows.

$$K_{Re} = 1 + \left(\left(\log(5 \times 10^5) / \log(100c/e) \right)^{2.25} - 1 \right) \left(1 - 5 \times 10^5 / Re_c \right) \quad (3.27)$$

The nozzle blade profile loss coefficient (ξ_{p1}) for zero blade inlet angle developed by Ainley-Mathieson is depicted in Fig.3.4(a). The impulse blade profile loss coefficient (ξ_{p2}) for a blade having $\beta_2 = \alpha'_1$ is also depicted in Fig.3.4(b). Both losses are strong functions of the pitch

3. Methods

to chord ratio and the outlet flow angle. Aungier has fitted two models to extrapolate them beyond the limits [86].

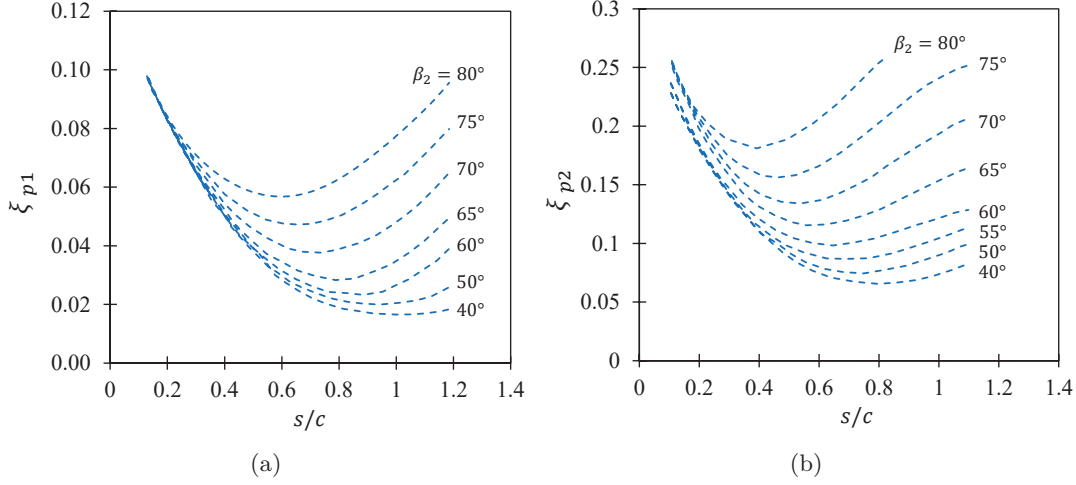


Figure 3.4: (a) Nozzle blade profile loss for $\alpha_1' = 0$, and (b) impulse rotor blade profile loss for $\beta_2 = \alpha_1'$.

Secondary loss

The secondary loss coefficient was developed by Dunham and Came [90], later revised by Kacker, and Okapuu [89] and corrected by Aungier [86]. The blade lift coefficient is calculated based on the force balance over the blade profile, which is finally converged to a relation between the flow inlet and outlet angles and blade solidity, as in Eq.3.28.

$$C_L = 2(s/c)(\tan \beta_1 + \tan \beta_2) \quad (3.28)$$

Ainley [79] defined the loading parameter (L_A) based on the mean flow angle definition $\tan \alpha_m = (\tan \alpha_1 + \tan \alpha_2)/2$.

$$L_A = C_L(c/s) \cos^2 \beta_2 / \cos^3 \alpha_m \quad (3.29)$$

To account for different blade aspect ratios than those of the cascade tests, F_{AR} is introduced in Eq.3.30 according to the blade height and chord length.

$$F_{AR} = \begin{cases} \frac{c}{h_b}; & h_b/c \geq 2 \\ \frac{1}{2} \left(\frac{2c}{h_b} \right)^{0.7}; & h_b/c < 2 \end{cases} \quad (3.30)$$

The original secondary loss coefficient by Kacker and Okapuu is a function of Ainley loading parameter, aspect ratio coefficient, and flow acceleration which is simply defined as $(\cos \beta_2 / \cos \alpha_1')$.

$$\xi_{se}^* = 0.0334 F_{AR} L_A \cos \beta_2 / \cos \alpha_1' \quad (3.31)$$

Aungier[86] suggests an upper asymptotic limit of 0.365 to avoid excessive unrealistic values of the secondary loss coefficient, which may be resulted in far off-design conditions. He also used

a compressibility correction factor for secondary loss shown in Eq.3.32 similar to that of profile loss but with a modification to include blade height effect and at the same time to prevent unrealistic values for very low blade heights. Therefore, the final secondary loss coefficient is formulated in Eq.3.33.

$$K_{Comp,se} = 1 - \frac{(1 - K_{Comp})c_{ax}^2}{h_b^2 (1 + (c_{ax}/h_b)^2)} \quad (3.32)$$

$$\xi_{se} = K_{Re} K_{Comp,se} \sqrt{\xi_{se}^{*2} / (1 + 7.5\xi_{se}^{*2})} \quad (3.33)$$

Tip clearance loss

A rotor blade has a tip clearance that imposes total pressure loss to the system. Dunham and Came [90] developed a correlation for the tip clearance loss that includes Ainley loading parameter, blade height to chord ratio, and the clearance between the blade tip and the turbine casing (δ), illustrated in Eq.3.34.

$$\xi_{cl} = 0.47 L_A (c/h_b) (\delta/c)^{0.78} \quad (3.34)$$

Trailing edge loss

Once a fluid flow in a passage experiences an abrupt enlargement, e.g., from a small circular duct to a sudden large one, the wakes and separations occur and create a source of the total pressure loss to the flow [91]. This enlargement in the flow passage exists at the turbine blade trailing edge but at a very moderate level. To account for the blade trailing edge associated loss, a classical expansion total loss formulation for flow area change is utilized, assuming a constant density immediately before and after the trailing edge, see Eq.3.35. As shown in the equation, the effective blade passage change is reflected in the passage area before mixing ($s \sin \beta_g$), which is reduced by the blade trailing edge thickness (t_2). Then, the trailing edge loss coefficient is calculated by dividing the total pressure loss by the dynamic discharge pressure, Eq.3.36.

$$\Delta P_t = 0.5 \rho V_2^2 (s \sin \beta_g / (s \sin \beta_g - t_2) - 1)^2 \quad (3.35)$$

$$\xi_{te} = \Delta P_t / (0.5 \rho V_2^2) \quad (3.36)$$

Supersonic expansion loss

The flow exiting a blade passage might become over-expanded to supersonic exit Mach numbers. Although this condition rarely happens, the resulting shock waves in supersonic flows will cause total pressure loss. The supersonic expansion loss is defined based on the relative blade outlet Mach number, as in Eq.3.37. Obviously, if the outlet Mach number is less than or equal to unity, the supersonic expansion loss will be zero.

$$\xi_{ex} = \left(1 - \frac{1}{M_{2,rel}}\right)^2 \quad (3.37)$$

Shock loss

Shock waves can be present at the blade leading edge even in relatively low inlet Mach numbers because of the highly curved blade leading edges and the associated flow acceleration in this region. The radial equilibrium in a turbine flow results in the radial distribution of gas condition, which corresponds to the highest Mach numbers at the blade hub region, compared to midspan and tip radius. Kacker and Okapuu [89] suggest a relation for obtaining the total pressure loss from a leading-edge shock on the inner end wall and the blade passage, as in Eq.3.38. With the aim of generalizing the loss at the hub region to the whole radius in the meanline loss system, the total pressure loss at the hub is multiplied by the hub-tip radius ratio (Eq.3.39). To calculate the shock loss coefficient, the related total pressure loss should be rewritten according to the dynamic outlet pressure, as formulated in Eq.3.40.

$$\left(\frac{\Delta P_t}{0.5\rho V_1^2} \right)_{hub} = 0.75(M_{1,hub} - 0.4)^{1.75} \quad (3.38)$$

$$\left(\frac{\Delta P_t}{0.5\rho V_1^2} \right)_{sh} = \frac{r_{hub}}{r_{tip}} \left(\frac{\Delta P_t}{0.5\rho V_1^2} \right)_{hub} \quad (3.39)$$

$$\xi_{sh} = \left(\frac{\Delta P_t}{0.5\rho V_1^2} \right)_{sh} \left(\frac{P_{s,1}}{P_{s,2}} \right) \left(\frac{1 - \left(1 + \left(\frac{\gamma-1}{2} M_1^2\right)\right)^{\gamma/(\gamma-1)}}{1 - \left(1 + \left(\frac{\gamma-1}{2} M_2^2\right)\right)^{\gamma/(\gamma-1)}} \right) \quad (3.40)$$

3.1.4 Program logic

There are different strategies for meanline turbine analysis, each of which takes a set of input data and try to solve flow equations at meanline to compute performance parameters. In this research, the meanline solver has a main loop based on the mass flow convergence along the turbine. The flow chart depicted in Fig.3.5 shows the whole procedure at a glance. A rather similar approach for meanline analysis was used by Sjödin [92] as well. Initially, the program takes the geometrical parameters, temperature, and pressure at the turbine inlet to calculate the rest of the parameters there. Then, based on a predefined turbine outlet static pressure, a first trial pressure distribution along the turbine is assumed. Denton's target pressure method [81] relates the pressure change at any turbine blade trailing edge to the mass flow change at one trailing edge upstream. An entropy loop is engaged to calculate each row kinematic and thermodynamic parameters. This entropy loop starts with a guess of entropy change throughout the blade row. Using the velocity triangle relations, the outlet flow angle model by Mamaev [93], and the loss correlations discussed earlier, the new entropy change will be computed and the loop continues to reach convergence. Sequentially, these calculations are done from the first row to the last turbine row. The turbine mass flow is continuously checked, and if no consistency is observed, Denton's method is applied and the new pressure distribution based on the mass flow adjustment is set for the new iteration. This method consecutively adjusts the pressure based on the mass flow change to reach a satisfactory converged solution. Newton Raphson's method is used inside the inner loops for loss calculations, outlet flow angle calculations, and entropy calculations to increase the computational efficiency of the program. The detail of the meanline program is shown in Fig.3.6 using a block diagram.

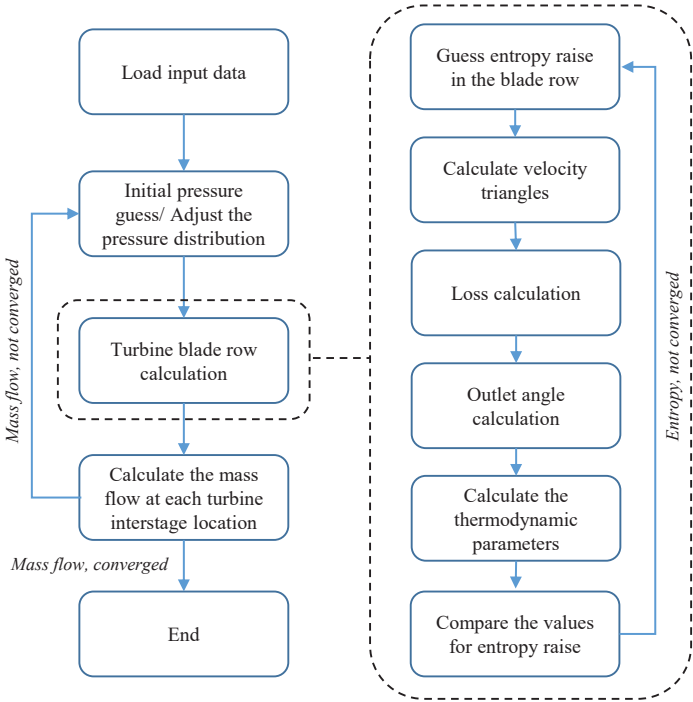


Figure 3.5: Overall flow chart of the turbine meanline performance analysis.

3.2 One-dimensional Euler solver

In a gas turbine engine, all components, including compressor, combustor, and turbine, are ideally designed to operate in steady-state conditions, on which the whole engine has the highest performance. Nevertheless, this steady-state condition can be easily switched to a transient operation by some changes, including, but not limited to, startup and shutdown, fuel flow change, inlet flow distortion, and any change in airflow. The transient operation of each engine component can lead to adverse operations such as loss of power or thrust, efficiency and even may cause engine damage due to high thermal or mechanical loads if not carefully behaved. Due to the nature of the unsteady operating condition of PGC devices, it must be expected that the turbomachine connected to such a device works under transient conditions. Since the unsteadiness in PGC devices ranges in a frequency of 10 Hz to 10 kHz, three-dimensional CFD simulations, e.g., time-dependent Reynolds Averaged Navier-Stokes equations solvers, are too computationally expensive to be utilized, specifically when several simulations are required. Any reduced order method should account for the temporal variations in flow and be robust enough to handle the complex three-dimensional flow inside a turbomachine accurately. One-dimensional methods has been used so far in turbomachinery flows [94]. Garrard [95] developed a one-dimensional modelling approach based on Euler equations to simulate the performance of a single spool gas turbine engine. The one-dimensional model by Garrard was calibrated using the data from Lycoming T55-L-712 turboshaft engine, which has the advantage of simulating the engine in post-stall compressor operations. Chiong et al. [96] used a one-dimensional solver and integrate it with a meanline analysis program for simulating a mixed flow turbocharger turbine. They used the meanline method for every discrete point on the inflow pulse to calculate the tangential velocities to the rotor blades. In this research, a model based on Euler equations are developed for unsteady turbine simulation working with

3. Methods

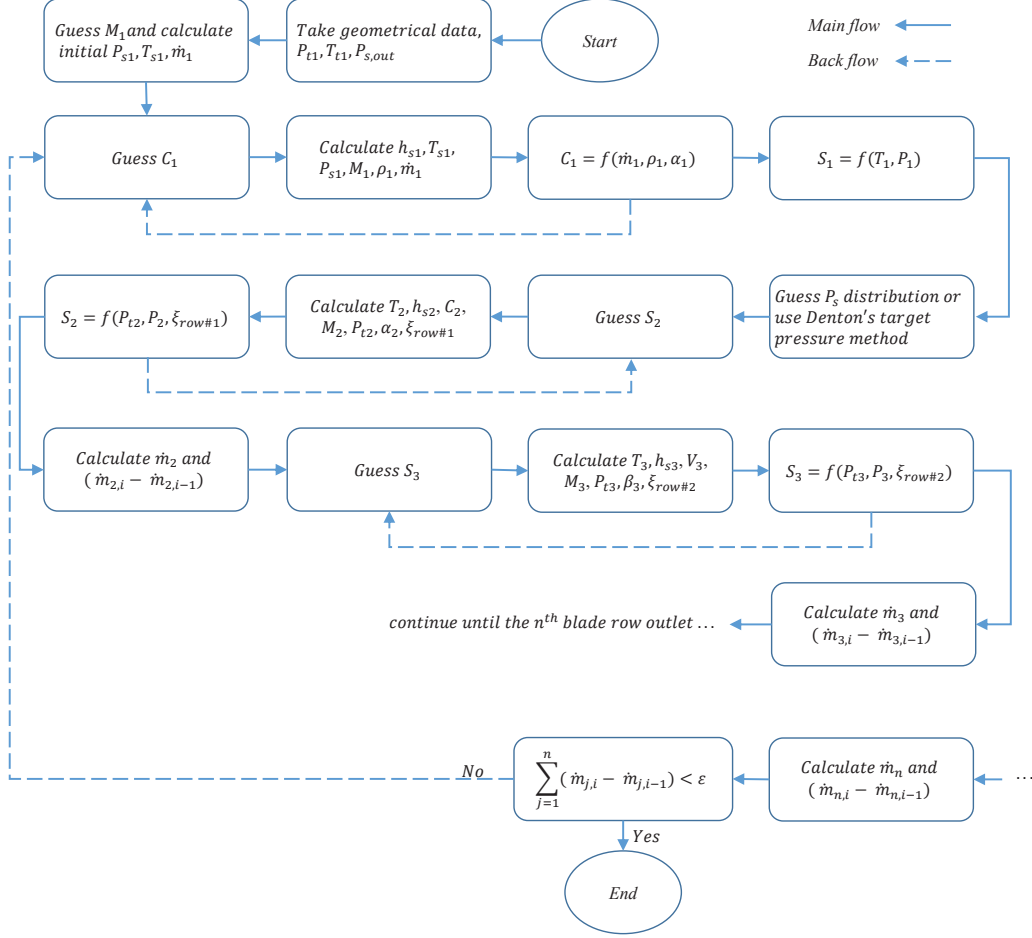


Figure 3.6: Meanline program block diagram including inner loops.

PGC devices. The model was initially developed for shockless explosion combustion [97, 98]. Euler equations are derived from continuity equations of mass, momentum and energy, in which the flow is assumed to be inviscid, while in the Navier-Stokes equations the viscosity parameter is included. In the following subsections, the governing equations and how the model takes advantage of the meanline program will be elucidated.

3.2.1 Governing equations

The governing equations comprise of three equations namely mass, momentum, and energy balance that are solved simultaneously using a finite volume numerical technique. The mass flow continuity equation in conservation form is written as in Eq.3.41, which shows no mass can be created or destroyed in a control volume.

$$\frac{\partial}{\partial t}(\rho) + \nabla \cdot (\rho C) = 0 \quad (3.41)$$

The momentum conservation equation is formulated as in Eq.3.42, in which \otimes is outer product. The left side of the equation depicts the acceleration and mass, and the right side represents forces, including hydrostatic effects of the pressure gradient (∇P_s), the internal stress forces, or viscous effect (τ) and body forces, like gravity (ρg).

$$\frac{\partial}{\partial t}(\rho C) + \nabla \cdot (\rho C \otimes C) = -\nabla P_s + \nabla \cdot \tau + \rho g \quad (3.42)$$

For energy conservation, the corresponding formula is represented by Eq.3.43, if heat transfer is excluded from the right side of the equation.

$$\frac{\partial}{\partial t}(\rho E) + \nabla \cdot (C(\rho E + P_s)) = \nabla \cdot (\tau C) \quad (3.43)$$

If viscous effects are neglected from the above equations, known as Navier-stokes equations, the Euler equations will be derived. Preserving the axial direction, the one-dimensional Euler equations can be formulated as Eq.3.44, if no mass, momentum, and energy source terms are considered.

$$\begin{aligned} \text{Mass} : \frac{\partial}{\partial t}(\rho) + \frac{\partial}{\partial x}(\rho C_a) &= 0 \\ \text{Momentum} : \frac{\partial}{\partial t}(\rho C_a) + \frac{\partial}{\partial x}(\rho C_a^2 + P) &= 0 \\ \text{Energy} : \frac{\partial}{\partial t}(\rho E) + \frac{\partial}{\partial x}(C_a(\rho E + P)) &= 0 \end{aligned} \quad (3.44)$$

The above Euler equations model the fluid flow in a symmetrical cylinder. In case the domain area is changed along the axial direction, e.g., a cone shape, the flow can still be modeled as a one-dimensional system. In such a model, the shape is symmetrical with respect to the axial direction, and the volume change is a function of the axial location, see Eq.3.45, where $A(x)$ is the cross-sectional area and v is the volume.

$$dv = A(x)dx \quad (3.45)$$

Using the expansion in Eq.3.45 in the integral three-dimensional form of the mass conservation equation will lead to the involvement of area as derived in Eq.3.46. Only in this formulation, r and dw are surface normal and surface element, respectively.

$$\begin{aligned} 0 &= \frac{\partial}{\partial t} \int_v \rho dv + \int_{\partial v} \rho C \cdot r dw \\ &= \frac{\partial}{\partial t} \int_v \rho A dx + \int_{\partial v} \rho C \cdot r dw \\ &= \int_v \left[\frac{\partial}{\partial t}(\rho A) + \frac{\partial}{\partial x}(\rho C A) \right] dx \Rightarrow \frac{\partial}{\partial t}(\rho A) + \frac{\partial}{\partial x}(\rho C A) = 0 \end{aligned} \quad (3.46)$$

In the same token, the conservation equations of momentum and energy can be reformulated, so that the quasi-one-dimensional Euler equations are derived as in Eq.3.47 and Eq.3.48, which relates the parameter variations in time and space to the source terms variation in space (O is the matrix of source terms).

$$\frac{\partial M}{\partial t} + \frac{\partial N}{\partial x} = \frac{\partial O}{\partial x} \quad (3.47)$$

$$M = \begin{bmatrix} \rho A \\ \rho C_a A \\ \rho E A \end{bmatrix}, N = \begin{bmatrix} \rho C_a A \\ \rho C_a^2 A + P_s A \\ C_a A(\rho E + P_s) \end{bmatrix} \quad (3.48)$$

For a pure flow field, e.g., a duct with no heat transfer and loss of energy, the source term matrix (O) in Eq.3.49 is zero except the term $P_s A$ standing for the pressure source term left from the derivation of the momentum equation [97]. Any mass flow extraction or injection must be specified as a mass flow source term. In a similar fashion, the external forces, heat and work changes must be included in O . For the turbine case, usually, a fraction of cold mass flow is injected to cool down the turbine blades and avoid high thermal loads and damages. The cooling mass flow comes from an external source like the compressor or ambient air, closing the mass continuity equation. The role of the turbine blades is to extract the energy from the working fluid. The turbine rotors extract the flow energy and convert it to the turbine shaft work. So that the shaft work is a source term in the energy balance equation. The other energy source term is related to the cooling mass flow injected into the turbine section. This mass flow brings its energy to the working flow; hence the related energy must be considered in the energy source term. If any heat extraction from or addition into the turbine section occurs, the corresponding amount of energy (Q) must take part in the energy equation. The fluid flow passing through the turbine inserts a force on the blades. This force is called blade force and has axial, radial, and tangential components. Since the modeling is one-dimensional in the axial direction, only the axial component is included in the source term matrix. To calculate the blade force, the force balance acting on a control volume, including a turbine blade, should be considered, shown in Fig.3.7. Assuming the fluid flows from left to the right, four types of forces act on the control volume. Pressure force at the inlet of the control volume and the same force but in the reverse direction at the outlet boundary is equal to the pressure times the related area. The blade force is the other force that comes from the presence of the blade inside the control volume. Due to the area change from the inlet to the outlet of the control volume, the endwall forces are acting at the top and bottom boundaries of the control volume. This endwall force is equal to the pressure times the projected area in the radial direction. According to Newton's second law, the sum of all forces acting on a control volume equals the momentum difference between its inlet and outlet. Therefore, the blade force is calculated and the source term matrix including mass, momentum, and energy source terms is formed as in Eq.3.49 to close the quasi one-dimensional Euler equations.

$$O = \begin{bmatrix} \dot{m}_b \\ F_x + P_s A \\ Q + W + \dot{m}_b h_{t,b} \end{bmatrix} \quad (3.49)$$

A second-order finite volume scheme is used to solve the governing equations together with the equation of state. The domain is discretized in the axial direction for solving the equations.

3.2.2 Integration of meanline and 1D-Euler methods

There are some possibilities to supply the momentum and energy source terms to the time-dependent Euler equations. One is to assume fixed source terms based on the turbine design

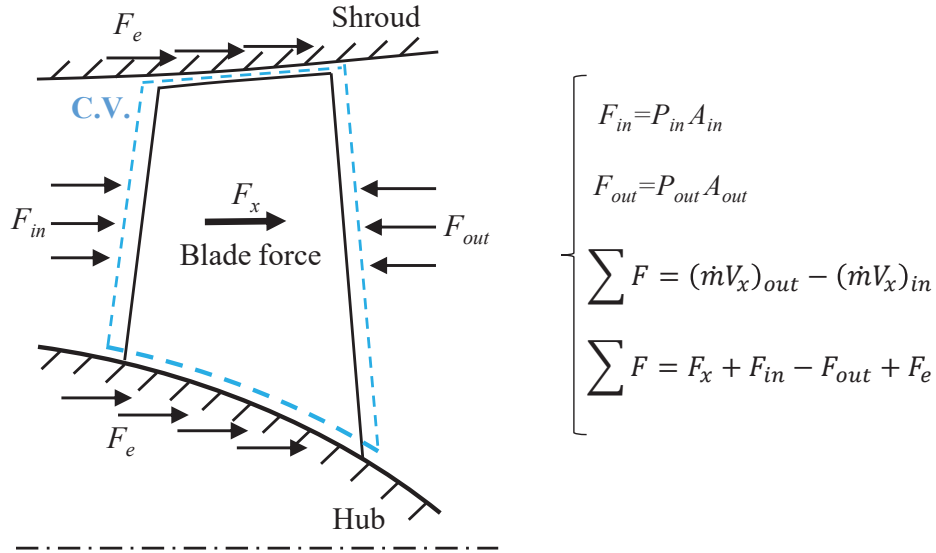


Figure 3.7: Force balance on a control volume around a turbine blade, taken from Publication IV.

operating point. Although this is very easy to implement since the design point of a turbine is usually known, the transient simulation cannot be very promising because the turbine may work at far off-design conditions. Specifically, in PGC applications that the amplitude of the turbine inlet fluctuations are usually more than 50%, a fixed force and energy source terms do not represent the blades correctly. Another possibility is to use the overall turbomachine map to compute the source terms as utilized in a compressor one-dimensional simulation by Dittmar and Stathopoulos [99]. Since the overall map does not provide the required specifications for each blade row separately, one has to presume a distribution of the overall force and work over the entire machine, e.g., Dittmar and Stathopoulos [99] distributed the source terms evenly throughout a multistage compressor. In this method, based on the pressure ratio of the machine, the mass flow and efficiency are read from the map. The total work can be computed using efficiency, pressure ratio, mass flow rate and inlet temperature. Additionally, the summation of force acting on all blade rows is calculated by knowing the mass flow rate, the temperature at the inlet, and the work extraction. However, this approach is controversial due to the fact that each blade row in a turbomachine experiences different loading depending on the blade design and the operating conditions. The other option that is used in this thesis takes advantage of the steady-state simulation of a turbomachine to provide the exact amount of source terms for each blade row for each off-design operating point. The simulation can be done using either high fidelity methods, e.g., steady 3D-CFD simulation, or the low fidelity method of meanline analysis. Since the meanline analysis has been proven accurate and fast enough, the emphasis is on using the meanline to calculate the Euler equation source terms.

The meanline analysis assesses off-design performance characteristics of the turbine, as described in sec.3.1. The method uses row-by-row analysis and calculates kinematic and thermodynamic parameters at each blade row leading and trailing edges. The parameters required for calculating the momentum and energy source terms in Eq.3.49 for every blade row are supplied in the form of a lookup table. The table includes thermodynamic parameters at each interstage location throughout the turbine as well as the force and work source terms

for each blade row. The values in the table cover the turbine's entire operating map at some discrete off-design points. Once the turbine geometry, including stator and rotor axial locations, is defined in the 1D-Euler solver, the solver takes the source terms where a blade is present. In a transient turbine simulation in which the turbine works under a pulsating boundary condition, the turbine is working under a different off-design condition at each instant. Additionally, the time-dependent flow in the turbine leads to a phase difference for each blade row. Suppose that the first blade row works with a condition similar to a steady off-design operating point of "A." At the same time instant, the adjacent blade row is working under a disparate condition named "B," while "A" and "B" do not correspond to the same point on the steady-state off-design operating map. Therefore, the source terms cannot be taken from the table based on instantaneous overall turbine pressure ratio, or only inlet or outlet condition, but should be read based on the local flow conditions. To find the most accurate source terms from the table, the program takes the pressure at the blade leading and trailing edge cells and reads the corresponding source terms. The program makes a simple average of the two values and implements it in the 1D-Euler solver at the corresponding time instant. In order to avoid the effect of any numerical disturbance at the computational cell, based on which the source terms are read from the table, the average pressure values of more than one cell are used as the pressure at the leading or trailing edges of the blade row.

The meanline program provides the source terms as unique values for each blade row, while the 1D-Euler method computes the flow field using more condensed computational cells. Therefore, the source term values for every blade row must be distributed from the blade inlet to the outlet. Considering the numerical solver stability issues, a parabolic distribution is utilized for this aim. The parabola distribution of the blade force is expressed in Eq.3.50 which is the same for work source term distribution over rotor blades. It is noted that a_1 , a_2 , and a_3 are the parabola constants.

$$\begin{aligned} Y &= a_1x^2 + a_2x + a_3 \\ F_x &= \int_{x_{le}}^{x_{te}} Y dx \end{aligned} \tag{3.50}$$

3.3 Pressure gain combustion devices

Rotating detonation and pulsed detonation combustors are the two PGC devices considered in this research for investigating turbomachinery interactions. The RDC configuration used in Publication I and Publication II, are based on the experimental RDC setup at the Energy Lab at TU Berlin. The exhaust annulus, together with the stationary blades, is modeled to give a deep insight into the domain, where experimental measurement is almost impossible. In Publication III and Publication IV, the PDC device is modeled using a numerical scheme. In this section, these two devices are described.

3.3.1 Rotating detonation combustor model

The RDC test rig at TU Berlin is a radially-inward design built up by Blümner et al. [100, 101] based on a design introduced by Shank et al. [102]. A cross-sectional view of the experimental

setup is depicted in Fig.3.8(a). In this configuration, hydrogen as the fuel (red vectors) is injected through equally-spaced hundred holes of 0.5 mm diameter. These holes are distributed tangentially on the outer surface of the combustion annulus. The airflow (blue vectors) as the oxidizer is injected radially inward. This injection configuration provides a jet in a crossflow scheme as shown in a zoomed view. The mixing pattern using two different air injection gap heights was investigated by Blümner et al. [103]. The combustor annulus comprises an outer wall, a center body on the sides, and a fuel plate at the bottom. The outer diameter is 90 mm and the annulus width is 7.6 mm providing an annulus area of 1967.39 mm^2 . The combustor annulus length is 112 mm, from the injector surface to the exit. These annulus dimensions can provide the operation with stable detonation waves. Nevertheless, different outer and center body lengths and different types of outlet restrictions were used to investigate the combustor length, and back pressure on RDC operation by Blümner [101]. Since currently, the setup has no cooling system, the run time is limited to around 500 ms to avoid any damage. To start the RDC, air is supplied with a pressure of around 13 bar and hydrogen is flowed at a pressure of around 35 bar to enable the RDC to operate at an equivalence ratio of 2. Before the ignition, hydrogen is run into the annulus for around 2 s to fill the domain. Using a spark plug, the required energy for initiating the combustion is supplied and the flame front enters the RDC. After each run, the control system allows the airflow to enter the system for some seconds to purge the remaining exhaust and cool down the test rig.

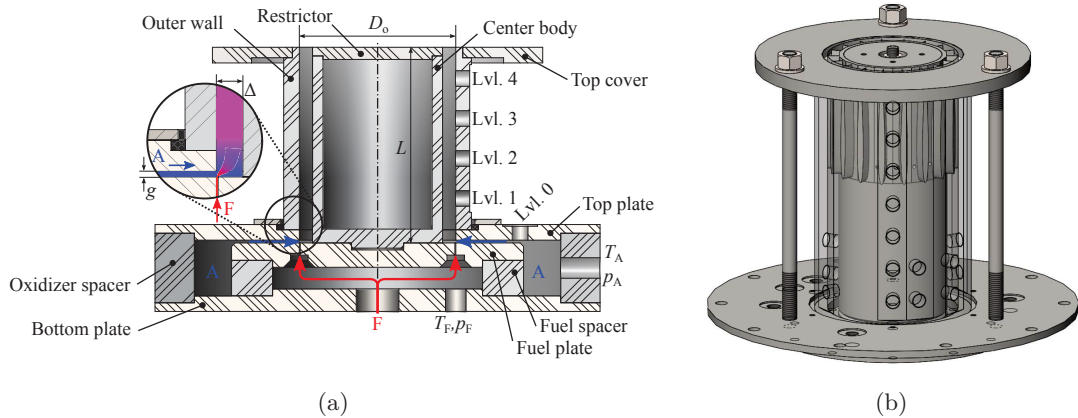


Figure 3.8: (a) A cross sectional view of the RDC setup, adapted from Blümner [101], and (b) the RDC annulus equipped with a row of stationary guide vanes, adapted from Bach et al. [74]

Bach et al. [73, 104] equipped the RDC annulus with a simple stationary guide vane row to study the effects of back pressurization on the performance of the RDC, depicted in Fig.3.8(b). The guide vane has a profile shape of NACA0006, a symmetrical airfoil with a maximum thickness-to-chord ratio of 6%. The maximum profile thickness (located at 30% chord length) and the chord length are 4.8 mm and 80 mm, respectively. Therefore, the RDC annulus length is extended to 192 mm. In the experimental setup, a total number of 18 vanes can be mounted on the annulus geometry providing a blockage ratio of 33.3%. The vanes are mounted on the center body using a pin located at 50% chord length so that the vanes can be re-staggered from -8.6° to 8.6° . Temperature and pressure can be measured upstream and downstream of the RDC nozzle. Assuming the choking flow condition at the vane throat, the mass flow rate can be calculated. A vane profile is instrumented with a Kiel probe at the leading edge, while

others are equipped with static pressure ports on both sides. A high-speed camera is used to look down into the exhaust channel to capture the operating detonation mode. Different instrumentation techniques were examined by Bach [104], and Blümner [101], whose theses provide more detail of the RDC experimental setup.

In the present thesis, the exact geometry of the RDC annulus described above is modeled to characterize the RDC exhaust flow passing through the stationary guide vanes. In Publication I the three-dimensional domain is modeled, and in Publication II the two-dimensional unwrapped model is used for URANS simulations. More detail about the geometrical specifications used for CFD analysis are explained in each publication, so not repeated here.

3.3.2 Pulsed detonation combustor model

A one-dimensional Euler method is applied to model PDC tubes to deliver the boundary conditions for the turbine. Each PDC tube is considered a one-dimensional domain in which all the phenomena are approximated to be time and axial location dependents. This means that pulsed detonation combustion of hydrogen is realized in a very small diameter tube, and the flow field is assumed cylindrically symmetric. Considering the high ratio of a PDC length to its diameter and the fact that the primary changes occurring in the flow field are in the axial direction, the one-dimensional assumption makes sense to be implemented instead of three-dimensional methods. The same Euler equations illustrated in Eq.3.47 and Eq.3.48 are used but with an additional conservation equation. The new equation models the chemical composition, which changes continuously in time and space. Therefore, the modified Euler equations for PDC modelling is as in Eq.3.51 and Eq.3.52. These equations, called reactive one-dimensional Euler equations, describe how chemical reactions transform one species into another. The equation of state Eq.3.5 closes the equation system to be defined for the 1D solver.

$$\frac{\partial M^*}{\partial t} + \frac{\partial N^*}{\partial x} = O^* \quad (3.51)$$

$$M^* = \begin{bmatrix} \rho \\ \rho C_a \\ \rho E \\ \rho Y_{sp} \end{bmatrix}, N^* = \begin{bmatrix} \rho C_a \\ \rho C_a^2 + P_s \\ C_a(\rho E + P_s) \\ \rho C_a Y_{sp} \end{bmatrix}, O^* = \begin{bmatrix} 0 \\ 0 \\ 0 \\ \rho \dot{Y}_{sp,chem} \end{bmatrix} \quad (3.52)$$

Y_{sp} stands for the vector of mass fraction of the species. The kinetical source term ($\dot{Y}_{sp,chem}$), which stands for chemical composition changes, is the only source term because there is no exchange in work, heat, force, or mass flow with outside the tube. A detailed introduction to chemical kinetics of the combustion of hydrogen-oxygen is given in ref. [105]. $\dot{Y}_{sp,chem}$ is derived by the multi-step hydrogen combustion mechanism and associated reaction rates. A global reaction for hydrogen-oxygen combustion to compute the chemical composition source term is formulated as follows [106].



$$r = 1.8 \cdot 10^{13} \cdot \exp\left(-\frac{17614}{T}\right) [\text{H}_2][\text{O}_2]^{0.5} \quad (3.54)$$

$$\dot{Y}_{sp,chem} = r \cdot \begin{bmatrix} -2M_{\text{H}_2} \\ -1M_{\text{O}_2} \\ 2M_{\text{H}_2\text{O}} \end{bmatrix} \quad (3.55)$$

r in the above equation is Arrhenius rate which combines the concepts of activation energy and the Maxwell-Boltzmann distribution law, expressed as in a modified version in Eq.3.56 [107]. In this model, the Arrhenius reaction rate depends on the temperature (T) and the activation energy (E_a). The factors of A_{arr} . and n are determined empirically to fit the available experimental data, tabulated by Westley [108] for several reactions. The one-dimensional Euler solver is coupled to a chemical kinetic solver via strong splitting described in ref. [109]. The details of the reaction mechanism used in the chemical kinetic solver are provided by Brucke et al. [110].

$$r = A_{arr} \cdot T^n \exp(-E_a/RT) \quad (3.56)$$

A PDC cycle comprises different phases explained in sec.1.2 using a graphical demonstration in Fig.1.3. In this thesis, a PDC configuration is composed of several PDC tubes which are connected to a zero-dimensional plenum, schematically depicted in Fig.3.9. The approach is a first approximation of the phenomena taking place within such a plenum that connects a PDC array and a turbine. However, it can still capture the basic unsteadiness expected from such a setup. The filling stage is triggered by adding a defined mass flow rate of H_2 to a domain cell close to the plenum-tube connecting interface. The model assumes all PDC tubes to be fed by a common compressor plenum upstream that has constant static pressure P_{cp} and static temperature T_{cp} and zero flow velocity. The pressure and temperature in the compressor plenum (equal to their total quantities because of the zero velocity assumption) are the average values in the compressor plenum of a preliminary simulation by Neumann et al. [111]. Air inflow from the compressor plenum to each PDC tube is implemented as a one-way valve. As long as the tube pressure is higher than the compressor plenum pressure, the valve remains close. Otherwise, the air expands isentropically to downstream conditions in the tube. The fuel is added essentially as a mass source with the same specific kinetic energy, i.e. the same velocity as the air inside the cell. Fuel mass flow is prescribed in such a way as to result in a stoichiometric mixture of H_2 and air. This fuel is subsequently advected downstream by the flow velocity until the tube is completely filled with the combustible mixture. The detonation phase is then started by an ignition event triggered at fixed time intervals, thus defining the desired operating frequency for each PDC tube. Ignition is implemented by placing a pre-calculated ZND detonation front profile at the upstream end of the tube. During the detonation phase, the detonation front propagates downstream with the characteristic detonation velocity until the fuel is consumed. Since this velocity reaches up to 2000 m/s, the detonation propagation only takes about 0.5 ms in a 1 m long PDC tube. As a consequence of the rapid combustion, tube pressure is abruptly raised above P_{cp} , resulting in the air mass flow from the compressor plenum being temporarily blocked until an ensuing sequence of expansion waves decreases pressure sufficiently to allow for the airflow to re-establish, thus initiating

the purge phase. The purpose is to remove the combustion products from the tube while maintaining an air buffer of 5 ms to separate them from fresh fuel. As soon as this is achieved, fuel is once again added to the tube and the cycle is restarted [111]. Boundary conditions at all tubes provide isentropic expansion of momentary tube pressure to momentary plenum pressure, while the specific axial kinetic energy is maintained. The resulting mass flow from the tubes into the plenum is taken as a mass and energy source term in the plenum's balancing equations. Since it is zero-dimensional, only mass, energy, and species fractions are considered here, while velocity is assumed to be always negligible. In Publication III and Publication IV, the model is illustrated quantitatively for PDC configurations, including three, five, and seven tubes. It should be noted that the modeling of the PDC tubes connected to a compressor via a plenum was done in another journal paper of the author and his colleagues [111], which is not included in this thesis.

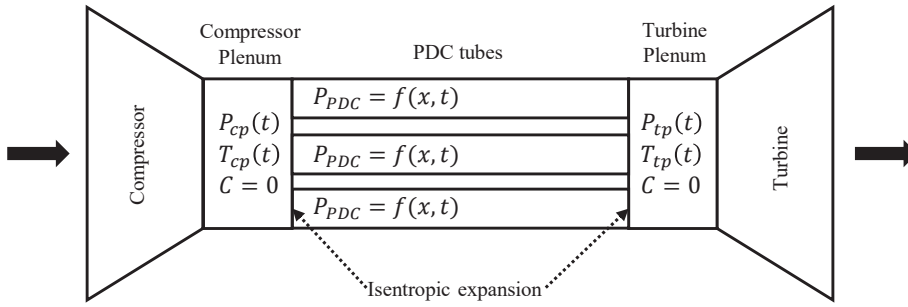


Figure 3.9: The model of a PDC configuration comprising three tubes.

3.4 Three-dimensional CFD

As a high fidelity numerical tool, Reynolds Averaged Navier-Stokes (RANS) simulation is utilized in each publication in this thesis. RANS calculations require a small fraction of the computational resources needed for direct numerical simulation and large eddy simulation and thus, remain the choice for most industrial CFD users [112]. Basically, RANS equations are a reduced form of the Navier-Stokes equations, discussed in sec.3.2.1, since these equations are of the most complex ones to use and solve. The Reynolds decomposition technique is utilized to split the flow variables (e.g. flow velocity) into the time-independent mean part (\bar{C}) and the fluctuating component (C'), as in Eq.3.57 and Eq.3.58 where $\lambda = (x, y, z)$ is the Cartesian vector of position.

$$C(\lambda, t) = \bar{C}(\lambda) + C'(\lambda, t) \quad (3.57)$$

$$\bar{C}(\lambda) = \lim_{T \rightarrow \infty} \frac{1}{T} \int_t^{t+T} C(\lambda, t) dt \quad (3.58)$$

Applying this decomposition technique in Navier-Stokes equations, the same equations for the mean variables are formed but with introducing an additional term. The Reynolds stress tensor is appeared to account for turbulent fluctuations in fluid momentum. This nonlinear term speaks for the transport of mean momentum due to turbulent fluctuations, defined in Eq.3.59. In this equation, C'_i and C'_j denote the density-weighted fluctuating parts

of the velocity components in x and y directions, respectively, and the over-symbol $\tilde{\cdot}$ stands for density-weighted averaged value [113].

$$\tau_{ij}^{Re} = -\tilde{\rho} \widetilde{C'_i C'_j} \quad (3.59)$$

This modification to the Navier-Stokes equations leads to a closure problem to close the RANS equations. In this regard, many turbulence models are developed to close the RANS equations. Second-order closure models are the most complex, but also the most flexible models, such as the Reynolds-Stress Transport (RST) [114] and Algebraic Reynolds-Stress (ARS) [115] models. These two models are not numerically efficient because of the stiffness in the RST model and the non-linearity in the ARS equations. First-order turbulence models provide more easy-to-solve equations; therefore, they are more widely used in engineering problems. In these models, the Reynolds stresses are represented using the turbulent eddy viscosity, which is a single scalar value based on the assumption that there is a linear relationship between the turbulent shear stress and the mean strain rate, similar to laminar flow [113]. Depending on the number of transport equations in a first-order model, they are categorized, ranging from zero to multiple-equation models. Zero-equation models, e.g., Baldwin and Lomax [116], are denoted as algebraic models, in which the turbulent eddy viscosity is computed from empirical correlations employing only local mean flow variables. This local flow variable feature prevents the model from simulating history effects; therefore, a reliable prediction of separated flow is not possible by zero equation models. In contrast, one- and two-equation models account for the history effects like convection and diffusion of turbulent energy. Among the one-equation turbulence models, Spalart and Allmaras [117] has been widely used, which is based on an eddy-viscosity-like variable. This model is numerically stable and easy to implement to different grid types. Among the two-equation models, the $K - \omega$ model by Wilcox [118] and the $K - \varepsilon$ model by Launder and Spalding [119] are of the most well-known turbulence models, specifically in engineering applications. A comparison of the Spalart and Allmaras model with two-equation turbulence models was done by Bardina et al. [120]. Another two-equation turbulence model is the Menter's Shear Stress Transport model (SST) developed by Menter [121], which combines $K - \omega$ and $K - \varepsilon$ in a way such that the former is applied inside the boundary layer, while the latter is used in the free shear flow. The SST model is very robust in predicting the flow separation in adverse pressure gradients. The two equations of SST models represent the specific turbulent kinetic energy, $\kappa(m^2s^{-2})$, in Eq.3.60 and the specific turbulent dissipation rate, $\omega(s^{-1})$, in Eq.3.61 [122]. It should be noted that the notation used in Eq.3.60 to Eq.3.66 represent only the parameters defined in this subsection.

$$\frac{\partial(\rho\kappa)}{\partial t} + \frac{\partial(\rho C_i \kappa)}{\partial \lambda_i} = \frac{\partial}{\partial \lambda_i} \left(\mu_\kappa \frac{\partial}{\partial \lambda_i} \kappa \right) + \hat{P}_\kappa - \nu^* \rho \omega \kappa \quad (3.60)$$

$$\frac{\partial(\rho\omega)}{\partial t} + \frac{\partial(C_i \rho \omega)}{\partial \lambda_i} = \frac{\partial}{\partial \lambda_i} \left(\mu_\omega \frac{\partial}{\partial \lambda_i} \omega \right) + \hat{P}_\omega - \nu \rho \omega^2 + 2\rho(1 - F_1) \frac{1}{\omega} \frac{1}{\sigma_{\omega,2}} \frac{\partial \kappa}{\partial \lambda_i} \frac{\partial \omega}{\partial \lambda_i} \quad (3.61)$$

3. Methods

The effective viscosities ($kg.m^{-1}.s^{-1}$) are defined as follows, where μ_t is the modified eddy viscosity and σ is the diffusion constant for each model.

$$\mu_\omega = \mu + \frac{\mu_t}{\sigma_\omega} \quad (3.62)$$

$$\mu_\kappa = \mu + \frac{\mu_t}{\sigma_\kappa} \quad (3.63)$$

P_ω is the rate of production of ω ($kg.m^{-3}.a^{-2}$) is defined in Eq.3.64, in which S_{ij} (s^{-1}) is the mean rate of deformation component and δ_{ij} is the Kronecker delta function. γ is a model constant in the equation.

$$P_\omega = \gamma \left(2\rho S_{ij}.S_{ij} - \frac{2}{3}\rho\omega \frac{\partial C_i}{\partial \lambda_j} \delta_{ij} \right) \quad (3.64)$$

P_κ represents the production rate of κ , defined in Eq.3.65. To avoid the build-up of turbulence in stagnation regions, the effective rate of production \hat{P}_κ is introduced as in Eq.3.66.

$$P_\kappa = 2\mu_t S_{ij}.S_{ij} - \frac{2}{3}\rho\kappa \left(\frac{\partial C_i}{\partial \lambda_j} \right) \delta_{ij} \quad (3.65)$$

$$\hat{P}_\kappa = \min(P_\kappa, 10\nu^* \rho\kappa\omega) \quad (3.66)$$

In Eq.3.61, F_1 is the blending function defined by Menter [123], which varies from unity at the wall to zero outside the wall boundary layers. Each constant in the Menter's SST model is obtained using the blending function as formulated in Eq.3.67, where φ can be replaced by σ_κ , σ_ω , ν or γ . The subscript 1 and 2 are related to the adjusted $K - \omega$ model and the standard $K - \epsilon$ model, respectively. The coefficient values are provided by Menter [124], not repeated here.

$$\varphi = \varphi_1 F_1 + \varphi_2 (1 - F_1) \quad (3.67)$$

The Menter's SST model is utilized in the RANS simulations in this thesis. The boundary conditions for the computational domain, the computational grid generation, the mesh sensitivity analysis, and the time-step independency of transient simulations have been performed and explained in each publication separately. The numerical simulations were done using a computer cluster at the Chair of Experimental Fluid Dynamics and also on a cluster at the North German Supercomputing Alliance (HLRN).

3.5 Surrogate-based optimization

Finding the optimum is an indispensable part of almost all problems in engineering and industry, whether to maximize a performance parameter like system efficiency or minimize a costly parameter like energy consumption and time. Most engineering problems are too complex to be represented by a simple function in such a way that the optimization can be done as a simple mathematical extremum finding problem. In some cases, performing experimental work instead of mathematical modeling is too expensive or even impossible. In this regard, the

mathematical model of the problem must be correctly prepared to be linked with an objective function evaluator in an optimization framework. Hence an optimization methodology can provide the process of finding the optimum by linking the mathematical model, and the objective function evaluator [125]. An important feature of an optimization algorithm is to effectively search for or generate new solutions from a set of known solutions. The faster this searching algorithm converges to the global optimum solution, the more powerful the algorithm is. The objective function in engineering applications can come from a system's measurement or computer simulation. In many cases, measurements or computer simulations cannot be embedded in optimization algorithms, in which several objective function evaluations for new samples are required. In some cases, the experimental measurement cannot be repeated, e.g., constructing and testing hundreds of different turbomachine geometries are not feasible. At the same time, numerical simulations for hundreds of samples in an optimization problem can be too time-consuming by some techniques, e.g., unsteady three-dimensional CFD simulation of a multistage turbomachine. In such cases, surrogate-based optimization (SBO) provides an effective technique for calling the expensive objective function evaluator as few times as possible in an optimization problem [126, 127]. SBO uses an auxiliary model associated with the high-fidelity model to be integrated into the heart of an iterative optimization problem. Once an approximation of the optimum solution is found, it has to be verified by the high-fidelity model. Based on the result of this verification, the optimization procedure may be stopped. Assuming the verification fails, the newly available sample data from the high-fidelity evaluation is added to the pool of sample points the SBO is constructed on, and hence the SBO is updated. In general, an SOB process can encompass the following steps [125].

1. Generating the initial surrogate model based on high-fidelity sample data.
2. Obtaining an approximate optimal solution by optimizing the surrogate model.
3. Evaluating the optimum solution using the high-fidelity model.
4. Closing the optimization loop if the termination criteria are satisfied; otherwise, go forward.
5. Updating the surrogate model using the new high-fidelity sample data of step 3 and go to step 2.

To generate an initial surrogate model, the samples must be allocated to maximize the amount of information acquired over the entire design space. This strategy is called Design of Experiments (DoE) [128]. Apparently, a higher number of samples can ensure more information about the design space. However, a trade-off between the number of samples and the amount of information these points can provide should be done. There are several sampling techniques, including the classical factorial designs [129], simple random sampling [130], Latin Hypercube method [131], Orthogonal Array method [131], Quasi-Monte Carlo sampling [132] or Hammersley sampling [133]. Each sampling technique has specific pros and cons depending on the prior knowledge about the problem, the design space, and the objective function. Among all, Latin Hypercube Sampling (LHS), which is a near-random method introduced by Michael McKay [131], is of the most popular techniques in engineering application [134]. To single out p samples using LHS, each variable range is divided into p

bins. So, for a design space with n number of variables, the design space is divided into p^n bins. Random sampling is done to ensure two criteria. The samples must place randomly in bins, and each bin can take only one sample, remembering which samples were taken so far. Once the design space samples are defined, a surrogate modeling technique is required to fit a function to the data from high-fidelity function values of the sample points. To date, several approximation methodologies have been introduced, such as Polynomial Regression [135], Radial Basis Functions [136] and Kriging [137].

In this thesis, the optimization problem is to find an optimum turbine blade shape that produces the lowest entropy while working in unsteady conditions prescribed by a pressure gain combustor configuration. This optimization problem is the subject of Publication IV. The variable selection and the objective function are described in this paper. The surrogate-based optimization process is done based on Complex Shape Method (CSM), which is a direct searching algorithm (also known as Nelder-Mead Simplex Method) [138, 139]. The searching algorithm works with four main operations of reflection, expansion, contraction, and compression, shown in Fig.3.10 assuming $f(X_b) < f(X_o) < f(X_w)$ where $f(X_i)$ is the objective function value of sample X_i . The algorithm flow chart showing the sequence of using these operations is illustrated in Fig.3.11. The method formulations are described in the method section of Publication IV. LHS method is utilized as the sampling technique that provides the samples having a suitable spatial uniformity and consequently can reflect the information of the design problem sufficiently [140]. The objective function evaluation is done using the developed one-dimensional Euler solver.

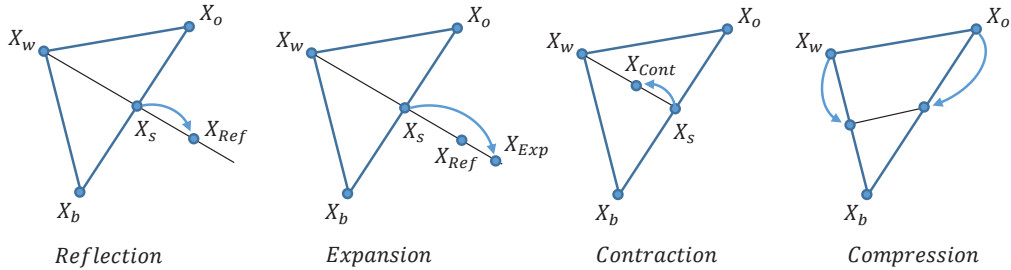


Figure 3.10: A representation of CSM operations in a two-dimensional design space, which is consistent with the notations in Publication IV.

3.6 Turbine test case

To evaluate the effectiveness of the one-dimensional turbine simulation method developed in the course of this thesis, a turbine test case has to be considered for unsteady simulation. Since there is no available experimental data on the unsteady performance of a turbine in open literature, specifically for PGC-driven ones, a turbine test case with the available steady performance characteristics was selected. Ideally, the turbine should have more than one blade row that the one-dimensional solver ability in simulation large multistage turbines can be better evaluated. In this regard, NASA E³ high-pressure turbine has been selected as a bench-marking test case. This turbine was developed for the General Electric Energy Efficient Engine. The design comprises two stages with a low thru-flow of moderate loading.

4

Publications

This chapter contains four peer-reviewed publications out of the research work in this thesis toward addressing the pressure gain combustion and turbine interaction challenge. Two of the publications focus on the interaction of RDC and turbine vane, while the others mainly discuss the interaction of PDC and turbine. Within the scope RDC-turbine, Publication I studies the flow field downstream an existing RDC. This publication tries to support the experimental measurements at the TU Berlin Energy lab by providing more detail on the flow features around the stationary blades mounted on the RDC exhaust annulus. Publication II characterizes the RDC exhaust flow passing through stationary vanes using URANS simulations. Different guide vane configurations are simulated in a two-dimensional unwrapped RDC exhaust domain, and pressure loss and fluctuation damping are assessed. In the context of PDC-turbine, a 1D-Euler method is presented in Publication III, and its applicability in simulating turbines driven by PDCs is evaluated. Once the 1D-Euler method as a fast approach for unsteady turbine simulation shows its usefulness, the technique is exploited for a turbine optimization problem working under PDC exhaust flow in Publication IV. For more clarity, upfront of each publication outlined in this chapter, a brief summary is provided aiming the main objective and outcomes to contextualize their positions within the dissertation. The publications are as follows:

- I.** Majid Asli, Cleopatra Cuciumita, Panagiotis Stathopoulos, and Christian Oliver Paschereit. “Numerical investigation of a turbine guide vane exposed to a rotating detonation exhaust flow”. In: *Proceedings of the ASME Turbo Expo 2019*, Volume 2B, V02BT40A018. DOI: <https://doi.org/10.1115/GT2019-91263>. (Publisher’s version)
- II.** Majid Asli, Panagiotis Stathopoulos, and Christian Oliver Paschereit. “Aerodynamic investigation of guide vane configurations downstream a rotating detonation combustor”. In: *Journal of Engineering for Gas Turbines and Power* 143. 6 (2021). DOI: <https://doi.org/10.1115/1.4049188>. (Publisher’s version)
- III.** Majid Asli, Niclas Garan, Nicolai Neumann, and Panagiotis Stathopoulos “A robust one-dimensional approach for the performance evaluation of turbines driven by pulsed

4. Publications

detonation combustion”. In: *Journal of Energy Conversion and Management* 248 (2021), p. 114784. DOI: <https://doi.org/10.1016/j.enconman.2021.114784>. (Publisher’s version)

- IV.** Majid Asli, and Panagiotis Stathopoulos “An optimization methodology for turbines driven by pulsed detonation combustors”. In: *Journal of Engineering for Gas Turbines and Power* (Accepted manuscript).

4.1 Publication I

Numerical investigation of a turbine guide vane exposed to rotating detonation exhaust flow

This paper was submitted to the ASME Turbo Expo 2019 in Phoenix, USA. After a peer-review process with three reviewers and being accepted, it was presented in the Axial Flow Turbine Aerodynamics session. The final manuscript was published in the Proceedings of the ASME Turbo Expo 2019, volume 2B, V02BT40A018.

Contribution

The paper takes an in-depth look at the unsteady flow field downstream an RDC with the presence of a stationary guide vane. The main objective is to simulate the flow field around the turbine guide vanes as in the RDC experimental setup at the TU Berlin Energy lab and explore the entropy generation sources in such an unsteady flow field. It tries to compensate for the shortages of measurement and visualization techniques in the RDC experimental campaign.

Methods

A Three-dimensional URANS solver is utilized for the unsteady flow field simulations in this paper. The boundary conditions for the simulations are obtained by two approaches. First, the inlet boundary condition is altered to reach the experimentally measured pressure around the vanes for an specific RDC operating point. In the second way, the mean values of total and static pressures are kept and a total pressure distribution is generated using an trend function based on literature.

Results

The results show an entirely subsonic flow field upstream of the vane row in the RDC exhaust annulus, which can ignore the possibility of shock waves effects on the experimental pressure measurements at the blade leading edge. The total pressure fluctuation amplitude was reduced 48% from upstream to downstream of the vanes, while the cycle average total pressure reduced by 7.9%. The critical time regarding the total pressure loss was observed to be at 70% to 90% of the cycle time period which has the greatest instantaneous value. This moment in the cycle is associated with the approximately constant inlet total pressure distribution in time. Shock waves and also boundary layer-shock wave interactions were detected within the blade passage that produces a considerable amount of entropy.

Proceedings of the ASME Turbo Expo 2019
Turbomachinery Technical Conference and Exposition
GT 2019
June 17-21, 2019, Phoenix, USA

GT2019-91263

NUMERICAL INVESTIGATION OF A TURBINE GUIDE VANE EXPOSED TO ROTATING DETONATION EXHAUST FLOW

Majid Asli*

Chair of Unsteady Thermodynamics in
Gas Turbine Processes, Technische Universität Berlin
Berlin, 10623, Germany
Email: asli@campus.tu-berlin.de

Cleopatra Cuciumita

Chair of Fluid Dynamics
Technische Universität Berlin
Berlin, 10623, Germany

Panagiotis Stathopoulos

Chair of Unsteady Thermodynamics in
Gas Turbine Processes, Technische Universität Berlin
Berlin, 10623, Germany

Christian Oliver Paschereit

Chair of Fluid Dynamics
Technische Universität Berlin
Berlin, 10623, Germany

ABSTRACT

Detonative Pressure Gain Combustion has the potential to increase the propulsion efficiency of aero-engines and the thermal efficiency of stationary gas turbines. Important advances were made in this field, especially in the case of Rotating Detonation Combustion (RDC). Although experimental and numerical studies reported in the literature have significantly increased in number, the major open problem is a lack of efficient turbomachinery to transform the fluctuating potential energy from an RDC into power output. For this problem to be properly addressed, time resolved data at the outlet of an RDC needs to be collected. As a first step, numerical data can be used to generate a geometry for the turbine which must be validated experimentally. To determine the performance of a turbine vane row, total pressure losses need to be measured. There are several challenges in measuring the total pressure between the outlet of an RDC and the inlet of a turbine vane row. The high temperature limits the distance at which the pressure transducer can be mounted and leads to measuring a mean value of the pressure. The confined space is also an issue, allowing for very few op-

tions in measuring the total pressure. Another major problem is the shock wave that may form as a detached shock wave with respect to the body of the pressure probe at certain moments in the flow cycle which leads to measuring a different value rather than the actual value of the flow field. To address these issues, this study presents numerical investigation of a guide vane row that was experimentally tested at the outlet of an RDC working on hydrogen and air under stoichiometric conditions. One of the vane rows was 3D printed with a geometry allowing the measurement of total pressure. Static pressure at the outlet of the RDC was also measured. It was observed that the measured pressures are average values in time. Based on these averages, the total inlet pressure and velocity variations in time were reconstructed in an exponential trend, according to the ones reported in the literature and the aforementioned experiments. These variations were set as inlet conditions for transient numerical simulations. Results show that the total pressure amplitude decreases significantly when the flow passes the annulus and the vanes as well. By looking in to the flow field detail, the presence of shock wave in front of the blade is investigated. Additionally, it is calculated that the average total pressure decreases 7.9% by the vane row.

*Address all correspondence to this author.

NOMENCLATURE

M	Mach Number.
P_t	Total Pressure.
P_s	Static Pressure.
T	Total Temperature.
TS	Time Step.
TP	Time Period.
e	Relative Error.
s	Second.
t	Time.

INTRODUCTION

The growing number of passengers who choose air transportation mode encourages aircraft manufacturers and the relevant market to have more contribution in the field. In this regard, the Organization for Economic Cooperation and Development forecasts that air transport CO₂ emissions will grow by 23% by 2050, if no measures are taken [1]. Considering this growth rate, stringent environmental regulations are already in place with the ultimate goal to cut net emissions to half of the 2005 level by 2050. This forces engine manufacturers to increase gas turbine efficiency. At the same time, stationary gas turbines are the only thermal power plant technology capable of delivering both secondary and tertiary reserve from idle. The rapid expansion of renewable generation in Europe is expected to double the demand for both reserves in the coming decade. Hence, an increase of gas turbine efficiency can prove very valuable for further reducing the cumulative CO₂ emissions of the power sector.

Among all possible solutions for increasing gas turbine efficiency, Detonative Pressure Gain Combustion (PGC) has the potential to increase the propulsion efficiency of aero-engines and the thermal efficiency of stationary gas turbines. Theoretically, implementing PGC in a gas turbine will increase the cycle performance, due to the lower entropy generation in the combustion process. However, pressure gain combustion results at higher turbine inlet temperatures, while at the same time the exhaust flow of detonative PGC chambers is characterized by strong pressure, temperature and velocity fluctuations. One of the main challenges in the practical implementation of PGC into gas turbines is the lack of designs for turbomachines that can cope efficiently with the PGC exhaust gas. Although still a topic of active research, it is generally accepted that conventional turbine expanders interacting with the exhaust of pressure gain combustors will have lower isentropic efficiency, compared to their design operation [2]. Fig. 1 shows the efficiency that a turbine should achieve in the Humphrey cycle in order to obtain the same cycle efficiency with a Brayton cycle at the same TIT and with a 90% isentropic turbine efficiency [3]. If the turbine efficiency drops below these values, the benefits of applying pressure gain combustion would be entirely lost, due to the

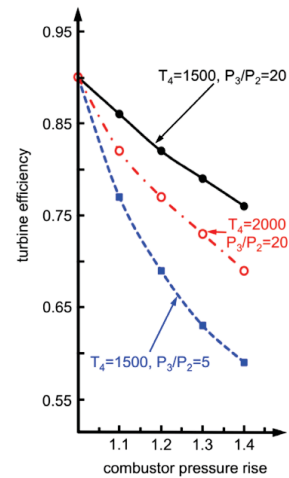


FIGURE 1: Turbine efficiency in a Humphrey cycle for the same cycle efficiency with a Brayton cycle with 90% turbine isentropic efficiency, taken from [3].

inability of the turbine to harvest the additional exergy present in the combustor exhaust gas.

During recent years, several research and development efforts have analyzed the interaction of turbines with pressure gain combustors [4–8]. Irrespective of whether pressure gain combustion was realized through Rotating Detonation Combustion or Pulsed Detonation Combustion, no turbine exhibited acceptable performance. The inherent highly unsteady exhaust flow of PGC combustors was found to be responsible for large turbine aerodynamic losses. Tellefsen [9] performed the first RDC axial turbine tests. Additionally, he placed convergent outlet sections on the RDC to simulate the back-pressurization that would occur when placing the turbine behind the it. The RDC operated similarly for both nozzle and turbine testing, demonstrating that a nozzle can properly simulate the presence of a turbine behind a RDC. Naples et al. [10] implemented RDC into a T63 gas turbine and successfully run the turbine about 20 minutes of accumulating time. While they designed an air dilution system for the engine, they showed the applicability of operation of RDC with the existing turbine as a unit. In another attempt to use turbine in RDC, Rhee et al. [11] replaced the combustor of a commercial jet engine by a newly designed rotating detonation combustor. They tested the engine and measured the temperature at turbine inlet and exit plane and also turbine rotational speed. Liu et al. [12] considered two axial turbine designs exposed to subsonic inlet Mach number at different inlet pressure fluctuation frequencies. They studied the effect of pulsating flow on the turbine efficiency numerically. The results revealed that stage efficiency drops for increasing inlet Mach number. Additionally, they showed that the angular inlet flow fluctuation has an effect

on turbine efficiency only when it is in the opposite direction to that of the rotor motion. Fernelius [8] showed that pulse amplitude of PDCs is the driving factor for decreased conventional turbine efficiency but not the pulsing frequency. The turbine he considered was a conventional subsonic turbine. He managed to suggest a correlation between fluctuation amplitude and turbine efficiency by using a corrected form for the amplitude. Paniagua et al. [3] developed a supersonic turbine design using Method of Characteristics and then Liu et al. [13] tried to characterize this supersonic turbine downstream of a RDC numerically. They conclude that the leading edge shock waves are the primary unsteady loss source in this flow condition.

A nozzle blade row exposed to RDC exhaust flow at TU Berlin RDC Lab has been already investigated experimentally [14]. It shows the applicability of the static and stagnation pressure measurement. Due to the presence of probes in the leading edge of blades, the measuring data could be affected by the waves in front of the probes before the flow reaches the blade. Due to some difficulties regarding the harsh flow field with extremely high temperature flow exhausted from the RDC, looking in to the details of flow field around the vanes is not provided by the experiments. Therefore, in this paper the nozzle blade row and the RDC annulus are modeled and simulated numerically using a three dimensional Unsteady Reynolds-Averaged Navier–Stokes solver. The objective here is to study the flow behavior within the annulus and the vane row in such an inlet fluctuating flow in detailed and evaluate the pressure loss. Additionally, the results of simulation will be compared with the experimental data acquired by the presence of measuring devices in the annulus.

Blade Row Model

The TU Berlin RDC annulus with outer diameter of 90 mm and the length of 114 mm from the injector to the exit plane is modeled. The combustor specifications were described in detail in [15]. The annulus width is 7.6 mm and a symmetrical blade row of NACA0006 type is mounted at the exit plane in order to evaluate flow behavior and impose back pressure boundary condition to the RDC operation. Considering the annulus dimension, 33.4% area reduction at the throat is caused by 18 blades. The annulus and the blade row model are shown in Fig. 2.

Numerical Approach

Governing Equations The computational solver applied for the present case is ANSYS 18.2 CFX which has been widely used for turbomachinery flow simulations [16–19]. Unsteady Reynolds-Averaged Navier–Stokes equations were solved using $k-\omega$ shear stress transport turbulent model proposed by Menter [20]. This turbulence model, which has been validated in a similar case [18], was chosen as it performs well in both near to and far from the wall and also in separated flow as in the present case it is expected to occur. The dimensionless wall distance y^+

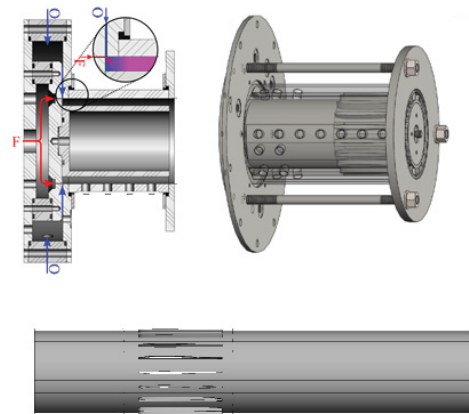


FIGURE 2: Schematics of the modeled RDC annulus with nozzle blade row.

is kept below 1 to ensure solving near wall regions well. The second order implicit time stepping scheme is applied for spatial discretizing of the governing equations. However, the transient scheme for turbulence equations remains first order. Turbulent intensity at the inlet boundary is considered 5%. Hydrogen-air mixture is assigned as the working fluid and it is assumed to be a perfect gas either thermally or calorically. Root-mean-square values for all the residuals and the maximum residual are set at 10^{-6} and 10^{-4} respectively as the numerical solution convergence criteria.

Computational Domain and Boundary Conditions

Based on the experiments [15], operating conditions will affect the combustion mode of operation. Increasing the reactant inflow results in changing the operating regime from two counter rotating waves at equal speeds to two counter rotating waves with a stronger wave and finally into a single rotating wave. Here, the RDC operating condition is set to achieve a single rotating wave across the combustor so that, hydrogen-air stoichiometric reaction is considered for the RDC operation. The computational domain and the generated mesh is depicted in Fig. 3. Inlet and outlet boundaries are placed far enough from the blade in order to let the flow complete mixing process within the computational domain. Inlet boundary is created at the distance of 1 blade chord length in front of the leading edge. In the experimental set up, the distance from the injector face to the blade leading edge is 1.25 of the chord length. Therefore, there is enough space for the reaction to be completed in the experimental set up before reaching the 1 blade chord length in front of the blade row, where the domain inlet located for the numerical simulation. The outlet boundary is placed 4 chord length far from the trailing edge according to the recommendation by Greitzer et al. [21].

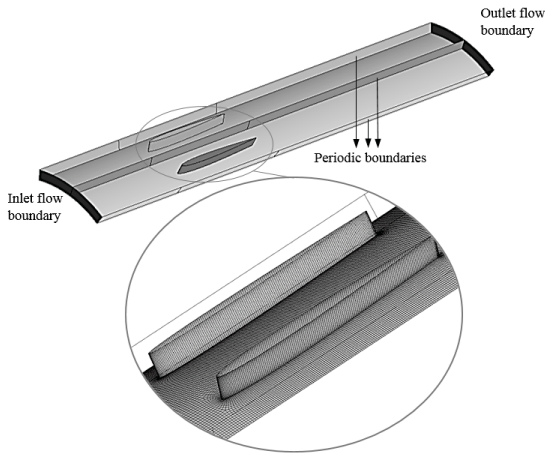


FIGURE 3: Computational domain and the grid around the blades.

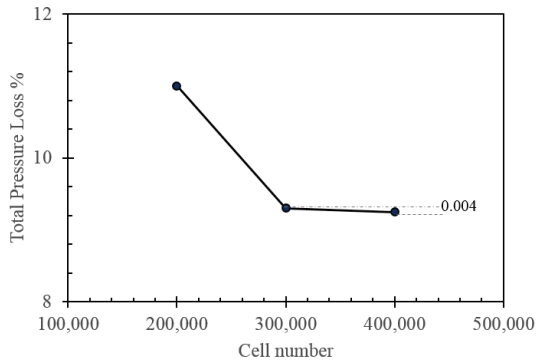


FIGURE 4: Mesh resolution effect on the total pressure loss percentage along the blade.

A three dimensional structured grid is generated for the flow passage. O grid type was generated around the blade and H grid type for the rest of the region. A grid dependency analysis has been performed by applying three configurations, coarse, intermediate and fine grids. Each of the grids has 200k, 300k and 400 cells. The total pressure loss percentages along the blade at a specific time step are compared after the solution is converged. According to the Fig. 4 the intermediate and fine mesh sizes can be considered to have the same results with the average error of relative error of 0.4%. So that, further refinement in mesh cell size would not change the flow field simulation results and hence, the intermediate mesh generation is adequate for the rest of the simulations.

The global time step must be chosen to capture the flow phe-

TABLE 1: Averaged Mach number for solutions with different time steps.

Time Step	Averaged Mach Number	Relative Error
TP/125 (Large TS)	0.132005	1.7%
TP/200 (Medium TS)	0.129751	0.2%
TP/333 (Small TS)	0.129438	–

nomena during the transient operation. It is considered to be 125, 200 and 333 time smaller than the period of inlet flow fluctuations to evaluate the effect of time steps on the flow transient physics. It is observed that the Mach number contour at 0.2c upstream of the blades does not change for the two latter time steps as depicted in Fig. 5. These contours are plotted at a certain time for all the solutions which is 3.6ms. Mass averaged value of Mach number at the surface is tabulated in the Tab. 1. It shows that the relative error for the greater time step respected to the smaller one is much higher than the relative error for the two smaller time steps which are 1.7% and 0.2% respectively. Thereafter, for the following simulations the time step related to the 200 times smaller than the period of fluctuations is selected as the optimum. The relative error defines as the normalized difference between parameter values as Eq. 1.

$$e = \frac{|M_{LargerTS} - M_{SmallerTS}|}{M_{SmallerTS}} \quad (1)$$

In order to apply the exhaust flow coming from the RDC as the inlet flow boundary condition, time dependent total pressure and temperature distribution should be specified for the numerical simulation. Experimental total and static pressure distribution trend which has been done by the authors [14] is considered. This trend has been also reported by [22]. The trend line is approximated as an exponential function of time with the mean value of 4.6 and 2.9 bar for total and static pressure respectively. By keeping the mean value, total pressure distribution is generated as depicted in Fig. 6 to be imposed as the inlet boundary condition. The trend function is shown in Eq. 2, while $a_1 : a_4$ are the constants which can be calculated based on the known values.

$$P(t) = a_1 \ln(a_2 t + a_3) + a_4 \quad (2)$$

Additionally, the temperature distribution at the inlet boundary is imposed as the same for the pressure trend with the peak value of 2500K and lowest value of 1000K. The RDC exhaust

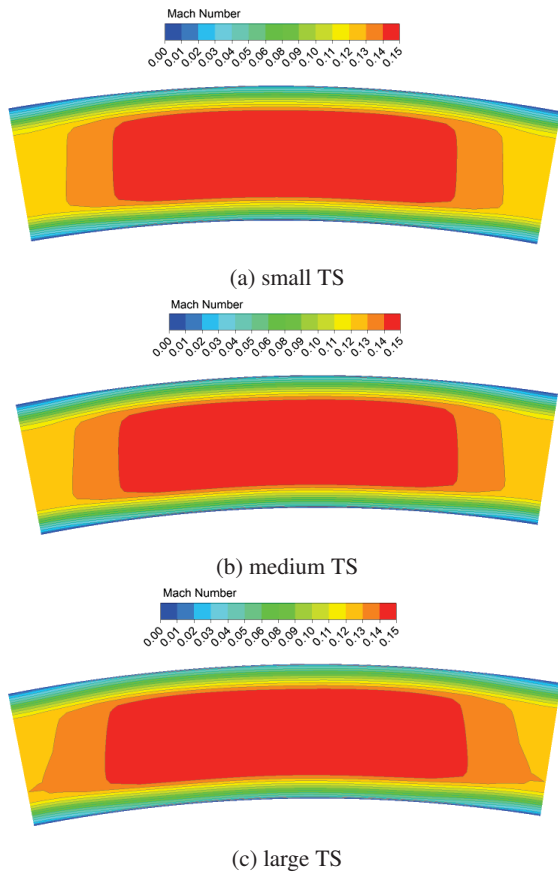


FIGURE 5: Mach number contour at 0.2c upstream of the blade

frequency is 10kHz which was measured by the experiment. The inlet and outlet boundary conditions are selected to be opening boundary type because it is expected to have back flow regarding the flow fluctuations.

Results and discussion

In order to study the flow behavior at the upstream and downstream flow field entering the blade row, total and static pressure variations are calculated at each time step to find the critical region which has the most variation. These regions are of interest because a high total pressure loss is expected there. The detected locations named 1, 2 and 3 are located at 0.2c, 0.01c upstream and 1c downstream far from the blade respectively. The values for pressure are mass flow averaged which is more applicable and recommended in turbomachinery [23]. To consider the effect of blade presence at the RDC exhaust, the flow field around the blade must be characterized. Total pressure variation along the blade, which includes upstream and downstream blade related phenomena is presented in Fig. 7.

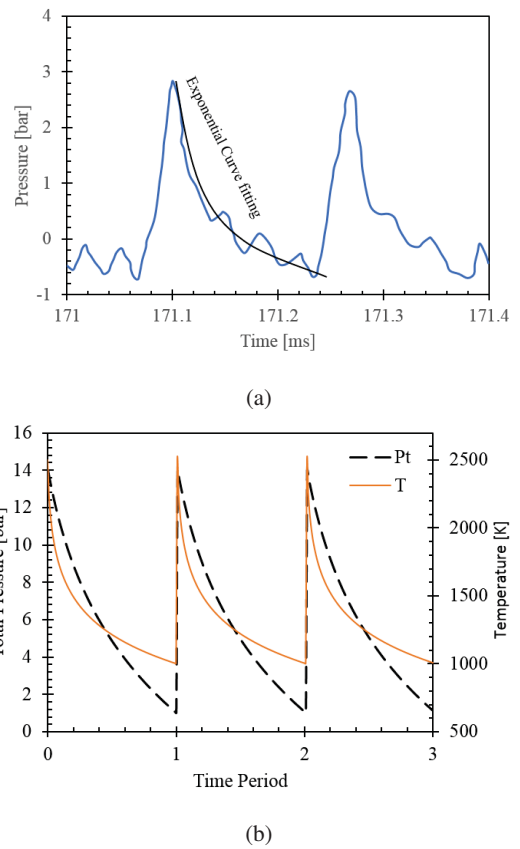
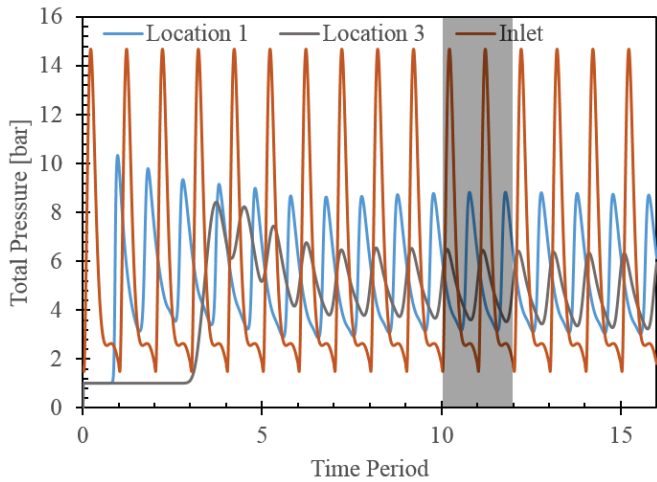
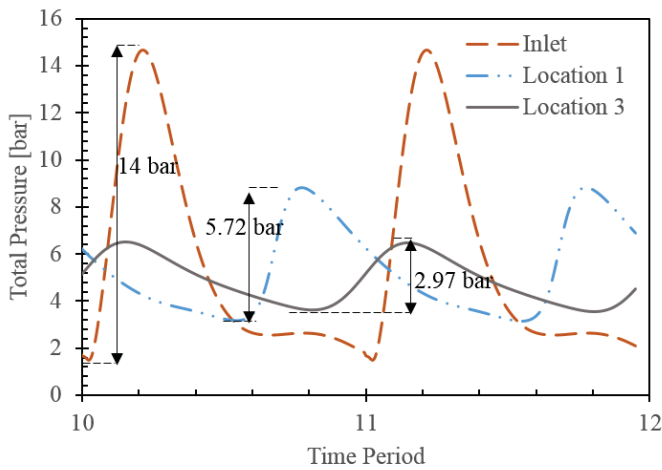


FIGURE 6: (a) The trend obtained by the experiments [14] and (b) total pressure distribution applied as the inlet boundary condition

It is seen that the cycles converged after the 6th time period for these three locations. So, the two consecutive cycles from 10 to 12 are zoomed in. Based on this figure, the total pressure peak to peak amplitude for the inlet flow which is 14bar reduces to 5.72bar at location 1. It means that while the fluctuating flow goes through the annulus, fluctuation amplitude reduces significantly. Additionally, the trend becomes smoother specifically at end of the cycle which can be seen on the inlet curve. On the other hand, the total pressure amplitude decreases to 2.97bar at location 3 which is downstream of the blade. This represents around 48% damping in total pressure fluctuation amplitude between the location 1 and the location 2. These values are tabulated in Tab. 2. The average total pressure for a cycle decreases 5.65bar at inlet location to 5.29bar at location 1 which represent 6.3% total pressure loss with respect to the inlet. This value between the two locations of 1 and 3 is 7.9%. Therefore, it is seen that the blade row cause a bit more total pressure loss than what occurs between inlet and location 1 in the annulus. This will be further investigated afterward. Due to the distance between the



(a)



(b)

FIGURE 7: Total pressure at the three locations upstream and downstream of the blade row

specified locations, there is time phase difference while maintaining the frequency of 10kHz.

Fig. 8 shows instantaneous entropy contours around the blade which explains how separation bubbles cause entropy generation and hence the related losses. As the blade profile is a symmetrical type and the blade sitting angle is zero, the flow phenomena is symmetrical around the blade. Bubbles are generated at 0.1TP as indicated in Fig. 8a with a dashed circle. As the time passes to the 0.4TP, the bubble goes to the trailing edge and then it is merged with the bubble from the other blade side. The Mach number lines at 0.2TP instance depicted in Fig. 8d, shows that the zone of high Mach number which decreases by shock wave is the high entropy zone. Therefore, the shock wave

TABLE 2: Total pressure at different locations.

Location	Total Pressure Amplitude	Time Averaged in a Cycle
Inlet	14bar	5.65bar
Location 1	5.72bar	5.29bar
Location 3	2.97bar	4.87bar

boundary layer interaction generate separation of the flow from the blade hence and entropy raise in addition to the shock waves. This explains the reason that the total pressure decreases more along blade row than the along the annulus which is from inlet to location 1.

Fig. 9 shows the instantaneous total pressure reduction along the blade row which is between location 1 and 3. The highest instantaneous total pressure difference between these two locations is associated with 0.8TP and the lowest occurs at 0.2TP. The total pressure contour at these two moments are depicted as well. The flow field shows that when the total pressure pulse passing the location 1 (entering the blade), there is lower pressure region at the location 3 (exit plane) which means the highest total pressure difference between the two locations of 1 and 3 occurs. Considering the inlet total pressure curve depicted in Fig. 7b, 0.7TP to 0.9TP is the time in which the inlet total pressure curve variation is much lower than the rest of the cycle. In this time period there would be some back flow in the inlet boundary.

In order to investigate the blade leading edge stagnation flow field and its effect on the experimental pressure measurement, total and static pressure distributions are plotted in Fig. 10 at the two points of the location 1 and the location 2. According to the figure, there is only a slight difference of total pressure around 0.8% of the total pressure at location 2 which is due to the loss associated with the passage between these two locations. The static pressure at leading edge is also lower than the location 1 while it is closer to the total pressure values, because the flow tries to adapt itself before reaching the blade and the flow speed decreases. The Mach number lines at leading edge are shown in Fig. 8e representing different zones at this region.

Conclusion

The present study was focused on the numerical simulation of RDC exhaust flow with the presence of a simple nozzle guide vanes row. The case has been experimentally tested [14] and the pressure data acquired. However, there were some uncertainties in the experimental results which this paper tried to address by numerical simulations. Therefore, the blade rows and the combustor annulus was modeled and URANS equations were solved numerically. The inlet boundary condition imposed were close to what obtained experimentally and also reported in the literatures [22]. The unsteady numerical solution results showed that

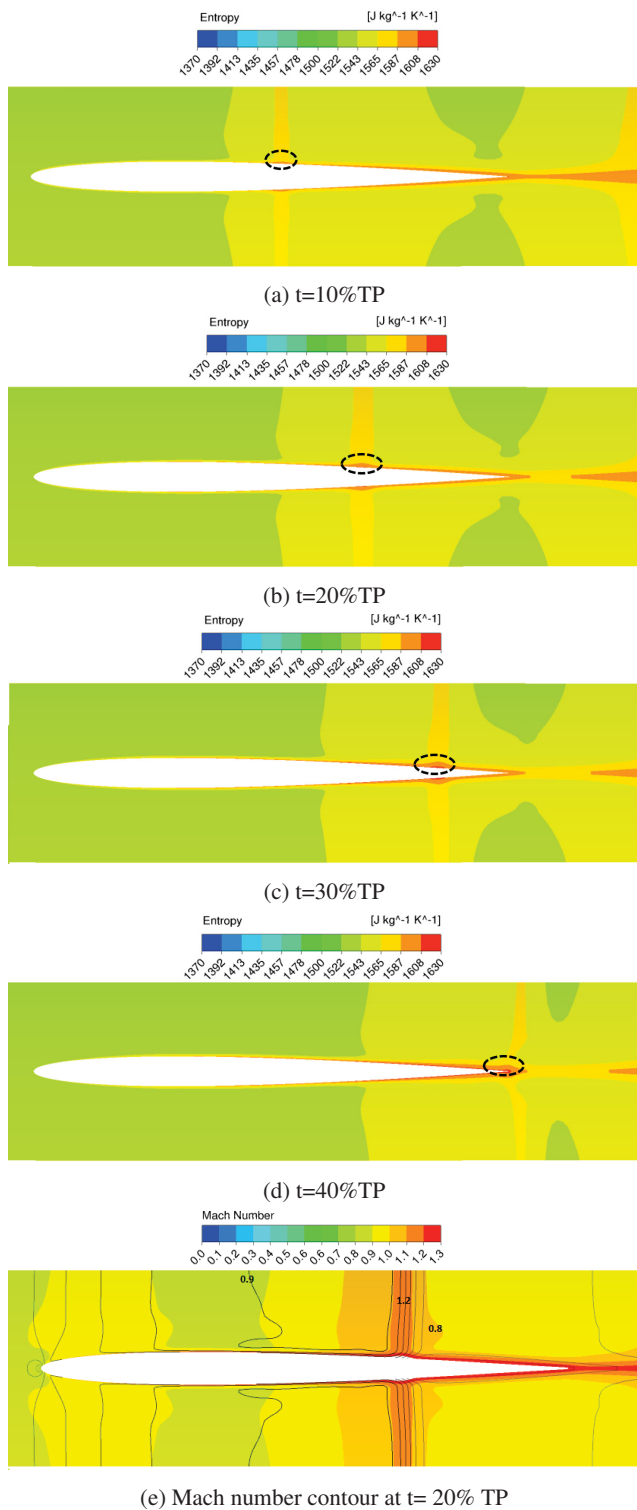


FIGURE 8: Instantaneous entropy and Mach number contours

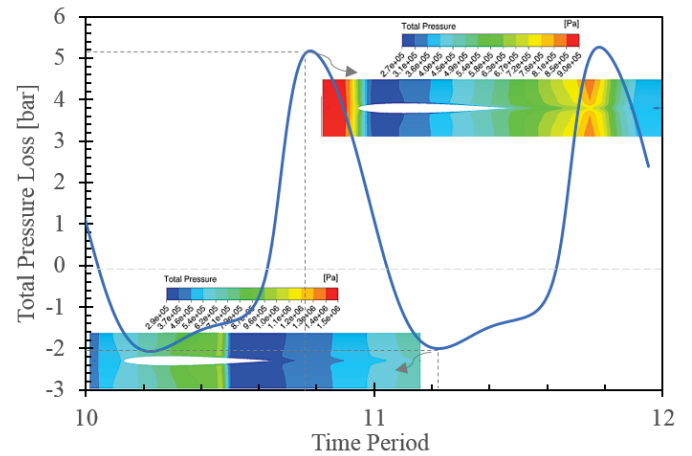


FIGURE 9: Instantaneous total pressure reduction along the blade row.

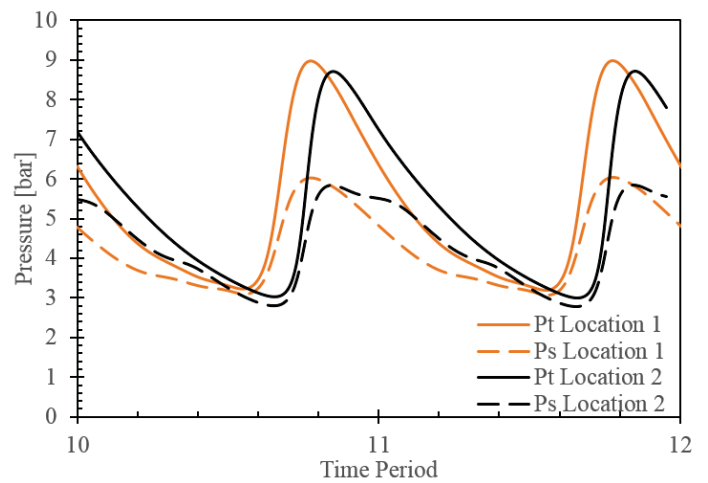


FIGURE 10: Instantaneous pressure values at two locations.

total pressure fluctuation amplitude was reduced 48% from upstream to downstream of the blade, while the cycle average total pressure reduced by 7.9%. The critical time regarding the total pressure loss was observed to be at 70% to 90% of the time period which has the greatest instantaneous value. This moment in the cycle is associated with the approximately constant inlet total pressure distribution of time. Shock waves and also boundary layer-shock wave interactions were detected within the blade passage. These phenomena play a great role in decreasing the total pressure while the flow go through the blade row. No shock wave in front of the blade were observed for the present mode of operation. Therefore, the presence of measuring devices and the

blade has negligible effects on measuring procedure. To sum up, the present study revealed that the measured data acquired by the Kiel probes was not affected by any shock wave in front of the blade leading edge. Further numerical study for other operational modes of the RDC is suggested as the future work.

REFERENCES

- [1] Zhang, A., Gudmundsson, S. V., and Oum, T. H., 2010. "Air transport, global warming and the environment". *Transportation Research Part D: Transport and Environment*, **15**(1), jan, pp. 1–4.
- [2] Van Zante, D., Envia, E., and Turner, M. G., 2007. "The Attenuation of a Detonation Wave By an Aircraft Engine Axial Turbine". *Isabe*(September), pp. 1–12.
- [3] Paniagua, G., Iorio, M., Vinha, N., and Sousa, J., 2014. "Design and analysis of pioneering high supersonic axial turbines". *International Journal of Mechanical Sciences*, **89**(1), dec, pp. 65–77.
- [4] Schauer, F., Bradley, R., and Hoke, J., 2003. "Interaction of a Pulsed Detonation Engine with a Turbine". *41st AIAA Aerospace Sciences Meeting and Exhibit*(January), pp. AIAA 2003–0891.
- [5] Rasheed, A., Furman, A., and Dean, A. J., 2005. "Experimental Investigations of an Axial Turbine Driven by a Multi-tube Pulsed Detonation Combustor System". *Aerospace*(July), pp. 1–13.
- [6] Glaser, A., Caldwell, N., and Gutmark, E., 2007. "Performance of an Axial Flow Turbine Driven by Multiple Pulse Detonation Combustors". In 45th AIAA Aerospace Sciences Meeting and Exhibit, no. January, American Institute of Aeronautics and Astronautics, pp. 1–10.
- [7] George, A. S., Driscoll, R., Gutmark, E., and Munday, D., 2014. "Experimental Comparison of Axial Turbine Performance Under Steady and Pulsating Flows". *Journal of Turbomachinery*, **136**(11), p. 111005.
- [8] Fernelius, M. H., and Gorrell, S. E., 2017. "Predicting Efficiency of a Turbine Driven by Pulsing Flow". In Volume 2A: Turbomachinery, ASME, p. V02AT40A008.
- [9] Tellefsen, J., 2012. "Build Up and Operation of an Axial Turbine Driven by a Rotary Detonation Engine". Msc thesis, Air Force Institute of Technology.
- [10] Naples, A., Hoke, J., Battelle, R. T., Wagner, M., and Schauer, F. R., 2017. "RDE Implementation into an Open-Loop T63 Gas Turbine Engine". In 55th AIAA Aerospace Sciences Meeting, no. January, American Institute of Aeronautics and Astronautics, pp. 1–9.
- [11] Rhee, H., Ishiyama, C., and Higashi, J., 2017. "Experimental Study on a Rotating Detonation Turbine Engine with an Axial Turbine". In 26th ICDERS, pp. 1–6.
- [12] Liu, Z., Braun, J., and Paniagua, G., 2017. "Performance of axial turbines exposed to large fluctuations". In 53rd AIAA/SAE/ASME Joint Propulsion Conference, no. July, American Institute of Aeronautics and Astronautics, pp. 1–14.
- [13] Liu, Z., Braun, J., and Paniagua, G., 2018. "Characterization of a Supersonic Turbine Downstream of a Rotating Detonation Combustor". *Journal of Engineering for Gas Turbines and Power*, **141**(March), pp. 1–13.
- [14] Bach, E., Bohon, M., Paschereit, C. O., and Stathopoulos, P., 2018. "Development of an Instrumented Guide Vane Set for RDC Exhaust Flow Characterization". In 2018 Joint Propulsion Conference, American Institute of Aeronautics and Astronautics.
- [15] Bluemner, R., Bohon, M. D., Paschereit, C. O., and Gutmark, E. J., 2018. "Single and Counter-Rotating Wave Modes in an RDC". In 2018 AIAA Aerospace Sciences Meeting, no. January, American Institute of Aeronautics and Astronautics.
- [16] Shu, M., Yang, M., Deng, K., Zheng, X., and Martinez-Botas, R. F., 2018. "Performance Analysis of a Centrifugal Compressor Based on Circumferential Flow Distortion Induced by Volute". *Journal of Engineering for Gas Turbines and Power*, **140**(12), p. 122603.
- [17] Mistry, H., Santhanakrishnan, M., Liu, J., Stein, A., Dey, S., and Slepiski, J., 2011. "Aerodynamic Performance Assessment of Part-Span Connector of Last Stage Bucket of Low Pressure Steam Turbine". In ASME 2011 Power Conference, Volume 1, ASME, pp. 545–550.
- [18] Duan, P., Tan, C. S., Scribner, A., and Malandra, A., 2018. "Loss Generation in Transonic Turbine Blading". *Journal of Turbomachinery*, **140**(4), p. 041006.
- [19] Asli, M., and Tousi, A., 2013. "Performance analysis of axial flow compressor and part load consideration in a gas turbine application". *Journal of Thermal Science and Technology*, **8**(3).
- [20] Menter, F. R., 1992. "Improved two-equation k-omega turbulence models for aerodynamic flows". *NASA Technical Memorandum*(103978), pp. 1 – 31.
- [21] Greitzer, E., Tan, C., and Graf, M., 2004. *Internal Flow: Concepts and Applications*. Cambridge University Press.
- [22] Kailasanath, K., 2013. "Rotating Detonation Engine Research at NRL". In International workshop on detonation for propulsion (IWDP 2013), pp. 1–14.
- [23] Cumpsty, N. A., and Horlock, J. H., 2006. "Averaging Nonuniform Flow for a Purpose". *Journal of Turbomachinery*, **128**(1), p. 120.

4.2 Publication II

Aerodynamic investigation of guide vane configurations downstream a rotating detonation combustor

This paper was submitted to the Turbo Expo 2020 in London, UK. Through a peer-reviewed process, it got accepted for presentation in the conference and publication in the ASME Journal of Engineering for Gas Turbine and Power. The final manuscript was published in the journal in June 2021, volume 143(6):061011.

Contribution

Toward characterizing the flow field downstream an RDC with a coupled turbine guide vane row, this paper gives emphasis on the connection between total pressure loss and the blade geometrical parameters in such an unconventional unsteady flow field. The aerodynamic performance of different blade types is investigated downstream of the RDC model, similar to the RDC test rig at the TU Berlin, and the damping role of the vanes is analyzed in detail.

Methods

The numerical analysis in this paper is performed using a URANS equations solver for the two-dimensional unfolded RDC exhaust flow channel at midspan radius. The RDC and the baseline vanes are modeled identical to the RDC experimental setup. Different blade geometries having different solidities and thickness to chord ratios are examined as well. The boundary conditions are taken from literature, which provides flow details at the RDC outlet.

Results

According to the numerical simulation results, it is observed that the vanes damp more than 57% of the upstream velocity angle fluctuation amplitude. The total pressure loss coefficient decreases by increasing each of the two geometrical parameters of solidity and thickness-to-chord ratio. This loss coefficient accounts for the profile loss caused by the vanes since no shock wave was captured inside the domain. Furthermore, the area reduction was found to be the significant driving factor for damping the velocity angle fluctuations, whether in the form of solidity or thickness-to-chord ratio increment. Besides, solidity has the highest impact on loss generation and total quantities distribution downstream.

Aerodynamic Investigation of Guide Vane Configurations Downstream a Rotating Detonation Combustor

Majid Asli¹

Chair of Unsteady Thermodynamics in Gas Turbine Processes,
Technical University of Berlin,
Berlin 10623, Germany
e-mail: asli@campus.tu-berlin.de

Panagiotis Stathopoulos

Professor
Chair of Unsteady Thermodynamics in Gas Turbine Processes,
Technical University of Berlin,
Berlin 10623, Germany
e-mail: stathopoulos@tu-berlin.de

Christian Oliver Paschereit

Professor
Chair of Fluid Dynamics,
Technical University of Berlin,
Berlin 10623, Germany
e-mail: oliver.paschereit@tu-berlin.de

Any outlet restriction downstream of pressure gain combustion (PGC), such as turbine blades, affects its flow field and may cause additional thermodynamic losses. The unsteadiness in the form of pressure, temperature, and velocity vector fluctuations has a negative impact on the operation of conventional turbines. Additionally, experimental measurements and data acquisition present researchers with challenges that have to do mostly with the high temperature exhaust of PGC and the high frequency of its operation. Nevertheless, numerical simulations can provide important insights into PGC exhaust flow and its interaction with turbine blades. In this paper, a rotating detonation combustor (RDC) and a row of nozzle guide vanes have been modeled based on the data from literature and an available experimental setup. Unsteady Reynolds-averaged Navier–Stokes (URANS) simulations were done for five guide vane configurations with different geometrical parameters to investigate the effect of solidity and blade type representing different outlet restrictions on the RDC exhaust flow. The results analyzed the connection between total pressure loss and the vanes solidity and thickness to chord ratio. It is observed that more than 57% of the upstream velocity angle fluctuation amplitude was damped by the vanes. Furthermore, the area reduction was found to be the significant driving factor for damping the velocity angle fluctuations, whether in the form of solidity or thickness on chord ratio increment. This RDC exhaust flow investigation is an important primary step from a turbomachinery standpoint, which provided details of blade behavior in such an unsteady flow field. [DOI: 10.1115/1.4049188]

Introduction

One of the fastest growing sources of greenhouse gas emissions is aviation. Direct emissions from aviation account for about 3% of the EU's total greenhouse gas emissions and more than 2% of global emissions. If global aviation were a country, it would rank in the top ten emitters, reported by European commission. Global international aviation emissions by 2050 could increase up to 700% compared to 2005, if no measures are taken [1]. On the other hand, the growing number of air passengers reported by International Civil Aviation Organization (ICAO) [1] and the related tourism market encourage aircraft manufacturers to have greater impact in the field. This is not only the case for aviation, but also for land-based applications of gas turbines for energy production. Although harvesting renewable energy is expanding, the capability of gas turbines for delivering energy and power reserve, keep them relevant in global energy markets. Therefore, gas turbine manufacturers are continuously seeking to increase efficiency and lower emissions.

To date, many efforts have been done to increase the existing gas turbine efficiency by improving component performance. In this regard, these components are so technologically mature that any effort to achieve higher efficiency will not increase the whole gas turbine efficiency above half percent [2–4]. Therefore, reconfiguring gas turbines by introducing innovative cycles is one of the most crucial options left to make a step-change in efficiency. Such a new configuration can be achieved through the Humphrey or the Zeldovich–von Neumann–Döring cycle. In these cycles, constant pressure combustion is replaced with pressure gain combustion (PGC), which leads to a lower entropy generation. The Humphrey cycle models gas turbines with ideal constant volume

combustion. The Zeldovich–von Neumann–Döring cycle models the application of detonative combustion in gas turbines [5]. Pulsed and Rotating Detonation Combustion are the two well-known types of detonative PGC. The higher frequency and self-sustained detonation waves of the latter make it the most suitable for future integration in continuously operating turbomachines [6].

One of the early efforts in turbine and PGC integration was done by Schauer et al. [7], who experimentally showed the feasibility of pulsed detonation combustion (PDC) and its operation with turbomachinery. They could sustain 25 min continuous run of a PDC driving a radial turbine. Rasheed et al. [8,9] tested a multitube PDC together with a single stage axial turbine, and a by-pass flow of air that mixed with the PDC exhaust before its entrance in the turbine. They showed that for their specific case, the turbine isentropic efficiency was effectively the same with the one under steady operation. The feasibility of rotating detonation combustor (RDC) and gas turbine integration has been also recently demonstrated. Wolański [10] investigated the integration of an RDC into a GTD-350 helicopter engine. He found that the engine can be operated with lean mixtures and that the specific fuel consumption was 5% to 7% lower than for the conventional system. In a similar work, Naples et al. [11] developed an RDC and successfully deployed it into a T63 gas turbine. They achieved 20 min of damage-free operation. In spite of observing substantially higher unsteadiness generated by the RDC, they concluded that this did not affect turbine efficiency significantly [12]. Rhee et al. [13] replaced the combustor of a commercial jet engine by a newly designed RDC. They tested the engine and measured the temperature at turbine inlet and exit plane and also turbine rotational speed.

Despite the lower entropy generation of pressure gain combustion, there are some major challenges for getting this type of combustor integrated in a gas turbine. The inherent strong unsteady exhaust flow of PGC make it unfitting for conventional turbine expanders. Tellefsen [14] performed RDC-nozzle and axial

¹Corresponding author.

Manuscript received August 31, 2020; final manuscript received September 10, 2020; published online March 16, 2021. Editor: Jerzy T. Sawicki.

4. Publications

turbine testing. He concluded that using a nozzle at the RDC outlet can experimentally simulate the effect of the turbine presence on the RDC operation. Rankin et al. [15] studied the behavior of a convergent divergent nozzle at RDC downstream. They demonstrated that the combination of a conical center body and converging-diverging nozzle could be a possible solution to alleviate RDC unsteadiness. Turbine integration with RDC has been studied at Purdue University as well. Braun et al. [16] studied different nozzle geometries at RDC outlet to assess nozzle performance with respect to the inlet flow fluctuations. A smooth divergent profile has delivered the highest flow momentum increase and the strongest damping of the Mach number distribution. These high Mach number fluctuations and the respective incidence angle variation are still a challenge for the operation axial turbines. The operation of a supersonic turbine exposed to RDC was studied numerically by Liu et al. [17]. Total pressure loss was computed and it was concluded that the leading edge shock wave is the dominant loss source. Braun et al. [18] investigated the influence of an integrated nozzle and supersonic axial turbine with an RDC. They observed that flow angle fluctuations could not be reduced through the nozzle. The flow turning, pressure loss, and the damping effect of the supersonic stator vanes were also evaluated by them numerically.

Recently, an instrumented guide vane has been setup to characterize RDC flow by Bach et al. [19] at TU Berlin. The aim was to address the effect of RDC outlet restriction on combustion through the combined effects of elevated initial reactant pressure and reflected shocks interacting with the detonation wave. They also performed pressure measurements upstream and downstream of the vanes to measure the average pressure loss through the vanes. The compact geometry, rapid, and high temperature flow limit the measurement and visualization capabilities. Furthermore, the presence of measuring probes mounted on the blades can cause uncertainties in the acquired experimental data. Therefore, numerical analysis can be a promising tool to understand the flow field around the vanes. Asli et al. [20] studied the same geometry numerically to look into the details of the vanes behavior and compared the measured data with the experiments. Following this research, the RDC configuration with different blade types has been modeled numerically in this work. Here, the objective is to evaluate how different vane types and different blade solidities affect the flow in the turbine blade row. Pressure loss has been computed and the damping role of the vanes has been investigated in detail.

Model Description

Rotating Detonation Combustor Configuration. The RDC setup is a radially inward configuration for oxidizer injection. In this configuration, hydrogen is injected through 100 equally spaced holes, while the oxidizer is injected through a circumferential slot. The annulus has an outlet diameter of 90 mm, a passage width of 7.6 mm, and its axial length is 114 mm. According to the scope of research, RDC exhaust flow at the outlet of the RDC annulus is considered as the nonreactive working fluid. Additionally, the annulus width is much shorter than axial length and circumference of the domain. The dominant flow phenomena and related fluctuations within the RDC occur in circumferential and axial directions rather than radial direction. Therefore, in this study the annulus radial height is neglected and the three-dimensional physics of the RDC exhaust channel is unwrapped and reduced in a two-dimensional domain to significantly reduce computational cost. The experimental model and the vanes mounted on the RDC annulus is shown in Fig. 1. The symmetrical blade profile of NACA0006 is selected to be modeled at the RDC outlet to study effect of presence of a general simple guide vane on RDC exhaust flow. This profile type is a simplification of real geometry to obtain a better understanding of the flow physics and investigate

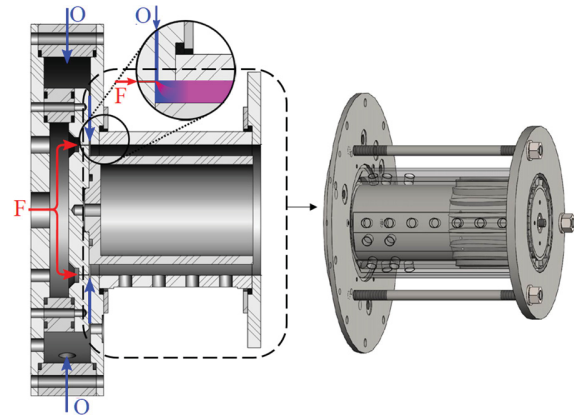


Fig. 1 Schematics of the modeled RDC annulus with a nozzle blade row [19]

effect of geometrical parameters on the RDC flow field. The same configuration has been tested experimentally at TU Berlin [19].

Numerical Setting. Unsteady Reynolds-averaged Navier–Stokes (URANS) simulations were carried out using ANSYS FLUENT density-based solver, which has been widely used for similar problems in turbomachinery [17,21,22]. Second-order discretization and the SIMPLE scheme for pressure–velocity coupling were applied. The transition-shear stress transport model, based on Wilcox $k-\omega$ turbulence model proposed by Menter [23] was utilized. This two-equations eddy-viscosity model combines advantages of both $k-\omega$ in the inner region of boundary layer and $k-\epsilon$ in the free-stream flow. Therefore, it performs well in both near and far walls domains, as well as in separated flow regions, which are probable in this study because RDC exhaust flow angle is highly fluctuating and can cause flow separation on the blades. The flow specifications as the domain inlet boundary conditions will be discussed later in detail. The working fluid is considered to be a mixture of nitrogen (N_2) and water vapor (H_2O) with mass fractions of 0.745 and 0.255, respectively, that are products of hydrogen–air combustion. The mixture is assumed to be a perfect gas thermally and calorically. Convergence criteria of the numerical solutions for each time-step is set at 10^{-6} for all the residuals.

The computational domain, which is the same for all the simulations, is formed to simulate the two-dimensional unwrapped RDC exhaust annulus at midspan radius. This creates a rectangular domain that extends one blade chord length upstream of the blade leading edge and ten blade chords downstream the blade trailing edge to let the flow developed within the computational domain [24]. The domain containing the mesh is depicted in Fig. 2. The mesh is dense enough in areas of high curvature around the blades using a curvature and proximity algorithm in

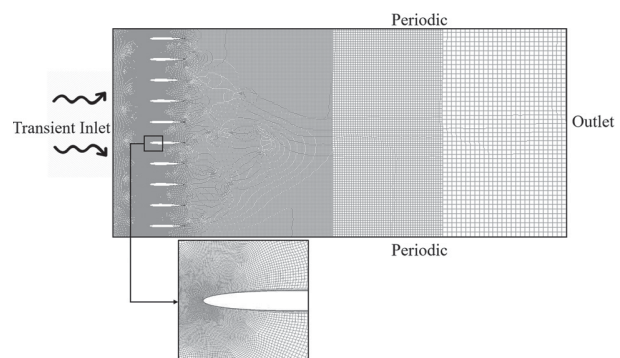


Fig. 2 Computational domain and grid around the blades

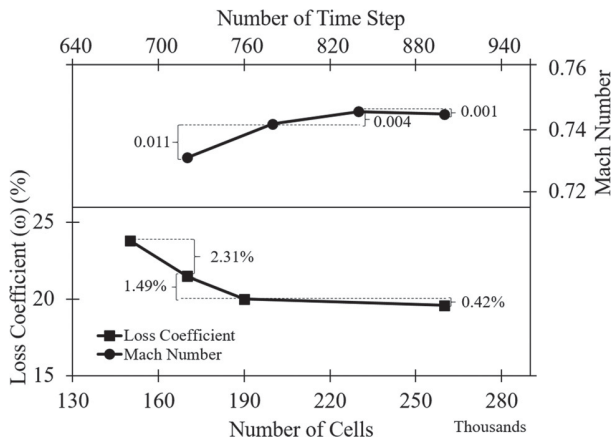


Fig. 3 Effect of grid size and time-step on total pressure loss coefficient and mass averaged Mach number at 0.2c upstream of the vanes

order to capture the geometry and boundary layer. The dimensionless wall distance (y^+) is kept below 1 to ensure a good resolution of the near wall regions. This is done by refining the mesh during simulation. Additionally, as the flow property gradients are high at the inlet boundary, the mesh was refined up to the four chord downstream of the blades during the simulations to achieve the optimum convergence time.

Four mesh configurations with different densities have been generated to evaluate effect of grid size on the results. Simulations were done for the case with 15 blades of NACA0006 profile having 150k, 170k, 190k, and 250k nodes. The total pressure loss coefficient defined as $\omega = 1 - P_t/P_{t,inlet}$ has been calculated between 0.2c upstream and 2c downstream of the vanes. According to Fig. 3, the simulation results for the latter two grids exhibit only 0.42% difference in total pressure loss coefficient along the vanes. Therefore, the grid density with 190k nodes was selected for the simulations of the present research.

In order to capture all the flow features in an unsteady simulation, the global time-step must be chosen small enough. An appropriate time-step value depends very much on the flow fluctuations. A time-step sensitivity analysis was performed previously for similar flows [20,25]. However, for the current research four different time steps ranging from 720 to 900 are considered to find the optimum value. Mass averaged values of Mach number at 0.2c upstream of the vanes are calculated for the case with 15 blades of NACA0006. According to Fig. 3, the mass averaged Mach number is increasing by increasing time-step up to 840 and then decreases slightly for the time-step of 900. The difference

between the two higher time steps is 0.001, which is much lower than that of the other time steps. Therefore, the suitable time-step for the simulations in this study is chosen to be 840 times smaller than the RDC time period.

In the present numerical simulations, the inlet flow boundary condition must be supplied by the RDC exhaust flow conditions. Pressure measurements in the RDC setup of the TU Berlin reported time averaged values that indicated a peak total pressure of 2.9 bar at the blade upstream [19]. This value shows that the experimental diagnostics have difficulties to acquire time-resolved measurements, since the peak pressure values are expected to be in the order of 10 bar [26]. However, the average measured values were quite promising as reported. The RDC annulus equipped with NACA0006 profile vanes mounted at the outlet has been numerically simulated [20]. This vane configuration will be introduced as profile C.1 later in the paper. The numerical results are compared with the experimental ones to verify the numerical method accuracy. In Fig. 4, total pressure distributions at upstream and downstream of the blade row are plotted. The numerically obtained pressure data reported here is measured exactly at the same locations as in the experimental setup. Based on the two curves of experiments and numerical simulation, an acceptable matching for total pressure results around the vanes is observed. This shows that the total pressure loss caused by the blade row in the experimental setup was accurately simulated. The consistency between the two set of results confirmed the validity of numerical simulation for the RDC exhaust flow.

Boundary Conditions. This work uses the simulated RDC flow characteristics provided by Schwer et al. [27] as the inlet boundary condition of the domain. The inlet boundary represents two rotating waves traveling around the annulus. This wave mode provides a pressure distribution with ~ 7 bar peak and a static temperature ranging from 1500 K to 2000 K as shown in Fig. 5. The frequency of the fluctuation is 7 kHz and the flow angle variation in blade to blade surface is approximately ± 40 deg with the mean value of -10.5 deg. The outlet boundary for the computational domain is considered as the pressure far field type and the two sides are unified as a periodic boundary to ensure periodicity and shape the unrolled presentation of the cylindrical annulus (see Fig. 2).

The aforementioned settings are the same for the five cases listed in Table 1. Different solidities have been achieved by changing blade numbers from 10 to 15 and 20 for case C.1 to case C.3, respectively. The solidity values are selected within the conventional range offered by Ainley–Mathieson correlation [28]. The two other cases with different blade types have been considered to evaluate effect of blade thickness while having the same solidity values and blade numbers. The numerical calculations

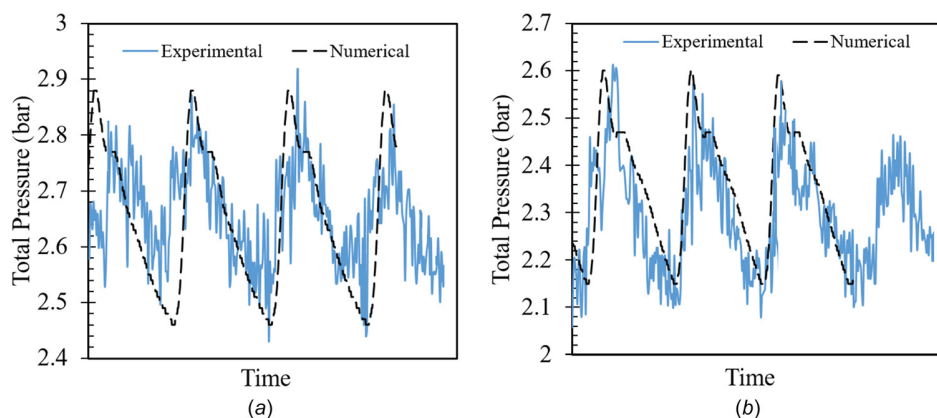


Fig. 4 Total pressure distribution at upstream and downstream of the blade row: (a) blade row upstream and (b) blade row downstream

4. Publications

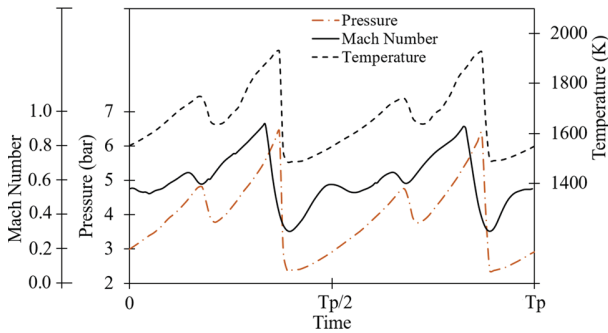


Fig. 5 RDC exhaust flow properties considered as the inlet condition

Table 1 Blade configuration specifications at RDC downstream

Case Nr.	Profile type	σ	τ	N	Area reduction
C.1	NACA0006	1.76	6%	10	10.55%
C.2	NACA0006	2.64	6%	15	15.83%
C.3	NACA0006	3.52	6%	20	21.10%
C.4	NACA0009	1.76	9%	10	15.83%
C.5	NACA0012	1.76	12%	10	21.10%

have been done using eight Intel(R) CPUs at 4.00 GHz with 4 cores and 32 GB of memory in parallel. The mean CPU time for each case was 25 h to achieve convergence.

Results and Discussion

Pressure Loss. The simulation of the RDC exhaust flow passing through the guide vanes entails a transient phase before reaching periodically steady operation in the entire computational domain. The main difference of the two modes is the presence of specific shock waves in transient operation, which are not present in the steady periodical operation. The flow features of both operational phases are discussed in this section.

To evaluate the impact of different blade configurations on the blade total pressure loss, the mass averaged total pressure has been computed at 0.2c and 2c downstream of the vanes. The total pressure loss coefficient has been calculated for each case. Figure 6 shows its values averaged in one combustor period with pattern filled bars. In the transient operational phase, an increase of the blades number from 10 to 15 and then to 20 leads to higher total pressure loss coefficients from 0.176 to 0.201 and then to 0.224, respectively. Additionally, the loss coefficients for different thickness on chord ratio corresponding to the cases C.1, C.4, and C.5 are 0.176, 0.190, and 0.212, respectively. Figures 7(a) and 7(b) indicate the instantaneous contours of Mach number and

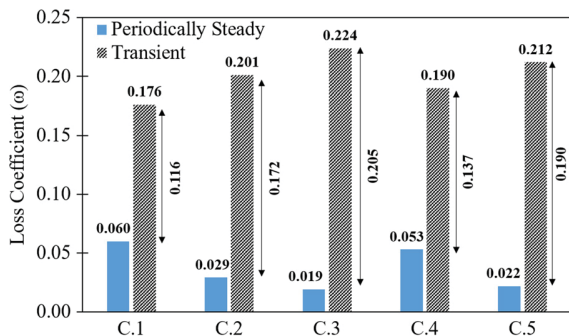


Fig. 6 Total pressure loss coefficient

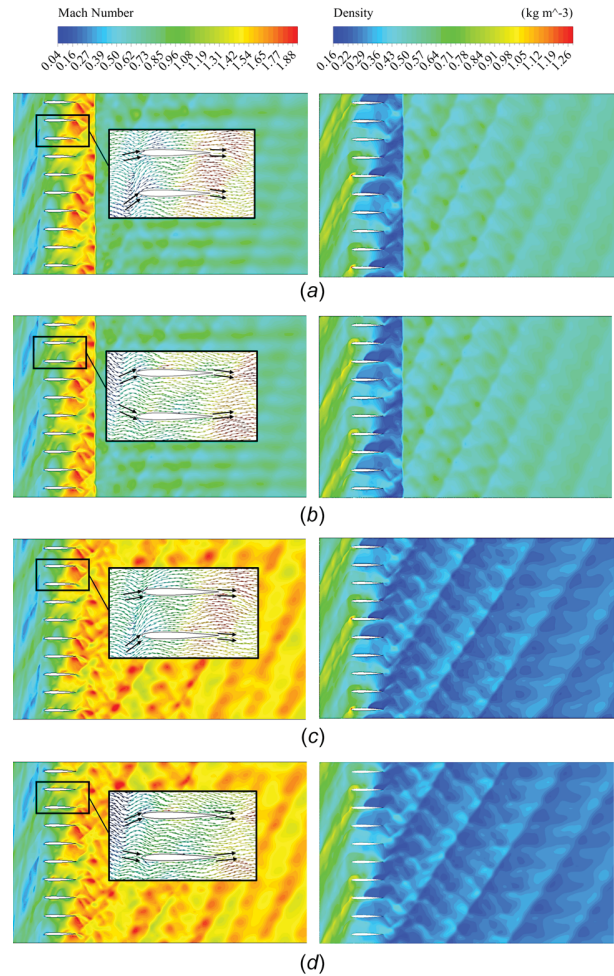


Fig. 7 Instantaneous contours of Mach number (left) and density (right) for C.4. (a) transient operation at $t = T_p$, (b) transient operation at $t = T_p + 1/4T_p$, (c) periodically steady operation at $t = T_p$, and (d) periodically steady operation at $t = T_p + 1/4T_p$.

density for C.4, as a sample, in two different time instances. According to the RDC exhaust flow, there are two rotating waves that cause two symmetric patterns traveling circumferentially. In this regard, half of the time period is considered in Fig. 7 and the two equal time intervals of the flow field are depicted. The contours pattern reveals that the fluctuating flow is subsonic up to the vane row. Flow Mach number at the passage inlet location ranges 0.69–0.97, 0.33–0.86, 0.62–0.96, and 0.46–0.98 for each of the four cases C.1, C.3, C.4, and C.5, respectively. In this subsonic flow regime, the presence of vanes may affect the combustion process, which is not in the scope of this study. The flow Mach number subsequently increases when the flow enters the vane passages and it continues to accelerate up to the vanes trailing edge. There is a sharp deceleration to supersonic Mach numbers at around one chord length downstream of the vanes, where a rather great increase in density exists. This confirms the presence of shock waves downstream of the vanes, which is an important source of total pressure loss indicated in Fig. 6 for the transient operational phase in addition to the vanes profile loss. The compression waves are present in the flow field of all the other configurations not depicted here. These shock waves are transferred downstream toward the outlet of the computational domain. Velocity vectors are zoomed-in around two sample blades and shown inside the contours of Mach number as well. It shows that velocity vectors are quite fluctuating at upstream of the vanes and where hitting the vanes leading edge. Thereafter, the velocity vectors are getting straighter while passing through the vane passages.

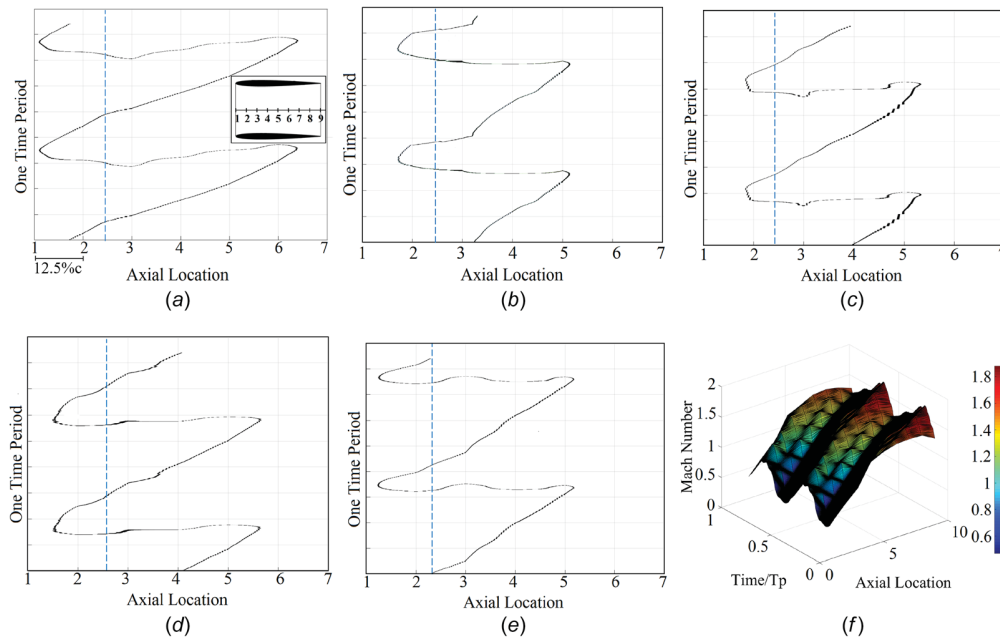


Fig. 8 Sonic condition inside the blade passages ((a)–(e)) and Mach number distribution for C.5 (f): (a) C.1, (b) C.2, (c) C.3, (d) C.4, (e) C.5, and (f) C.5

The flow field reaches periodically steady condition when the shock waves move out from the domain outlet. The periodically steady operating flow field is shown in Figs. 7(c) and 7(d) in two different time instants. Total pressure loss has been calculated at 0.2c downstream of the vanes for all the cases and the related coefficients are indicated in Fig. 6 with filled bars. The loss coefficient in steady operation, which represents profile loss, is decreasing from 0.06 to 0.029 and then to 0.019 when the solidity is increased from 1.76 to 2.64 and then to 3.52, respectively. Additionally, the loss coefficients of C.1, C.4, and C.5 are 0.06, 0.053, and 0.022 each. These trends are not consistent with the conventional profile loss correlation of Ainley–Mathieson and the empirical model by Aungier [28]. Based on the conventional loss correlation, higher solidity should result in higher loss coefficients. The inconsistency arises due to the flow unsteadiness with high amplitude of flow angle fluctuation in RDC exhaust flow. Furthermore, comparing loss coefficient of the periodically steady operation with the transient one shows that the share of shock loss in total amount of loss in transient operation is very high with respect to the profile loss. Higher solidity and higher area reduction cause higher Mach number downstream of the vanes and hence stronger shock waves and higher shock loss coefficients marked in Fig. 6.

Passage Chocking. Chocking is likely to happen in turbine blades and fixes the reduced mass flow. To evaluate the flow inside the vanes, the Mach number on the centrally located line between two adjacent blades is measured during a whole RDC period. The locations where sonic Mach number is observed on this line are captured and plotted for the five cases within one period as displayed in Fig. 8. The axial location numbers are described graphically in Fig. 8(a) which are equally (12.5%c) distributed on the centerline of the vane passage from leading edge to trailing edge. The vane throat is located at 30% chord for the cases C.1, C.2, C.3, and C5 and at 33% chord for case C.4. If the flow field would have been steady, the maximum Mach number or sonic condition would have been expected at the throat location in each case (marked with dashed line in Fig. 8). However, the sonic Mach number location changes within an RDC period. The respective locations along the centerline are different for each case. A comparison of Fig. 8(a) with Fig. 8(b) and Fig. 8(c) shows

that the higher solidity moves the point in which the sonic Mach number is reached downstream with shorter range of sonic Mach number locations. Additionally, although the two cases of C.3 and C.5 have the same area reduction, C.3 exhibits shorter range of sonic Mach number locations, mostly due to its higher solidity. By drawing a vertical line in the plots, it can be seen that each

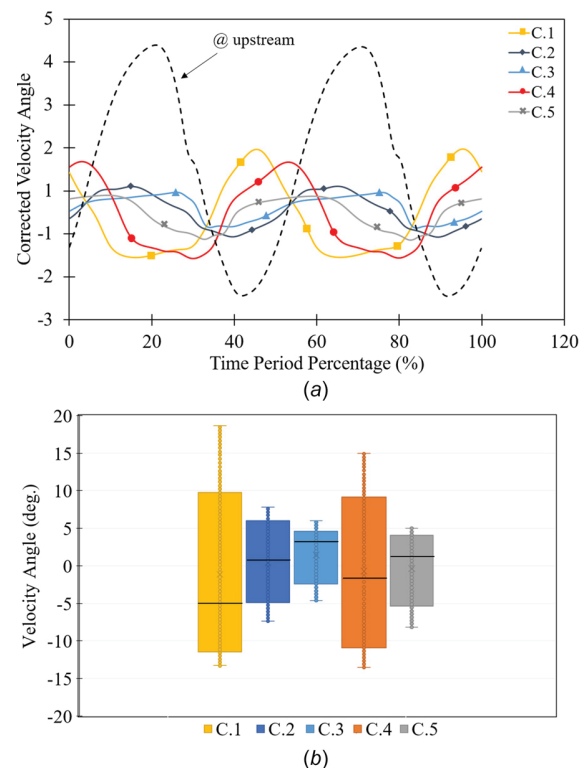


Fig. 9 Velocity angle in one time period at 20%c downstream of the vanes: (a) instantaneous distribution of corrected velocity angle and (b) box and whisker diagram of measured velocity angle

4. Publications

Table 2 Corrected velocity angle amplitude at 20%*c* downstream

	C.1	C.2	C.3	C.4	C.5
\bar{A}_α	2.52	1.19	0.83	2.24	1.03
Reduction (%)	57	79	86	62	82

location experiences sonic condition four times within one time period. This means that the fluctuating exhaust flow of the RDC creates supersonic flow conditions when passing through the vanes over the entire RDC period. The Mach number distribution inside the vane passage of C.5 is shown in Fig. 8(f). It indicates that the flow reaches the supersonic regime while exiting the vane passage. The Mach number at the vane passage outlet is in the range of 1.28–1.64, 1.29–1.82, 1.31–1.91, 1.45–1.76, and 1.41–1.88 for the cases C.1 to C.5, respectively.

Flow Unsteadiness Damping. One of the most important parameters affecting the flow within turbomachinery blade rows is the flow incidence angle. Theoretically, blades are designed to work in a defined (design) incidence angle to reduce aerodynamic losses. Any deviation from the design value causes considerable aerodynamic losses. For the present case study, the inherent flow velocity angle fluctuations make the study of their effect on the flow within the rows necessary. The time trace corrected velocity angle, defined as $\bar{\alpha} = \alpha/\alpha_{\text{average@upstream}}$ at 20%*c* downstream of the vanes, is plotted for all cases in one RDC period in Fig. 9(a). The corrected flow angle at 20%*c* upstream of the vanes is marked by a dashed line, which is almost the same for all the cases. The corrected velocity angle amplitude, defined as $\bar{A}_\alpha = \alpha_{\text{max}} - \alpha_{\text{min}}$, is 2.52, 1.19, 0.83, 2.24, and 1.03 for C.1 to C.5, respectively, as tabulated in Table 2. By considering its value at the upstream location 5.85, it can be stated that the amplitude of the velocity angle fluctuation is reduced by more than 57%. By increasing solidity from 1.76 to 3.52 (in C.1 and C.3), the velocity angle amplitude is reduced even more (by 86%). At the same time, an increase of the thickness to chord ratio from 6 to 12, while maintaining the same solidity, results in a higher damping of the velocity angle amplitude. Although the cases C.3 and C.5 have the same area reduction, the velocity angle damping in C.5 is 4% lower than C.3 that has a higher solidity. This higher damping caused by C.3 is achieved at the expense of 0.01 higher loss coefficient (see Fig. 6). It can be concluded that area reduction by either an increase of the solidity or the thickness to chord ratio plays a great role in velocity angle fluctuation damping.

To look into the details of the velocity angle downstream of the vanes in one RDC period, a box-and-whisker diagram of the measured data is plotted in Fig. 9(b). In this plot, the first segment is the first quartile of the data. The second and third segments represent the difference between the median and the first quartile and the difference between the third quartile and the median, respectively. The difference between the upper and lower limits of the whiskers shows the data range known as the velocity angle amplitude here, which has been already discussed in nondimensional form. According to the diagram, the median value is much closer to the whisker upper limit in C.3 and C.5 rather than the other cases. These two cases have the highest area reduction with different solidity and thickness to chord ratio. Although the thickness to chord ratio of case C.5 is two times greater than C.3, the higher solidity of C.3 compared to C.5 causes not only shorter range but also much steadier velocity angle downstream of the vanes. This can be also observed from the closer median value to the upper whisker limit. The median value is located at approximately mid of the box and whisker plots in other cases (C.1, C.2, and C.4), which shows rather equally distributed values of the velocity angle in one RDC period.

To evaluate how the vanes affect total quantities downstream where rotor blades could be installed, time trace corrected total

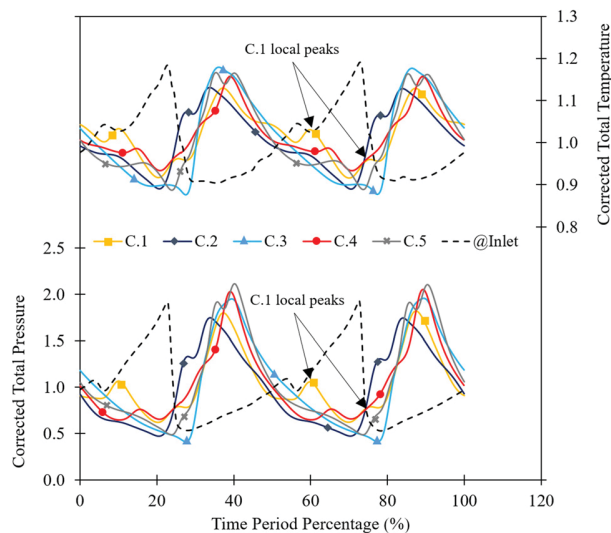


Fig. 10 Instantaneous distribution of total quantities at inlet and 20%*c* downstream of the vanes

Table 3 Corrected total pressure and total temperature amplitude at inlet and 20%*c* downstream of the vanes

	C.1	C.2	C.3	C.4	C.5	Inlet
\bar{A}_{P_t}	1.2017	1.2771	1.5482	1.4075	1.6302	1.2210
\bar{A}_{T_t}	0.2138	0.2415	0.3028	0.2236	0.2791	0.2866

pressure ($\bar{P}_t = P_t/P_{t,\text{average@upstream}}$) and total temperature ($\bar{T}_t = T_t/T_{t,\text{average@upstream}}$) are calculated at 20%*c* downstream of the vanes in one RDC time period. According to Fig. 10, increasing solidity corresponding to C.1, C.2, and C.3 exhibits smoother total pressure and total temperature distributions. The two local peaks observable on both curves of C.1 are moderated in C.2 and almost become smoothed in C.3. The same behavior can be seen by comparing C.1, C.4, and C.5. It indicates that a blade row with higher thickness to chord ratio has more damping effect on local unsteadiness of total pressure and total temperature. On the other hand, the curves of Fig. 10 show a rather slight difference in amplitude of the two total quantities distribution. The corrected amplitudes are listed in Table 3. Although local peaks get smoother by increasing area reduction, the fluctuation amplitudes of both total pressure and total temperature are increased. Additionally, the comparison of the total pressure amplitude at the inlet with the downstream reveals that C.1 configuration damps total pressure fluctuation by 1.6% while the amplitudes at downstream of the other cases are higher than the inlet. The total temperature amplitude is alleviated from inlet to downstream for all the cases except C.3 which has the highest solidity. Despite the same area reduction of C.3 and C.5, total temperature damping role of these two configurations is different that confirms dominant impact of solidity.

Conclusion

This work focused on the aerodynamic behavior of different outlet guide vane configurations located downstream of a rotating detonation combustor. Numerical analysis was utilized as the method of investigation because it eliminates the difficulties and uncertainties of experiments within the high temperature RDC exhaust flow. Two dimensional URANS simulations have been performed to evaluate the effect of blade geometrical parameters on total pressure loss and velocity angle fluctuation damping. Five

configurations with different solidity and thickness to chord ratio in the unwrapped combustor annulus have been modeled and simulated while one of them (C.1) has also been tested experimentally [19] and compared to the numerical simulation. Time and location dependent boundary conditions were imposed as the inlet boundary of the domain, which reproduces the two rotating waves operating mode of an RDC.

The results revealed that the total pressure loss coefficient in periodically steady flow field decreases by increasing each of the two geometrical parameters of solidity and thickness to chord ratio. This loss coefficient accounts profile loss caused by the vanes. However, in transient operation where moving strong shock waves are present downstream of the flow field, loss coefficient including shock loss and profile loss, increases by increasing solidity and thickness to chord ratio. It was shown that shock wave can add more than two times of blade profile loss to the flow field in transient operation. Choked flow condition was observed within the blades passages. Velocity angle measurements upstream and downstream of the vanes showed that more than 57% velocity angle fluctuation damping can be achieved by passing RDC exhaust flow through these vane configurations. Higher velocity angle damping was resulted by either increasing thickness to chord ratio or solidity, which means higher area reduction. However, in the configurations having the same area reduction and thickness to chord ratio, velocity angle damping was affected by solidity. Higher solidity configurations exhibit steadier velocity angle distribution in one RDC period. According to the studied configurations, it can be concluded that solidity had the highest impact on loss generation and total quantities distribution at downstream while area reduction was the most driving factor for velocity angle fluctuation damping. Future work will focus on other vane configurations.

Nomenclature

\bar{A}	= corrected amplitude
c	= chord length
M	= Mach number
N	= number of blade
Pt	= total pressure
s	= second
t	= time
T_p	= time period
T_t	= total temperature
α	= velocity angle
σ	= solidity (chord/space)
τ	= thickness to chord ratio (thickness/chord)
ω	= total pressure loss coefficient

References

- [1] International Civil Aviation Organization, 2019, "ICAO Global Environmental Trends—Present and Future Aircraft Noise and Emissions," The Council of ICAO, Montreal, PQ, Canada, Report No. A40-WP/54.
- [2] Popović, I., and Hodson, H. P., 2013, "Improving Turbine Stage Efficiency and Sealing Effectiveness Through Modifications of the Rim Seal Geometry," *ASME J. Turbomach.*, **135**(6), p. 061016.
- [3] Asli, M., and M. Tousi, A., 2013, "Performance Analysis of Axial Flow Compressor and Part Load Consideration in a Gas Turbine Application," *J. Therm. Sci. Technol.*, **8**(3), pp. 476–487.
- [4] Odgers, J., Kretschmer, D., and Pearce, G. F., 1993, "The Combustion of Droplets Within Gas Turbine Combustors: Some Recent Observations on Combustion Efficiency," *ASME J. Eng. Gas Turbines Power*, **115**(3), pp. 522–532.
- [5] Stathopoulos, P., 2018, "Comprehensive Thermodynamic Analysis of the Humphrey Cycle for Gas Turbines With Pressure Gain Combustion," *Energies*, **11**(12), p. 3521.
- [6] Lu, F. K., and Braun, E. M., 2014, "Rotating Detonation Wave Propulsion: Experimental Challenges, Modeling, and Engine Concepts," *J. Propul. Power*, **30**(5), pp. 1125–1142.
- [7] Schauer, F., Bradley, R., and Hoke, J., 2003, "Interaction of a Pulsed Detonation Engine With a Turbine," *AIAA Paper No. 2003-0891*.
- [8] Rasheed, A., Tangirala, V. E., Vadervort, C. L., Dean, A. J., and Haubert, C., 2004, "Interactions of a Pulsed Detonation Engine With a 2D Blade Cascade," *AIAA Paper No. 2004-1207*.
- [9] Rasheed, A., Furman, A. H., and Dean, A. J., 2011, "Experimental Investigations of the Performance of a Multitube Pulse Detonation Turbine System," *J. Propul. Power*, **27**(3), pp. 586–596.
- [10] Wolański, P., 2015, "Application of the Continuous Rotating Detonation to Gas Turbine," *Appl. Mech. Mater.*, **782**, pp. 3–12.
- [11] Naples, A., Hoke, J., Battelle, R. T., Wagner, M., and Schauer, F. R., 2017, "RDE Implementation Into an Open-Loop T63 Gas Turbine Engine," *AIAA Paper No. 2017-1747*.
- [12] Naples, A., Hoke, J., Battelle, R., and Schauer, F., 2019, "T63 Turbine Response to Rotating Detonation Combustor Exhaust Flow," *ASME J. Eng. Gas Turbines Power*, **141**(2), p. 021029.
- [13] Rhee, H., Ishiyama, C., and Higashi, J., 2017, "Experimental Study on a Rotating Detonation Turbine Engine With an Axial Turbine," *26th ICEDERS*, Boston, MA, Jul. 30–Aug. 4, pp. 1–6.
- [14] Tellefsen, J., 2012, "Build Up and Operation of an Axial Turbine Driven by a Rotary Detonation Engine," *M.Sc. thesis*, Air Force Institute of Technology, Wright-Patterson Air Force Base, OH.
- [15] Rankin, B. A., Hoke, J., and Schauer, F., 2014, "Periodic Exhaust Flow Through a Converging-Diverging Nozzle Downstream of a Rotating Detonation Engine," *AIAA Paper No. 2014-1015*.
- [16] Braun, J., Saavedra Garcia, J., and Paniagua, G., 2017, "Evaluation of the Unsteadiness Across Nozzles Downstream of Rotating Detonation Combustors," *AIAA Paper No. 2017-1063*.
- [17] Liu, Z., Braun, J., and Paniagua, G., 2019, "Characterization of a Supersonic Turbine Downstream of a Rotating Detonation Combustor," *ASME J. Eng. Gas Turbines Power*, **141**(3), pp. 1–13.
- [18] Braun, J., Cuadrado, D. G., Andreoli, V., Paniagua, G., Liu, Z., Saavedra, J., Athmanathan, V., and Meyer, T., 2019, "Characterization of an Integrated Nozzle and Supersonic Axial Turbine With a Rotating Detonation Combustor," *AIAA Paper No. 2019-3873*.
- [19] Bach, E., Bohon, M., Paschereit, C. O., and Stathopoulos, P., 2018, "Development of an Instrumented Guide Vane Set for RDC Exhaust Flow Characterization," *AIAA Paper No. 2018-4479*.
- [20] Asli, M., Cuciumita, C., Stathopoulos, P., and Paschereit, C. O., 2019, "Numerical Investigation of a Turbine Guide Vane Exposed to Rotating Detonation Exhaust Flow," *ASME Paper No. GT2019-91263*.
- [21] Papa, F., Madanan, U., and Goldstein, R. J., 2017, "Modeling and Measurements of Heat/Mass Transfer in a Linear Turbine Cascade," *ASME J. Turbomach.*, **139**(9), p. 091002.
- [22] Asli, M., and Tousi, A. M., 2011, "Sensitivity Analysis of a Centrifugal Compressor Using the Linearization Method," *ASME Paper No. AJK2011-05013*.
- [23] Menter, F. R., 1992, "Improved Two-Equation k-Omega Turbulence Models for Aerodynamic Flows," NASA Ames Research Center, Washington, DC, Report No. TM-103975, pp. 1–31.
- [24] Greitzer, E., Tan, C., and Graf, M., 2004, *Internal Flow: Concepts and Applications*, Cambridge University Press, Cambridge, UK.
- [25] Chen, L., Zhuge, W., Zhang, Y., Xie, L., and Zhang, S., 2011, "Effects of Pulsating Flow Conditions on Mixed Flow Turbine Performance," *ASME Paper No. GT2011-45164*.
- [26] Kailasanath, K., 2013, "Rotating Detonation Engine Research at NRL," *International Workshop on Detonation for Propulsion (IWDP 2013)*, Taiwan, Taipei, July 26–28, pp. 1–14.
- [27] Schwer, D. A., Brophy, C. M., and Kelso, R. H., 2018, "Pressure Characteristics of an Aerospike Nozzle in a Rotating Detonation Engine," *AIAA Paper No. 2018-4968*.
- [28] Aungier, R. H., 2006, *Turbine Aerodynamics: Axial-Flow and Radial-Flow Turbine Design and Analysis*, ASME Press, New York.

4.3 Publication III

A robust one-dimensional approach for the performance evaluation of turbines driven by pulsed detonation combustion

The first manuscript was submitted to the journal of Energy Conversion and Management on 2 July 2021. The final version was accepted on 18 September 2021 and published on 15 November in volume 248, 114784.

Contribution

A fast approach based on a one-dimensional Euler equations solver for unsteady turbine simulation is presented in the paper. It is examined for a two-stage turbine model connected to different PDC tube configurations. A back-to-back comparison with 3D-CFD analysis is made for assessing the method's capabilities.

Methods

The Euler equations are used along the turbine rotational axis in a one-dimensional form. A meanline turbomachinery analysis method is exploited for providing the source terms in the Euler equations. An analogous one-dimensional Euler solver, but with different source terms, is utilized to model the PDC tubes to provide the boundary conditions for the turbine simulations. A three-dimensional URANS equations solver is employed to simulate the two-stage turbine for verifying the results.

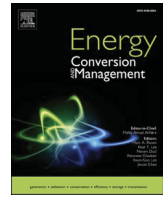
Results

The methodology shows its robustness in simulating the unsteady behavior of a multistage turbine. Therefore, based on the accuracy level comparable to high-fidelity CFD methods and very low computational cost, the approach is recommended for being used in early design and optimization stages. In addition, it is indicated that around 45% of the total unsteadiness is damped throughout the first blade row, which is almost irrespective of the inlet fluctuation amplitude.



Contents lists available at ScienceDirect

Energy Conversion and Management

journal homepage: www.elsevier.com/locate/enconman

A robust one-dimensional approach for the performance evaluation of turbines driven by pulsed detonation combustion

Majid Asli^{a,*}, Niclas Garan^b, Nicolai Neumann^c, Panagiotis Stathopoulos^a

^a TU Berlin, Institute of Fluid Dynamics and Technical Acoustics, Chair for Unsteady Thermodynamics in Gas Turbine Processes, Müller-Breslau-Straße 8, 10623 Berlin, Germany

^b TU Berlin, Institute of Fluid Dynamics and Technical Acoustics, Chair of Combustion Kinetics, Müller-Breslau-Straße 8, 10623 Berlin, Germany

^c TU Berlin, Institute of Aeronautics and Astronautics, Chair for Aero Engines, Marchstraße 12-14, 10587 Berlin, Germany

ARTICLE INFO

Keywords:

Pressure gain combustion
Unsteady simulation
Turbine performance
1D-Euler
Pulsed detonation combustion

ABSTRACT

Among the solutions to reduce emissions from stationary gas turbines, replacing conventional combustion through pressure gain combustion is one of the most promising options. Nevertheless, coupling pressure gain combustion with a turbine can result in increased losses within the cycle, mainly because of the resulting very unsteady turbine inflow conditions. A reliable simulation tool can help to overcome this challenge and optimize turbine geometries and designs for the specific application. The harsh unsteady flow downstream of pressure gain combustors makes three-dimensional CFD computationally expensive. Thus, the development of a fast computational method is crucial. This paper introduces and explores such an alternative methodology. A one-dimensional Euler gas dynamic approach is combined with blade source terms, computed out of a steady-state turbine meanline analysis. To evaluate the methodology, three-dimensional CFD simulations are performed in parallel and the results are compared with those of the 1D method. The energy extraction of a turbine expander is computed with both methods for three different configurations of pulsed detonation combustor arrays connected at the turbine inlet. The results show that the proposed approach is capable of simulating the turbine in such an unsteady environment accurately. Additionally, it is indicated that around 45% of the total unsteadiness is damped throughout the first blade row, which is almost irrespective of the inlet fluctuation amplitude. Due to its accuracy and very low computational cost, the developed methodology can be integrated into optimization loops in the early design and development stages of turbomachinery for pressure gain combustion applications.

1. Introduction

The rapid increase in the average global temperature during the past decades has urged legislators to take actions to limit global warming. Curbing the adverse effect of climate change needs a profound decrease in green house gas emissions. The power and transportation sectors are responsible for a high share of the total global CO₂ emissions. According to the long-term air traffic forecasts by ICAO [1], the number of air passengers is expected to grow by 2.2 times by the next twenty years. Therefore, a radical enhancement in gas turbine engine efficiency is necessary, to provide flexible, dispatchable generation and the lowest possible emissions. Pressure gain combustion, either in the form of Rotating Detonation Combustion (RDC) or Pulsed Detonation Combustion (PDC), is one of the concepts that can cut the current gas turbine emissions significantly. In PGCs, the unsteady detonative combustion

process can raise the total pressure by up to 30% compared to a 2–3% total pressure loss caused by conventional combustion chambers [2,3]. Average total pressure gain in the combustion process can improve the thermodynamic efficiency in a gas turbine cycle. Several researchers have focused on the integration of PGC into conventional gas turbines so far, whether in the form of RDC [4,5], PDC [6–8] or overall thermodynamic cycle investigation [9]. Nevertheless, a remaining open question is the adaptation of turbine expanders to the unsteady PGC outlet flow with the aim to efficiently convert the exhaust gas energy into mechanical work. The gas turbine cycle efficiency is very sensitive to the component performances. Additionally, for a gas turbine with PGC, the cycle efficiency becomes even more sensitive to turbine efficiency because of the increased expansion ratio. Since turbine expanders are designed for steady inlet flows, they show relatively low performance when driven by the periodically unsteady harsh exhaust flow of PGCs [10]. Strong fluctuations in the thermodynamic quantities cause the

* Corresponding author.

E-mail address: asli@campus.tu-berlin.de (M. Asli).

<https://doi.org/10.1016/j.enconman.2021.114784>

Received 2 July 2021; Accepted 18 September 2021
0196-8904/© 2021 Elsevier Ltd. All rights reserved.

Nomenclature*Abbreviations*

CJ	Chapman–Jouguet
E ³	Energy Efficient Engine
GCI	Grid Convergence Index
PDC	Pulsed Detonation Combustion
PGC	Pressure Gain Combustion
ZND	Zel'dovich, von Neumann, Döring

Greek symbols

A	Cross sectional area
\overline{A}_p	Relative pressure amplitude
E	Internal energy
e	Error
f	Frequency
H	Total enthalpy
h	Specific enthalpy
L	Length of the PDC tubes
N	Number of nodes
\dot{m}	Mass flow rate
P	Pressure
\overline{P}	Normalized pressure

rpm	Round per minute
T	Temperature
\overline{T}_t	Normalized total temperature
V_x	Axial velocity
W	Work
Y	Mass fraction
y^+	Dimensionless wall distance
γ	Heat capacity ratio
δ_m	Mass flow deviation
ρ	Density
τ	Time period
b	Bleed
cp	Compressor plenum
e	Turbine exit plane
i	Turbine inlet plane
k	PDC tube index
<i>rel.</i>	Relative value
<i>sp</i>	Species index
s	Static quantity
t	Total quantity
tp	Turbine plenum

turbine blades to work in far off-design conditions and exhibit low efficiencies.

To date, several authors have characterized the interaction of turbine blades with the flow of PGCs. Among experimental studies, Glaser et al. [10] investigated the performance of an array of multiple pulsed detonation combustors connected to an axial turbine. They showed that the efficiency of the PDC-driven turbine is decreased by increasing the combustion tube fill-fractions. Later, the experimental studies of Anand et al. [11] on the same setup but without bypass air focused on the effect of pulsing frequency, fill fraction, and rotor revolution frequency on the extracted power. Qiu et al. [12] performed experimental studies of a turbine connected to two PDC tubes directly that achieved 27% higher specific thrust than that of the traditional Brayton cycle systems. Within the scope of RDC and turbine interaction experimental investigation, Tellefsen [4] performed one of the first RDC-axial turbine tests. He placed convergent outlet sections on the RDC to study the effect of back pressure on its operation. Naples et al. [13] implemented an RDC into a T63 gas turbine and successfully ran the turbine for about 20 min. Their design incorporated an air dilution system to reduce the turbine inlet temperature and the pressure fluctuations. This way, they have proven the feasibility of operating an RDC with an existing turbine as a unit.

While the complex unsteady, high-temperature flow and compact geometry of PGCs present limitations in experimental measurement and visualization, numerical tools can provide deep insight into the PGC flow field. Van Zante et al. [14] performed a three-dimensional CFD simulation of a detonation tube–turbine interaction to evaluate average pressure transmission loss and turbine stage performance. They observed attenuation in pressure fluctuations through an aircraft engine axial turbine stage and reverse flow in the early stages of PDC blow-down. A full turbine stage unsteady CFD simulation was performed by Liu et al. [15] to characterize a supersonic turbine downstream of an RDC. They revealed that the main contributor to the unsteady loss mechanism was the leading edge shock waves. Asli et al. [16] studied the performance of a turbine stationary vanes downstream of an RDC using two-dimensional URANS simulation and showed a velocity angle fluctuation amplitude decay of more than 57% by the vanes.

Although 3D-CFD tools have been proven very useful in PGC-turbine interaction studies, the highly unsteady nature of PGC exhaust flow requires high computational costs, specifically in multistage turbine

configurations. Meanline methods in turbomachinery provide a fast tool for performance evaluation of turbomachines, but are limited to steady state analysis. Therefore, the need for a fast and reliable method for performance evaluation of turbomachinery integrated into a PGC has drawn the authors attention to the 1D-Euler approach. It has been shown to be appropriate for turbomachinery simulation in conventional applications [17–19]. Chiong et al. [20] integrated meanline and one-dimensional methods for prediction of pulsating performance of a turbocharger turbine, where unsteady flow makes 3D simulations time-consuming. Concerning PGC–compressor interaction, recently Dittmar and Stathopoulos [21] used the 1D-Euler method to simulate a multistage compressor connected to a zero-dimensional plenum representing a PDC array. They applied equally distributed blade source terms across the blade rows based on the overall compressor map, which is a very rough estimation of blade force specifically at off-design conditions. This study has been extended and further developed by Neumann et al. [22]. They used a mean line model to provide the source terms for the 1D unsteady Euler solver. At the same time, they coupled the compressor with an array of PDC tubes, which were in turn modelled with a reactive unsteady 1D-Euler code. This way, they managed to study the compressor operation with more realistic boundary conditions and also couple the compressor operation to the inlet boundary conditions of the PDC array. Within the scope of PGC-turbine interaction, the current research focuses on applying and evaluating an unsteady 1D approach to simulate a multistage turbine connected to a PDC by solving Euler equations with source terms. The current work is an extension and adaptation of the work presented from Neumann et al. [22]. To the knowledge of the authors, no such study has been carried out so far. The turbine blade row behavior and the propagation of flow unsteadiness across the turbine rows are studied and compared to the 3D-CFD simulation results. To allow for these simulations, a methodology to calculate PDC outlet conditions is introduced, which can then be used as boundary conditions for both the 3D-CFD and the Euler-based simulations. The objective is to show that the 1D-Euler approach with rather low complexity and computational cost can be used in the early design and optimization of turbine expanders working with PGCs, and here specifically with PDC arrays.

2. Models and methods

The methodology of the current work includes integrating different simulation techniques for the PDC combustors, their connection to each other in an array constellation by using a plenum at their outlet and that for the turbine expander. All methods will be elaborated on in this section.

The pulsed detonation combustors are modelled with the same solver used for the turbine model. For both a solver for the unsteady 1D inviscid Euler equations with appropriate source terms is used. Mass and energy source terms are used in the combustors, while energy and force terms are used to model the blade forces in the turbine model. The meanline method for steady-state turbine performance estimation is utilized to compute source terms for the 1D-Euler equations that represent the blade rows. In parallel, three dimensional steady and unsteady CFD simulations are used to verify and tune the results of the mean line analysis and the 1D-Euler solver. It should be noted that, in the course of this paper, the CFD term is referred to as 3D-CFD.

The flow chart of Fig. 1 shows how these methods are integrated. Firstly, using the geometrical specifications of the turbine, the map of the E³ turbine geometry [23] is computed by both the meanline and 3D-CFD methods. Once the steady-state results are compared and validated against the experimental data, the source terms obtained by the meanline method are added to the 1D turbine model. Steady-state simulations are done using both 3D-CFD and 1D-Euler to check the agreement between the results in this step. Afterward, the PDC model uses the overall steady-state turbine map and provides the time-dependent inlet boundary conditions for unsteady turbine simulations. Finally, the 1D-Euler and 3D-CFD methods both simulate the turbine for the time-dependent operational case with the PDC arrays and the results are compared.

2.1. Test and reference case

The test case for the current work is the high-pressure turbine of the Energy Efficient Engine project reported by NASA [23]. This turbine is selected because it has two stages with available performance test results also between the blade rows, thus making it a vary useful validation and bench-marking test case. A summary of aerodynamic parameters of NASA E³ high-pressure turbine at design point is listed in Table 1.

2.2. 3D-CFD method

The CFD analysis in this paper has been done by solving the unsteady three-dimensional Reynolds Averaged Navier–Stokes (RANS) equations using ANSYS CFX. The computational domain of the turbine is discretized using O and H grid types. The domain including the grids on

Table 1

Design point parameters of NASA E³ high pressure turbine.

Parameter	Value
Reduced mass flow ($\text{kg}\sqrt{\text{K}}/\text{s}/\text{kPa}$)	0.892
Reduced speed ($\text{rpm}/\sqrt{\text{K}}$)	316.9
Energy function ($\text{J}/\text{kg}/\text{K}$)	339.9
Pressure ratio	5.010
Efficiency	0.925

surfaces is shown in Fig. 2. Regarding the scope of the present study and the circumferentially uniform flow at the boundary conditions, a periodic-type interface is applied between the adjacent blade passages. The mixing plane approach is set as the interface between each blade row. This method assumes circumferentially averaged flow features in the outlet plane of the upstream row and uses them as the inlet condition of the downstream row. Since the PDC fluctuations are mainly in the axial direction, the stage mixing plan approach is valid for the present study as it has been applied in similar cases in [15,21]. The mesh refinement close to the walls is done iteratively to keep y^+ below unity and to accurately capture boundary layer effects. To reduce the effect of grid size on the solution results, a mesh sensitivity study is done using four different grid sizes having 122 k, 449 k, 1,132 k, and 2,276 k nodes, named as N_1 to N_4 . Fig. 3 indicates mass flow rate and total temperature ratio for each grid size. The relative error representing the normalized difference between the two consecutive values ($e_{rel.} = (\phi_1 - \phi_2)/\phi_{mean}$) of results shown in the figure for the three finest grids. According to the results for N_3 and N_4 , the relative error of mass flow and total temperature ratio are 0.011% and 0.024% respectively, which are very low. The Grid Convergence Index (GCI) is calculated following the approach presented by Celik et al. [24]. This parameter is an estimation to indicate how much further refinement of the computational grid can affect the results. The GCI values corresponding to N_3 are 0.1% and 0.2% for mass flow and total temperature ratio, respectively, which are low enough for an acceptable mesh size. Therefore, with regard to computational cost and accuracy, the computational domain with 1,132 k nodes is selected for the current numerical study.

The Shear Stress Transport model, which is a two equations eddy viscosity approach, is used for turbulence modeling. The model combines the advantages of the k- ϵ and Wilcox k- ω model. The robustness of this turbulence modelling approach has been already proven for similar flows [25,16]. For the time-dependent solution cases, the equations have been discretized in time with an implicit second-order Euler method. The second-order backward Euler method is applied to provide the transient scheme for turbulence equations.

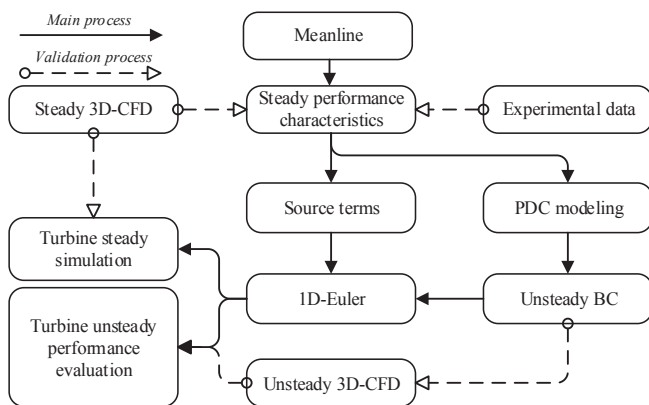


Fig. 1. Overall flow chart of the simulations and the combination of the different tools.

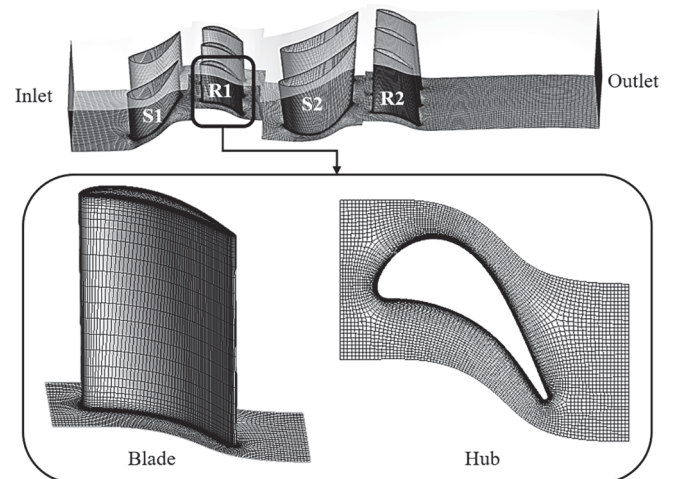


Fig. 2. Turbine geometry model and a zoomed view of the computational grid.

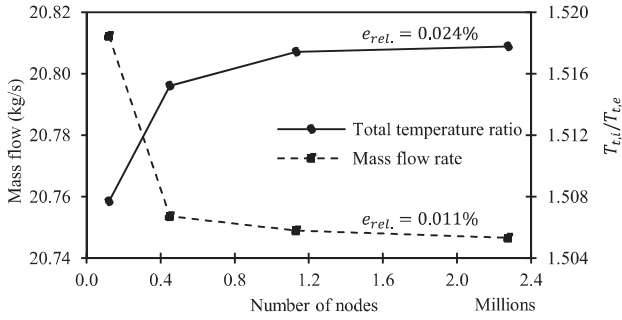


Fig. 3. Effect of computational grid resolution on the computed mass flow rate and total temperature ratio.

Time step in transient solutions is a key parameter to capture the transient flow physics within the domain. A time step dependency analysis has been carried out for the current work using the transient inlet boundary condition caused by three PDC tubes. Considering the rotor blade passing frequencies (≈ 15 kHz) and the PDC flow frequency (≈ 100 Hz), three time step sizes were chosen, which are 500, 1000, and 2000 times smaller than the period of the inlet boundary condition fluctuations. The results of the simulations in terms of overall turbine efficiency are compared in Table 2. The relative change in efficiency decreases by lowering the time step size. The change between the two smaller time steps is deemed a negligible amount (0.02%) regarding the higher computational cost associated with the smallest time step. Therefore, a time step size of $10 \mu s$ is selected for all the transient simulations in the current study. Besides, periodic convergence must be fulfilled as part of a reliable unsteady simulation. Throughout this paper, the periodicity of the results at the domain outlet was monitored based on the method of Clark and Grover [26], which relies on the discrete Fourier transform, cross correlation and Parseval's theorem. Once the overall convergence level (overall fuzzy set) for two consecutive cycles reaches a value greater or equal to 0.95, the transient solution is considered periodically converged.

2.3. Meanline method

Meanline method in turbomachinery is a well-known, simple, and reliable methodology for steady-state performance prediction, which remains popular today [27–29]. This method solves velocity triangles for every blade row on a reference radius of the machine and takes advantage of empirical correlations to account for energy loss in both design and off-design conditions. A schematic of velocity triangle and force vectors on a rotor blade is shown in Fig. 4(a).

A meanline program has been coded for the current study, which includes the loss correlations from open literature most of which are reported and developed by Aungier [30]. The input matrix to the program contains the blades' geometrical parameters such as blade angle at leading and trailing edges, chord lengths, annulus radius, and rotational speed as well as total pressure and total temperature at the turbine inlet and static pressure at the outlet as the boundary conditions. The program starts with a pressure distribution guess through the machine and calculates the flow properties at each trailing edge in an entropy loop for each blade row. Once all the flow properties are computed, mass flow convergence is checked and the program continues by imposing a new

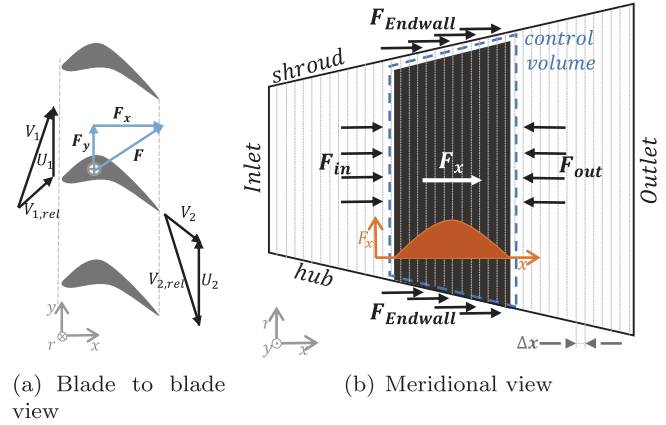


Fig. 4. View of a sample turbine rotor blade, (a): velocity triangle and blade force used in the meanline method (b): force source terms and control volume used in the 1D-Euler solver.

pressure distribution using the target pressure method proposed by Denton [31] to reach a satisfactory convergence. Denton's method adjusts the pressure at each trailing edge based on the change in mass flow at one trailing edge downstream. Additionally, the Came's target pressure approach [32] is included where the Denton's method fails.

The results of the meanline program are used to compute the force and energy source terms representing every blade row in the 1D-Euler program for unsteady simulation. Therefore, it is very crucial that the code is able to accurately predict the flow features at inter-stages. The validity of the meanline program will be discussed in Section 3.1.

2.4. 1D-Euler model

In general, the physics of the problem specify the required number of dimensions in its mathematical model. The nature of flow in turbomachinery shows that even one-dimensional modeling along the machine axis can provide a satisfactory model as the dominant flow phenomena occur in the axial direction. The time-dependent one-dimensional Euler solver utilized in the current work, for both the PDC model and the 1D turbine model, has been developed firstly for the purpose of shockless explosion combustion simulations [33]. It uses a finite volume scheme with a second-order monotonic upstream-centered scheme for conservation laws. The governing equations include the mass, momentum, and energy conversion equations, with source terms adjusted to meet the purpose of the corresponding component to be simulated.

2.4.1. 1D turbine model

To allow for the simulation of time-resolved turbomachinery applications, the original code was extended in the work of Dittmar and Stathopoulos [21] and in that of Neumann et al. [22]. Within the course of the current research, this approach is further extended so that the calculation of the source terms representing the turbomachinery is now provided by the meanline method also for the turbine. The resulting governing equations are described in Eq. 1, where Q is the matrix of source terms.

$$\frac{\partial B}{\partial t} + \frac{\partial G}{\partial x} = \frac{\partial Q}{\partial x} \tag{1}$$

$$B = \begin{bmatrix} \rho A \\ \rho V_x A \\ \rho E A \end{bmatrix}, \quad G = \begin{bmatrix} \rho V_x^2 A \\ \rho V_x^2 A + P A \\ \rho V_x A (\rho E + P) \end{bmatrix}$$

$$Q = \begin{bmatrix} \dot{m}_b \\ F_x + P A \\ W + \dot{m}_b h_{t,b} \end{bmatrix}$$

Table 2 Effect of time step size on turbine efficiency.

Time step (s)	2×10^{-5}	1×10^{-5}	5×10^{-6}
Efficiency	88.9	89.5	89.48
Relative change (%)	-	0.67	0.02
Pressure Ratio	5.110	5.132	5.133
Relative change (%)	-	0.43	0.03

The source term to close the mass continuity equation is the bleed mass flow, which is assumed to be zero to simplify the simulations in this paper. Blade force and wall force represent the presence of blades and the force due to any change in cross-sectional area, respectively. Fig. 4 (b) shows the control volume and the force balance on it in a meridional view. According to the second law of motion, the net force acting on the control volume including the blade is equal to the momentum difference between the inflow and outflow. Therefore, the blade force can be computed as shown in Eq. 2. The last three terms in Eq. 2 are calculated based on the information from the meanline program. The endwall force is calculated within the 1D-Euler solver since it is included in the governing equations. The source terms in the energy equation are the shaft work by rotor blades and the enthalpy change due to the bleed (when applicable). The shaft work is calculated by the meanline data based on the first law of thermodynamics as described in Eq. 3, noting that the blade row is assumed adiabatic and no heat is exchanged.

$$F_x = -F_{Endwalls} + F_{in} - F_{out} - \Delta(\dot{m}V_x) \quad (2)$$

where:

$$F_{in} = P_{in}A_{in} \quad \text{and} \quad F_{out} = P_{out}A_{out}$$

$$W = (\dot{m}h_t)_{out} - (\dot{m}h_t)_{in} \quad (3)$$

All source term related data for a range of steady-state operating points obtained by the meanline program is stored in a table. The 1D-Euler solver uses this table to extract the related force or work terms for each station in each iteration. Since the stored data is for discrete operating points of the turbine, the code has to interpolate the related source terms based on the calculated pressure at leading and trailing edge of the corresponding blade. To help the solution stability, the source term values are distributed based on an upside-down parabola function with the highest point at the blade axial center, which is shown in 4(b) graphically. The boundary conditions to the solver include total pressure and total temperature at the inlet and static pressure at the outlet. The computational domain is divided into 800 cells with a spatial resolution of $\Delta x = 0.5 \text{ mm}$. The initial condition from which the transient simulation starts is provided by average values from the meanline result. The geometry is defined to the solver by specifying the axial coordinates of the inlet and the outlet of the domain, stator, and rotor blades as well as the annulus area at each axial location.

2.4.2. Pressure gain combustion model

To ensure that the boundary conditions for the 1D and 3D turbine simulations reflect conditions that can be expected from PGC combustion as accurately as possible, a multitube PDC configuration was compiled. It combines several 1D PDC tubes with a zero-dimensional

turbine plenum volume and a turbine model based on an interpolated turbine performance map. The complete numerical setup can be seen in Fig. 5. The goal was to derive a time-dependent turbine plenum state that could be prescribed as a boundary condition in the two turbine models. Conceptually, this is an extension of the work done in [34], where in this case sinusoidal pressure fluctuations are replaced by a pressure evolution directly tied to each PDC tube. The approach is of course only a first approximation of the phenomena taking place within such a plenum that connects a PDC array and a turbine, but it can still capture the basic unsteadiness expected from such a setup.

Each detonation tube is represented by a one-dimensional domain that undergoes the typical PDC cycle schematically depicted in Fig. 6. Every cycle starts with the ignition of the tube that is completely filled with a stoichiometric H_2 -air mixture at the upstream end at ①. This

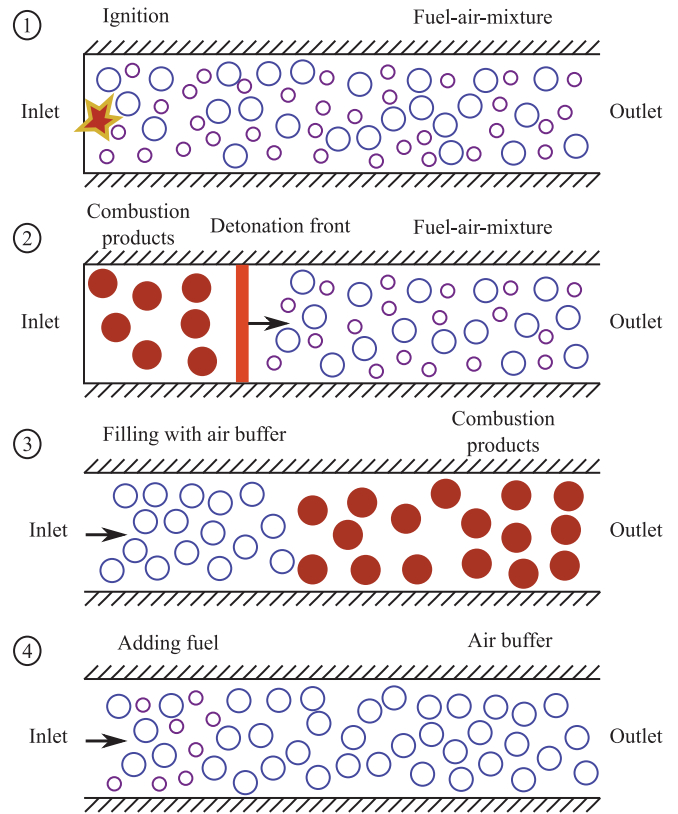


Fig. 6. Single operating cycle of PDC tube.

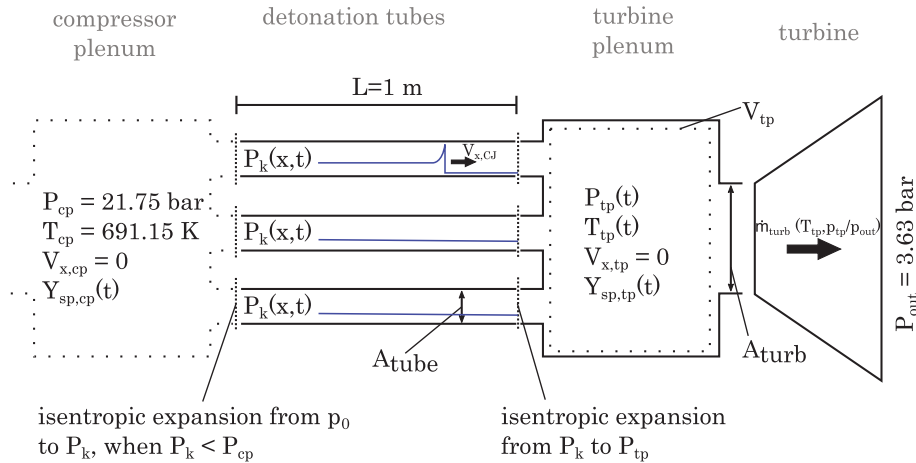


Fig. 5. Multitube PDC model to obtain unsteady boundary condition.

ignition event is triggered by the insertion of a precomputed detonation profile based on classic ZND theory [35–37] at the upstream end of the tube. The resulting detonation wave then proceeds to propagate downstream with CJ velocity in ②, consuming all remaining fuel and oxygen to form the combustion products (primarily N_2 and H_2O) at high temperature and pressure. With the outlet pressure far below the pressure of the combustion products, expansion waves reflect back and forth through the domain as soon as the detonation wave has reached the outlet. Eventually, they reduce pressure far enough for it to fall below the upstream pressure and trigger the inlet to open in ③. First, an air buffer is introduced to separate hot products from fresh mixture. After purging of the combustion products, H_2 is added to the gas inflow in ④ to refill the tube and restart the cycle.

The number of tubes in the numerical setup can be varied. They all have a length of $L = 1m$ and are ignited sequentially with an individual operating frequency of 20Hz for each tube. The model assumes all PDC tubes to be fed by a common compressor plenum upstream, of which static pressure P_{cp} and static temperature T_{cp} are assumed constant and the flow velocity in it is assumed to be zero. T_{cp} and P_{cp} have been found to be the average values in the compressor plenum of a preliminary simulation that combined the compressor map provided in [38] with several detonation tubes. Air inflow from the compressor plenum to each of the PDC tubes is implemented as a one-way valve which remains closed for $P_k > P_{cp}$ and isentropically expands gas to downstream conditions in the k^{th} tube when $P_{cp} > P_k$. The chemical composition Y_{sp} of the inflowing gas is time-dependent for each tube and consists of pure air for the majority of each cycle and a stoichiometric H_2 –air mixture during fill time ($t_{fill} = 10ms$).

Within each tube, the same 1D-Euler solver as for the 1D turbine model is used. However, balance equations and source term are modified and listed in Eq. 4.

$$\frac{\partial B^*}{\partial t} + \frac{\partial G^*}{\partial x} = Q^* \quad (4)$$

$$B^* = \begin{bmatrix} \rho \\ \rho V_x \\ \rho E \\ \rho Y_{sp} \end{bmatrix}, G^* = \begin{bmatrix} \rho V_x \\ \rho V_x^2 + P \\ \rho V_x(\rho E + P) \\ \rho V_x Y_{sp} \end{bmatrix}$$

$$Q^* = \begin{bmatrix} 0 \\ 0 \\ 0 \\ \rho \dot{Y}_{sp,chem} \end{bmatrix}$$

Because each tube has a constant cross section area, A can be removed from the balancing equations. However, chemical composition is now changing in space and time. For this reason, additional balancing equations for each species mass fraction Y_{sp} are required and the Euler flow solver is coupled to a chemical kinetics solver via Strong splitting. Changes in composition as a result from chemical reactions $\dot{Y}_{sp,chem}$ are the only remaining source term, with the underlying reaction equations provided by the multi-step H_2 –air mechanism published by Burke et al. [39].

At their outlets, all tubes are connected to a common plenum, represented by a zero-dimensional volume of fixed size $V_p = 0.1m^3$. Boundary conditions at all tubes provide isentropic expansion of momentary tube pressure to momentary plenum pressure, while the specific axial kinetic energy is maintained. The resulting mass flow from the tubes into the plenum is taken as a mass and energy source term in the plenum's balancing equations. Since it is zero-dimensional, only mass, energy and species fractions are considered here, while velocity is assumed to be always negligible.

The outflow from the plenum is calculated based on interpolated experimental data from the same two-stage turbine as in the turbine models (see above) [23]. With an assumed constant turbine speed, the

mass flow at the turbine inlet is a function of the plenum's temperature and the pressure ratio between plenum pressure and constant outlet pressure $P_{out} = 3.63bar$. The latter value was chosen to allow for average pressure ratios across the turbine that are close to its design point.

In addition to the plenum volume, the ratio between detonation tube cross section area A_{tube} and turbine inlet A_{turb} is another important parameter that defines the extent of pressure and temperature fluctuations in the plenum. To ensure comparability between configurations with a varying number of tubes, this ratio is fixed to

$$\frac{A_{tube} \cdot n_{tubes}}{A_{turb}} = 1 \quad (5)$$

in all simulations, with n_{tubes} being the number of PDC tubes. This is roughly equivalent to enforcing the same average mass flow through the plenum and turbine model, regardless of n_{tubes} . Roughly only, because this neglects the additional mass coming from the fuel/combustion products, which is increased for a larger number of tubes and thus more ignitions during the same time interval. However, for the chosen operating frequency and tube length, this contribution is minuscule.

With fluctuating inflow of varying composition from the tubes and outflow to the turbine that depends on the current plenum state, pressure and temperature inside the plenum are subject to periodic change. The results of these simulations are discussed in Section 3.2.1 and then used as boundary conditions for the calculations discussed in the remainder of Section 3.2 and 3.3.

3. Results and discussion

In this section, the simulation tools are validated by comparing their results against experimental data. This is done only for steady-state operation, since only steady-state experimental results are available. Once this validation is carried out, the time-dependent boundary conditions produced by the PDC model will be elaborated. Subsequently, the turbine unsteady simulation results for the case with three PDC tubes will be presented. This section concludes with the presentation of turbine simulations using two alternative PDC configurations with five and seven tube with the aim to further evaluate the 1D-Euler method.

3.1. Model Validation

The turbine overall characteristic in terms of pressure ratio and efficiency is calculated using the meanline and 3D-CFD tools for the test case in question. Based on the available experimental data [23], the steady-state map is computed for three different total to static pressure ratios of 4, 5.5 and 7 spanning around the design reduced rotational speed point (see Table 1). The results of the steady-state calculations are depicted in Fig. 7, noting that the isentropic efficiency curve is plotted only for total to static pressure ratio at the design point to avoid the complexity of the presentation. The results reveal that both the CFD and meanline method can accurately capture the steady-state performance of the two-stage turbine. A very small deviation between the results of the two computational methods and those of experiments is observable when moving away from the design point. This deviation takes its largest value at high speeds, which is nevertheless lower than 1% in pressure ratio and thus almost negligible. It is thus concluded that the meanline method is accurate enough to calculate the blade source terms for the 1D-Euler code.

In order to evaluate the validity of the 1D-Euler simulation, inter-stage thermodynamic properties of static pressure, static temperature, and total temperature throughout the turbine axis are calculated using the 1D-Euler, meanline, and 3D-CFD methods, depicted in Fig. 8. It should be noted that the meridional sketch of the turbine in some figures in this paper is only for additional clarification of blade locations along the axial direction and does not represent the real shape of the blade. The CFD results are extracted at a plane between the blade rows and

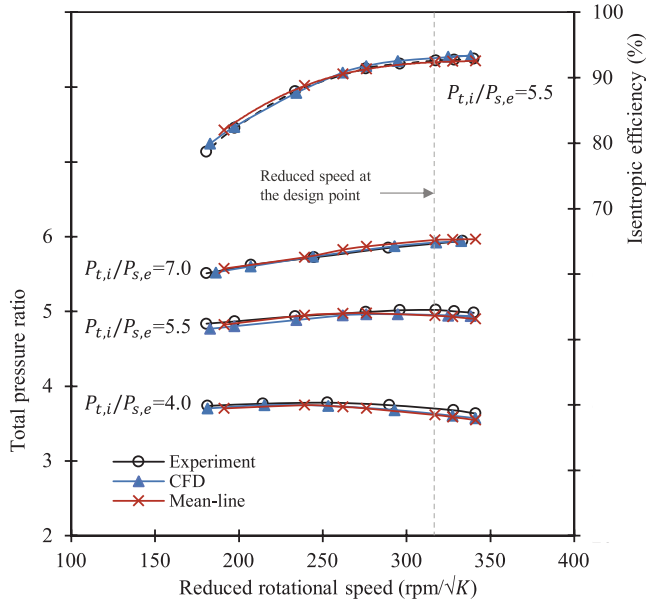


Fig. 7. Turbine steady state performance characteristics, meanline, 3D-CFD and experiment [23].

mass averaged values over the surface are reported. The meanline results are computed exactly at the blade leading and trailing edges, and the 1D-Euler results are calculated throughout the turbine axial direction in each computational cell. The simulations were done at the turbine design point using the related fixed inlet total pressure and total temperature and outlet static pressure. The interstage static pressure distribution shows a very good match between the results, asserting that the 1D-Euler method can capture the static pressure through the machine very well. The total temperature distribution is also consistent between the three methods. Therefore, it can be concluded that the 1D-Euler code can effectively use the source terms from the meanline method to simulate the turbine operation. Also the interstage static temperature values are in agreement at stator inlets while there is a level of deviation at rotor inlets between the 1D-Euler and the two other methods. This mismatch can be explained by the nature of the 1D method. In CFD and meanline method, the axial velocity is used for mass calculation and the absolute velocity for kinetic energy. Since the only velocity component in the 1D method is axial velocity, both mass flow and kinetic energy calculations are done using the axial velocity. Therefore, wherever swirl is imparted by the vane and axial the velocity value deviates from that of the absolute velocity, there is a deviation in the kinetic energy calculation. In other words, the higher the tangential velocity, the lower the kinetic energy calculated in the 1D-Euler method compared to the CFD and meanline methods. Generally, in axial turbines, some level of swirl is added to the velocity by the stator rows, so that the tangential velocity increases. For more clarification, the velocity vectors around the second stator obtained by CFD are depicted within the Fig. 8. It shows that the absolute velocity deviates from the axial direction at the stator exit, while it is mainly axial at the stator's inlet. For the stator rows, the only source term representing the blade is the force term, which includes axial velocity. As a result, the kinetic energy at the stator exit calculated from the 1D-Euler tool is lower than the actual value. Consequently, a higher static temperature value is computed in this tool compared to the results of the computed by CFD and meanline methods. Additionally, when the flow passes through the rotor blades, the extracted work reduces the swirl velocity and makes the flow axial at the rotor outlet. This occurs in reality, which is captured well in CFD and meanline, but in 1D-Euler simulation it is the axial velocity that is reduced. Therefore, the deviation in velocity at the stator outlet is compensated at the rotor outlet, which is obvious from a good

agreement between the 1D-Euler, CFD, and meanline results of static temperature.

3.2. Unsteady turbine simulation

In this section, the unsteady simulation of the two-stage turbine connected to a plenum that is operated by a PDC configuration is elaborated. The PDC configuration includes three tubes, which produce a relatively high amplitude of fluctuations. The PDC model and the related boundary condition of the turbine will be explained hereafter. A back-to-back comparison of CFD and 1D-Euler unsteady simulation results will be done to evaluate the applicability of the latter method in unsteady simulation of the turbine.

3.2.1. Boundary condition for the time dependent turbine simulations

The resulting turbine plenum pressure for three variants of the multitube PDC configuration introduced in Section 2.4.2 can be seen in Fig. 9(a). After a short transient starting phase, a periodic pattern emerges for all three tube numbers. With each individual tube's operating frequency fixed at 20Hz, the repetition frequency of this pattern is equal to $n_{\text{tubes}} \cdot 20\text{Hz}$. Table 3 lists the average, maximum and minimum pressure observed for each of the configurations. It also calculates the relative pressure fluctuation amplitude defined in Eq. 6.

$$A_p = \frac{P_{\max} - P_{\min}}{\frac{2}{\tau} \int_{t_0}^{t_0+\tau} P_{tp} dt} \quad (6)$$

An increase in the number of PDC tubes significantly reduces the fluctuation amplitude inside the turbine plenum due to the fact that each tube's relative contribution to the overall mass flow is reduced, ensured by the condition set in Eq. 5. This also explains why the effect is far more pronounced for an increase from three to five tubes than it is from five tubes to seven. The mean pressure inside the plenum remains mostly constant for all three configurations, because it is primarily a result of the average mass flow, which also remains constant (except for the amount of fuel, as pointed out before).

For a closer analysis of the fluctuation pattern inside the plenum, Fig. 9(b) shows pressure and temperature evolution during a single 60Hz cycle of the configuration with three PDC tubes. The dashed lines connect this pattern to states inside the PDC tubes at the same moment, which were depicted in Fig. 6. The last ignition inside one of the tubes took place at ①. It is only after the detonation wave has completed its propagation through the tube (②) and reaches the plenum inlet, that a steep increase in plenum pressure and temperature is visible. While the pressure increase is halted after a few ms due to increased outflow towards the turbine and the propagation of expansion waves upstream into the PDC tube, temperature remains high for about two thirds of the overall cycle, even though purge air begins to flow into the inlet of the PDC tube already at ③. The reason for this seeming phase shift between pressure and temperature lies in the vast difference in their characteristic velocities: The local speed of sound inside the combustion products is very high due to their extreme temperature, allowing pressure waves to travel fast and quickly mitigate fluctuations and even causing temporary overexpansion that results in a slow increase of pressure during the latest third of the cycle. At the same time, also due to the inviscid nature of the numerical model, temperature perturbations only travel at the local flow velocity, which is much smaller. Thus, the decrease in plenum temperature coincides with the arrival of the contact surface between combustion products and purge air at the plenum inlet.

Both turbine plenum pressure and temperature obtained by this method for a configuration with three PDC tubes are used as inlet boundary conditions for the 1D and 3D simulations discussed in the following sections. The results for five and seven tubes are used in the comparison presented in Section 3.3. Here it is noted that the physical rotational speed (12630 rpm) and the static pressure at the domain outlet (3.63 bar) are kept constant in the unsteady turbine simulations.

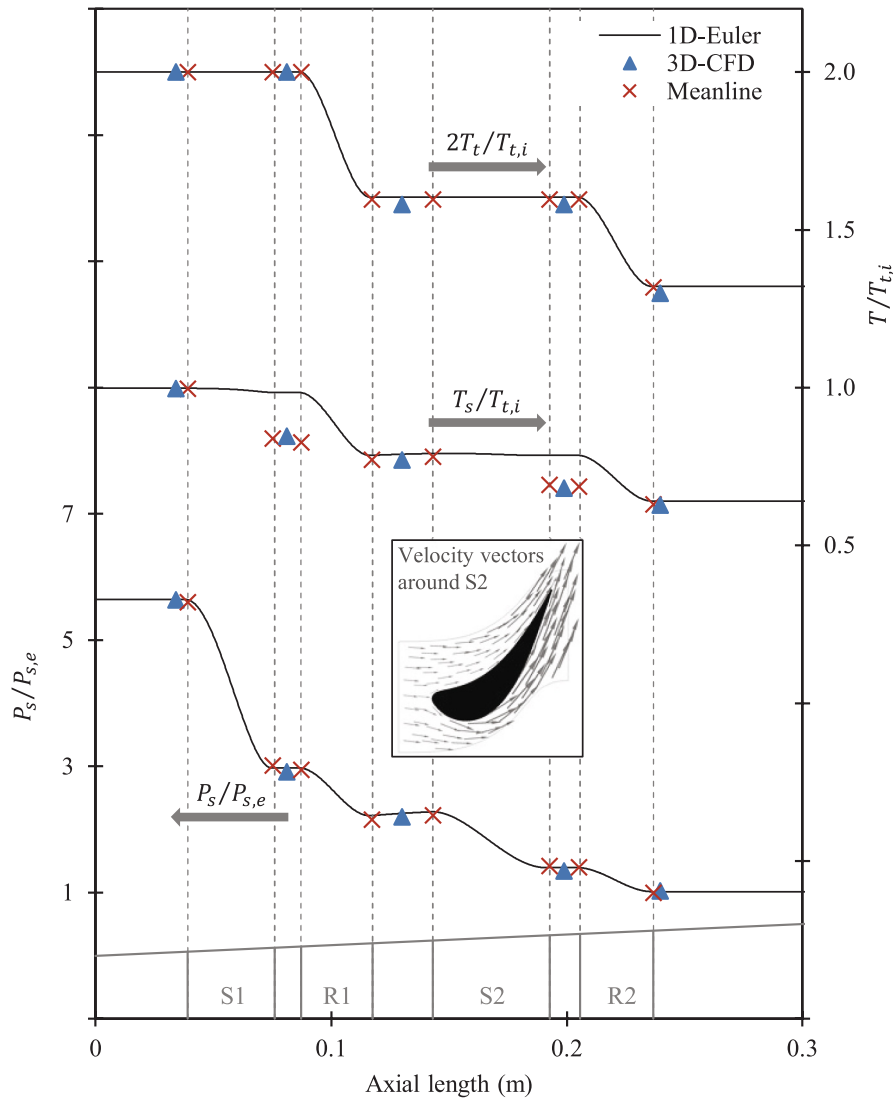


Fig. 8. Streamwise distribution of thermodynamic parameters at the design point.

Different lengths of outlet domain were modeled and the results of the unsteady simulations showed that the turbine completely damps the inlet pressure fluctuation. Therefore, in this paper, the constant outlet pressure boundary is reasonable in the unsteady simulations.

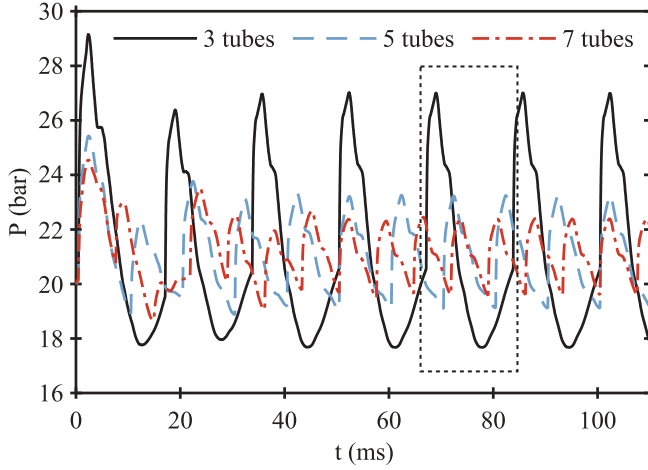
3.2.2. Pressure damping

The fluctuating flow coming from the PDC tubes causes the turbine blades to work under off-design conditions, since the inlet velocity and the incidence angle are continuously deviating from their design values. The pressure fluctuation is expected to be damped throughout the turbine stages, with the damping level of each blade row being different. This causes the turbine rows to operate in different off-design ranges. The pressure distributions between the stages, obtained by the 1D-Euler and CFD methods, are shown in Fig. 10 in the form of normalized pressure ($\bar{P}_s = P_s / \text{mean}(P_{s,i})$) for a cycle time period. The CFD results are mass-averaged values. The planes of measurement are located exactly between the blade rows, except for the first stator inlet and the last rotor outlet, which are located exactly adjacent to the blade row leading and trailing edge, respectively. According to the results, the trend of pressure distribution is almost identically computed using both methods. Additionally, the pressure upstream of the stators is predicted similarly by both methods as well. Nevertheless, the 1D-Euler computed the pressure at stator outlets lower than CFD, which is traceable from a downshift in

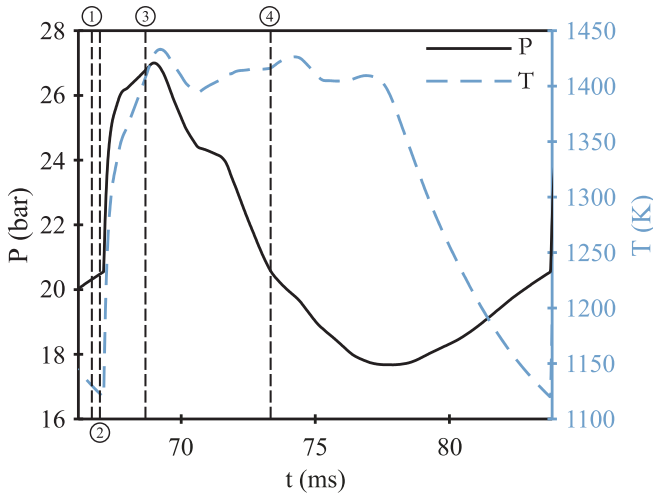
both Fig. 10(c) and Fig. 10(e). The difference is related to the flow direction at these two locations. The stators deflect the axial incoming flow to increase tangential momentum for the downstream rotors. Therefore, the absolute velocity magnitude is deviating from the axial velocity, while the latter is the only velocity component used in the 1D-Euler approach. Having a detailed look at the peak pressure location from upstream to downstream of the turbine, a small phase shift is observable. This is related to the axial distance and the local speed of sound because the prescribed pressure fluctuation propagates at the speed of sound. It is reminded that this in turn is related to the local temperature, which itself is advected by the flow velocity.

To evaluate the pressure fluctuation damping throughout the turbine, the relative static pressure amplitude defined in Eq. 6 is calculated and depicted in Fig. 11.

Starting from the domain inlet up to the first stator leading edge, both the 1D-Euler and CFD methods computed the static pressure amplitude identically, which is evident from Fig. 10(a) and Fig. 10(b) as well. Considering the boundary condition applied to the domain inlet in the form of total pressure in both methods, it implies that the kinetic energy is calculated the same at this point. After passing the first stator, a slightly higher relative pressure amplitude is calculated by CFD, with a difference of less than 0.5%. Moving further downstream shows a good match in relative pressure amplitude at the first rotor and the second



(a) Turbine plenum pressure for varying number of PDC tubes, marked area depicted enlarged in Fig.9(b) for three tubes



(b) Turbine plenum and temperature during a single fluctuation cycle for three PDC tubes, dashed lines mark tube states depicted in Fig.6

Fig. 9. Time-resolved turbine plenum state.

Table 3
Turbine plenum pressure fluctuations.

n_{tubes}	P_{mean} (bar)	P_{max} (bar)	P_{min} (bar)	\bar{A}_p (%)
3	21.67	27.00	17.68	21.5
5	21.33	23.25	19.13	9.7
7	21.20	22.45	19.61	6.7

stator outlet. A very small discrepancy between the values computed by CFD compared to those of 1D-Euler downstream of the second rotor blade row can be seen. This difference may be explained by the damping role of endwall viscous effects. The static pressure at the domain outlet is fixed in both methods as the outlet boundary condition. Since the 1D-Euler does not take into account the end wall viscous effects in between blade rows, the CFD calculation shows slightly more damping from the second rotor outlet to the domain outlet, where the static pressure has no fluctuation.

Regarding the damping of the pressure fluctuations, it is evident that the share of the first stator in damping is much higher than the other

rows. The first stator damps 45.5% of the high-amplitude pressure fluctuation imposed at the domain inlet. This is consistent with the work of Bakhtiari et al. [34] that shows a 47% damping by the first row. It is noted that they prescribed a sinusoidal pressure fluctuation with an amplitude of 5% at the domain inlet, which is much lower than in the present study. The rest of the fluctuation amplitude is attenuated by the other rows.

3.2.3. Efficiency

Isentropic efficiency is defined as the actual work output from the turbine divided by the work output if the turbine with the same pressure ratio undergoes an isentropic process as in Eq. 7. In steady-state operation, both terms can be simply calculated. In unsteady cases, where the turbine is subject to unsteady periodic inlet flow, the calculation of the isentropic efficiency is not straightforward through the well-known expression in Eq. 8. In this case, the instantaneous inlet and outlet conditions cannot be used in efficiency calculation since the mass and energy fluxes are not conserved.

$$\eta_{\text{isentropic}} = \frac{\Delta H_{\text{actual}}}{\Delta H_{\text{ideal}}} \quad (7)$$

$$\eta_{\text{isentropic}} = \frac{1 - T_{t,e}/T_{t,i}}{\left[1 - \left(\frac{P_{t,e}}{P_{t,i}}\right)^{(\gamma-1)/\gamma}\right]} \quad (8)$$

The current work utilizes for efficiency calculations the definition proposed by Suresh et al. [40] for a turbine downstream a pulse detonation combustor. Taking into account that mass and energy fluxes are conserved within a time period of unsteadiness, the actual turbine work will be as Eq. 9.

$$\Delta H_{\text{actual}} = c_p \int_0^{\tau} (\rho_i V_{x,i} A_i T_{t,i} - \rho_e V_{x,e} A_e T_{t,e}) dt \quad (9)$$

To calculate the ideal work output, the "theoretical isentropic" turbine is considered to work between the same inlet and outlet boundary conditions of the actual turbine. Hence, a flow particle entering the turbine at t_1 with all thermodynamic quantities related to t_1 exits at t_2 having the related time-dependent quantities. If it is assumed that the expansion process in the turbine is sufficiently fast, so that the difference between t_1 and t_2 is negligible, the ideal extracted work can be calculated by Eq. 10. This assumption has been discussed in detail by Suresh et al. [40].

$$\Delta H_{\text{ideal}} = c_p \int_0^{\tau} \rho_i V_{x,i} A_i T_{t,i} \left[1 - \left(\frac{P_{t,e}}{P_{t,i}}\right)^{(\gamma-1)/\gamma}\right] dt \quad (10)$$

Using Eq. 9 and 10, the isentropic efficiency in unsteady turbine operation can be calculated through Eq. 7. Since in this approach, the time traces in both actual and ideal work calculations are fixed, it is more realistic than the time-averaged efficiency, which uses the averaged flow quantities at inlet and outlet in Eq. 8. The isentropic efficiencies calculated based on the 1D-Euler and CFD simulation results are outlined in Table 4. The steady-state efficiency reported here is out of the 3D-CFD turbine simulation while the boundary conditions are imposed equal to the mean value of the transient boundary conditions.

According to the CFD calculated value, a decrease of 2.9% in efficiency is seen by moving from steady-state operation to the transient turbine operation. The efficiency deviation between the 1D-Euler and the 3D-CFD simulations is 1.4 percentage points. To inquire into this difference, time-dependent total pressure and total temperature at the outlet are plotted in Fig. 12. Here, it is to be remembered that the CFD results are mass-averaged values. Fig. 12(a) shows that the 1D-Euler solver predicted the total pressure at the domain outlet relatively similar to its CFD counterpart within the second half of the time period, while the overall trend is identical. The maximum relative difference, which lies within the first half of the time period, is 1.7%. The other

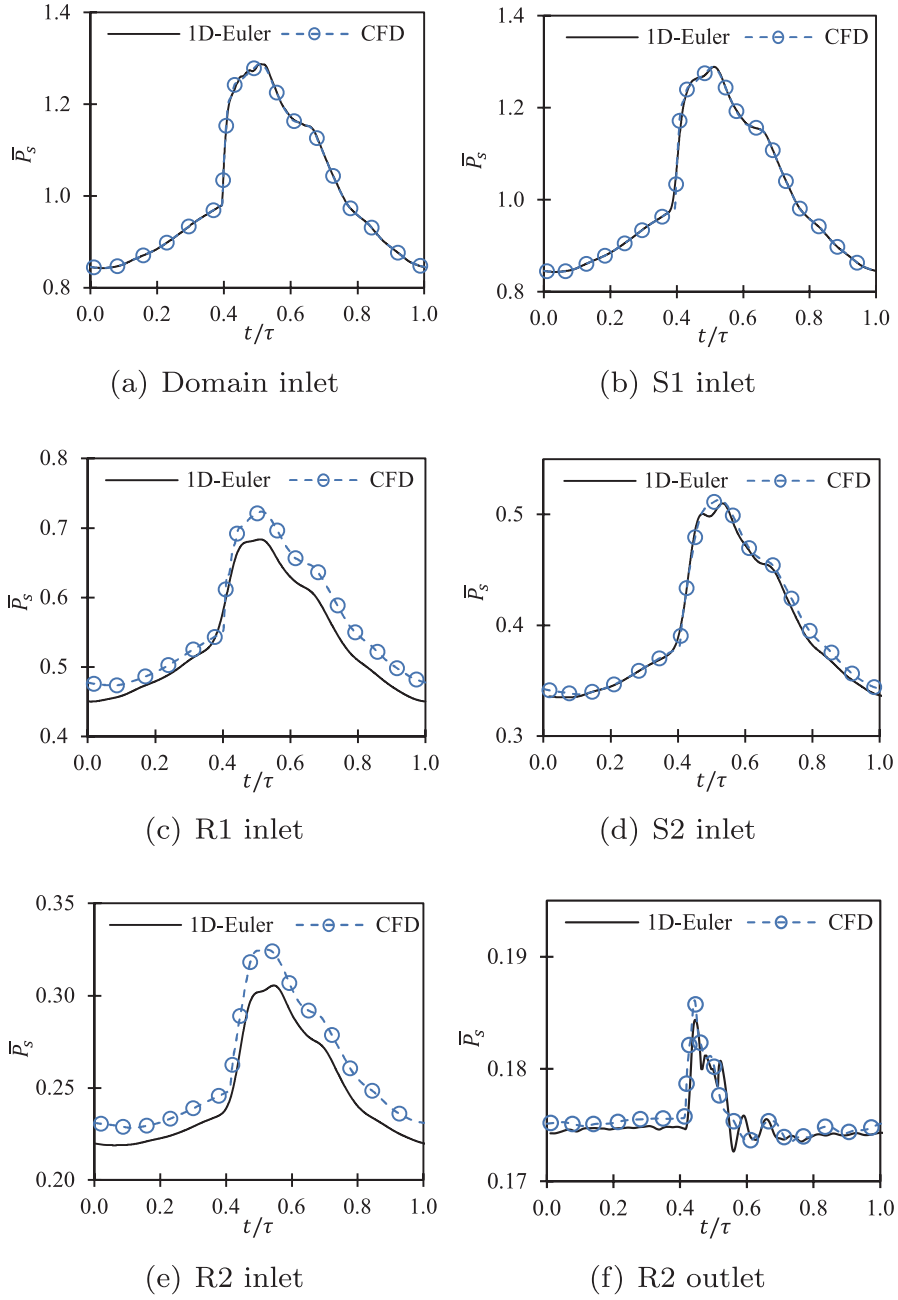


Fig. 10. Static pressure distribution over an inlet fluctuation time period at interstage locations.

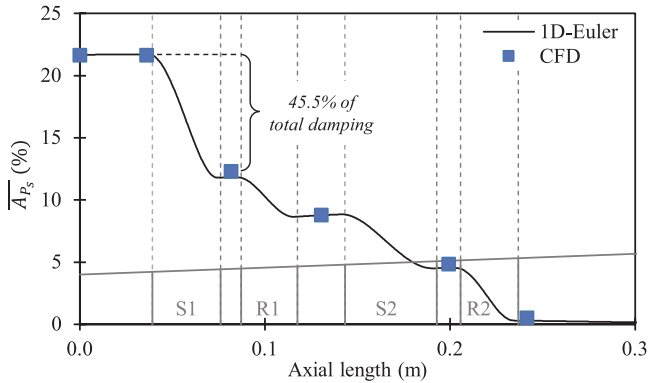


Fig. 11. Static pressure damping throughout the turbine.

Table 4

Isentropic efficiency of the turbine working with three PDC tubes.

	3D-CFD	1D-Euler	Steady-state
Efficiency (%)	89.5	88.1	92.4

cause for the efficiency difference between the two methods is related to the total temperature prediction. According to Fig. 12(b), the 1D-Euler simulation results in a higher total temperature at the turbine outlet with an instantaneous maximum relative difference of 4.1%. This difference indicates that the work extracted from the turbine as computed by the 1D-Euler is lower than the actual value, which is related to the work source term for rotor blades. Since the source terms are looked up from the meanline-derived values based on static pressure upstream of the blades, the discrepancy already reported in static pressure upstream of

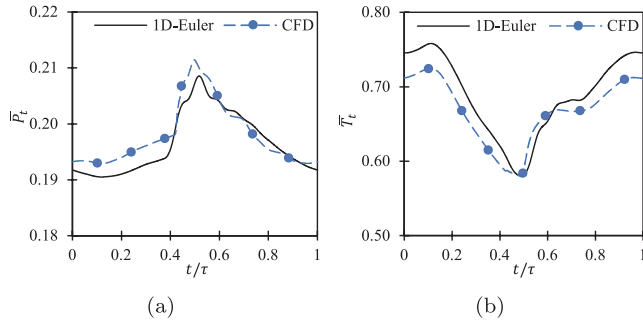


Fig. 12. Normalized total pressure (a) and total temperature (b) at the turbine outlet over a time period.

the rotor blades may cause the solver to read a lower work value from the source terms table. Again, both methodologies can capture a similar trend in total temperature very well.

3.2.4. Performance characteristics

The turbine operating map is usually represented by a function of its pressure ratio and reduced mass flow. This function is a single curve for each rotational speed and includes several possible steady-state operating points of the turbine. In the case of periodic unsteady inflow, the turbine operating condition is no longer a single curve on the characteristic map but illustrated by closed loops of points. The shape and size of the characteristic loops depend on the shape, amplitude, and frequency of the pulsed inflow [41]. The characteristic hysteresis loops computed by both 3D-CFD and 1D-Euler methods are shown in Fig. 13 (a), in which the steady-state characteristic line is plotted by a dashed line for reference. Since the inlet total temperature is time-dependent and the physical rotational speed is constant, the reduced speed (rpm/\sqrt{K}) is a function of time too. The steady characteristic curves for different reduced speeds lie on top of each other and create a single

constant reduced mass flow line because the range of operation is within the choked flow condition. To explain the unsteady behavior of the turbine, the unsteady map can be traced back to the local gradient of inlet pulsed flow quantities. According to the inflow pulse shown in Fig. 13(b), from point *a* to *b*, where inlet total pressure is building up but the total temperature is decreasing rather smoothly, the reduced mass flow is kept constant, identically predicted by both methods. From *b* to *c*, a sharp increase in both total pressure and total temperature causes the instant pressure ratio and reduced mass flow to increase rapidly, up to the maximum reduced mass flow. From *c* to *d*, the pressure ratio keeps its increasing trend and reaches a maximum value at point *d*, which is before maximum inlet total pressure, where the steep slope ends. Afterward, from *d* to *a*, the pressure ratio decreases while maintaining an almost constant reduced mass flow. In this region, there are some small loops in the unsteady map mainly because of the inlet total temperature that has some small perturbations.

The unsteady hysteresis loops obtained by both methods have the same shape and the reduced mass flow range is identically predicted. The only difference is related to the instant pressure ratio and reduced mass flow within the filling zone between point *b* and *d*, where a very sharp increase in inlet total quantities is imposed by the boundary conditions. To put it another way, generally, the information from the inlet boundary in the form of pressure and temperature is transferred to the outlet with the speed of sound and flow speed, respectively. Hence, even small differences in temperature or velocity between both methods result in a phase shift in terms of the instantaneous total pressure at the domain outlet and subsequently the pressure ratio predicted by each method. This phase shift comes into view when the instantaneous pressure ratio is plotted over the reduced mass flow rate, which is calculated based on the information at the domain inlet. Since the mass flow is not conserved at every instant, the present little difference in instant pressure ratio in the unsteady map is plausible. Furthermore, the non-symmetrical shape of the hysteresis loop around the steady-state characteristic line is explained by the shape of inlet flow fluctuation, which is not a smooth and symmetrical pulse. In this regard, the hysteresis loop deviates considerably from the steady-state line within the region of high-gradient in inlet flow properties. In this region, the change in pressure over time is not slow enough to create a balanced state between the pressure ratio and mass flow rate. Obviously, the hysteresis gets closer when the gradient in inlet flow is moderate. It is expected in a smoother shape of inlet flow fluctuation, the hysteresis loop encapsulates the steady map curve rather symmetrically, as observed in Ref. [17] for a mixed flow turbine.

3.3. Results for different PDC configurations

The applicability of the methodology for turbine simulation under pulse detonation combustion flow is further evaluated by changing the number of PDC-tubes in the combustor configuration. In this section, the simulation results for the PDC-turbine configurations with five and seven tubes will be presented. Compared to the three-tube configuration, the two new configurations provide unsteady turbine inlet flows with higher frequencies ($f_{5tubes} = 100\text{Hz}$, $f_{7tubes} = 140\text{Hz}$) and lower amplitudes ($\overline{A}_{P_s,5tubes} = 9.7\%$, $\overline{A}_{P_s,7tubes} = 6.7\%$). Therefore, it is expected that the turbine performance is less affected by the unsteadiness. For this reason, instead of repeating all the results previously presented for the three-tube configuration, this section only focuses on the efficiency and pressure damping characteristics.

Table 5 outlines the time-resolved efficiency of the turbine for both configurations obtained by CFD and 1D-Euler methods. It is observed that by increasing the number of PDC tubes and consequently lowering fluctuation amplitude, the efficiency predicted by both methods increases. The change in CFD calculated efficiency from three to five-tube and five to seven-tube configurations are 0.8% and 0.2% respectively (the same trend is observed for 1D-Euler calculated efficiencies).

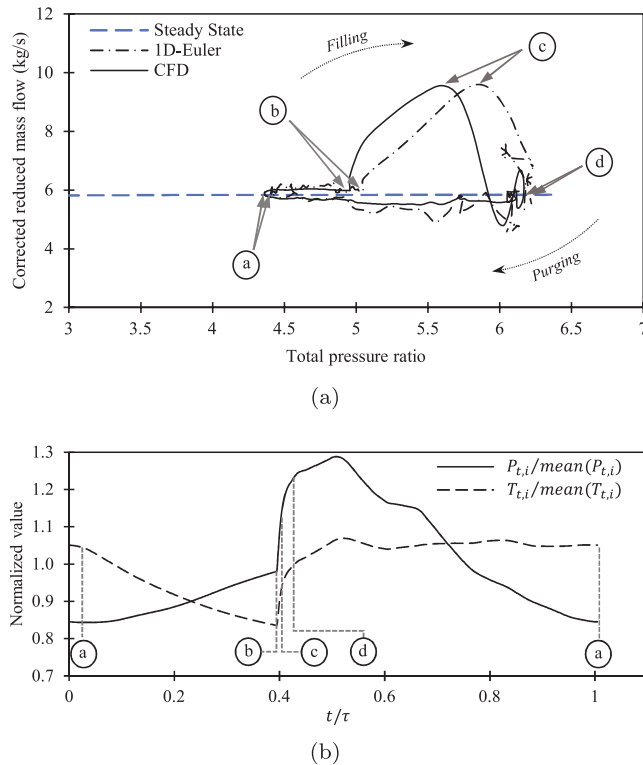


Fig. 13. Turbine hysteresis loop over the steady state characteristic line (a) and the total quantities imposed at the turbine inlet boundary (b).

Table 5
Turbine isentropic efficiency for all combustor configurations.

	3D-CFD	1D-Euler
Efficiency (%), 3-tubes config.	89.5	88.1
Efficiency (%), 5-tubes config.	90.3	89.2
Efficiency (%), 7-tubes config.	90.5	89.7

Regarding the difference between the efficiency calculated by the two methods, the 1D-Euler predicted lower values ($\leq 1.1\%$) than the CFD counterpart as previously observed for three tubes. However, as the fluctuation amplitude decreases, the deviation between the 1D and 3D-CFD efficiency diminishes, so that in the case with seven tubes the 1D-Euler underpredicts the efficiency by just 0.8 percentage points. The turbine output power is also computed here as a performance parameter. The time-averaged turbine power values are 337.7 kW, 343.8 kW and 347.0 kW for 3, 5 and 7-tubes configurations, respectively. As is expected, increasing the number of PDC tubes raises turbine power. The 3D-CFD computed turbine power values are almost identical to those of 1D-Euler results, considering the fact that the 1D-Euler solver uses the prescribed force and energy source terms in the equations.

Pressure damping is evaluated for the two configurations by both methods, depicted in Fig. 14. It is seen that the 1D-Euler solver delivers very close results to what is obtained through the CFD simulations and the trends are well captured as well. A quantitative look at the damping results indicates that 47.1% and 45.6% of the total inlet fluctuation are damped while the unsteady inlet flow passes through the first row in five and seven-tube configurations, respectively. Having captured almost the same result for the three-tube case in Fig. 11 and the damping reported by Bakhtiari et al. [34] applying a different inlet boundary condition, at this point, it can be concluded that the amount of damping through the blade rows depends more on the geometry than the flow fluctuation features. More investigations are required to generalize this claim.

The deviation of mass flow rate by the 1D-Euler from the 3D-CFD computed values as a metric involved in hysteresis loops is calculated to quantify the model accuracy in the instantaneous mass flow prediction. The instantaneous mass flow rate difference is normalized by the maximum values for each configuration ($\delta_m = \frac{\dot{m}_{1D} - \dot{m}_{CFD}}{\dot{m}_{max}}$). In Section 3.2.4, it was shown that the mass flow range is accurately captured by the 1D-Euler method for the configuration with three PDC tubes, when it is compared with the CFD results. This is also observed in the results for the two current configurations, which are not repeated graphically here. Fig. 15 depicts the distribution of instantaneous deviation in mass flow rate in the form of a histogram. The horizontal axis indicates the percentile of mass flow deviation and the vertical axis represents the number of instantaneous mass flow rate points normalized by the total points in each configuration. According to the histogram of all of the configurations, more than 80% of the instantaneous mass flow rate

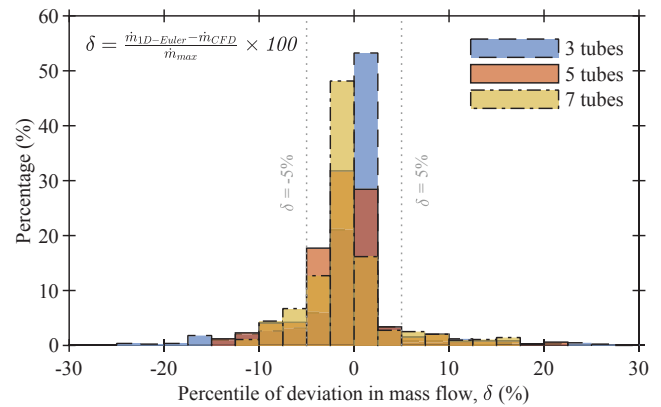


Fig. 15. Histogram of mass flow rate deviation for turbine working with different PDC configurations.

points have a deviation within $\pm 5\%$ (83% in 3tubes, 81.3% in 5tubes and 80.5% in 7tubes). This is consistent with Fig. 13(a) indicating the main difference in the hysteresis loops of 1D-Euler and CFD is between the points *b* and *d*, which corresponds to a short time within a time period shown in Fig. 13(b). This confirms that within the majority of the fluctuation time period, the 1D-Euler method predicts the instantaneous turbine performance well compared to the 3D-CFD results.

4. Conclusions

A fast and reliable tool for turbine unsteady simulation in conjunction with PDC arrays has been presented and evaluated. The method integrates a 1D-Euler, an in-house meanline analysis program and a PDC numerical model. The latter takes the steady-state turbine performance and delivers the unsteady boundary conditions for unsteady turbine simulations. The meanline method also provides the source terms for the 1D-Euler solver. The developed approach was run using three different combustor configurations providing different boundary conditions for the turbine. A back-to-back comparison of the results with those of unsteady 3D-CFD was done to evaluate the accuracy of the approach. A summary of the main outcomes is as follows.

The PDC numerical scheme simulated three PDC-plenum configurations having three, five, and seven tubes. The simulation results provide the time-dependent pressure and temperature in the plenum. For all configurations, a periodic pattern with a frequency depending on the number of tubes and the tubes' individual operating frequency emerged inside the plenum. It was shown that increasing the number of PDC tubes while maintaining the overall area ratio between combustion chambers and turbine inlet significantly mitigates the amplitude of the fluctuations. Temperature and pressure evolution inside the plenum displays a phase shift that can be attributed to the difference in their characteristic velocity of information, one being the local speed of sound and the other one being the flow velocity.

The unsteady simulation results of both 1D-Euler and 3D-CFD showed that the two-stage turbine is capable of damping the fluctuations throughout the stages. Additionally, it was indicated that the first row has a considerable damping role (around 45%), irrespective of the imposed fluctuation amplitude at the inlet boundary.

In terms of isentropic efficiency, unsteady simulations by both 3D-CFD and 1D-Euler showed an efficiency drop of up to 3% compared to the corresponding steady-state operation. In general, the isentropic efficiency calculated by the 1D-Euler is lower than that predicted from the 3D-CFD, while this discrepancy becomes less with lower inlet fluctuation amplitudes.

The performance hysteresis loop of the turbine encapsulates the steady-state characteristic line, though it is not symmetrically distributed. The reason was explained by the sharp gradient in the inlet flow

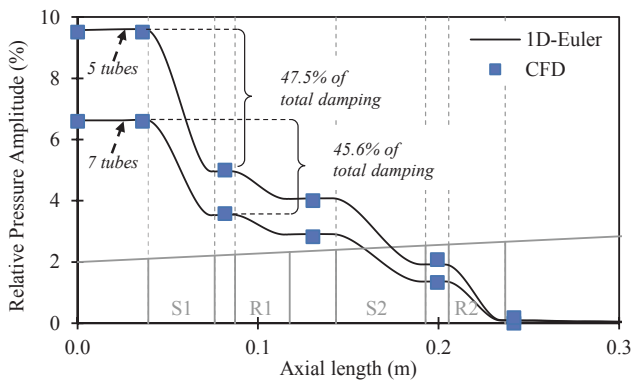


Fig. 14. Static pressure damping for five and seven PDC tubes.

conditions within the filling zone. Both methods have identically captured the overall shape of the hysteresis. In this context, the instantaneous mass flow rate is well predicted by the 1D-Euler method compared to the 3D-CFD. The results indicate that the majority of the instantaneous reduced mass flow rate in a pulse cycle lies within $\pm 5\%$ deviation from the CFD-computed values.

All in all, the developed methodology based on the 1D-Euler showed its ability for simulating the multistage turbine working with pulsed detonation combustion exhaust flow. The deviation in the results compared to those of the unsteady 3D-CFDs is mainly because of the inherent nature of one-dimensional modeling, which does not fully consider circumferential and radial flow features. Nevertheless, the methodology is fast and accurate enough to provide a robust tool for performance evaluations of turbines specifically in early design and development stages, where still a multitude of different configurations is under consideration.

Finally, two early decisions made to ease the tool development and keep it as generalized as possible must be mentioned here. The first is that the current work neglected any entropy generation caused by shock waves in the plenum and at the turbine inlet. This can be easily corrected with additional entropy generation terms, in the existing 1D-Euler and plenum models. These terms should be however calibrated for the specific geometrical design of each plenum. The second decision was to neglect any cooling air injection both in the plenum and the turbine models. Again, this shortcoming can be easily corrected with mass source terms in both models. Although these decisions might have some limited impact on the quantitative results of the presented models, they have no effect on the basic qualitative results and the demonstrated fidelity of the suggested 1D-Euler modelling approach of the turbine.

CRediT authorship contribution statement

Majid Asli: Methodology, Conceptualization, Software, Validation, Formal analysis, Writing – original draft, Visualization, Project administration. **Niclas Garan:** Methodology, Software, Formal analysis, Writing – original draft, Visualization. **Nicolai Neumann:** Validation, Formal analysis, Writing – review & editing. **Panagiotis Stathopoulos:** Conceptualization, Writing – review & editing, Supervision, Project administration, Funding acquisition.

Declaration of Competing Interest

The authors declare that they have no known competing financial interests or personal relationships that could have appeared to influence the work reported in this paper.

Acknowledgement

The authors would like to acknowledge the financial support from Deutsche Forschungsgemeinschaft (DFG) as part of the Collaborative Research Center SFB 1029 in Project D01 as well as part of the research grant 317741329 and Elsa Neumann Foundation (NaFöG). Additionally, Norddeutscher Verbund für Hoch- und Höchstleistungsrechnen (HLRN) is gratefully acknowledged for providing the high performance computing resources.

References

- [1] International Civil Aviation Organization, Annual report of the council, Tech. rep., International Civil Aviation Organization (2019). url:[https://www.icao.int/annual-report-2018/Pages/the-world-of-air-transport-in-2018.aspx#:text=The 4.3 billion airline passengers, some 90 million in 2040.](https://www.icao.int/annual-report-2018/Pages/the-world-of-air-transport-in-2018.aspx#:text=The%204.3%20billion%20airline%20passengers%2C%20some%2090%20million%20in%202040.)
- [2] Bach E, Stathopoulos P, Paschereit CO, Bohon MD. Performance analysis of a rotating detonation combustor based on stagnation pressure measurements. *Combust Flame* 2020;217:21–36. <https://doi.org/10.1016/j.combustflame.2020.03.017>.
- [3] Kaemming TA, Paxson DE. Determining the Pressure Gain of Pressure Gain Combustion. In: 2018 Joint Propulsion Conference. Reston, Virginia: American

- Institute of Aeronautics and Astronautics; 2018. p. 1–15. <https://doi.org/10.2514/6.2018-4567>.
- [4] Tellefsen J, Build Up and Operation of an Axial Turbine Driven by a Rotary Detonation Engine, Ph.D. thesis, Air Force Institute of Technology (2012).
- [5] Wolański P. Application of the Continuous Rotating Detonation to Gas Turbine. *Appl Mech Mater* 2015;782:3–12. <https://doi.org/10.4028/www.scientific.net/AMM.782.3>.
- [6] Gray JAT, Vinkeloe J, Moeck J, Paschereit CO, Stathopoulos P, Berndt P, et al. Thermodynamic Evaluation of Pulse Detonation Combustion for Gas Turbine Power Cycles. In: Volume 4B: Combustion, Fuels and Emissions. ASME; 2016. V04BT04A044. <https://doi.org/10.1115/GT2016-57813>.
- [7] Xisto C, Petit O, Grönstedt T, Rolt A, Lundblad A, Paniagua G. The efficiency of a pulsed detonation combustor–axial turbine integration. *Aerosp. Sci. Technol.* 2018; 82–83(August):80–91. <https://doi.org/10.1016/j.ast.2018.08.038>.
- [8] Sakurai T, Nakamura S. Performance and Operating Characteristics of Micro Gas Turbine Driven by Pulse, Pressure Gain Combustor. In: Diagnostics, and Instrumentation; Cycle Innovations; Cycle Innovations: Energy Storage. 5. American Society of Mechanical Engineers; 2020. <https://doi.org/10.1115/GT2020-15000>.
- [9] Stathopoulos P. An alternative architecture of the Humphrey cycle and the effect of fuel type on its efficiency. *Energy Sci Eng* 2020;8(10):3702–16. <https://doi.org/10.1002/ese3.776>.
- [10] Glaser A, Caldwell N, Gutmark E. Performance of an Axial Flow Turbine Driven by Multiple Pulse Detonation Combustors. In: 45th AIAA Aerospace Sciences Meeting and Exhibit, no. January. Reston, Virginia: American Institute of Aeronautics and Astronautics; 2007. p. 1–10. <https://doi.org/10.2514/6.2007-1244>.
- [11] Anand V, St A, George E, Knight E Gutmark. Investigation of pulse detonation combustors – Axial turbine system. *Aerosp Sci Technol* 2019;93:105350. <https://doi.org/10.1016/j.ast.2019.105350>.
- [12] Qiu H, Xiong C, Zheng L. Experimental investigation of an air-breathing pulse detonation turbine prototype engine. *Appl Therm Eng* 2016;104:596–602. <https://doi.org/10.1016/j.applthermaleng.2016.05.077>.
- [13] Naples A, Hoke J, Battelle R, Schauer F. T63 turbine response to rotating detonation combustor exhaust flow. *J Eng Gas Turbines Power* 2019;141(2):1–8. <https://doi.org/10.1115/1.4041135>.
- [14] Van Zante D, Envia E, Turner MG, The Attenuation of a Detonation Wave By an Aircraft Engine Axial Turbine, in: 18th ISABE Conference, no. ISABE-2007-1260, 2007, pp. 1–12.
- [15] Liu Z, Braun J, Paniagua G. Characterization of a Supersonic Turbine Downstream of a Rotating Detonation Combustor. *J Eng Gas Turbines Power* 2019;141(3): 1536–9. <https://doi.org/10.1115/1.4040815>.
- [16] Asli M, Stathopoulos P, Paschereit CO. Aerodynamic Investigation of Guide Vane Configurations Downstream a Rotating Detonation Combustor. *J. Eng. Gas Turbines Power* 2021;143(6). <https://doi.org/10.1115/1.4049188>.
- [17] Yang M, Deng K, Martines-Botas R, Zhuge W. An investigation on unsteadiness of a mixed-flow turbine under pulsating conditions. *Energy Convers Manage* 2016;110: 51–8. <https://doi.org/10.1016/j.enconman.2015.12.007>.
- [18] Taddei SR. Time-marching solution of transonic flows at axial turbomachinery meanline. *Proc Inst Mech Eng, Part G: J Aerosp Eng* 2020. <https://doi.org/10.1177/0954410020977350>. 0954410020977350.
- [19] Michel Feidt TKJB, Paweł Ziólkowski, The efficiency of turbomachinery in the zero- and three-dimensional approaches, *Entropy: Thermodynamics – Energy – Environment – Economy 1* (Issue 3). doi:10.21494/ISTE.OP.2021.0620.
- [20] Chiong MS, Rajoo S, Romagnoli A, Costall AW, Martinez-Botas RF. Integration of meanline and one-dimensional methods for prediction of pulsating performance of a turbocharger turbine. *Energy Convers Manage* 2014;81:270–81. <https://doi.org/10.1016/j.enconman.2014.01.043>.
- [21] Dittmar L, Stathopoulos P. Numerical Analysis of the Stability and Operation of an Axial Compressor Connected to an Array of Pulsed Detonation Combustors. In: Proceedings of the ASME Turbo Expo 2020, ASME; 2020. <https://doi.org/10.1115/GT2020-15381>.
- [22] Neumann N, Asli M, Garan N, Peitsch D, Stathopoulos P. A fast approach for unsteady compressor performance simulation under boundary condition caused by pressure gain combustion. *Appl Therm Eng* 2021;196:117223. <https://doi.org/10.1016/j.applthermaleng.2021.117223>.
- [23] Timko LP, Energy Efficient Engine High Pressure Turbine Component Test Performance Report, Tech. Rep. NASA Contract Report 168289, General Electric Co. Cincinnati, OH, United States (1984).
- [24] Celik IB, Ghia U, Roache PJ, Freitas CJ, Coleman H, Raad PE. Procedure for Estimation and Reporting of Uncertainty Due to Discretization in CFD Applications. *J Fluids Eng* 2008;130(7):078001. <https://doi.org/10.1115/1.2960953>.
- [25] Sousa J, Paniagua G, Saavedra J. Aerodynamic response of internal passages to pulsating inlet supersonic conditions. *Computers Fluids* 2017;149:31–40. <https://doi.org/10.1016/j.compfluid.2017.03.005>.
- [26] Clark JP, Grover EA. Assessing Convergence in Predictions of Periodic-Unsteady Flowfields. *J Turbomach* 2007;129(4):740–9. <https://doi.org/10.1115/1.2720504>.
- [27] Sadagopan A, Camci C. Viscous flow and performance issues in a 6:1 supersonic mixed-flow compressor with a tandem diffuser. *Aerosp Sci Technol* 2019;88:9–21. <https://doi.org/10.1016/j.ast.2019.02.027>.
- [28] Adams MG, Adami P, Collins M, Beard PF, Chana K, Povey T. Impact of rotor-casing effusion cooling on turbine performance and operating point: an experimental, computational, and theoretical study. *J Turbomach* 2021;143 (March):1–24. <https://doi.org/10.1115/1.4050019>.

- [29] Neumann N, Peitsch D, Introduction and validation of a mean line solver for present and future turbomachines. In: Proceedings of ISABE Canberra 2019, Canberra, Australia, 22–26 September, ISABE-2019-24441, 2019.
- [30] Aungier RH. Turbine Aerodynamics: Axial-Flow and Radial-Flow Turbine Design and Analysis. ASME Press; 2006. <https://doi.org/10.1115/1.802418>.
- [31] Denton JD. Throughflow Calculations for Transonic Axial Flow Turbines. J Eng Power 1978;100(2):212–8. <https://doi.org/10.1115/1.3446336>.
- [32] Came PM, Streamline Curvature Throughflow Analysis of Axial-Flow Turbines, in: 1st European conference, Vol 1; Computational methods, VDI Verlag, 1995, pp. 291–308.
- [33] Berndt P, Klein R. Modeling the kinetics of the Shockless Explosion Combustion. Combust Flame 2017;175:16–26. <https://doi.org/10.1016/j.combustflame.2016.06.029>.
- [34] Bakhtiari F, Schiffer H-P. Numerical approach to the modelling of transient interaction of prospective combustor concepts and conventional high pressure turbines. Propul Power Res 2019;8(1):1–12. <https://doi.org/10.1016/j.jprr.2019.01.008>.
- [35] Zel'dovich Y. To the question of energy use of detonation combustion. J Propuls Power 2006;22(3):588–92. <https://doi.org/10.2514/1.22705>.
- [36] Von Neumann J. Theory of detonation waves. In: Taub AJ, editor. John von Neumann, collected works, Vol. 6. New York: Macmillan; 1942. <https://apps.dtic.mil/sti/pdfs/ADB967734.pdf>.
- [37] Döring W. Über den Detonationsvorgang in Gasen. Ann Phys 1943;435(6–7): 421–36. <https://doi.org/10.1002/andp.19434350605>.
- [38] P. Holloway, C. Koch, G. Knight, S. Shaffer, Energy efficient engine - high pressure compressor detail design report, NASA-CR-165558, 1982.
- [39] Burke MP, Chaos M, Ju Y, Dryer FL, Klippenstein SJ. Comprehensive H₂/O₂ kinetic model for high-pressure combustion. Int J Chem Kinet 2012;44(7):444–74. <https://doi.org/10.1002/kin.20603>.
- [40] Suresh A, Hofer DC, Tangirala VE. Turbine Efficiency for Unsteady, Periodic Flows. J. Turbomach. 2012;134(3):034501. <https://doi.org/10.1115/1.4003246>.
- [41] George ASt, Gutmark E. Trends in Pulsating Turbine Performance: Pulse-Detonation Driven Axial Flow Turbine. In: 50th AIAA Aerospace Sciences Meeting including the New Horizons Forum and Aerospace Exposition, no. January. Reston, Virginia: American Institute of Aeronautics and Astronautics; 2012. p. 1–16. <https://doi.org/10.2514/6.2012-769>.

4.4 Publication IV

An optimization methodology for turbines driven by pulsed detonation combustors

The fourth paper has been submitted to the Turbo Expo 2022 in Rotterdam, the Netherlands, in December 2021. At the time of writing the thesis, it is accepted to be presented at the conference and published in the ASME Journal of Engineering for Gas Turbine and Power.

Contribution

In the course of this paper, the developed one-dimensional Euler solver is integrated into a turbine optimization process. The primary goal is to propose a methodology for optimizing a turbine working with the unsteady flow of a pulsed detonation combustor array. The novelty of this work is utilizing an unsteady solver for objective function evaluation in an iterative optimization procedure, which could be too expensive if CFD simulations are used instead.

Methods

A one-dimensional Euler equation solver is utilized in this paper for two purposes, turbine simulation and PDC tube modeling. The former is fed with turbomachinery source terms by an in-house developed meanline analysis program. An adaptive surrogate-based optimization algorithm using the complex shape method is brought into play, and a three-dimensional URANS equation solver is employed to evaluate the optimization results.

Results

The outcomes confirm a successful integration of the unsteady one-dimensional solver into an iterative optimization algorithm. Compared to the baseline geometry, the optimization results show that the optimized turbine produces 16% lower entropy and 14% higher output power in a five PDC tube configuration. The optimized design has a lower solidity in the first stationary vanes but higher in the rotor blades than in the base case. The blade outlet angles are recommended to open slightly so that the blade turnings were reduced while the maximum thickness-to-chord ratio of the first rotor blades is almost unchanged.

AN OPTIMIZATION METHODOLOGY FOR TURBINES DRIVEN BY PULSED DETONATION COMBUSTORS

Majid Asli*

Chair of Fluid Dynamics
Institute of Fluid Dynamics and Technical Acoustics
Technical University of Berlin
Berlin, Germany

Panagiotis Stathopoulos

Institute of Low-Carbon
Industrial Processes
German Aerospace Center (DLR)
Cottbus, Germany

ABSTRACT

A step-change in efficiency of gas turbine technology and, subsequently, an emissions reduction from this technology requires conceptual changes. Substituting conventional combustion chambers with pressure gain combustion in the form of pulsed detonation combustion (PDC) is one of the promising methods that can reduce gas turbine emissions significantly. Nevertheless, the component matching for the respective systems and specifically that of turbine expanders working with the exhaust flow of PDC tubes is still not solved. The unsteady nature of PDC exhaust flow makes 3D-CFD simulations too expensive to be applied in optimization loops in early design stages. To address this question, the present paper introduces a new cost-effective but reliable methodology for turbine analysis and optimization, based on the unsteady exhaust flow of pulsed detonation combustors. The methodology unitizes a robust unsteady one-dimensional solver, a meanline performance analysis, and an adaptive surrogate optimization algorithm. A two-stage axial turbine is optimized considering all unsteady flow features of a hydrogen-air PDC configuration with five PDC tubes. A three-dimensional URANS simulation is performed for the optimized geometry and the baseline to evaluate the methodology. The results showed that the optimized turbine produces 16% lower entropy than the original one. Additionally, the turbine output power is increased by 14% by the optimized design. Based on the results, it is concluded that the approach is fast and reliable

enough to be applied in optimizing any turbine working with unsteady flows, more specifically in PDC applications.

NOMENCLATURE

A	Cross sectional area.
E	Internal energy.
F	Force.
F_e	Endwall force.
f	Frequency.
H	Total enthalpy.
h	Specific enthalpy.
\dot{m}	Mass flow rate.
NB	Number of blade.
n	Number of sample points.
P	Pressure, static pressure.
Pr	Pressure ratio.
rpm	Round per minute.
S	Non-dimensional entropy.
\bar{S}	Time averaged non-dimensional entropy.
T	Temperature.
t	Time.
$t_{r,max}/c$	Thickness to chord ratio for the first rotor blade.
V	Flow velocity.
W	Work.
X	Sample point in a design space.
Y	Mass fraction.

*Address all correspondence to this author at asli@campus.tu-berlin.de.

- y^+ Dimensionless wall distance.
 β Blade outlet angle.
 ρ Density.
 γ Heat capacity ratio.
 ω Total pressure loss coefficient.

Abbreviations

- CSM* Complex Shape Method.
 E^3 Energy Efficient Engine.
GCI Grid Convergence Index.
LHD Latin Hypercube Design.
PDC Pulsed Detonation Combustion.
PGC Pressure Gain Combustion.
RDC Rotating Detonation Combustion.
SBO Surrogate Based Optimization.
URANS Unsteady Reynolds-Averaged Navier Stocks.

Subscript

- b Best sample point.
 bl Bleed flow.
 $Cont$ Contraction.
 Exp Expansion.
 o Sample point that is neither the best nor the worst.
 R Rotor number 1.
 Ref Reflection.
 ref Reference value.
 s Geometric center of the complex shape.
 sp Species.
 t Total quantity.
 V Nozzle number 1.
 w Worst sample point.
 x Axial direction.

Superscript

- (j) Complex shape j^{th} .

INTRODUCTION

The power generation and transport sectors have been responsible for most of the global growth of greenhouse gas emissions for the last decade. They also accounted for over two-thirds of emissions in 2019 [1]. This is only a piece of statistics indicating that achieving net-zero economies by 2050 very much depends on measures in areas other than the energy sector. Gas turbines can be considered the heart of energy and aviation sectors that need to be modified for this purpose.

Among the solutions for significantly cutting gas turbine emissions, using pressure gain combustion (PGC) instead of constant pressure combustion has shown its potential [2]. Despite the higher thermal efficiency of PGC-driven gas turbine cycles, which have been proven theoretically [3, 4], almost all practical PGC processes include unsteady physical phenomena. The associated unsteady exhausting flow results in an operation of turbomachinery components under fluctuating off-design conditions. In turn, this causes a reduction in their performance and can

counteract all benefits from the introduction of PGC. In order to make the PGC-gas turbine concept practical, efficient turbomachinery components capable of working in a wide range of operating conditions are required. Several researchers have focused on integrating turbines into the PGC concepts of pulsed detonation combustion (PDC) and rotating detonation combustion (RDC). In most experimental studies, existing turbines are placed downstream of PGCs to evaluate their performance. Glaser et al. [5] quantified a turbine's performance connected to a circular array of six PDC tubes by measuring the turbine power. They showed a comparable turbine efficiency between PDC-driven and steady operating turbines across the tested pressure ratios. They also concluded that an increase in fill fraction leads to a reduction in turbine efficiency. Rasheed et al. [6] connected six PDC tubes to a single-stage axial turbine and measured the work extraction and peak pressure attenuation through the blade rows. They also concluded the necessity of design optimization for a turbine working with PDCs [7]. Anand et al. [8] measured a higher thermal efficiency for the PDC cycle than the theoretical Brayton cycle, despite a substantial reduction in turbine efficiency. Fernelius and Gorrell [9] utilized a rotating ball valve to generate a sinusoidal pressure pulse to mitigate PDC exhaust flow for a combustion-free turbine test rig. They observed a decrease in turbine efficiency and pressure ratio and concluded that the cause is the pressure pulse amplitude, not the frequency.

While the highly unsteady exhaust flow of PDC and the compact geometry bring measurement challenges, numerical methods can provide more details, specifically where it is not possible to observe experimentally. A three-dimensional simulation of a PDC tube connected to an aircraft engine axial turbine stage was done by Van Zante et al. [10] to evaluate the pressure attenuation through the turbine stage. They measured a very low turbine efficiency of 26.7% since it operated for a significant part of the PDC cycle at off-design conditions. Xisto et al. [11] performed a two-dimensional URANS simulation of a coupled PDC-turbine system to study the different loss sources in turbines. They observed that the mismatch between the rotor speed and time-varying exhaust flow of PDC tubes is responsible for large incidence angle variation and, consequently, flow separation and significant losses. Their numerical simulation has shown that the turbine operates more efficiently under purge conditions for the particular turbine design. Cuciumita and Paschereit [12] compared the performance of a supersonic turbine stage under steady inlet and unsteady flow of PDC tubes using a two-dimensional RANS solver. They computed a pressure loss that was 50% smaller in the case of PDC operated turbine, which was mainly due to the turbine being exposed to the shock waves for less time.

Despite the accuracy of unsteady two and three-dimensional CFD methods in capturing detailed flow physics, their computational price does not allow these methods to be utilized in optimization loops, where many simulations have to be performed.

Instead, low fidelity methods are required to carry out design and optimization simulations fast and reliably. Within the scope of turbine and PDC optimization, Fernelius and Gorrell [13] utilized a two-dimensional steady RANS solver to calculate the objective function and optimize the rotor blades of a turbine stage. To simplify the optimization problem, they assumed a sinusoidal pressure pulse as the turbine inlet boundary condition. They performed steady simulations, one at a maximum and one at a minimum of the pressure pulse in each objective function call. However, the unsteady features of the PDC exhaust flow field were ignored for the sake of reducing computational time. While the mean line methods in turbomachinery are steady solvers, one-dimensional methods can be used in unsteady cases [14–16]. Chiong et al. [17] proposed integration of a 1D-Euler solver with a meanline analysis for a mixed-flow turbocharger turbine. They used the meanline method for every discrete point on the inflow pulse to calculate the tangential velocity to the rotor. Recently, the authors have developed a 1D-Euler methodology for simulating turbines working under PDC exhaust flows [18]. We have shown the approach’s applicability with an acceptable level of accuracy.

According to the literature, no systematic procedure has been introduced providing a turbine optimization method that considers the PDC unsteady flow features inside the optimization loops. The present paper aims to fill this gap by presenting an optimization procedure based on a surrogate model using a time-dependent one-dimensional Euler solver to evaluate the objective function. The solver uses mean line performance analysis to provide source terms in the governing equations. A PDC model provides the unsteady turbine simulations with the inlet boundary conditions. The test case is a two-stage high-pressure turbine connected to a five-tube PDC array and a plenum in between. To evaluate the methodology, three-dimensional URANS simulations will be utilized to compare the optimum design against the baseline.

METHODS

The paper focuses on introducing of an optimization procedure in the initial design procedure of a turbine for PDC. This includes methodologies to calculate the objective function and its prerequisites, optimization algorithm, and verification method. In this section, firstly, the test case is described. This is followed by the discussion of a coupled combustion model for calculating PDC exhaust flow condition, a 1D-Euler solver for evaluating the objective function, and the optimization algorithm. Finally, the unsteady 3D-CFD simulation will be explained and applied for the optimized and baseline geometries under the same boundary conditions.

Turbine Model

The baseline design for the current work is the high-pressure turbine of the Energy Efficient Engine project reported by NASA [19]. The turbine has two stages of moderate loading, which have been tested in a full-scale test rig. The turbine’s performance was mapped over a wide range of operating conditions to prove its off-design capabilities, which cover the range of operating conditions of the current research. This model is selected because the details of its geometry and performance parameters are available in the open literature, and it can be used as a benchmarking test case. In short, the turbine at its design point has a pressure ratio of 5.01, an efficiency of 92.5%, a reduced speed of 316.9 rpm/ \sqrt{K} and a reduced mass flow of 0.892 kg \sqrt{K} /s/kPa.

1D-Euler Turbine simulation tool

To evaluate the transient behavior of the turbine, a tool has been developed to solve the equations of mass, momentum, and energy conservation as the one dimensional compressible Euler equations described in Eqn. 1. The code has been initially developed for shockless explosion combustion [20] and further developed by the authors [18] for unsteady turbine simulations. The presence of turbine blades and their effect on the flow are included in the governing equations by source terms on the right side of the equations. The bleed mass flow rate that can be inserted into the turbine for cooling purposes closes the mass continuity equation. The momentum conservation equation is equipped with the blade force acting on a control volume around the blade. A schematic of a turbine rotor blade, the related control volume, and the force balance equations are shown in Fig.1. According to the second law of motion, the sum of the forces acting on the control volume can be computed as the momentum difference between the inlet and the outlet. Therefore, the blade force representing the turbine blade’s presence in the momentum continuity equation is calculated (see the equations in Fig.1). The computed blade force is distributed in a concave down parabola shape from the blade inlet station to the outlet to have a more realistic representation of the blade into the equation. If it is assumed that the blade row is adiabatic, the shaft work to close the energy continuity equation is computed by the enthalpy balance around the blade based on the first law of thermodynamics, i.e., $W = (\dot{m}h_t)_{out} - (\dot{m}h_t)_{in}$. If a bleed mass flow is injected into the turbine, the related energy terms represented by its enthalpy are added to the right side of the energy equation too.

$$\begin{aligned}
 \text{Mass} : \frac{\partial(\rho A)}{\partial t} + \frac{\partial(\rho V_x A)}{\partial x} &= \frac{\partial \dot{m}_{bl}}{\partial x} \\
 \text{Momentum} : \frac{\partial(\rho V_x A)}{\partial t} + \frac{\partial(\rho V_x^2 A + PA)}{\partial x} &= \frac{\partial(F_x + PA)}{\partial x} \\
 \text{Energy} : \frac{\partial(\rho EA)}{\partial t} + \frac{\partial(V_x A(\rho E + P))}{\partial x} &= \frac{\partial(W + \dot{m}_{bl} h_{t,bl})}{\partial x}
 \end{aligned} \tag{1}$$

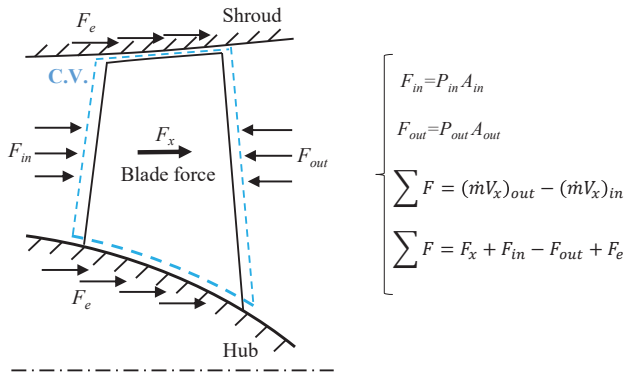


FIGURE 1. A MERIDIONAL VIEW OF A TYPICAL TURBINE ROTOR BLADE AND THE FORCE BALANCE ON A CONTROL VOLUME AROUND THE BLADE.

The mentioned force and work source terms are computed by a meanline analysis method. An in-house developed code has been prepared and validated against the experimental results of E³ high-pressure turbine previously [18]. The meanline program receives the turbine geometry, including the number of blades, blade inlet and outlet angles, and overall dimensions to calculate aerothermodynamic parameters between the blade rows. Since the accuracy of meanline methods depends basically on the used correlations, all the loss correlations have been fine-tuned for the test case in question based on the recommendations in open literature [21]. The source terms, which are calculated for a range of the turbine operating conditions, are provided to the 1D-Euler solver in the form of lookup tables. The solver reads the source terms from the tables based on the blade upstream and downstream pressure magnitudes. On account of stability issues, average pressure values of five to seven neighboring cells are taken. Based on a grid size dependency analysis, each cell has a length of 0.5 mm in a domain of 470 mm length. The inlet boundary condition is computed by the PDC model that is described in the following section. Based on the experimental data, the outlet boundary condition is supplied to the solver as a constant static pressure of 3.63 bar. The constant pressure is applied since the turbine showed that it is capable of damping all the pressure fluctuations coming from the PDC configuration of this research throughout its four blade rows [18]. The details of the boundary conditions will be discussed in the course of the paper.

Pulsed Detonation Combustor Model

The 1D-Euler solver used for simulating the turbine mentioned above has been also modified to model the phenomena and the exhaust flow conditions on each PDC tube. Since the PDC tubes are assumed as straight ducts, the area term is omitted from the governing equations of Eqn.1. Also, all the mass and force source terms are set equal to zero. Considering the combus-

tion process occurring inside the tubes, the chemical composition continuously changes in time and space. Therefore, a conservation equation for each species mass fraction is required to be solved together with the Euler equations, presented in Eqn.2. The right side of the equation represents the changes in composition resulting from chemical reactions ($\dot{Y}_{sp,chem}$) with the underlying reaction equations provided by the multi-step H₂-air mechanism described by Burke et al. [22].

$$\frac{\partial(\rho Y_{sp})}{\partial t} + \frac{\partial(\rho V_x Y_{sp})}{\partial x} = \rho \dot{Y}_{sp,chem} \quad (2)$$

Typical pulsed detonation combustion of H₂-air mixture takes place in each PDC tube, which has been explained in detail in our previous work [18]. In the current research, five tubes comprise the PDC-array configuration. Each PDC tube has a length of 1 m, and they are fired sequentially. The firing frequency of each tube is set equal to 20 Hz, resulting in a frequency for the PDC-array of 100 Hz. Following our compressor-PDC modeling [23], the PDC tubes are connected to an upstream plenum fed by NASA-E³ compressor. The flow inside the upstream plenum is assumed to have a zero velocity, a pressure of 21.75 bar, and a temperature of 691.15 K. Once the pressure inside the tubes drops below that of the upstream plenum, air flows into the tubes. A similar plenum as at the inlet is considered at the outlet of the PDC tubes. Having the specific axial kinetic energy preserved, tube pressure is expanded to the downstream plenum pressure through an instant isentropic process. With the assumption of a zero-dimensional plenum, only mass, energy, and species fractions are considered in the conservation equations, while velocity is assumed to be always zero. The mass flow from the tubes going into the plenum is considered as mass and energy source terms within the plenum's balancing equations.

3D-CFD Method

As an expensive computational tool, the unsteady 3D-CFD analysis is utilized twice in this paper for the base turbine geometry, which is the original E³ high-pressure turbine, and the optimized geometry for the aforementioned PDC-array. The ANSYS CFX solver is employed to solve the unsteady Reynolds Averaged Navier-Stocks (RANS) equations in a three-dimensional computational domain. The domain consists of four blade rows, and the inlet and outlet planes placed one chord length upstream of the first blade row and four chord lengths downstream of the last blade row, respectively. A blade-to-blade view of the domain at midspan surface is shown in Fig.2. Since the PDC exhaust flow as the turbine inlet boundary is circumferentially symmetrical, one blade passage of each blade row has been modeled. A periodic boundary condition is assigned to the adjacent blade passages. In addition, the stage mixing plane is considered as the interface between the blade rows because fluctuations in the

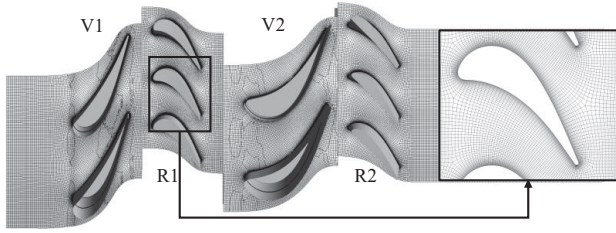


FIGURE 2. AN ILLUSTRATION OF THE COMPUTATIONAL DOMAIN AT MIDSPAN SURFACE.

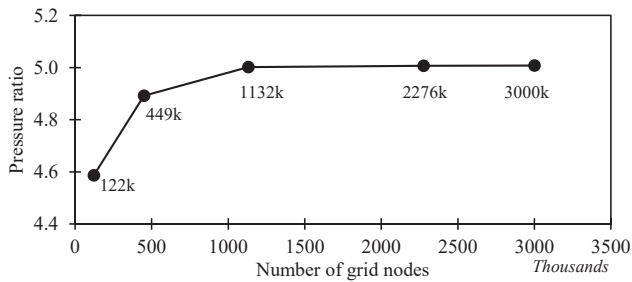


FIGURE 3. TURBINE PRESSURE RATIO VARIATION WITH MESH SIZE.

PDC exhaust flow are mainly in the axial direction. Therefore, the averaging in circumferential direction done in the stage mixing plane approach is applicable here. The Shear Stress Transport model developed by Menter [24] is utilized for turbulence modeling, which has been used in similar flow problems [25,26]. The approach combines the benefits of $k-\epsilon$ and $k-\omega$ models, which can model the turbulence well in near and far wall regions. The mesh discretizing the computational domain is a combination of O-H grids, depicted in Fig.2. To keep y^+ close to unity and consequently not lose the boundary layer effects, the mesh refinement is performed several times. Additionally, a mesh sensitivity study has been done with grids ranging from 122 k to 3000 k nodes. The CFD simulations have been done with these grids, and the resulting pressure ratios are compared in Fig.3. According to the results, the pressure ratio approaches the design value of 5.01 by increasing the number of grid nodes. However, more refinement from 1132 k nodes does not change the pressure ratio significantly as the relative error $((Pr_{i+1} - Pr_i) / Pr_{mean})$ becomes less than 0.1%. The Grid Convergence Index (GCI) as a metric for the mesh quality is also calculated based on the formulation by Celik et al. [27]. The GCI values corresponding to the computational domain having 1132 k grids are 0.15% and 0.2% for pressure ratio and mass flow rate, respectively, which show that further grid refinement would not have any considerable effect on the results. In the current work, a domain with 1132 k nodes is thus selected for the CFD analysis. The time step for the time-

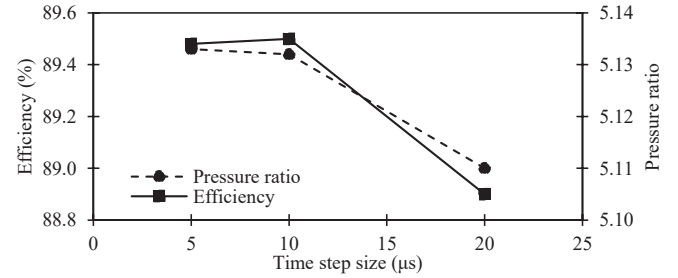


FIGURE 4. EFFECT OF TIME STEP SIZE ON PERFORMANCE PARAMETERS.

dependent simulations is a key parameter that should be specified carefully. Again, a time step dependency analysis is done for different time step sizes ranging from $20 \mu s$ to $1 \mu s$. Having an inlet boundary condition time period of 0.01 s, the mentioned time step range corresponds to 1/500 to 1/2000 of the inlet fluctuation period. Fig.4 indicates the results of three unsteady simulations with different time step sizes in terms of pressure ratio and efficiency. The comparison of the results shows that the appropriate time step is $10 \mu s$ and any further reduction leads to a negligible change in the results of the transient simulation at a substantial computational cost. Each unsteady 3D-CFD simulation in this research takes around 36 computational hours to converge using a computer cluster with 64 Intel® Xeon® CPUs at 3.8 GHz.

Adaptive Surrogate Model-Based Optimization

Surrogate model-based optimization (SBO) methods effectively solve implicit, complex, and time-consuming optimization problems that need several calls to the objective function. These methods are widely used in engineering-related problems, specifically in aerospace engineering [28]. In general, an SBO includes a process of sampling, evaluating high fidelity objective functions, creating a surrogate model, and finding the optimum design. The computational cost of an optimization problem depends mainly on the number of objective function calls. Therefore, creating a surrogate model will reduce this number by quickly and intelligently selecting the optimum design points. An adaptive sampling-based surrogate model can provide a high accuracy by employing infilling strategies to use auxiliary points for modifying the surrogate model. A proper searching approach to find the sampling infill criteria would guide the solution and increase the effectiveness of the optimization procedure. An adaptive surrogate model-based optimization framework is applied in this paper, which is shown in Fig.5. The process starts by selecting initial samples from the whole design space, which includes the optimization variables. The accuracy of the surrogate model itself is a function of sample numbers, and their spatial distribution [29]. In this paper, the initial samples from the design space, which will be elaborated later, are selected by a

Latin Hypercube Design (LHD). An LHD provides the samples having a suitable spatial uniformity and consequently can reflect the information of the design problem sufficiently [30]. High fidelity objective values are found for all of these sample points. According to the type of optimization problems, the initial sample set is divided into two or more sample subsets. In this paper, there are five variables in the optimization problem in question, and the total number of initial samples is 50, which have been selected by the LHD method. The variable selection procedure will be discussed later. The subsets are selected randomly again by LHD, and five sets of 10 samples are created. Each of the subsets is used to generate a complex shape problem. For each complex shape, a surrogate model is constructed. Then the Complex Shape Method (CSM), which is a direct search algorithm, is utilized to find a proper new infill point by doing some operations of reflection, expansion, contraction, and compression expressed in Eqn.3.

Sample points : $X_i, i = 1, 2, \dots, n$

Objective function value : $f(X_i)$

$f(X_w) = \text{maximum}(f(X_i)), i = 1, 2, \dots, n$

$f(X_b) = \text{minimum}(f(X_i)), i = 1, 2, \dots, n$

$$X_s = \frac{1}{n-1} \sum_{i=1}^n X_i, i \neq w \quad (3)$$

Reflection : $X_{Ref} = X_s + \zeta(X_s - X_w), \zeta > 1$

Expansion : $X_{Exp} = X_{Ref} + \kappa(X_{Ref} - X_s), \kappa > 0$

Contraction : $X_{Cont} = X_s + \vartheta(X_s - X_w), \vartheta < 0$

Compression : $X_{i,new} = X_b - 0.5(X_b - X_i), i = 1, 2, \dots, n \text{ \& } i \neq b$

X_w is the worst sample point among the current sample point subset, which corresponds to the maximum objective function value. By creating the complex shape and doing the reflection operation (with a recommended reflection factor of $\zeta = 1.3$), the new sample point is generated. If the objective function value of the new sample point is lower than the lowest function value in the current complex shape, the expansion operation is done. The expansion factor is initially selected greater than 1. Provided that the expansion operation fails to generate a better sample point, the expansion factor is reduced by a factor of 0.5 until $\kappa = 10^{-5}$. If the objective function value of the reflected sample point is greater than the worst sample point, the contraction operation is run to move away from the worst point. Presuming that none of the mentioned operations leads to an objective function value better than the worst one, $n - 1$ new sample points will be generated using the compression operation. This operation compresses the sample points toward X_b as the best sample among the sample point subset to form a new complex shape together with it. Then the calculation starts anew. The existing criteria must be checked within all of the operations, and the sample points must be inside the range. Using these operations, the new sample point by which the worst point is replaced is constantly approaching

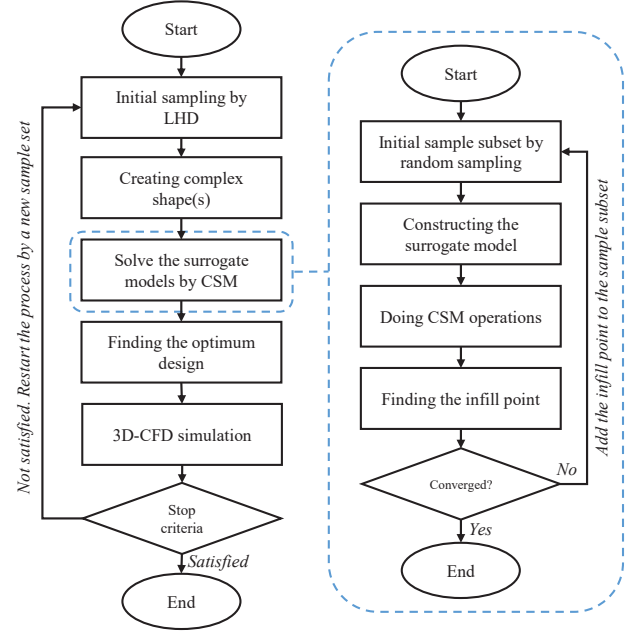


FIGURE 5. THE ADAPTIVE OPTIMIZATION FRAMEWORK.

the optimum solution while continuously improving the surrogate model's local precision.

A sample process of complex shape creation in a two-dimensional design space with three initial sample points is shown in Fig.6. In this example, the searching process uses reflection or expansion operation in each iteration to create a new complex shape and finally reaches point 8, which is the optimum solution (minimum objective function value). Dashed lines represent the operations to find the new sample points passing through the geometric center of the complex shape, excluding the worst point. For design spaces with higher dimensions and more initial sample point numbers, the complex shape is no longer presented by a triangle and becomes more intricate. The basics of CSM have been elaborated and applied for some engineering applications by Xu et al. [31]. Once the new infill point is getting close enough to the previous one and the convergence criteria, i.e., $\Delta X_{i,i+1}/(X_{max} - X_{min}) < 10^{-4}$, is satisfied, the operation ends, and the optimum design out of the complex shape is found. Otherwise, the infill sample point is substituted for the worst sample point in the initial sample subset, and the surrogate model is updated. The Kriging method, a popular spatial interpolation model based on the Gaussian process, is utilized to construct the surrogate model. Since the Kriging method provides nonlinear functions with satisfactory approximation abilities by using a unique error estimation function, it is widely used in similar applications [32–34]. The final optimum design, which is the best optimum one out of all the complex shapes, will be simulated using a 3D-CFD analysis and compared to the original

design. If the optimum design does not satisfy the expectations, the whole procedure will be restarted by a new initial sample set. Since the construction process of the surrogate model is closely merged with the optimization process, the mentioned optimization method has the advantages of having a simple modeling process, a small sample size, and high optimization efficiency. CSM combines the process of finding the infill points and the optimization process into one loop. In this method, the surrogate model is continuously updated and directed to the optimal solution. Therefore, unlike the other optimization approaches, the accuracy of the surrogate model does not need to be verified in the iterative process outside the searching process. Although the efficiency of the optimization algorithm depends on the nature of the problem, CSM proves its superior efficiency over the other approaches in benchmark function problems having multiple local minimums, e.g., the well-known test functions of Sasena, Goldstein price, three-dimensional Hartman, and six-dimensional Hartman [31]. As a direct searching algorithm, CSM uses fewer sample points, and hence fewer objective function calls than the expected improvement algorithm [35], candidate point approaches [36] and maximized response surface method [37], in solving each of the mentioned test functions. In general, if multiple extremums exist in the objective function, increasing the number of complex shapes can prevent the algorithm from getting stuck in a local optimum solution. Nevertheless, because different complex shapes may search in the same direction, too much increasing the number of complex shapes brings unnecessary sample points to the calculation and subsequently increases the computational cost and reduces the algorithm efficiency. Therefore, a fair number of complex shapes can help the search efficiency of the optimization algorithm. Depending on the optimization problem, an initial number of complex shapes should be selected. Then, based on the searching directions and the optimums found out of the complex shapes, one can decide whether more complex shapes are required. If a majority of the complex shapes are converged to an optimum which is the best, it can be ensured that the algorithm has reached the global optimum.

RESULTS AND DISCUSSION

In this section, firstly, the variable selection and the objective function for the optimization purpose are explained. After that, the boundary conditions for the objective function calculations are defined. Consequently, the optimization results will be elaborated, including the convergence trend and the optimum values. Finally, the unsteady 3D-CFD simulation results for the optimum design will be compared against the original one to evaluate the process. The comparisons are made mainly in the scope of turbine performance parameters of entropy generation, total pressure loss, and turbine power.

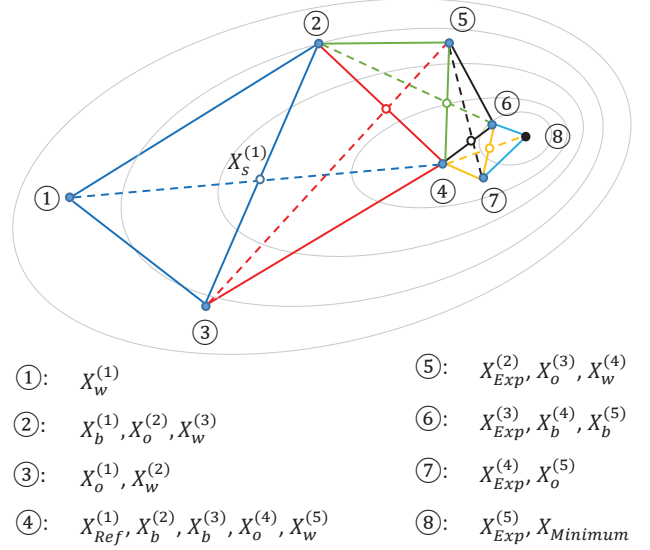


FIGURE 6. A SAMPLE CSM ITERATION PROCESS IN A TWO DIMENSIONAL DESIGN SPACE.

Objective Function and Variables

The goal of the optimization process in this paper is to find an optimum turbine design having the highest efficiency while working under PDC exhaust flow. The efficiency term includes both pressure ratio and work output. In this regard, entropy generation quantifies the losses and directly affects efficiency. For this reason, it is used to visualize and identify losses in the current work [13]. The non-dimensional entropy, defined in Eqn.4, is used as the objective to be minimized. The temperature and pressure reference values are set to 1 K and 1 pa, respectively. Non-dimensional entropy generation is computed by subtracting the non-dimensional entropy at the turbine outlet from the inlet. It should be noted that, in the course of this paper, the entropy term refers to as non-dimensional entropy, defined in Eqn.4.

$$S = (T/T_{ref})^{\frac{\gamma}{\gamma-1}} (P/P_{ref})^{-1} \quad (4)$$

There are many parameters that can be involved in a turbine optimization process which include geometrical parameters, thermodynamic parameters, or basic turbine design parameters [21]. According to the scope of this paper and the available test case geometry, the optimization focuses on the geometrical parameters to evaluate the optimization methodology. To have the highest possible involvement of the 1D-Euler methodology as the objective function evaluation method, the focus is set on the turbine geometrical variables that affect loss. Therefore, it is assumed that the overall annulus geometry of the original turbine is fixed. Besides, previous studies [18, 25, 38] showed that almost half of the unsteadiness is damped through the first blade row, meaning

TABLE 1. OPTIMIZATION VARIABLES AND THEIR BOUNDS.

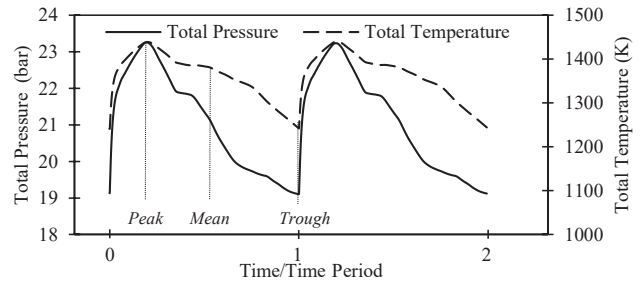
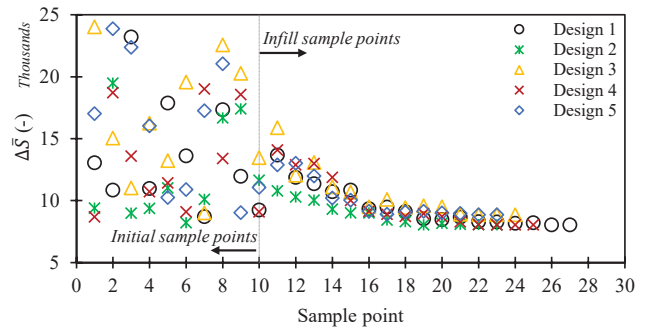
Variable	NB_V	NB_R	β_V	β_R	$t_{r,max}/c$
Base value	46	76	16	24	0.258
Bounds	29-116	54-198	20-50	20-50	0.15-0.30

that the first turbine stage experiences most of the PDC exhaust flow unsteadiness. Hence, the emphasis is put on the first stage geometrical variables. According to the loss correlations for turbine blades used in the meanline method, blade inlet and outlet metal angles, blade thickness, and solidity play significant roles in loss generation. Solidity is defined as the ratio of chord length to blade spacing. If the chord length is assumed to be fixed, the solidity will be a function of the blade number. Since the turbine inlet is connected to a plenum with the assumption of axially fluctuating flow entering the turbine, the first blade inlet metal angle could be fixed since it already has a zero incidence angle. Consequently, based on the profile loss correlation [21], the effect of the maximum thickness of the first blade row on loss generation is canceled. To decouple the relatedness of the upstream blade outlet angle from the downstream blade inlet angle, only the blade outlet angle is considered as a variable. As a result, the design space includes five optimization variables of two solidities, two blade outlet angles, and a maximum thickness to chord ratio.

According to the available loss correlations reported by Aungier [21], the blade solidity can vary from 0.8 to 5. If the chord lengths are assumed to be fixed, the number of blades for each blade row can vary in a space not exceeding the solidity range. According to the blade thickness, some high values of solidity can not be chosen due to the space limitation between the adjacent blades, which is a design space constraint. Blade outlet angle ranges are also provided in the loss correlation between 20 and 50 degrees. It is generally recommended that a maximum thickness to chord ratio of 0.2 is a proper choice for the turbine blades. Nevertheless, a range is assigned to the thickness to chord ratio of the rotor blade, which is from 0.15 to 0.30. The optimization variables, the original values, and the ranges are tabulated in Tab.1.

Boundary Conditions

The optimization process is done using the unsteady 1D-Euler simulation of the turbine as the objective function evaluation tool. The unsteadiness comes from the upstream boundary condition, where a five PDC tube configuration is operating. The PDC model, presented in the methods section, computes the total pressure and the total temperature at the turbine inlet. Figure 7 indicates the computed turbine inlet boundary condition. The pressure and temperature fluctuations has an relative

**FIGURE 7.** TURBINE INLET BOUNDARY CONDITIONS.**FIGURE 8.** CONVERGENCE TREND OF THE OPTIMIZATION PROCESS.

amplitude of 9.7% and 7.2%, respectively, which is defined as $((\phi_{max} - \phi_{min})/2\phi_{mean})$. The simulation has been repeated several times by trying different distances from the last blade row to the outlet plane, and the intermediate results were checked downstream of the turbine. It was observed that the turbine could dampen all the levels of fluctuations existing in the inlet boundary condition. For this reason, the turbine outlet boundary condition is set to have a fixed static pressure of 3.63 bar. The same boundary condition is applied for the 3D-CFD simulations in this research.

Optimization Results

Following the optimization procedure described in the method section, the optimization is run, and five designs were generated out of the created complex shapes. Each of the complex shapes was iterated less than 20 times to reach its optimum objective function value satisfying the convergence criteria. Figure 8 depict the convergence trend for each design, starting from their randomly selected initial sample points. It is observed that three out of five designs based on complex shapes converge to the same minimum objective function of $\Delta S = 8034$, which shows global optimum design. The optimum design parameters are listed in Tab.2 with an illustration of the related blade shape modifications in Fig.9.

TABLE 2. OPTIMIZATION RESULTS.

	$\Delta \bar{S}$	NB_V	NB_R	β_V	β_R	$t_{r,max}/c$
Base	9595	46	76	16.0	24	0.258
Optimized	8034	40	84	24.1	31.5	0.259

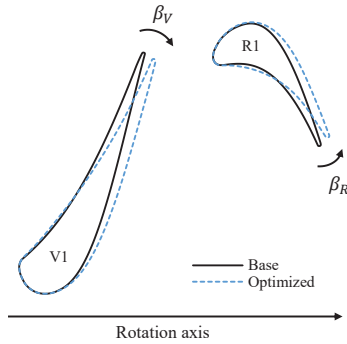


FIGURE 9. BLADE ANGLE MODIFICATIONS AT MID-SPAN SURFACE.

The optimization procedure suggests a decrease in the number of blades from 46 to 40 which corresponds to a reduction in solidity from 1.30 to 1.13 and an 8 degree increase in blade outlet angle for nozzle blades. For rotor blades, the number of blades is increased from 76 to 84, meaning an increase in solidity from 1.26 to 1.40. As is suggested for nozzle blades, the rotor outlet angle is increased by 5.5 degrees. Rotor thickness to chord ratio almost remains unchanged for the optimum design. Based on these changes in the first turbine stage blade rows, the overall entropy generation, averaged over a pulse of the PDC, is reduced by 16%.

Entropy Generation To evaluate the optimized geometry and compare the consequence of the modifications to the blades more precisely, transient 3D-CFD simulations have been performed for both base and optimized cases. Mass-averaged entropy values at inlet and outlet turbine planes have been computed once the periodic convergence has been achieved. Figure 10 illustrates the instantaneous entropy over a pulse period for the base and optimum designs. The overall trend in entropy in the outlet plane is the same as in the inlet plane with a right shift in time which is related to the flow passing time through the domain. In general, a downshift in the outlet entropy can be seen for the optimized case compared to the base design.

To better visualize how the blades reduce the entropy generation in the optimized design, the entropy contour around the first stage rows is plotted in Fig.11 at the instant of peak entropy

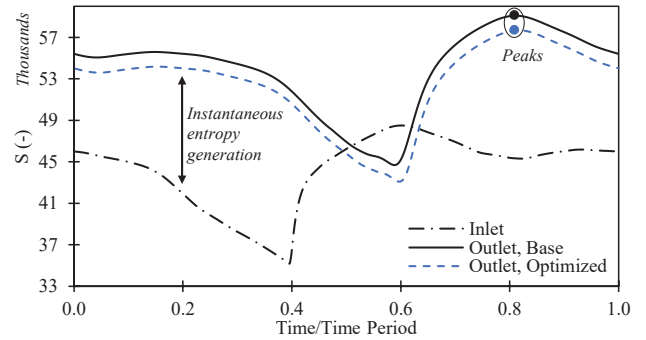


FIGURE 10. TIME DEPENDENT ENTROPY AT THE TURBINE INLET AND OUTLET.

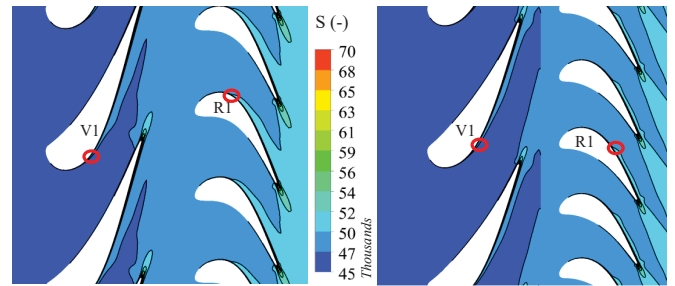


FIGURE 11. ENTROPY CONTOUR AROUND THE FIRST STAGE BLADES AT MIDSPAN SURFACE AT THE OVERALL PEAK ENTROPY GENERATION INSTANT, BASE (LEFT) AND OPTIMIZED (RIGHT) DESIGNS.

at the outlet. Red circles show the start of increment in entropy on the suction surfaces of the blades. According to the circles' locations moving toward the trailing edges, both blade rows perform better in terms of entropy generation, while the share of rotor blades is more pronounced. In the optimized geometry, the divergent section of the blade passages becomes smoother so that the flow tends to be more attached and produce less entropy. A lower entropy region downstream of the rotor blades can be seen in the optimum design contour as well. The higher entropy regions on the suction surface of the blades in the base case can be explained by their greater uncovered turning angles. The lower uncovered turning downstream of the blade throat in the optimized design, which results from the blade outlet angle increment, make the flow follow the trailing edge and preserve the pressure gradient so that the boundary layer remains attached. In some cases where the uncovered turning is too large, the flow deviates from the trailing edge, affecting flow turning and the work output adversely [13, 39].

Each of the blade rows has a different contribution to the overall entropy generation. Figure 12 shows the time-averaged entropy calculated at upstream and downstream planes of the

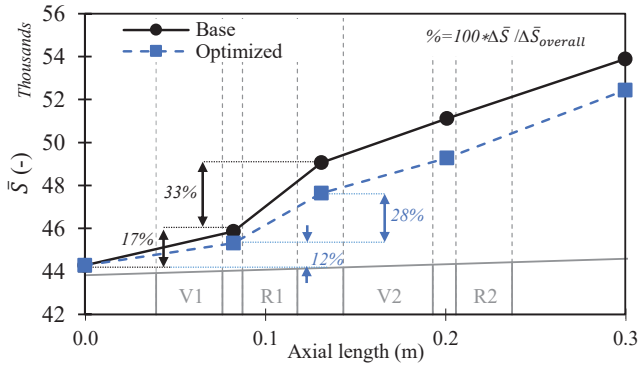


FIGURE 12. AVERAGED ENTROPY DISTRIBUTION THROUGHOUT THE TURBINE.

blade rows for both cases. The blade rows in the meridional view are schematically depicted inside the figure just as an axial location reference and do not represent the actual view. Comparing the entropy generation by the first stationary row in the optimum design against the base design shows a reduction from 17% to 12% of the whole amount of entropy generated in the turbine. The same comparison for the first rotor row indicates that the optimum design has 5% lower entropy generation than the base case. It can be seen that the share of entropy generation by the first stage is reduced from 50% in baseline to 40% in the optimum design. This shows the second stage has a higher entropy generation contribution than the first stage in the optimum design. Having a qualitative look at the interstage entropy results in Fig.12, the entropy difference between the two designs is increasing from the inlet up to the upstream of the last blade row. In contrast, the difference from there to the outlet plane does not follow the same trend. This discrepancy, together with the fact that in the optimized design, the share of the first stage in the overall turbine entropy generation is lower than that of the second stage (40% versus 60%), indicates that the optimization process was successful in modifying the first stage toward lowering entropy generation even to a level even lower than the second stage which is less affected by the unsteadiness.

Total Pressure Loss Total pressure loss is a second reference parameter measuring the performance of a blade, specifically in cascade flow analysis from which loss correlations are developed. Table 3 lists the total pressure loss coefficients of the first stage rows, defined here as $\omega = \Delta P_t / P_{t,inlet}$. According to the table, it is apparent that the first stator could perform better in the optimized version and generate 28.2% lower total pressure loss. The associated total pressure loss for the first rotor blades is also reduced by 11.6%. Since the modifications to the blades affect the profile shape and the blade's solidity and the fact that no shock wave was captured during the turbine operation, the

TABLE 3. TOTAL PRESSURE LOSS COEFFICIENT.

	Stator 1	Rotor 1	Overall
Base	0.0336	0.0292	0.0870
Optimized	0.0241	0.0258	0.0801
Change (%)	-28.2	-11.6	-7.9

duction of pressure loss is, to a large extent, due to the profile loss reduction. According to the general profile loss formulation by Ainley-Mathieson [40], both changes are toward lowering the pressure loss coefficient within the stator row. In contrast, the solidity increment is against lowering the profile loss within the rotor row, although the optimized rotor blade achieves an overall lower total pressure loss. The overall turbine pressure loss is reduced by 7.9% as an optimization achievement.

Turbine Power Since the turbine blade geometries are modified in the optimized design, the new turbine performance metrics change. Although the optimization process has achieved the goal of minimizing entropy generation through the turbine, the turbine output work as an important performance parameter must be checked in parallel. Ideally, it is desired to increase or maintain the turbine work as is in the base design. The total enthalpy change, namely work per unit mass, together with the averaged entropy change for each rotor row is plotted in Fig.13 for both base and optimized designs. The values are time-averaged over a pulse which are mass-averaged on the planes upstream and downstream the rows. It is seen that the optimization process reduces the first rotor work 15.7% respecting the base design while the entropy is decreased favorably by 27.5%. This enthalpy reduction can be explained by the Euler turbine equation, i.e. $\Delta H = U \Delta V_\theta$, where U is rotational velocity at a reference radius and V_θ represents tangential flow velocity. The outlet angle of the first rotor blades is increased in the optimized version from the base design. While the inlet angle is kept constant, the blade curvature is decreased so that the blade role in turning the incoming flow is reduced (see Fig.9). The averaged flow turning by the first rotor blade is calculated over a pulse, and the corresponding values are 92 degree and 78 degree for the base and optimized cases, respectively. Thus, less enthalpy change is anticipated in the optimized case. Contrary to the first rotor row, the second rotor row exhibits a reverse change in work extraction and entropy generation. It has 20.5% higher work per unit mass than the base design in the optimized turbine configuration. The second rotor generates higher entropy in the optimized configuration than the baseline. Since the blade geometry of the second rotor row is identical in both cases, the reason can be found in axial velocity magnitude and the first stationary vane modifications made in the optimized design. The outlet blade an-

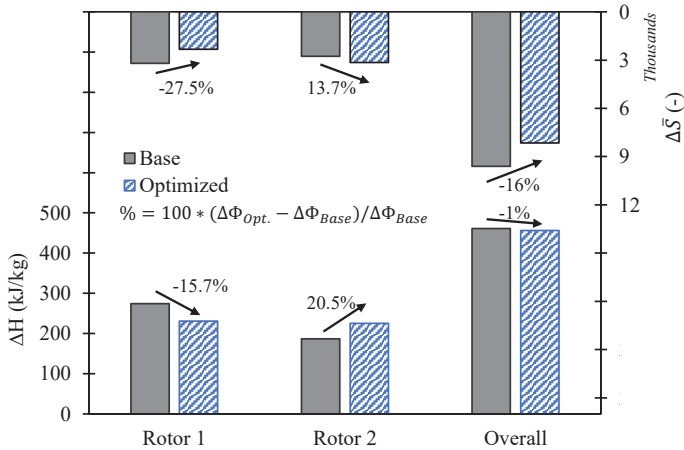


FIGURE 13. TOTAL ENTHALPY AND ENTROPY CHANGE IN ROTORS.

gle of the first vane is increased similar to the first rotor blades, and also the number of blades is decreased. While the rotational speed is fixed, these changes, together with the resulting increase in the inlet flow area of the first stationary vanes, lead to an increase in the overall mass flow rate. Since the number of the rotor blades is increased in the optimized case, a higher axial velocity inside the rotor blade passages has resulted than the base case. The time-averaged mass flow rates are 53.1 kg/s and 61.4 kg/s for base and optimized designs respectively. Therefore, according to the velocity triangle, higher work output is expected from the second rotor row. In the case of the first rotor row, the effect of change in blade turning angle on the output work is more dominant than that of the related change in axial velocity magnitude. The overall work per unit mass for the whole turbine is also calculated, showing a 1% reduction in the optimized design compared to the base case. As reported before, the overall entropy is reduced in the optimum design by 16%. To compare the output turbine power, the time-dependent power over a pulse is depicted in Fig.14. While the overall trends of the instantaneous power are identical for both designs, the optimized case produces more power over the entire pulse. The highest power is achieved at around 0.6 of time period where the entropy is the lowest (see Fig.10). The higher power is mainly due to the higher mass flow rate in the optimized design than its counterpart. The time-averaged power is 24.7 MW and 28.2 MW for the base and optimized cases, respectively. This difference indicates a 14.2% higher power that obtained by the optimization process.

Steady-State operation To evaluate how the optimized geometry performs in steady-state conditions, the inlet pulse is divided into three discrete points of trough, mean and peak of the pulse (see Fig.7). Steady 3D-CFD simulations are performed

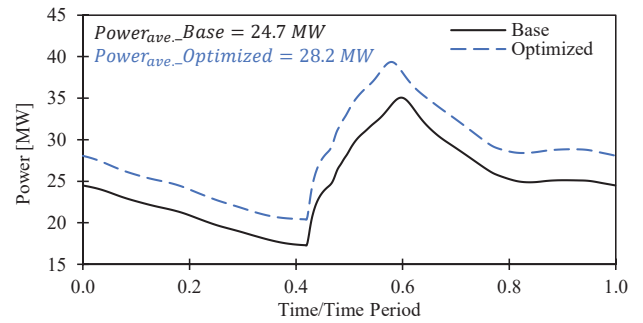


FIGURE 14. INSTANTANEOUS TURBINE OUTPUT POWER.

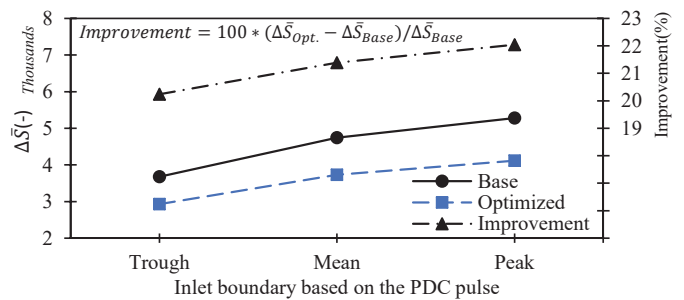


FIGURE 15. ENTROPY GENERATION OF THE FIRST STAGE IN STEADY-STATE OPERATION AT THE INLET BOUNDARIES EQUAL TO TROUGH, MEAN, AND PEAK OF THE PDC PULSE.

by applying each of these conditions as the inlet boundary. The mass-averaged entropy generation for the first stage is calculated and depicted in Fig.15. The results show that the optimized stage, which is optimized based on the unsteady operation over the entire inlet pulse, has a lower entropy generation in steady operations as well. The differences between the entropy generation by the two geometries, displayed with a dash-dot curve in Fig.15, are 20.2%, 21.3%, and 22% at trough, mean, and peak points, respectively. Although the optimized stage has a little better performance at the peak point than at the other points, it is concluded that the optimization process brings a geometry that can work almost the same under different steady conditions over a pulse. In contrast, an optimization based on the steady operations at trough and peak points by Fernelijs et al. [13] for an unsteady turbine, working under a sinusoidal boundary condition, showed that the entropy generation improvement by the geometries optimized at these points can be very different (a difference around 50%).

CONCLUSION

In this paper, a fast approach for a PDC-operated turbine performance optimization is presented and evaluated. A method has been introduced to evaluate the objective function as the main

part of the optimization, which integrates an unsteady 1D-Euler turbine simulation, a meanline steady-state analysis, and a PDC numerical model. The latter two provide the 1D-Euler simulation with the turbomachinery source terms and the time-dependent PDC boundary conditions, respectively. The optimization was performed using an adaptive surrogate model-based framework that utilizes the complex shape method as a searching algorithm. The approach was run for a two-stage turbine to minimize the entropy generation by modifying some geometrical parameters in the first stage, which experiences the highest unsteadiness from PDC exhaust flow. The optimized design was compared to the base design using the unsteady 3D-CFD simulations to evaluate the accuracy of the optimization approach and validate the new design.

The optimization results showed that the new design has a lower solidity in the first stationary vanes but higher in rotor blades than the base case. The blade outlet angles were recommended to open slightly so that the blade turnings were reduced while the maximum thickness to chord ratio of the first rotor blades was almost unchanged. The optimum design showed a 16% reduction in entropy generation and a 14.2% gain in the overall turbine power. The unsteady 3D-CFD results indicated that the lower entropy generation is due to the shortening of the flow wake region on the suction surface of the blades in the optimized geometries, and the higher output power is mainly because of the higher mass flow rate in the new design. Additionally, the rotor blades showed a more noticeable role in lowering the entropy generation than the stationary vanes.

All in all, the optimization methodology, coupled with a fast unsteady turbine simulation tool, was proven to be effective in unsteady turbine optimization problems. The main advantage of the proposed algorithm lies in the objective function evaluation procedure that considers unsteadiness within the optimization loops. Although the unsteady effects in turbomachinery make any 3D-CFD method highly expensive and almost impossible to be integrated into the related optimization problems, the proposed approach showed its robustness and applicability. Therefore, the methodology enables the designers to perform optimizations over a wide range of variables within a reasonable time. It should be noted that since it is the meanline analysis that provides the source terms to the unsteady 1D-Euler simulation tool, considering the nature of this method, there might be a limitation in selecting the optimization variables. Suppose the desired optimization variables cannot be included directly in the meanline analysis, e.g., specific modifications to the blade profile or any hub or shroud contouring, for which there is no correlation available. In that case, one can replace the meanline method with the steady-state CFD simulation, which does not impose much computational cost.

ACKNOWLEDGMENT

The authors would like to acknowledge the financial support from Elsa Neumann Foundation (NaFöG). Additionally, Norddeutscher Verbund für Hoch- und Höchstleistungsrechnen (HLRN) is acknowledged for providing the high performance computing resources.

REFERENCES

- [1] International Energy Agency, 2021. “Global Energy Review 2021”. *Global Energy Review 2020*, pp. 1–36.
- [2] Stathopoulos, P., 2018. “Comprehensive Thermodynamic Analysis of the Humphrey Cycle for Gas Turbines with Pressure”. *Energies*, **11**(3521).
- [3] Paxson, D. E., and Kaemming, T. A., 2012. “Foundational performance analyses of pressure gain combustion thermodynamic benefits for gas turbines”. *50th AIAA Aerospace Sciences Meeting Including the New Horizons Forum and Aerospace Exposition*(January), pp. 1–13.
- [4] Stathopoulos, P., Rähse, T., Vinkeloe, J., and Djordjevic, N., 2020. “First law thermodynamic analysis of the recuperated humphrey cycle for gas turbines with pressure gain combustion”. *Energy*, **200**, 6, p. 117492.
- [5] Glaser, A., Caldwell, N., and Gutmark, E., 2007. “Performance of an Axial Flow Turbine Driven by Multiple Pulse Detonation Combustors”. *45th AIAA Aerospace Sciences Meeting and Exhibit*(January), pp. 1–10.
- [6] Rasheed, A., Furman, A., and Dean, A., 2005. “Experimental Investigations of an Axial Turbine Driven by a Multi-Tube Pulsed Detonation Combustor System”. In 41st AIAA/ASME/SAE/ASEE Joint Propulsion Conference & Exhibit, no. July, American Institute of Aeronautics and Astronautics, pp. 1–13.
- [7] Rasheed, A., Furman, A. H., and Dean, A. J., 2011. “Experimental Investigations of the Performance of a Multitube Pulse Detonation Turbine System”. *Journal of Propulsion and Power*, **27**(3), pp. 586–596.
- [8] Anand, V., St. George, A., Knight, E., and Gutmark, E., 2019. “Investigation of pulse detonation combustors — Axial turbine system”. *Aerospace Science and Technology*, **93**, 10, p. 105350.
- [9] Fernelius, M. H., and Gorrell, S. E., 2020. “Mapping Efficiency of a Pulsing Flow-Driven Turbine”. *Journal of Fluids Engineering*, **142**(6), 6, pp. 1–8.
- [10] Van Zante, D., Envia, E., and Turner, M. G., 2007. “The Attenuation of a Detonation Wave By an Aircraft Engine Axial Turbine”. In ISABE, no. September, pp. 1–12.
- [11] Xisto, C., Petit, O., Grönstedt, T., Rolt, A., Lundbladh, A., and Paniagua, G., 2018. “The efficiency of a pulsed detonation combustor–axial turbine integration”. *Aerospace Science and Technology*, **82-83**(August), 11, pp. 80–91.
- [12] Cuciumita, C., and Paschereit, C. O., 2019. “Numerical

- Performance Assessment of a Turbine Blade Row Operating Under Pulsed Detonation Combustion Inlet Conditions”. In Volume 2B: Turbomachinery, American Society of Mechanical Engineers.
- [13] Fernelius, M. H., and Gorrell, S. E., 2021. “Design of a Pulsing Flow Driven Turbine”. *Journal of Fluids Engineering, Transactions of the ASME*, **143**(4), pp. 1–9.
- [14] Yang, M., Deng, K., Martines-Botas, R., and Zhuge, W., 2016. “An investigation on unsteadiness of a mixed-flow turbine under pulsating conditions”. *Energy Conversion and Management*, **110**, pp. 51–58.
- [15] Taddei, S. R., 2020. “Time-marching solution of transonic flows at axial turbomachinery meanline”. *Proceedings of the Institution of Mechanical Engineers, Part G: Journal of Aerospace Engineering*, 12, p. 095441002097735.
- [16] Dittmar, L., and Stathopoulos, P., 2020. “Numerical Analysis of the Stability and Operation of an Axial Compressor Connected to an Array of Pulsed Detonation Combustors”. In Volume 5: Controls, Diagnostics, and Instrumentation; Cycle Innovations; Cycle Innovations: Energy Storage, American Society of Mechanical Engineers.
- [17] Chiong, M. S., Rajoo, S., Romagnoli, A., Costall, A. W., and Martinez-Botas, R. F., 2014. “Integration of meanline and one-dimensional methods for prediction of pulsating performance of a turbocharger turbine”. *Energy Conversion and Management*, **81**, pp. 270–281.
- [18] Asli, M., Garan, N., Neumann, N., and Stathopoulos, P., 2021. “A robust one-dimensional approach for the performance evaluation of turbines driven by pulsed detonation combustion”. *Energy Conversion and Management*, **248**, 11, p. 114784.
- [19] Timko, L. P., 1984. Energy Efficient Engine High Pressure Turbine Component Test Performance Report. Tech. rep., General Electric Co. Cincinnati, OH, United States.
- [20] Berndt, P., Klein, R., and Paschereit, C. O., 2016. “A kinetics model for the shockless explosion combustion”. *Proceedings of the ASME Turbo Expo*, **4B-2016**, pp. 1–8.
- [21] Aungier, R. H., 2006. *Turbine Aerodynamics: Axial-Flow and Radial-Flow Turbine Design and Analysis*. ASME Press, Three Park Avenue New York, NY 10016-5990, 1.
- [22] Burke, M. P., Chaos, M., Ju, Y., Dryer, F. L., and Klippenstein, S. J., 2012. “Comprehensive H₂/O₂ kinetic model for high-pressure combustion”. *International Journal of Chemical Kinetics*, **44**(7), 7, pp. 444–474.
- [23] Neumann, N., Asli, M., Garan, N., Peitsch, D., and Stathopoulos, P., 2021. “A fast approach for unsteady compressor performance simulation under boundary condition caused by pressure gain combustion”. *Applied Thermal Engineering*, 6, p. 117223.
- [24] Menter, F. R., 1994. “Two-equation eddy-viscosity turbulence models for engineering applications”. *AIAA Journal*.
- [25] Asli, M., Stathopoulos, P., and Paschereit, C. O., 2021. “Aerodynamic Investigation of Guide Vane Configurations Downstream a Rotating Detonation Combustor”. *Journal of Engineering for Gas Turbines and Power*, **143**(6), 6.
- [26] Sousa, J., Paniagua, G., and Saavedra, J., 2017. “Aerodynamic response of internal passages to pulsating inlet supersonic conditions”. *Computers and Fluids*, **149**, pp. 31–40.
- [27] Celik, I. B., Ghia, U., Roache, P. J., Freitas, C. J., Coleman, H., and Raad, P. E., 2008. “Procedure for Estimation and Reporting of Uncertainty Due to Discretization in CFD Applications”. *Journal of Fluids Engineering*, **130**(7), p. 078001.
- [28] Yondo, R., Andrés, E., and Valero, E., 2018. “A review on design of experiments and surrogate models in aircraft real-time and many-query aerodynamic analyses”. *Progress in Aerospace Sciences*, **96**(March), 1, pp. 23–61.
- [29] Jin, Y., 2005. “A comprehensive survey of fitness approximation in evolutionary computation”. *Soft Computing*.
- [30] Montgomery, D. C., 2017. *Montgomery: Design and Analysis of Experiments*.
- [31] Xu, H., Liu, L., and Zhang, M., 2020. “Adaptive surrogate model-based optimization framework applied to battery pack design”. *Materials & Design*, **195**, 10, p. 108938.
- [32] Han, Z.-H., Zhang, Y., Song, C.-X., and Zhang, K.-S., 2017. “Weighted Gradient-Enhanced Kriging for High-Dimensional Surrogate Modeling and Design Optimization”. *AIAA Journal*, **55**(12), 12, pp. 4330–4346.
- [33] Baert, L., Chérière, E., Sainvitu, C., Lepot, I., Nouvellon, A., and Leonardon, V., 2020. “Aerodynamic Optimization of the Low-Pressure Turbine Module: Exploiting Surrogate Models in a High-Dimensional Design Space”. *Journal of Turbomachinery*, **142**(3), 3, pp. 1–11.
- [34] Gao, H. F., Zio, E., Wang, A., Bai, G. C., and Fei, C. W., 2020. “Probabilistic-based combined high and low cycle fatigue assessment for turbine blades using a substructure-based kriging surrogate model”. *Aerospace Science and Technology*.
- [35] Jones, D. R., Schonlau, M., and Welch, W. J., 1998. “Efficient Global Optimization of Expensive Black-Box Functions”. *Journal of Global Optimization*, **13**(4), pp. 455–492.
- [36] Regis, R. G., and Shoemaker, C. A., 2007. “A stochastic radial basis function method for the global optimization of expensive functions”. *INFORMS Journal on Computing*.
- [37] Regis, R. G., and Shoemaker, C. A., 2013. “A quasi-multistart framework for global optimization of expensive functions using response surface models”. In *Journal of Global Optimization*.
- [38] Bakhtiari, F., and Schiffer, H.-P., 2019. “Numerical approach to the modelling of transient interaction of prospective combustor concepts and conventional high pressure turbines”. *Propulsion and Power Research*, **8**(1), 3, pp. 1–12.
- [39] Coull, J. D., 2017. “Endwall loss in turbine cascades”.

Journal of Turbomachinery, **139**(8), pp. 1–12.

- [40] Ainley, D. G., and Mathieson, C. R., 1951. A Method of Performance Estimation for Axial-Flow Turbines. Tech. Rep. 2974.

5

Discussion

In this chapter, the main findings of the publications presented in the previous chapter are reviewed and placed into an overall context. Since the main objectives of the thesis are twofold, the discussion of the results is divided into two categories. Firstly in sec.5.1, the findings on the interaction of turbine guide vanes with RDC exhaust flows are discussed, which mainly covers the Publication I and Publication II with some supports from other publications of the author. The nominal operation of the RDC with a coupled turbine guide vanes, effects of some blade geometrical parameters on the performance of the vanes, the role of guide vanes in different RDC operating regimes, and the vane setting angle effect on the performance of the guide vanes are examined as well.

Secondly, in sec.5.2, the interaction of PDC tubes configurations with a two-stage turbine is reviewed, which was addressed within the context of Publication III and Publication IV. Although the main focus in these two publications is introducing a fast and reliable simulation methodology and its applicability to be integrated into an unsteady turbine optimization problem, the results of the simulations provide a deeper insight into the PDC-turbine interaction. Three different PDC configurations are considered upstream of a conventional turbine, and the turbine performance results are compared. Furthermore, an optimized turbine geometry for one of the PDC configurations is assessed with respect to the performance of the baseline turbine geometry.

5.1 RDC-turbine

As discussed earlier in this thesis, the presence of any outlet restriction in an RDC exhaust channel may have an impact on the RDC operating conditions, addressed recently by Bach et. al [73]. The turbine blades for extracting the energy from the RDC exhaust is a restriction that changes the flow field upstream. Experimental measurements are not fully capable of shedding light into the entire flow field and describing what is happening inside. As an example, the compact geometry and hot exhaust gases do not allow placing probes inside the RDC exhaust domain. Apart from that, assessing the performance of the turbine blades requires a much closer look at the flow around the blades. The first blade row of a turbine, usually nozzle guide

vanes, is exposed to the most energetic and unsteady version of the RDC exhaust flow. In this regard, analyzing the RDC exhaust flow passing through stationary vanes numerically, supported by the experimental work, addresses the question of integrating RDC and turbine by clarifying how the vanes act in such a flow field.

Within the scope of Publication I, the numerical analysis of the stationary vanes downstream an RDC is presented. The geometrical model is similar to the experimental setup [104]. The RDC operating point for which the numerical simulation is done produce a single rotating detonation wave with a frequency of 5 kHz. In the first campaign of simulations, the experimental pressure data upstream and downstream of the vanes are kept as the references in a way such the boundary conditions get tuned. The velocity angle at the turbine inlet is assumed to be constant. This approach and the simplification related to the velocity angle were considered because the only available experimental data, at that point in time, were at the blade's upstream and downstream. Nevertheless, it provides a primary step toward characterizing the RDC-like fluctuating exhaust flow passing through a vane row. The simulated domain shows that the upstream flow field is entirely subsonic, and no shock wave is captured upstream of the vanes. However, near the blade trailing edge, where the flow leaves the vanes and expands, the highest Mach number in the supersonic regime is observed. This supersonic Mach number through a shock wave comes to the subsonic regime while the static pressure increases. This can address the doubt that having subsonic or supersonic flow upstream of the vanes may affect the experimental measurements.

Using the same model and numerical method, four different blade setting angles, ranging from 0° to 15° , are examined [142]. Having the boundary conditions fixed, in all cases, the maximum Mach number, which occurs just before the trailing edge shock wave, is identical. This implies that the shock wave strength and the related pressure loss are almost independent of the blade setting angle in these simulations. Figure 5.1 shows the instantaneous total pressure at one chord length downstream of the vanes during a time period. It is seen that as the blade setting angle increases, the overall total pressure decreases, hinting that the total pressure loss increases (see Tab.5.1). Having said the total pressure loss due to the

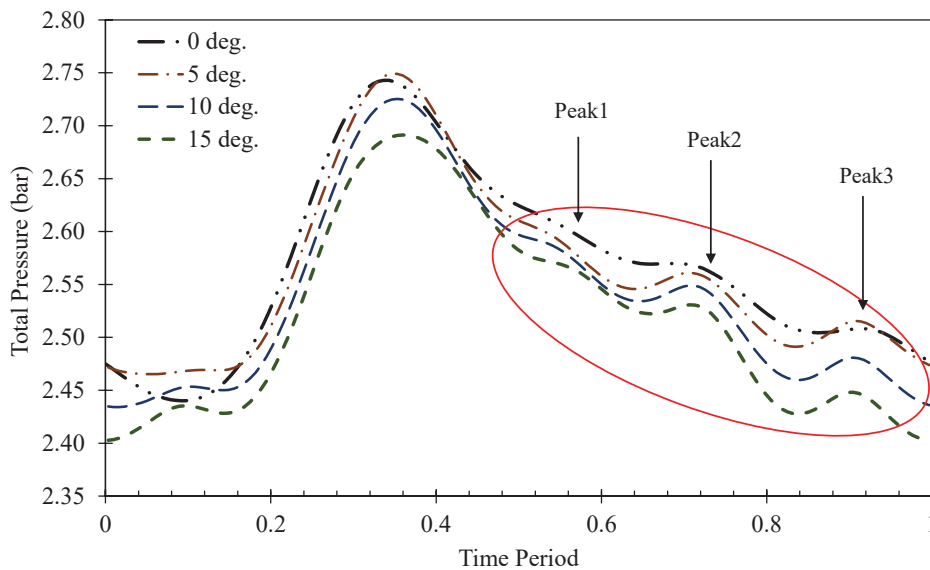


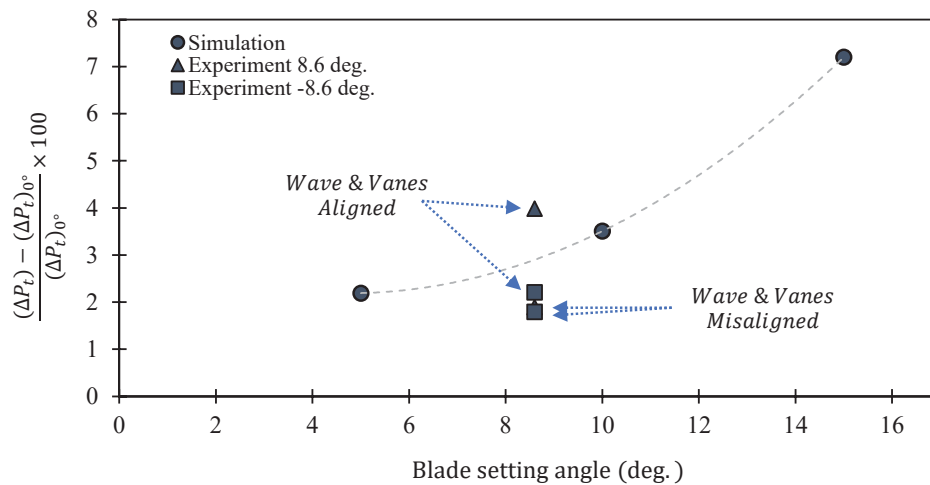
Figure 5.1: Total pressure trace at the blade downstream over a detonation time period.

Table 5.1: Total pressure loss along the stationary vane downstream the RDC for different setting angles.

Blade setting angle	0°	5°	10°	15°
Total pressure loss (kPa)	27.37	27.97	28.33	29.34
Total pressure loss (%)	10.5	10.74	10.87	11.24

trailing edge shock wave is identical, the discrepancies in total pressure loss are mostly related to the profile loss differences. That itself is related to the flow separation over the blade surfaces resulting from the increased incidence angle. Another salient point is that as the blade setting angle increases, total pressure distribution at the blade downstream gets more unstable, indicated by three peaks surrounded by a red ellipse in Fig.5.1. These local peaks are magnified by increasing the blade setting angle, covering almost 50% of the time period, while the fluctuation amplitude does not change. This add-on instability can adversely affect the rotor performance downstream in a turbine configuration.

A comparison between the experimental findings for the staggered vanes [73] and the total pressure loss for different setting angles is shown in Fig.5.2. To allow a comparison, total pressure loss is made non-dimensional by the total pressure loss for zero-staggered vanes. The experimental results are only available for setting angle of ± 8.6 , which are categorized as aligned and misaligned based on the detonation wave and the vane setting angle directions. Although the operating point of the RDC in experimental setup and the numerical simulation is not identical, the total pressure results are in range. The discrepancy may also arise because of the stated assumptions made in the numerical simulation. In the simulations, the blade incidence angle is almost constant for each blade inclination. This causes a rather constant separation and profile loss. In the experimental work, the exhausting flow direction and hence the incidence angle is changing in an RDC cycle, so depending on the overall (averaged) incidence angle, it can provide less separation and losses. Further interpretations requires the experimental velocity angle variation data which is not available due to the related measurement difficulties [73].

**Figure 5.2:** Comparison of total pressure loss for staggered vanes downstream of the RDC.

Applying a different boundary condition having a frequency of 10 kHz from the literature creates a different flow field with a presence of shock waves inside the vane passages. In this

case, the total pressure fluctuations are traced from the domain inlet to the outlet of the vanes. The total pressure amplitude damping from the vanes' inlet to the vanes' outlet is 48%. Using the instantaneous entropy contours superimposed by Mach number contour lines, a moving shock wave is detected inside the vane passage, generating flow separations while interacting with the boundary layer on both sides of the vane. Shock waves and the resulting boundary layer separation can be counted as the primary sources of losses for this specific operating condition. Comparing the averaged total pressure loss over a detonation cycle between the non-blade region from the inlet domain to the blade leading edge and around the vanes indicates that the vanes generate a more significant total pressure loss than what occurs within the non-blade region, although a shock wave is captured in the latter region. Tracking the instantaneous total pressure loss reveals that the critical time during which the vanes' highest instantaneous total pressure loss is between 70-90% of the inlet pressure pulse. This can be of interest in proposing a remedy for mitigating the overall blade loss, like an active flow control method possibly. However, this time duration is a case-dependent parameter which is a function of the RDC operating condition, the domain geometrical parameters, and the blade profile.

Publication II further investigates the RDC and the vane interactions with a focus on the blade geometrical parameters. From a methodological standpoint, the difference between Publication I and Publication II is that the former uses a 3D domain while ignoring any circumferential variation, whereas the latter employs a 2D-unwrapped domain and fully considers the RDC exhaust flow features. Blade space-to-chord ratio and thickness-to-chord ratio are altered, and five vane configurations are simulated using the same boundary conditions. The simulation results are analyzed for two operating regimes of transient operation before reaching a periodically steady flow encompassing a moving shock wave and when the flow field becomes developed once the shock wave moves out from the domain. The total pressure loss results for the cases with different solidities (chord-to-pitch ratio) are unlike trends of conventional loss correlations. The solidity bound for which the simulations are carried out is from 1.76 to 3.53, which corresponds to $s/c = [0.28 \ 0.57]$. Considering the conventional loss coefficient correlations (see Fig.3.4), the traditional coefficient of loss has an increasing trend within the mentioned solidity range, whereas the unsteady simulation results exhibited a reverse trend. This contradiction suggests that the existing loss correlations derived from steady-state turbomachinery operations should be updated for unsteady cases, specifically for turbines working under RDC exhaust flow. Another notable finding is the location of flow choking inside the vane passages. As the solidity increases, the location of the sonic Mach number moves toward the vanes' trailing edge. Additionally, the sonic Mach number location range is shortened within the RDC cycle period by increasing the solidity. The fluctuating flow having time and circumferential-dependent velocity vector causes the choking flow condition not to stay at the vanes' geometrical throat. The mentioned trend for the location of sonic Mach number and its position range implies that the velocity vectors fluctuation gets more dampened in higher solidities. This trend is observed in increasing the maximum thickness-to-chord ratio. These two observations can conclude that the flow area reduction plays a role in damping the velocity angle fluctuation. This is also confirmed by studying the outlet velocity angle fluctuation, shown in Publication II, Fig.9. The vanes attenuate more than 57% of the velocity

angle amplitude, which is enhanced up to 86% by shortening the flow path area, either in the form of increasing solidity or the maximum thickness-to-chord ratio. Tracking the time trace of total temperature and total pressure reveals that increasing solidity makes these two parameter variations smoother, meaning that the local peaks are diminished. A similar trend is also observed by increasing the maximum thickness-to-chord ratio, denoting the effect of area ratio reduction in smoothing the total pressure and temperature trends. Although this consequence is beneficial for potential rotor blades downstream the guide vanes, the fluctuation amplitude of both quantities is adversely affected. The effect of solidity is dominant over the thickness-to-chord ratio in damping total temperature amplitude since the two cases have the same area reduction, but different solidities exhibit dissimilar damping effects. In the transient operation of the RDC-stationary vane, in which a moving shock wave is observed, the amount of loss caused by the shock wave is around two times greater than the generated profile loss. Besides, the total pressure loss trend in unsteady operation contrasts the trend in periodically steady operation. For example, the total pressure loss increases by increasing solidity, which is more related to the strength of the shock wave and the related amount of loss. Higher solidity accelerates the flow more, and hence the shock wave will be stronger. This proves the necessity of avoiding a shock wave inside the domain, particularly in periodically steady operation, either by changing the RDC operating point or designing a customized vane.

To put it in a nutshell, the numerical RDC-vane studies through Publication I and Publication II assert that the blade profile loss in such an unsteady flow field does not follow the conventional loss correlations trends. Having a guide vane can damp the flow velocity fluctuation amplitude so that it provides a steadier flow to any downstream rotor blades. This will be advantageous for rotor blades, which performance is more sensitive to the incidence angle than the stationary vanes. It was shown that solidity has a significant effect on loss generation and total quantities distribution downstream, whereas area reduction can be considered as the most driving factor for velocity angle fluctuation damping.

5.2 PDC-turbine

The unsteady flow simulations through the articles mentioned above showed that the 3D or 2D CFD methods could not provide a handy and quick tool for performance analysis of multistage turbines. Although they are accurate, the required time for each transient simulation makes them difficult to be implemented in early design steps. Usually, several simulations are needed within the process of a turbomachinery design. Additionally, any optimization process requires many simulations, which are not feasible using time-consuming methods. Hence, a 1D-Euler simulation tool has been introduced in Publication III. The methodology is based on solving the Euler equations in the turbine axis direction. The presence of the turbine blade rows in the computational domain is introduced using the related force and work source terms in the equations. The methodology suggests that these source terms can be effectively calculated using a meanline turbine analysis. The in-house developed meanline tool is fast enough to compute the source terms over the turbine operating range. Hence the 1D-Euler solver takes the related source terms for each cell where a blade is located based on the blade's upstream and downstream conditions. To shape a PDC-turbine configuration, a model was

developed in which the PDC tubes blowdown to a plenum that is connected to the turbine inlet. The same 1D-Euler solver is utilized to simulate each PDC tube operation. To evaluate the method's capability, a two-stage turbine was selected comprising four blade rows that makes the simulation problem complicated enough. Three PDC tube configurations having three, five, and seven tubes are considered, and the resulted boundary conditions are applied to the turbine simulation. Simultaneously, 3D-CFD simulations were performed to verify the 1D-Euler simulations. The 1D-Euler method showed very close results with the CFD simulations at the rotor outlets. Temperature and pressure distributions downstream of the rotor well match the CFD results. However, the low order method slightly underestimates the pressure at the stators' downstream. This discrepancy comes from the nature of the 1D method. Within a turbine, the stator deflects the incoming flow within a turbine to increase the tangential flow momentum. The generated momentum is transferred to mechanical work by the succeeding rotor blades. By the same token, the flow velocity vector is divided into two components of tangential and axial parts, assuming zero radial velocity. At the same time, the 1D method only considers the axial velocity in the governing equations. Therefore, it takes a lower velocity magnitude and consequently lower kinetic energy than in reality. This difference is compensated when the flow passes through the rotor blades. The source terms prescribe that the actual amount of work must be extracted from the rotor blades, and hence the tangential velocity must be reduced. The 1D-Euler solver reduces the axial velocity through the process of work extraction so that the flow field downstream of the rotor row is well simulated. Since the main objective of the reduced-order methodology is to predict the overall turbine performance in transient operations, this level of discrepancy just downstream of the stators is acceptable. Besides, instantaneous static pressure distributions at each interstage location (see Fig.10 in Publication III) show that the deviations between the CFD and 1D-Euler simulations are not that high. As a metric in the unsteady operation of a turbine, pressure fluctuation amplitude, mass-averaged over an inlet pulse, is plotted in Fig.5.3 for three PDC-tube configurations. The 3D-CFD and 1D-Euler simulations almost identically capture the averaged pressure amplitude along the turbine. A very small deviation exists at the stator outlet, which is less than 0.5% of static pressure amplitude for the three tubes configuration, as the worst case. The results of the two methods are matched better by increasing the number of PDC tubes and consequently decreasing the fluctuation amplitude at the turbine inlet. A remarkable point in Fig.5.3 is that the first row of the turbine plays a significant role in damping the overall unsteadiness, observed in each PDC configuration. This is aligned with the findings of Bakhtiari and Schiffer [36] who reported 47% damping through the first row of the same turbine but with a sinusoidal shape boundary condition. Having captured almost identical damping levels by the first blade row for different inlet fluctuation amplitude and frequency, one can draw a conclusion that the damping role of the vane row is more a function of geometry than inlet fluctuation features of amplitude and frequency. In addition, it is concluded that the first blade row or the first stage of a turbine exposed to the high level of unsteadiness plays a considerable role in damping the incoming fluctuations and should be carefully designed or modified.

The robustness of the 1D methodology can be reflected in its capability to simulate the transient turbine map accurately. The turbine map is conventionally illustrated by the turbine total pressure ratio over its reduced mass flow rate, or vice versa. The turbine characteristic is

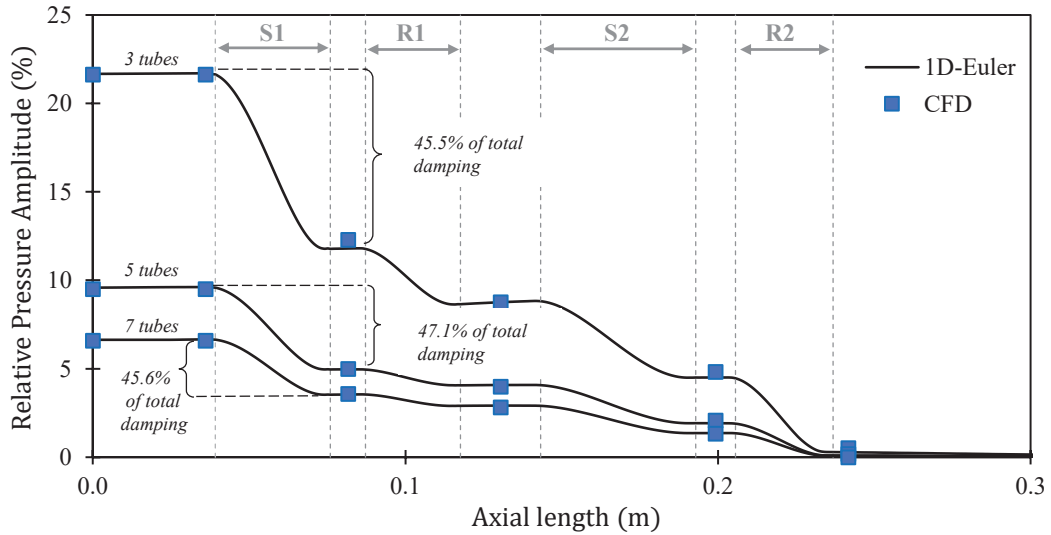


Figure 5.3: Static pressure damping throughout the turbine connected to different PDC tube arrangements.

a close loop encapsulating the steady-state performance curve in a transient periodic boundary condition. Depending on the fluctuation features of the boundary conditions, the characteristic loop will widen or shrink around the steady-state curve. In general, the sharper change in the boundary condition, the broader closed loop. The 1D-Euler method could correctly calculate the unsteady performance characteristic of the turbine compared to the 3D-CFD results, shown by Fig.13 in Publication III. This means that the developed methodology precisely models both instantaneous mass flow rate and pressure ratio. Having a deeper look at the instantaneous mass flow rate showed that the majority of the instantaneous reduced mass flow rate in a pulse cycle lies within $\pm 5\%$ deviation from the CFD-computed values.

Regarding the plenum modeling, it was assumed that no shock wave exists inside the plenum space, which was not the case as observed in the experimental investigations by Reza Haghdoust [143]. However, the proposed 1D methodology can easily consider shock wave effects inside the plenum by taking the related loss source terms in the governing equations. Since the strength of shock wave and the related amount of losses depend on the plenum geometry and the connection between PDC tubes and the plenum, these losses must be calibrated for each plenum, which is out of this dissertation scope. It is good to mention that the 1D-Euler approach has been modified and tested for multistage compressor applications in another publication of the author and his colleagues [111] which is not included in this thesis. The results were promising for a multistage compressor connected to a PDC-tube configuration.

An important need for a fast and reliable simulation tool is to use it in a design and optimization process. Once the capabilities of the 1D-Euler methodology in simulating a multistage turbine's unsteady operation is verified through a back-to-back comparison with the high fidelity but time-consuming method of 3D-CFD, an optimization problem is defined to assess the practical implementation of the developed tool. This has been done within the scope of Publication IV. The test case for the optimization was selected to be a conventional turbine designed for steady operations, as used in the previous publication. Minimizing the entropy generation is the objective of the optimization process using geometrical variables of blade solidity, thickness-to-chord ratio, and outlet blade angle. These parameters have been

selected because they play a considerable role in entropy generation in axial turbines according to the conventional loss correlations. Additionally, the available geometrical information of the baseline geometry allows for such a variable selection. According to the previous findings, the first stage is the most vulnerable part in a turbine connected to a pressure gain combustor. So, the mentioned variables are changed only for the first stator and rotor blades in the optimization problem. In this regard, a five-dimensional design space is created. The bounds for each variable are specified based on the recommendations and available data in the open literature, mostly related to the ranges for which the loss correlations were developed. For example, solidity (c/s) can vary in a range based on the bound in Fig.3.4. The boundary condition for the turbine is computed based on the presence of five PDC tubes upstream of the turbine blowing down to a plenum. A surrogate-based optimization algorithm based on the complex shape method is utilized as the optimization tool. Several calls to the objective function evaluator within the optimization procedure are made. The objective function evaluator is the developed 1D-Euler methodology which takes just a few minutes to deliver the amount of generated entropy as the objective function value.

The optimization results showed that if the two-stage turbine is working under the PDC exhaust flow, the first stage can be optimized to reduce the whole turbine entropy generation by 16%. This amount of reduction in entropy generation is caused by shrinking the wake region on the blade suction surfaces. Since both blades' outlet angles are increased in the optimized geometry, the uncovered turnings of the blades are reduced. The lower uncovered turning makes the flow remains more attached after the blade's throat section. If the uncovered turning is too high, it will increase the flow deviation angle, which unfavorably affects the overall flow turning by the blades and consequently work output from the rotor row. Since the blade inlet angles are kept fixed, it is expected that the change in the stator outlet angle is made in a way that the rotor incidence angle is as small as possible during the transient operation.

Comparing the share of the first stage entropy generation in the whole turbine between the baseline and optimum geometry indicated that the first stage produces 40% of the whole turbine entropy in the optimum design. At the same time, this percentage is 50% in the baseline design. This comparison implies that the optimization process was successful to reduce the entropy generation by modifying the first stage geometry, but the second stage is responsible for 60% of the overall entropy generation now. Ideally, this amount can be lowered to 50%. That means the second stage in the unsteady operation may not work at its best condition; hence it could also be subjected to an optimization procedure. This opens the question of how much the entropy generation can be lowered if all blade rows are optimized simultaneously.

Assessing the total pressure loss in the optimized blade rows shows 28.2% and 11.6% reductions in the total pressure loss coefficient of stator and rotor, respectively. Considering the fact that no shock wave has been captured during the unsteady operation of the turbine, the profile loss type can be responsible for the majority of the losses. According to the traditional profile loss correlation explained in sec.3.1.3, the lower solidity of the stator is in a range that the optimized geometry should have a lower total pressure loss coefficient, which is confirmed by the optimization results. In the case of rotor blades, the optimized

geometry has a higher solidity than the baseline. Looking up the related trend in the profile loss correlation depicted in Fig.3.4 and formulated in Eq.3.21, ascertains that this change in solidity increases the total pressure loss coefficient. Nevertheless, the rotor total pressure loss coefficient decreases in the optimized version. This conflict, which has been observed in Publication II for RDC-vane interaction as well, confirms that turbines working under unsteady flow of pressure gain combustion do not necessarily follow the conventional loss correlations developed for steady turbomachineries. This brings up another open question that how the loss correlations can be modified to cover unsteady operations of turbomachineries.

The optimized turbine also showed an increase in the output power. The time-averaged turbine output power increases by 14.2% by modifying the first stage. Although the optimization objective is to minimize the entropy generation, a higher output power is achieved. Since the overall total enthalpy decreases by 1% (shown in Publication IV, Fig. 13) as a result of optimization, the mass flow rate increment is responsible for the positive change in the turbine power. The number of blades in the first stator row is decreased, leading to an increase in the incoming flow area. Additionally, the number of rotor blades is increased in the optimized case. Hence, a higher axial velocity inside the rotor blade passages has resulted in the optimized case than the baseline geometry. These two consequences of the blade geometry changes raise the turbine mass flow rate so that the turbine output power increases accordingly.

This optimization work presented a practical use of the 1D-Euler methodology in a turbine design and optimization process. The heart of the proposed method is the 1D-Euler solver, which is supported by a meanline turbomachinery analysis. The meanline analysis module can be replaced by any other steady-state turbomachinery analysis such as streamline curvature method or two- or three-dimensional CFD analysis. It mainly depends on the user preference by which methodology the source terms are computed. Also, the meanline analysis or streamline curvature method has some limitations. For instance, the effect of minor changes in blade profile or endwall shape cannot be easily implemented in these steady-state analysis tools unless the related correlations are available. So, if one needs to consider such variables in an optimization problem using the presented 1D-Euler method, the CFD steady-state tool would be the best to supply the source terms.

6

Conclusions and Outlook

The present work investigated the turbine integration with two pressure gain combustion devices of rotating detonation and pulsed detonation combustors. Following a comprehensive literature review and presenting the involved methods, the results were illustrated in terms of four peer-reviewed papers.

The first two papers focused on the interaction of RDC exhaust flow and a stationary guide vane row to explore the flow field and the unsteady phenomena thereof numerically. URANS simulations were performed using different inlet boundary conditions representing different RDC exhaust flows to visualize the flow field and evaluate the blade performance in such unsteady domains. The studies successfully budget total pressure losses and the fluctuation damping achieved through the vanes and shed some light on what happens around the vanes, where it is unreachable in experimental works. Additionally, some important blade geometrical parameters were varied to assess the associated losses and performance. The results analyzed the connection between total pressure loss and the vanes solidity and thickness-to-chord ratio. Any turbine expander downstream an RDC should be able to work with the unsteady flow. In this regard, the role of stationary vanes in damping the fluctuation is crucial for the adjacent rotor blades since the rotor blades are susceptible to the incidence angle variations and lose their nominal performance while being exposed to such large fluctuations. The results showed that more than 57% of the upstream velocity angle fluctuation was damped through a simple symmetrical guide vane row. Area reduction by the vanes' presence was found to be a key parameter in alleviating the velocity angle fluctuation amplitude. Based on the studied cases, it is concluded that solidity had the highest impact on loss generation in stationary vanes and total quantities distribution downstream. Area reduction, through increasing whether solidity or thickness-to-chord ratio, was the most driving factor for velocity angle fluctuation damping. These geometrical parameters have a high impact on loss generation by the turbomachinery blades, and as this study has confirmed, they play a significant role in damping the fluctuation coming from the RDC exhaust flow and must be carefully selected in design procedures.

The third and fourth papers focused on presenting a fast and reliable methodology for multistage turbine transient simulation. As an essential part of any design and optimization procedure, simulating an unsteady multistage turbine using 3D- or 2D-CFD methods can be

computationally too expensive. As seen in the related literature, designers and researchers shift to using steady-state simulation methods in optimization processes as an alternative to reduce the associated costs. Nevertheless, the real unsteady effects do not reflect in the design optimization procedures if steady simulations are employed. Hence, a 1D-Euler simulation methodology was introduced in the third publication, and its pros and cons were scrutinized using back-to-back URANS simulations. The configurations with which the methodology was examined comprised multiple PDC tubes connected to a two-stage turbine using a plenum. The PDC tubes were fired sequentially to generate pulsating flow for the turbine. The 1D-Euler methodology was used to simulate the PDC operations with the source terms computed from the chemical reaction calculations. For turbine simulation, the same 1D methodology as for PDC simulations was utilized but with taking advantage of a coupled meanline turbine analysis tool to provide the turbomachinery source terms. The detailed analysis of the results in terms of time-dependent thermodynamic quantities and performance parameters proclaimed a perfect matching between the results from the developed 1D methodology and 3D-URANS simulations for different PDC configurations. A practical implementation of the method was presented in the fourth paper. The developed 1D-Euler method was employed as the objective function evaluator in an optimization procedure. The objective was to minimize the entropy generation of the two-stage turbine by finding the optimum geometrical parameters of the first turbine stage. The blade outlet angles, solidity and the thickness-to-chord ratio shaped the design space for the optimization problem. These geometrical variables were selected based on their profound effects on the turbine loss, reported in the literature. The optimum parameters were found through a surrogate-based optimization technique, leading to decreased turbine entropy generation by 16% and increased turbine power by 14% while working under PDC tubes exhaust flow. The optimization results suggest that both stator and rotor outlet angles should open up slightly, and the first stator vanes should have lower solidity. In contrast, the rotor row solidity needs to be increased to perform optimally. A 3D-URANS simulation was utilized to verify the results with which the 1D method findings agreed. Besides the detailed discussion of the optimization results, in general, this work proposes a promising way to the pressure gain combustion and turbomachinery community toward developing or modifying turbine expanders for efficient energy extraction from the unsteady and high-temperature exhaust flow of the PGC devices.

Future works

In summary, this thesis addressed some fundamental questions in pressure gain combustion applications by looking into the details of the flow field around a row of vane downstream an RDC and developing a reliable methodology for simulating unsteady turbine working with PDC tubes. Within the scope of turbine integration with pressure gain combustors, there are still different open questions that could not be covered in the current work but can be suggested as future works. Toward addressing the efficient ways of energy extraction from PGC devices, the developed methodology in this dissertation can be an easy-to-use tool for trying different concepts, ranging from evaluating the existing turbines working with PGCs to examining the new concepts such as shock divider concepts [144], bladeless turbine [145] and even unprecedented approaches.

The accuracy of the 1D-Euler methodology was assessed in PDC-turbine simulation. Considering the inherent differences between RDC and PDC flows, further modifications are required to extend the methodology for RDC-turbine applications. The exhaust flow of RDC is characterized by time-dependent circumferential variations. Therefore, more adjustments are needed for the 1D-Euler method to capture most of the flow phenomena in RDC-turbine applications.

As stated in the scope of the last two publications, the PDC-turbine configuration comprises a plenum between the two devices. This plenum was modeled as a zero-dimensional volume neglecting any entropy generation inside it despite the fact that shock waves can be present as observed by Rezay Haghdoost [143]. Flow expansion inside the plenum and the related pressure gradient can also cause entropy generation. For a more realistic PDC-turbine modeling, these loss sources and the related amount should be estimated and inserted as a source term in the developed approach. This can be done using a numerical simulation of the plenum via conventional CFD tools for specific applications. It would also be possible to go one step further and develop a rather generalized loss model for a typical plenum geometry using a series of numerical simulations.

The numerical simulations in this dissertation, as well as another published article by the author and his colleagues [111] prove the applicability of the 1D-Euler method for simulating PDC-turbine and compressor-PDC configurations separately. A unified 1D-Euler methodology that considers compressor, PGC, and turbine all together can provide a beneficial performance evaluation tool at the engine level with low computational cost. This tool will have the advantage of considering the interaction between these three devices instead of modeling them individually.

As part of the results presented in this thesis, the turbines working under the boundary conditions caused by pressure gain combustion do not necessarily follow the existing loss correlations. Basically, the conventional loss correlations have been developed for steady-state turbomachinery. Therefore, these correlations should be updated for such out-of-the-ordinary applications. This loss correlation development can be done numerically with the support of experimental work to ease the process and reduce the related costs.

References

- [1] Sylvain Ponserre, Justin Ginnetti, and IDMC. *Disaster Displacement: A global review 2008-2018, Thematic Report*. Tech. rep. 2019, pp. 1–56. URL: <https://www.internal-displacement.org/sites/default/files/publications/documents/201905-disaster-displacement-global-review-2008-2018.pdf>.
- [2] Kanta Kumari Rigaud et al. *Groundswell: Preparing for internal climate migration*. Tech. rep. 2018.
- [3] Mohammad S. Masnadi et al. “From fossil fuels towards renewables: Inhibitory and catalytic effects on carbon thermochemical conversion during co-gasification of biomass with fossil fuels”. In: *Applied Energy* (2015). ISSN: 03062619. DOI: 10.1016/j.apenergy.2014.12.006.
- [4] Hannah Ritchie and Max Roser. “CO and Greenhouse Gas Emissions”. In: *Our World in Data* (2020). URL: <https://ourworldindata.org/co2-and-other-greenhouse-gas-emissions>.
- [5] M. V. Rodionova et al. *Biofuel production: Challenges and opportunities*. 2017. DOI: 10.1016/j.ijhydene.2016.11.125.
- [6] Bernhard C. Bobusch et al. “Shockless explosion combustion: An innovative way of efficient constant volume combustion in gas turbines”. In: *Combustion Science and Technology*. 2014. DOI: 10.1080/00102202.2014.935624.
- [7] Daniel E. Paxson and Kevin Dougherty. “Operability of an ejector enhanced pulse combustor in a gas turbine environment”. In: *46th AIAA Aerospace Sciences Meeting and Exhibit*. 2008. ISBN: 9781563479373. DOI: 10.2514/6.2008-119.
- [8] Lijun Pan and Wancheng Sheng. “The scalar Zeldovich-von Neumann-Döring combustion model (I) interactions of shock and detonation”. In: *Nonlinear Analysis: Real World Applications* (2009). ISSN: 14681218. DOI: 10.1016/j.nonrwa.2007.10.008.
- [9] Panagiotis Stathopoulos, Johann Vinkeloe, and Christian Oliver Paschereit. “Thermodynamic evaluation of constant volume combustion for gas turbine power cycles.” In: *International Gas Turbine Congress (accepted for publication)*. Tokyo, 2015.
- [10] William H. Heiser and David T. Pratt. “Thermodynamic Cycle Analysis of Pulse Detonation Engines”. In: *Journal of Propulsion and Power* (2002). ISSN: 0748-4658. DOI: 10.2514/2.5899.
- [11] G. D. Roy et al. *Pulse detonation propulsion: Challenges, current status, and future perspective*. 2004. DOI: 10.1016/j.pecs.2004.05.001.

REFERENCES

- [12] C. A. Nordeen et al. “Role of inlet reactant mixedness on the thermodynamic performance of a rotating detonation engine”. In: *Shock Waves* 26.4 (July 2016), pp. 529–529. ISSN: 0938-1287. DOI: 10.1007/s00193-016-0681-9. URL: <http://link.springer.com/10.1007/s00193-016-0681-9>.
- [13] Fabian Enrico Habicht. “Towards the implementation of a pulse detonation combustor into a gas turbine”. PhD thesis. Berlin: Technische Universität Berlin, 2021. DOI: 10.14279/depositonce-12456. URL: <http://dx.doi.org/10.14279/depositonce-12456>.
- [14] Mohammad Rezay Haghdoost et al. “Mitigation of Pressure Fluctuations From an Array of Pulse Detonation Combustors”. In: *Journal of Engineering for Gas Turbines and Power* 143.7 (July 2021). ISSN: 0742-4795. DOI: 10.1115/1.4049857. URL: <https://asmedigitalcollection.asme.org/gasturbinespower/article/143/7/071011/1096720/Mitigation-of-Pressure-Fluctuations-From-an-Array>.
- [15] Vijay Anand et al. “Longitudinal pulsed detonation instability in a rotating detonation combustor”. In: *Experimental Thermal and Fluid Science* 77 (2016), pp. 212–225. ISSN: 08941777. DOI: 10.1016/j.expthermflusci.2016.04.025. URL: <http://dx.doi.org/10.1016/j.expthermflusci.2016.04.025>.
- [16] Fatma Cansu Yücel. “Shockless explosion combustion - Controlled autoignition in stratified mixtures for pressure gain combustion”. PhD thesis. Berlin: Technische Universität Berlin, 2021. DOI: 10.14279/depositonce-12246. URL: <http://dx.doi.org/10.14279/depositonce-12246>.
- [17] Dean P. Petters and James L. Felder. “Engine system performance of pulse detonation concepts using the NPSS program”. In: *38th AIAA/ASME/SAE/ASEE Joint Propulsion Conference and Exhibit*. 2002. ISBN: 9781624101151. DOI: 10.2514/6.2002-3910.
- [18] Scott M. Jones and Daniel E. Paxson. “Potential benefits to commercial propulsion systems from pressure gain combustion”. In: *49th AIAA/ASME/SAE/ASEE Joint Propulsion Conference*. 2013. ISBN: 9781624102226. DOI: 10.2514/6.2013-3623.
- [19] Frederick Schauer, Royce Bradley, and John Hoke. “Interaction Of a PDE With A Turbine”. In: *41st Aerospace Sciences Meeting and Exhibit*. January. Reston, Virginia: American Institute of Aeronautics and Astronautics, Jan. 2003, pp. 2003–0891. ISBN: 978-1-62410-099-4. DOI: 10.2514/6.2003-891. URL: <https://arc.aiaa.org/doi/10.2514/6.2003-891>.
- [20] John Hoke et al. “Integration of a pulsed detonation engine with an ejector pump and with a turbo-charger as methods to self-aspirate”. In: *40th AIAA Aerospace Sciences Meeting & Exhibit*. January. Reston, Virginia: American Institute of Aeronautics and Astronautics, Jan. 2002. DOI: 10.2514/6.2002-615. URL: <https://arc.aiaa.org/doi/10.2514/6.2002-615>.
- [21] Kurt Rouser et al. “Time-Accurate Flow Field and Rotor Speed Measurements of a Pulsed Detonation Driven Turbine”. In: *49th AIAA Aerospace Sciences Meeting including the New Horizons Forum and Aerospace Exposition*. January. Reston, Virginia: American Institute of Aeronautics and Astronautics, Jan. 2011, pp. 1–16. ISBN: 978-1-

- 60086-950-1. DOI: 10.2514/6.2011-577. URL: <http://arc.aiaa.org/doi/10.2514/6.2011-577>.
- [22] Kurt P. Rouser et al. “Experimental performance evaluation of a turbine driven by pulsed detonations”. In: *51st AIAA Aerospace Sciences Meeting including the New Horizons Forum and Aerospace Exposition 2013*. 2013. ISBN: 9781624101816. DOI: 10.2514/6.2013-1212.
- [23] Adam Rasheed, Anthony Furman, and Anthony Dean. “Experimental Investigations of an Axial Turbine Driven by a Multi-Tube Pulsed Detonation Combustor System”. In: *41st AIAA/ASME/SAE/ASEE Joint Propulsion Conference & Exhibit*. July. Reston, Virginia: American Institute of Aeronautics and Astronautics, July 2005, pp. 1–13. ISBN: 978-1-62410-063-5. DOI: 10.2514/6.2005-4209. URL: <http://arc.aiaa.org/doi/abs/10.2514/6.2005-4209>.
- [24] Adam Rasheed, Anthony H. Furman, and Anthony J. Dean. “Experimental Investigations of the Performance of a Multitube Pulse Detonation Turbine System”. In: *Journal of Propulsion and Power* 27.3 (2011), pp. 586–596. ISSN: 0748-4658. DOI: 10.2514/1.B34013. URL: <http://arc.aiaa.org/doi/abs/10.2514/1.B34013>.
- [25] Aaron Glaser, Nicholas Caldwell, and Ephraim Gutmark. “Performance of an Axial Flow Turbine Driven by Multiple Pulse Detonation Combustors”. In: *45th AIAA Aerospace Sciences Meeting and Exhibit* January (2007), pp. 1–10. DOI: 10.2514/6.2007-1244. URL: <http://arc.aiaa.org/doi/10.2514/6.2007-1244>.
- [26] Vijay Anand et al. “Investigation of pulse detonation combustors — Axial turbine system”. In: *Aerospace Science and Technology* 93 (Oct. 2019), p. 105350. ISSN: 12709638. DOI: 10.1016/j.ast.2019.105350. URL: <https://doi.org/10.1016/j.ast.2019.105350> <https://linkinghub.elsevier.com/retrieve/pii/S1270963819303189>.
- [27] Philip Panicker et al. “Application of a Pulsed Detonation Engine for Electric Power Generation”. In: *45th AIAA Aerospace Sciences Meeting and Exhibit*. Vol. 21. January. Reston, Virginia: American Institute of Aeronautics and Astronautics, Jan. 2007, pp. 14906–14918. ISBN: 978-1-62410-012-3. DOI: 10.2514/6.2007-1246. URL: <https://arc.aiaa.org/doi/10.2514/6.2007-1246>.
- [28] Hua Qiu et al. “Propulsive Performance of Ideal Detonation Turbine Based Combined Cycle Engine”. In: *Journal of Engineering for Gas Turbines and Power* 134.8 (2012), p. 081201. ISSN: 07424795. DOI: 10.1115/1.4006483. URL: <http://gasturbinespower.asmedigitalcollection.asme.org/article.aspx?articleid=1430047>.
- [29] Hua Qiu, Cha Xiong, and Longxi Zheng. “Experimental investigation of an air-breathing pulse detonation turbine prototype engine”. In: *Applied Thermal Engineering* 104 (2016), pp. 596–602. ISSN: 13594311. DOI: 10.1016/j.applthermaleng.2016.05.077. URL: <http://dx.doi.org/10.1016/j.applthermaleng.2016.05.077>.
- [30] Xiaofeng Li et al. “Experimental investigations on the power extraction of a turbine driven by a pulse detonation combustor”. In: *Chinese Journal of Aeronautics* 26.6

REFERENCES

- (2013), pp. 1353–1359. ISSN: 10009361. DOI: 10.1016/j.cja.2013.07.015. URL: <http://dx.doi.org/10.1016/j.cja.2013.07.015>.
- [31] A. St. George et al. “Experimental Comparison of Axial Turbine Performance Under Steady and Pulsating Flows”. In: *Journal of Turbomachinery* 136.11 (2014), p. 111005. ISSN: 0889-504X. DOI: 10.1115/1.4028115. URL: <http://turbomachinery.asmedigitalcollection.asme.org/article.aspx?doi=10.1115/1.4028115>.
- [32] Mark Fernelius et al. “Effect of Periodic Pressure Pulses on Axial Turbine Performance”. In: *49th AIAA/ASME/SAE/ASEE Joint Propulsion Conference*. Reston, Virginia: American Institute of Aeronautics and Astronautics, July 2013, pp. 1–15. ISBN: 978-1-62410-222-6. DOI: 10.2514/6.2013-3687. URL: <http://arc.aiaa.org/doi/10.2514/6.2013-3687>.
- [33] Mark H Fernelius and Steven E Gorrell. “Predicting Efficiency of a Turbine Driven by Pulsing Flow”. In: *Volume 2A: Turbomachinery*. 50787. ASME, June 2017, V02AT40A008. ISBN: 978-0-7918-5078-7. DOI: 10.1115/GT2017-63490. URL: <http://dx.doi.org/10.1115/GT2017-63490%20http://proceedings.asmedigitalcollection.asme.org/proceeding.aspx?doi=10.1115/GT2017-63490>.
- [34] Mark H. Fernelius and Steven E. Gorrell. “Mapping Efficiency of a Pulsing Flow-Driven Turbine”. In: *Journal of Fluids Engineering* 142.6 (June 2020), pp. 1–8. ISSN: 0098-2202. DOI: 10.1115/1.4045993. URL: <https://asmedigitalcollection.asme.org/fluidsengineering/article/doi/10.1115/1.4045993/1072680/Mapping-Efficiency-of-a-Pulsing-FlowDriven-Turbine>.
- [35] Mark H. Fernelius and Steven E. Gorrell. “Design of a Pulsing Flow Driven Turbine”. In: *Journal of Fluids Engineering, Transactions of the ASME* 143.4 (2021), pp. 1–9. ISSN: 1528901X. DOI: 10.1115/1.4049114.
- [36] F. Bakhtiari and H.-P. Schiffer. “Numerical approach to the modelling of transient interaction of prospective combustor concepts and conventional high pressure turbines”. In: *Propulsion and Power Research* 8.1 (Mar. 2019), pp. 1–12. ISSN: 2212540X. DOI: 10.1016/j.jprr.2019.01.008. URL: <http://dx.doi.org/10.1016/j.jprr.2019.01.008%20https://linkinghub.elsevier.com/retrieve/pii/S2212540X19300082>.
- [37] Dale Van Zante, Edmane Envia, and Mark G. Turner. “The Attenuation of a Detonation Wave By an Aircraft Engine Axial Turbine”. In: *ISABE*. September. 2007, pp. 1–12. URL: <http://ntrs.nasa.gov/archive/nasa/casi.ntrs.nasa.gov/20070034924.pdf>.
- [38] Ambady Suresh, Douglas C. Hofer, and Venkat E. Tangirala. “Turbine Efficiency for Unsteady, Periodic Flows”. In: *Journal of Turbomachinery* 134.3 (2012), p. 034501. ISSN: 0889504X. DOI: 10.1115/1.4003246. URL: <http://turbomachinery.asmedigitalcollection.asme.org/article.aspx?articleid=1468846>.
- [39] V. E. Tangirala and A. J. Dean. “Performance estimations of a pulse detonation engine with exit nozzle”. In: *Collection of Technical Papers - AIAA/ASME/SAE/ASEE 42nd Joint Propulsion Conference*. 2006. ISBN: 1563478188. DOI: 10.2514/6.2006-4792.

- [40] Carlos Xisto et al. “The efficiency of a pulsed detonation combustor–axial turbine integration”. In: *Aerospace Science and Technology* 82-83. August (Nov. 2018), pp. 80–91. ISSN: 12709638. DOI: 10.1016/j.ast.2018.08.038. URL: <https://doi.org/10.1016/j.ast.2018.08.038> <https://linkinghub.elsevier.com/retrieve/pii/S1270963818305054>.
- [41] Tae Hyeong Yi et al. “Propulsive performance of a continuously rotating detonation engine”. In: *Journal of Propulsion and Power* (2011). ISSN: 15333876. DOI: 10.2514/1.46686.
- [42] Piotr Wolański. “Detonative propulsion”. In: *Proceedings of the Combustion Institute* (2013). ISSN: 15407489. DOI: 10.1016/j.proci.2012.10.005.
- [43] S. M. Frolov, A. V. Dubrovskii, and V. S. Ivanov. “Three-dimensional numerical simulation of operation process in rotating detonation engine”. In: 2013. DOI: 10.1051/eucass/201304467.
- [44] Jorge Sousa, Guillermo Paniagua, and Elena Collado Morata. “Thermodynamic analysis of a gas turbine engine with a rotating detonation combustor”. In: *Applied Energy* 195 (2017), pp. 247–256. ISSN: 03062619. DOI: 10.1016/j.apenergy.2017.03.045. URL: <http://dx.doi.org/10.1016/j.apenergy.2017.03.045>.
- [45] Peter A. Strakey et al. “Computationally quantifying loss mechanisms in a rotating detonation engine”. In: *54th AIAA Aerospace Sciences Meeting*. 2016. ISBN: 9781624103933. DOI: 10.2514/6.2016-0900.
- [46] Chandrashekhhar Sonwane et al. “Recent Advances in Power Cycles Using Rotating Detonation Engines with Subcritical and Supercritical CO₂”. In: *The 4th International Symposium - Supercritical CO₂ Power Cycles*. 2014.
- [47] Douglas A. Schwer, Christopher M. Brophy, and Robert H. Kelso. “Pressure Characteristics of an Aerospike Nozzle in a Rotating Detonation Engine”. In: *2018 Joint Propulsion Conference*. Reston, Virginia: American Institute of Aeronautics and Astronautics, July 2018, pp. 1–16. ISBN: 978-1-62410-570-8. DOI: 10.2514/6.2018-4968. URL: <https://arc.aiaa.org/doi/10.2514/6.2018-4968>.
- [48] S. L. Dixon and C. A. Hall. *Fluid mechanics and thermodynamics of turbomachinery, 7th edition*. 2013. ISBN: 9780124159549. DOI: 10.1016/C2011-0-05059-7.
- [49] Tae-Hyeong Yi et al. “Effect of Nozzle Shapes on the Performance of Continuously-Rotating Detonation Engine”. In: *48th AIAA Aerospace Sciences Meeting*. Orlando, Florida, Jan. 2010. ISBN: 978-1-60086-959-4. DOI: 10.2514/6.2010-152.
- [50] P. Wolański. “Application of the Continuous Rotating Detonation to Gas Turbine”. In: *Applied Mechanics and Materials* 782 (2015), pp. 3–12. ISSN: 1662-7482. DOI: 10.4028/www.scientific.net/AMM.782.3.
- [51] Piotr Kalina et al. “Report on the implementation of the POIG project, turbine engine with a detonation combustion chamber”. In: *Journal of KONES. Powertrain and Transport* 23.2 (Jan. 2016), pp. 177–184. ISSN: 1231-4005. DOI: 10.5604/12314005.1213590. URL: <http://10048.indexcopernicus.com/abstracted.php?level=5&ICID=1213590>.

REFERENCES

- [52] Hyunseung Rhee, Chikara Ishiyama, and Junichi Higashi. “Experimental Study on a Rotating Detonation Turbine Engine with an Axial Turbine”. In: *26th ICDERS*. Boston, MA, USA, 2017, pp. 1–6. URL: http://icders2017.com/wp-content/uploads/26th_ICDERS_Program/Oral/26th%20ICDERS_submission_1080.pdf.
- [53] Shengbing Zhou et al. “Experimental study on a rotating detonation combustor with an axial-flow turbine”. In: *Acta Astronautica* 151 (Oct. 2018), pp. 7–14. ISSN: 00945765. DOI: 10.1016/j.actaastro.2018.05.047. URL: <https://linkinghub.elsevier.com/retrieve/pii/S009457651830479X>.
- [54] Andrew Naples et al. “RDE Implementation into an Open-Loop T63 Gas Turbine Engine”. In: *55th AIAA Aerospace Sciences Meeting*. January. Reston, Virginia: American Institute of Aeronautics and Astronautics, Jan. 2017, pp. 1–9. ISBN: 978-1-62410-447-3. DOI: 10.2514/6.2017-1747. URL: <http://arc.aiaa.org/doi/10.2514/6.2017-1747>.
- [55] J. Kindracki, P. Wolański, and Z. Gut. “Experimental research on the rotating detonation in gaseous fuels-oxygen mixtures”. In: *Shock Waves* 21.2 (2011), pp. 75–84. ISSN: 09381287. DOI: 10.1007/s00193-011-0298-y.
- [56] Daniel E. Paxson and Andrew Naples. “Numerical and Analytical Assessment of a Coupled Rotating Detonation Engine and Turbine Experiment”. In: *55th AIAA Aerospace Sciences Meeting*. Reston, Virginia: American Institute of Aeronautics and Astronautics, Jan. 2017, pp. 1–13. ISBN: 978-1-62410-447-3. DOI: 10.2514/6.2017-1746. URL: <http://arc.aiaa.org/doi/10.2514/6.2017-1746>.
- [57] Andrew Naples et al. “T63 Turbine Response to Rotating Detonation Combustor Exhaust Flow”. In: *Journal of Engineering for Gas Turbines and Power* 141.2 (Feb. 2019), pp. 1–8. ISSN: 0742-4795. DOI: 10.1115/1.4041135. URL: <https://asmedigitalcollection.asme.org/gasturbinespower/article/doi/10.1115/1.4041135/476153/T63-Turbine-Response-to-Rotating-Detonation>.
- [58] Venkat Athmanathan et al. “Development of a turbine-integrated high-pressure optical rde (Thor) for time-resolved fluid dynamic measurements using high-speed optical diagnostics”. In: *AIAA Propulsion and Energy Forum and Exposition, 2019* (2019), pp. 1–15. DOI: 10.2514/6.2019-4041.
- [59] James Braun et al. “Characterization of an integrated nozzle and supersonic axial turbine with a rotating detonation combustor”. In: *AIAA Propulsion and Energy 2019 Forum*. August. Reston, Virginia: American Institute of Aeronautics and Astronautics, Aug. 2019, pp. 1–11. ISBN: 978-1-62410-590-6. DOI: 10.2514/6.2019-3873. URL: <https://arc.aiaa.org/doi/10.2514/6.2019-3873>.
- [60] Z. Liu, J. Braun, and G. Paniagua. “Characterization of a Supersonic Turbine Downstream of a Rotating Detonation Combustor”. In: *Journal of Engineering for Gas Turbines and Power* 141.3 (Mar. 2019), pp. 1536–1539. ISSN: 0742-4795. DOI: 10.1115/1.4040815. URL: <https://asmedigitalcollection.asme.org/gasturbinespower/article/doi/10.1115/1.4040815/366412/Characterization-of-a-Supersonic-Turbine>.

- [61] Zifei Ji et al. “Comprehensive Performance Analysis of the Turbofan with a Multi-Annular Rotating Detonation Duct Burner”. In: *Journal of Engineering for Gas Turbines and Power* 142.2 (2020). ISSN: 15288919. DOI: 10.1115/1.4045518.
- [62] F. A. Bykovskii, V. V. Mitrofanov, and E. F. Vedernikov. “Continuous detonation combustion of fuel-air mixtures”. In: *Combustion, Explosion and Shock Waves* (1997). ISSN: 00105082. DOI: 10.1007/BF02671875.
- [63] F. A. Bykovskii et al. “Detonation burning of anthracite and lignite particles in a flow-type radial combustor”. In: *Combustion, Explosion and Shock Waves* (2016). ISSN: 15738345. DOI: 10.1134/S0010508216060101.
- [64] F. A. Bykovskii et al. “Detonation combustion of a hydrogen–oxygen mixture in a plane–radial combustor with exhaustion toward the center”. In: *Combustion, Explosion and Shock Waves* (2016). ISSN: 15738345. DOI: 10.1134/S0010508216040080.
- [65] Vijay Anand and Ephraim Gutmark. “Rotating detonation combustors and their similarities to rocket instabilities”. In: *Progress in Energy and Combustion Science* 73 (July 2019), pp. 182–234. ISSN: 03601285. DOI: 10.1016/j.pecs.2019.04.001. URL: <https://linkinghub.elsevier.com/retrieve/pii/S0360128518301783>.
- [66] Riley Huff et al. “Design and Operation of a Radial Rotating Detonation Engine”. In: *Journal of Propulsion and Power* 35.6 (Nov. 2019), pp. 1143–1150. ISSN: 1533-3876. DOI: 10.2514/1.B37578. URL: <https://arc.aiaa.org/doi/10.2514/1.B37578>.
- [67] Riley Huff et al. “Exit Condition Measurements of a Radial Rotating Detonation Engine Bleed Air Turbine”. In: *AIAA Scitech 2019 Forum*. January. Reston, Virginia: American Institute of Aeronautics and Astronautics, Jan. 2019, pp. 1–12. ISBN: 978-1-62410-578-4. DOI: 10.2514/6.2019-1011. URL: <https://arc.aiaa.org/doi/10.2514/6.2019-1011>.
- [68] Junichi Higashi et al. “Experimental Study of the Disk-Shaped Rotating Detonation Turbine Engine”. In: *55th AIAA Aerospace Sciences Meeting*. January. Reston, Virginia: American Institute of Aeronautics and Astronautics, Jan. 2017, pp. 1–11. ISBN: 978-1-62410-447-3. DOI: 10.2514/6.2017-1286. URL: <http://arc.aiaa.org/doi/10.2514/6.2017-1286>.
- [69] Chikara Ishiyama et al. “Experimental Study of Research of Centrifugal-Compressor-Radial-Turbine Type Rotating Detonation Engine”. In: *52nd AIAA/SAE/ASEE Joint Propulsion Conference*. Vol. 2. Reston, Virginia: American Institute of Aeronautics and Astronautics, July 2016, pp. 1–6. ISBN: 978-1-62410-406-0. DOI: 10.2514/6.2016-5103. URL: <http://arc.aiaa.org/doi/10.2514/6.2016-5103>.
- [70] Nick DeBarmore et al. “Nozzle Guide Vane Integration into Rotating Detonation Engine”. In: *51st AIAA Aerospace Sciences Meeting including the New Horizons Forum and Aerospace Exposition*. January. Reston, Virginia: American Institute of Aeronautics and Astronautics, Jan. 2013, pp. 7–10. ISBN: 978-1-62410-181-6. DOI: 10.2514/6.2013-1030. URL: <https://arc.aiaa.org/doi/10.2514/6.2013-1030>.

REFERENCES

- [71] Daniel J. Welsh et al. “RDE integration with T63 turboshaft engine components”. In: *52nd AIAA Aerospace Sciences Meeting - AIAA Science and Technology Forum and Exposition, SciTech 2014*. 2014. ISBN: 9781624102561. DOI: 10.2514/6.2014-1316.
- [72] Nick D DeBarmore. “Characterization of Rotating Detonation Engine Exhaust Through Nozzle Guide Vanes”. PhD thesis. Air Force Institute of Technology, 2013, p. 63.
- [73] Eric Bach et al. “Rotating Detonation Wave Direction and the Influence of Nozzle Guide Vane Inclination”. In: *AIAA Journal* (2021), pp. 1–12. ISSN: 0001-1452. DOI: 10.2514/1.j060594.
- [74] Eric Bach et al. “Development of an Instrumented Guide Vane Set for RDC Exhaust Flow Characterization”. In: *2018 Joint Propulsion Conference*. Reston, Virginia: American Institute of Aeronautics and Astronautics, July 2018. ISBN: 978-1-62410-570-8. DOI: 10.2514/6.2018-4479. URL: <https://arc.aiaa.org/doi/10.2514/6.2018-4479>.
- [75] Richard Bluemner et al. “Single and Counter-Rotating Wave Modes in an RDC”. In: *2018 AIAA Aerospace Sciences Meeting*. January. Reston, Virginia: American Institute of Aeronautics and Astronautics, Jan. 2018. ISBN: 978-1-62410-524-1. DOI: 10.2514/6.2018-1608. URL: <https://arc.aiaa.org/doi/10.2514/6.2018-1608>.
- [76] Shengbing Zhou et al. “Effects of a turbine guide vane on hydrogen-air rotating detonation wave propagation characteristics”. In: *International Journal of Hydrogen Energy* 42.31 (Aug. 2017), pp. 20297–20305. ISSN: 03603199. DOI: 10.1016/j.ijhydene.2017.06.115. URL: <https://linkinghub.elsevier.com/retrieve/pii/S0360319917324321>.
- [77] Wan li Wei et al. “Influence of propagation direction on operation performance of rotating detonation combustor with turbine guide vane”. In: *Defence Technology* xxxx (2020). ISSN: 22149147. DOI: 10.1016/j.dt.2020.08.009. URL: <https://doi.org/10.1016/j.dt.2020.08.009>.
- [78] Yuwen Wu et al. “Experimental research on the performance of a rotating detonation combustor with a turbine guide vane”. In: *Energy* 218.March (Mar. 2021), p. 119580. ISSN: 03605442. DOI: 10.1016/j.energy.2020.119580. URL: <https://linkinghub.elsevier.com/retrieve/pii/S0360544220326876>.
- [79] D. G. Ainley and C. R. Mathieson. *A Method of Performance Estimation for Axial-Flow Turbines*. Tech. rep. 2974. 1951. URL: <http://citeseerx.ist.psu.edu/viewdoc/download?doi=10.1.1.226.7624&rep=rep1&type=pdf>.
- [80] S F Smith. “A Simple Correlation of Turbine Efficiency”. In: *The Journal of the Royal Aeronautical Society* 69.655 (1965), pp. 467–470. ISSN: 0368-3931. DOI: DOI: 10.1017/S0001924000059108.
- [81] J. D. Denton. “Throughflow Calculations for Transonic Axial Flow Turbines”. In: *Journal of Engineering for Power* 100.2 (Apr. 1978), pp. 212–218. ISSN: 0022-0825. DOI: 10.1115/1.3446336. URL: <https://asmedigitalcollection.asme.org/gasturbinespower/article/100/2/212/403866/Throughflow-Calculations-for-Transonic-Axial-Flow>.

- [82] T. Schobeiri and M. Abouelkheir. “Row-by-row off-design performance calculation method for turbines”. In: *Journal of Propulsion and Power* (1992). ISSN: 07484658. DOI: 10.2514/3.23555.
- [83] Meng Soon Chiong et al. “Unsteady Performance Prediction of a Single Entry Mixed Flow Turbine Using 1-D Gas Dynamic Code Extended With Meanline Model”. In: *Volume 5: Manufacturing Materials and Metallurgy; Marine; Microturbines and Small Turbomachinery; Supercritical CO₂ Power Cycles* 5 (2012), p. 781. DOI: 10.1115/GT2012-69176. URL: <http://www.scopus.com/inward/record.url?eid=2-s2.0-84881182578&partnerID=tZ0tx3y1>.
- [84] Simone Rosa Taddei. “Time-marching solution of transonic flows at axial turbomachinery meanline”. In: *Proceedings of the Institution of Mechanical Engineers, Part G: Journal of Aerospace Engineering* (Dec. 2020), p. 095441002097735. ISSN: 0954-4100. DOI: 10.1177/0954410020977350. URL: <http://journals.sagepub.com/doi/10.1177/0954410020977350>.
- [85] A Yu Tkachenko, Ya A. Ostapyuk, and E. P. Filinov. “Mean-line Modeling of an Axial Turbine”. In: *IOP Conference Series: Materials Science and Engineering* 302.1 (Jan. 2018), p. 012038. ISSN: 1757-8981. DOI: 10.1088/1757-899X/302/1/012038. URL: <https://iopscience.iop.org/article/10.1088/1757-899X/302/1/012038>.
- [86] Ronald H Aungier. *TURBINE AERODYNAMICS AXIAL-FLOW AND RADIAL-INFLOW TURBINE DESIGN AND ANALYSIS*. 2005.
- [87] G. F. C. Rogers H.I.H. Saravanamuttoo H. Cohen and P. V. Straznicky A.C. Nix. *Gas Turbine Theory SEVENTH EDITION Gas Turbine Theory*. 2017, p. 606. ISBN: 9781292093093.
- [88] L Fielding. *Turbine design: The effect on axial flow turbine performance of parameter variation*. English. United States: American Society of Mechanical Engineers International, New York, NY (US), 2000.
- [89] S. C. Kacker and U. Okapuu. “A Mean Line Prediction Method for Axial Flow Turbine Efficiency”. In: *Journal of Engineering for Power* 104.1 (1982), p. 111. ISSN: 00220825. DOI: 10.1115/1.3227240. URL: <http://gasturbinespower.asmedigitalcollection.asme.org/article.aspx?articleid=1420407>.
- [90] J. Dunham and P. M. Came. “Improvements to the Ainley-Mathieson Method of Turbine Performance Prediction”. In: *Journal of Engineering for Power* 92.3 (July 1970), pp. 252–256. ISSN: 0022-0825. DOI: 10.1115/1.3445349. URL: <https://asmedigitalcollection.asme.org/gasturbinespower/article/92/3/252/404009/Improvements-to-the-AinleyMathieson-Method-of>.
- [91] Robert P. Benedict and Nicola A. Carlucci. “Losses across Abrupt Enlargements and Contractions”. In: *Handbook of Specific Losses in Flow Systems*. Boston, MA: Springer US, 1966, pp. 23–26. DOI: 10.1007/978-1-4684-6063-6_6. URL: http://link.springer.com/10.1007/978-1-4684-6063-6_6.
- [92] Joel Sjödin. “Meanline method for design and off-design turbine performance predictions”. PhD thesis. 2019. URL: www.energy.lth.se.

REFERENCES

- [93] B. I. Mamaev and V. L. Murashko. “Calculation of gas turbine characteristic”. In: *Thermal Engineering* 63.4 (2016), pp. 239–245. ISSN: 00406015. DOI: 10.1134/S0040601516040054.
- [94] Meinhard T. Schobeiri. *Turbomachinery flow physics and dynamic performance*. Vol. 9783642246. 2012, pp. 1–725. ISBN: 9783642246753. DOI: 10.1007/978-3-642-24675.
- [95] Glenn Douglas Garrard. “The Aerodynamic Turbine Engine Code for the Analysis of Transient and Dynamic Gas Turbine Engine System Operations”. PhD thesis. University of Tennessee, Knoxville, 1995. URL: http://trace.tennessee.edu/utk_graddiss/1605.
- [96] M. S. Chiong et al. “Integration of meanline and one-dimensional methods for prediction of pulsating performance of a turbocharger turbine”. In: *Energy Conversion and Management* 81 (2014), pp. 270–281. ISSN: 01968904. DOI: 10.1016/j.enconman.2014.01.043. URL: <http://dx.doi.org/10.1016/j.enconman.2014.01.043>.
- [97] Phillip Berndt. “Mathematical Modeling of the Shockless Explosion Combustion”. PhD thesis. Freie Universität Berlin, 2016.
- [98] Phillip Berndt and Rupert Klein. “Modeling the kinetics of the Shockless Explosion Combustion”. In: *Combustion and Flame* 175 (2017), pp. 16–26. ISSN: 15562921. DOI: 10.1016/j.combustflame.2016.06.029. URL: <http://dx.doi.org/10.1016/j.combustflame.2016.06.029>.
- [99] Louise Dittmar and Panagiotis Stathopoulos. “Numerical Analysis of the Stability and Operation of an Axial Compressor Connected to an Array of Pulsed Detonation Combustors”. In: *Volume 5: Controls, Diagnostics, and Instrumentation; Cycle Innovations; Cycle Innovations: Energy Storage*. American Society of Mechanical Engineers, Sept. 2020. ISBN: 978-0-7918-8414-0. DOI: 10.1115/GT2020-15381. URL: <https://asmedigitalcollection.asme.org/GT/proceedings/GT2020/84140/Virtual,%20online/1094889>.
- [100] Richard Bluemner et al. “Effect of inlet and outlet boundary conditions on rotating detonation combustion”. In: *Combustion and Flame* 216 (June 2020), pp. 300–315. ISSN: 00102180. DOI: 10.1016/j.combustflame.2020.03.011. URL: <http://www.sciencedirect.com/science/article/pii/S0010218020301127> <https://linkinghub.elsevier.com/retrieve/pii/S0010218020301127>.
- [101] Richard Blümner. “Operating mode dynamics in rotating detonation combustors”. PhD thesis. Berlin: Technische Universität Berlin, 2020. DOI: 10.14279/depositonce-10401. URL: <http://dx.doi.org/10.14279/depositonce-10401>.
- [102] Jason C. Shank et al. “Development and testing of a modular rotating detonation engine”. In: *50th AIAA Aerospace Sciences Meeting Including the New Horizons Forum and Aerospace Exposition*. 2012. DOI: 10.2514/6.2012-120.
- [103] Richard Bluemner et al. “Experimental Study of Reactant Mixing in Model Rotating Detonation Combustor Geometries”. In: *Flow, Turbulence and Combustion* (2018). ISSN: 15731987. DOI: 10.1007/s10494-018-9966-7.

- [104] Eric Bach. “Stagnation Pressure Gain in Rotating Detonation Combustors”. PhD thesis. Technische Universität Berlin, 2022.
- [105] Michael P Burke et al. “Comprehensive H₂/O₂ kinetic model for high-pressure combustion”. In: *International Journal of Chemical Kinetics* 44.7 (July 2012), pp. 444–474. ISSN: 05388066. DOI: 10.1002/kin.20603. URL: <https://onlinelibrary.wiley.com/doi/10.1002/kin.20603>.
- [106] N. M. Marinov, C. K. Westbrook, and W. J. Pitz. “Detailed and Global Chemical Kinetics Model for Hydrogen”. In: *Transport phenomena in combustion* (1996). URL: <https://www.osti.gov/servlets/purl/90098>.
- [107] Charles K. Westbrook and Frederick L. Dryer. “Chemical kinetic modeling of hydrocarbon combustion”. In: *Progress in Energy and Combustion Science* 10.1 (Jan. 1984), pp. 1–57. ISSN: 03601285. DOI: 10.1016/0360-1285(84)90118-7. URL: <https://linkinghub.elsevier.com/retrieve/pii/0360128584901187>.
- [108] Francis Westley. “Table of Recommended Rate Constants for Chemical Reactions Occurring in Combustion”. In: *National Bureau of Standards, National Standard Reference Data Series* (1980). ISSN: 00831840.
- [109] Phillip Berndt, Rupert Klein, and C. Oliver Paschereit. “A kinetics model for the shockless explosion combustion”. In: *Proceedings of the ASME Turbo Expo 4B-2016* (2016), pp. 1–8. DOI: 10.1115/GT2016-57678.
- [110] Michael P. Burke et al. “Comprehensive H₂/O₂ kinetic model for high-pressure combustion”. In: *International Journal of Chemical Kinetics* (2012). ISSN: 05388066. DOI: 10.1002/kin.20603.
- [111] Nicolai Neumann et al. “A fast approach for unsteady compressor performance simulation under boundary condition caused by pressure gain combustion”. In: *Applied Thermal Engineering* (June 2021), p. 117223. ISSN: 13594311. DOI: 10.1016/j.applthermaleng.2021.117223. URL: <https://www.sciencedirect.com/science/article/pii/S135943112100661X> <https://linkinghub.elsevier.com/retrieve/pii/S135943112100661X>.
- [112] A.G. Straatman and R.J. Martinuzzi. “A study on suppression of vortex shedding from a square cylinder near a wall”. In: *Engineering Turbulence Modelling and Experiments* 5. Elsevier, 2002, pp. 403–411. DOI: 10.1016/B978-008044114-6/50038-7. URL: <https://doi.org/10.1016/B978-008044114-6/50038-7> <https://linkinghub.elsevier.com/retrieve/pii/B9780080441146500387>.
- [113] Jiri Blazek. *Computational Fluid Dynamics: Principles and Applications: Third Edition*. 2015. ISBN: 9780128011720. DOI: 10.1016/C2013-0-19038-1.
- [114] J. Rotta. “Statistische Theorie nichthomogener Turbulenz”. In: *Zeitschrift für Physik* (1951). ISSN: 14346001. DOI: 10.1007/BF01330059.
- [115] W. Rodi. “A New Algebraic Relation for Calculating the Reynolds Stresses”. In: *ZAMM - Journal of Applied Mathematics and Mechanics / Zeitschrift für Angewandte Mathematik und Mechanik* (1976). ISSN: 0044-2267. DOI: 10.1002/zamm.19765613093.

REFERENCES

- [116] B. BALDWIN and H. LOMAX. “Thin-layer approximation and algebraic model for separated turbulentflows”. In: 1978. DOI: 10.2514/6.1978-257.
- [117] P. R. Spalart and S. R. Allmaras. “One-equation turbulence model for aerodynamic flows”. In: *Recherche aerospaciale* (1994). ISSN: 00341223. DOI: 10.2514/6.1992-439.
- [118] David C. Wilcox. “Reassessment of the scale-determining equation for advanced turbulence models”. In: *AIAA Journal* (1988). ISSN: 00011452. DOI: 10.2514/3.10041.
- [119] B. E. Launder and D. B. Spalding. “The numerical computation of turbulent flows”. In: *Computer Methods in Applied Mechanics and Engineering* (1974). ISSN: 00457825. DOI: 10.1016/0045-7825(74)90029-2.
- [120] J. E. Bardina, P. G. Huang, and T. J. Coakley. “Turbulence Modeling Validation, Testing, and Development”. In: *Nasa Technical Memorandum* (1997).
- [121] F. R. Menter. “Two-equation eddy-viscosity turbulence models for engineering applications”. In: *AIAA Journal* (1994). ISSN: 0029554X. DOI: 10.1016/0029-554X(80)90461-9.
- [122] P. A. Costa Rocha et al. “K- ω SST (shear stress transport) turbulence model calibration: A case study on a small scale horizontal axis wind turbine”. In: *Energy* (2014). ISSN: 03605442. DOI: 10.1016/j.energy.2013.11.050.
- [123] F. R. Menter. “Improved two-equation k- ω turbulence models for aerodynamic flows”. In: *NASA Technical Memorandum 103978* (1992), pp. 1–31. ISSN: 0001-1452. DOI: 10.2514/6.1993-2906.
- [124] F. R. Menter. “Zonal two equation κ - ω turbulence models for aerodynamic flows”. In: *AIAA 23rd Fluid Dynamics, Plasmadynamics, and Lasers Conference, 1993*. 1993. DOI: 10.2514/6.1993-2906.
- [125] Slawomir Koziel and Xin-She Yang, eds. *Computational Optimization, Methods and Algorithms*. Vol. 356. Studies in Computational Intelligence. Berlin, Heidelberg: Springer Berlin Heidelberg, 2011. ISBN: 978-3-642-20858-4. DOI: 10.1007/978-3-642-20859-1. URL: <http://link.springer.com/10.1007/978-3-642-20859-1>.
- [126] L. Jeff Hong and Xiaowei Zhang. “Surrogate-Based Simulation Optimization”. In: *Tutorials in Operations Research: Emerging Optimization Methods and Modeling Techniques with Applications*. 2021. DOI: 10.1287/educ.2021.0225.
- [127] Atharv Bhosekar and Marianthi Ierapetritou. *Advances in surrogate based modeling, feasibility analysis, and optimization: A review*. 2018. DOI: 10.1016/j.compchemeng.2017.09.017.
- [128] Alessandro Freddi and Mario Salmon. *Design Principles and Methodologies*. Springer Tracts in Mechanical Engineering. Cham: Springer International Publishing, 2019, pp. 1–297. ISBN: 978-3-319-95341-0. DOI: 10.1007/978-3-319-95342-7. URL: <http://link.springer.com/10.1007/978-3-319-95342-7>.
- [129] Aleksandar Jankovic, Gaurav Chaudhary, and Francesco Goia. “Designing the design of experiments (DOE) – An investigation on the influence of different factorial designs on the characterization of complex systems”. In: *Energy and Buildings* (2021). ISSN: 03787788. DOI: 10.1016/j.enbuild.2021.111298.

- [130] P K Pathak. “Simple random sampling”. In: *Sampling*. Vol. 6. Handbook of Statistics. Elsevier, 1988, pp. 97–109. DOI: [https://doi.org/10.1016/S0169-7161\(88\)06006-7](https://doi.org/10.1016/S0169-7161(88)06006-7). URL: <https://www.sciencedirect.com/science/article/pii/S0169716188060067>.
- [131] M. D. McKay, R. J. Beckman, and W. J. Conover. “Comparison of three methods for selecting values of input variables in the analysis of output from a computer code”. In: *Technometrics* (1979). ISSN: 15372723. DOI: 10.1080/00401706.1979.10489755.
- [132] Christiane Lemieux. *Monte Carlo and Quasi-Monte Carlo Sampling*. 2009. ISBN: 9780387781648.
- [133] Tien-Tsin Wong, Wai-Shing Luk, and Pheng-Ann Heng. “Sampling with Hammersley and Halton Points”. In: *Journal of Graphics Tools* (1997). ISSN: 1086-7651. DOI: 10.1080/10867651.1997.10487471.
- [134] Slawomir Koziel, David Echeverría Ciaurri, and Leifur Leifsson. *Computational Optimization, Methods and Algorithms*. Ed. by Slawomir Koziel and Xin-She Yang. Vol. 356. Studies in Computational Intelligence. Berlin, Heidelberg: Springer Berlin Heidelberg, 2011, pp. 33–59. ISBN: 978-3-642-20858-4. DOI: 10.1007/978-3-642-20859-1. URL: <http://link.springer.com/10.1007/978-3-642-20859-1>.
- [135] Nestor V. Queipo et al. *Surrogate-based analysis and optimization*. 2005. DOI: 10.1016/j.paerosci.2005.02.001.
- [136] Jack P.C. Kleijnen. *Regression and Kriging metamodels with their experimental designs in simulation: A review*. 2017. DOI: 10.1016/j.ejor.2016.06.041.
- [137] Zhong-Hua Han et al. “Weighted Gradient-Enhanced Kriging for High-Dimensional Surrogate Modeling and Design Optimization”. In: *AIAA Journal* 55.12 (Dec. 2017), pp. 4330–4346. ISSN: 0001-1452. DOI: 10.2514/1.J055842. URL: <https://arc.aiaa.org/doi/10.2514/1.J055842>.
- [138] Huanwei Xu, Liangwen Liu, and Miao Zhang. “Adaptive surrogate model-based optimization framework applied to battery pack design”. In: *Materials & Design* 195 (Oct. 2020), p. 108938. ISSN: 02641275. DOI: 10.1016/j.matdes.2020.108938. URL: <https://doi.org/10.1016/j.matdes.2020.108938><https://linkinghub.elsevier.com/retrieve/pii/S026412752030472X>.
- [139] Emilio Spedicato, Zunquan Xia, and Liwei Zhang. “Algorithms for Optimization”. In: *Encyclopedia of Optimization*. Boston, MA: Springer US, 2008, pp. 7–13. ISBN: 9780262039420. DOI: 10.1007/978-0-387-74759-0_{_}2. URL: http://link.springer.com/10.1007/978-0-387-74759-0_2.
- [140] Douglas C. Montgomery. *Montgomery: Design and Analysis of Experiments*. 2017.
- [141] L. P. Timko. *Energy Efficient Engine High Pressure Turbine Component Test Performance Report*. Tech. rep. General Electric Co. Cincinnati, OH, United States, 1984. URL: <https://ntrs.nasa.gov/citations/19900019237>.

REFERENCES

- [142] Majid Asli, Panagiotis Stathopoulos, and Christian Oliver Paschereit. “Effect of Blade Setting Angle on Damping Role of Turbine Guide Vanes Downstream of an RDC”. In: *Proceedings of the International Gas Turbine Congress 2019 Tokyo*. Tokyo, 2019. ISBN: 9784891110109.
- [143] Mohammad Rezay Haghdoost. “Pulse Detonation Exhaust and Methods for Damping its Transient Characteristic Vorwort”. PhD thesis. Technische Universität Berlin, 2021.
- [144] Mohammad Rezay Haghdoost et al. “Evaluation of shock dividers using numerical and experimental methods”. In: *AIAA Scitech 2020 Forum*. 2020. ISBN: 9781624105951. DOI: 10.2514/6.2020-0926.
- [145] James Braun, Guillermo Paniagua, and Francois Falempin. “Aerothermal Optimization of Bladeless Turbines”. In: *Journal of Engineering for Gas Turbines and Power* 143.3 (Mar. 2021), pp. 1–11. ISSN: 0742-4795. DOI: 10.1115/1.4049355. URL: <https://asmedigitalcollection.asme.org/gasturbinespower/article/doi/10.1115/1.4049355/1092417/Aerothermal-Optimization-of-Bladeless-Turbines>.



Associated Publications

Through the course of this thesis, eight research papers were prepared, presented, and published in peer-reviewed scientific journals and international conferences. Additionally, three internships and four Master theses were done and published under the author's supervision, closely related to the present dissertation. The associated papers are listed in reverse chronological order as follows.

1. Majid Asli, and Panagiotis Stathopoulos “An optimization methodology for turbines driven by pulsed detonation combustors”. In: *Journal of Engineering for Gas Turbines and Power* (Accepted).
2. Roman Klopsch, Niclas Garan, Myles Bohon, Eric Bach, Majid Asli, and Panagiotis Stathopoulos “2D Euler modeling of rotating detonation combustion in preparation for turbomachinery matching”. In: *AIAA 2022-0836. AIAA SCITECH 2022 Forum*, (2022). DOI: <https://doi.org/10.2514/6.2022-0836>.
3. Majid Asli, Niclas Garan, Nicolai Neumann, and Panagiotis Stathopoulos “A robust one-dimensional approach for the performance evaluation of turbines driven by pulsed detonation combustion”. In: *Journal of Energy Conversion and Management* 248, (2021), p. 114784. DOI: <https://doi.org/10.1016/j.enconman.2021.114784>.
4. Majid Asli, Panagiotis Stathopoulos, and Christian Oliver Paschereit. “Aerodynamic investigation of guide vane configurations downstream a rotating detonation combustor”. In: *Journal of Engineering for Gas Turbines and Power* 143. 6 (2021). DOI: <https://doi.org/10.1115/1.4049188>
5. Nicolai Neumann, Majid Asli, Niclas Garan, Dieter Peitsch, and Panagiotis Stathopoulos “A fast approach for unsteady compressor performance simulation under boundary condition caused by pressure gain combustion”. In: *Journal of Applied Thermal Engineering* 196, (2021), p. 117223. DOI: [10.1016/j.applthermaleng.2021.117223](https://doi.org/10.1016/j.applthermaleng.2021.117223).
6. Majid Asli, Panagiotis Stathopoulos, and Christian Oliver Paschereit “Investigation of stationary vanes aerodynamic performance under different RDC exhaust”. In: *Proceedings*

A. Associated Publications

of the 22nd Australasian Fluid Mechanics Conference AFMC2020, Published by The University of Queensland, (2020). DOI: 10.14264/9e7ac3e.

7. Majid Asli, Cleopatra Cuciumita, Panagiotis Stathopoulos, and Christian Oliver Paschereit. “Numerical investigation of a turbine guide vane exposed to a rotating detonation exhaust flow”. In: *Proceedings of the ASME Turbo Expo 2019*, (2019) Volume 2B, V02BT40A018. DOI: <https://doi.org/10.1115/GT2019-91263> .
8. Majid Asli, Panagiotis Stathopoulos, and Christian Oliver Paschereit “Effect of blade setting angle on damping role of turbine guide vanes downstream of an RDC”. In: *Proceedings of the International Gas Turbine Congress 2019 Tokyo*, (2019). ISBN: 978-4-89111-010-9.